Max-Planck-Institut für Polymerforschung

Max Planck Institute for Polymer Research

From the colloidal dispersion to the solid-state: Controlling properties by inter-particle distance and orientation

Dissertation

Zur Erlangung des Grades

“Doktor der Naturwissenschaften” (Dr. rer. nat.)

im Promotionsfach Chemie

am Fachbereich Chemie, Pharmazie und Geowissenschaften

der Johannes Gutenberg Universität in Mainz

Rebecca Momper

geboren in Mainz

Mainz, 2020

Diese Arbeit wurde in der Zeit von November 2016 bis Februar 2020 am Max Planck Institut für Polymerforschung unter der Betreuung von Frau Prof. Dr. Katharina Landfester, Herrn Dr. Andreas Riedinger und Herrn Dr. Markus Bannwarth durchgeführt.

Erster Gutachterin: Prof. Dr. Katharina Landfester

Zweiter Gutachter: Prof. Dr. Michael Maskos

Erklärung:

Hiermit versichere ich, die vorliegende Arbeit selbstständig und ohne Benutzung anderer als der angegebenen Hilfsmitte angefertigt zu haben. Alle Stellen, die wörtlich oder sinngemäß aus Veröffentlichungen oder anderen Quellen entnommen sind, wurde als solche eindeutig kenntlich gemacht. Diese Arbeit ist in gleicher oder ähnlicher Form noch nicht veröffentlicht und auch keiner anderen Prüfungsbehörde vorgelegt worden.

Rebecca Momper

Mainz, April 2020

Danksagung

Prof. Dr. Katharina Landfester bin ich dankbar für die Möglichkeit meine Doktorarbeit in ihrem Arbeitskreis durchzuführen und in einem bunten international geprägten und interdisziplinären Arbeitsumfeld zu arbeiten. Besonders danke ich ihr für die Möglichkeit im Max Planck - UT Center for Complex Fluid Dynamics mitzuwirken. Weiterhin möchte ich mich bedanken für die Ermöglichung der Teilnahme am Ada-Lovelace Programm. So konnte ich mich persönlich weiterentwickeln.

Bei Dr. Andreas Riedinger möchte ich mich für die herzliche Aufnahme in seine Arbeitsgruppe bedanken. Ebenso für seine Expertise und fachlichen Diskussionen, seine moralische Unterstützung sowie sein offenes Ohr bei fachlichen als auch bei anderen Problemen.

Auch möchte an dieser Stelle Dr. Markus Bannwarth für seine Betreuung im ersten Jahr der Doktorarbeit danken.

Gunnar Glasser gilt ein besonderer Dank für unzählige Stunden, die er für mich und meine Projekte am Rasterelektronenmikroskop verbracht hat. Auch dem restlichen Elektronenmikroskopie-Team und der Polymeranalytik gilt ein herzliches Dankeschön.

Meinen Kooperationspartnern danke ich ebenfalls. Ohne sie wäre die Umsetzung vieler Projekte nicht möglich gewesen. Im Besonderen danke ich Antonio Ibanez Landeta für die spannenden gemeinsamen Experimente am 3D-Drucker.

Nicht zu Letzt bedanke ich mich bei der gesamten Arbeitsgruppe für die sehr angenehme Atmosphäre. Ich werde die gemeinsame Zeit im Büro, Labor oder beim gemeinsamen Grillen vermissen. Besonders bedanke ich mich bei Timo Rheinberger, Stefan Peil, Jens Markwart und Mareike Deuker für die seelisch und moralische Unterstützung. Unsere Skifahrten werden hoffentlich zu einer Tradition.

Zum Abschluss möchte ich mich auch bei meiner Familie und meinem Freund Martin Frei bedanken für ihre stetige Unterstützung.

Der Vater lebt und das Kind ist gesund.

List of abbreviations

one-photon absorption	1PA
two-photon absorption	2PA
atomic force microscopy	AFM
carbon dots	CDs
carbon dot systems	CDS
density of states	DOS
Drude-Smith	DS
1,2-ethylendiamine	EDA
electroluminescence	EL
focused ion beam	FIB
Fourier-transform infrared spectroscopy	FTIR
Förster resonance energy transfer	FRET
gel permeation chromatography	GPC
laser power	LP
monolayer	ML
microsphere	MS
microwave	MW
nanoparticles	NPs
nanoplatelets	NPLs
1-octadecene	ODE
optical pump-THz probe	OPTP
polydimethylsiloxane	PDMS
poly(dioctylfluorene)	PFO
photoluminescence	PL
thiol-terminated polymethylmethacrylate	PMMA-SH
polystyrene	PS
quantum dots	QDs

scanning electron microscopy	SEM
stereolithography	SLA
transmission electron microscopy	TEM
terahertz	THz
tetraoctylammoniumbromide	TOAB
two-photon polymerization	TPP
van der Waals	vdW

Content

Zusammenfassung

Die Eigenschaften von Nanopartikel können über ihre Größe oder Form eingestellt werden. Um den Zusammenhang zwischen Partikelinteraktionen und der Erzeugung und Verbesserung neuer Eigenschaften, wie zum Beispiel gesteigerter und polarisierte Photolumineszenz oder Photoleitfähigkeit, weiter zu erforschen, müssen die Nanopartikel aus der Dispersion in den festen Zustand überführt werden. Eine Herausforderung hierbei ist die Verhinderung der unkontrollierten Agglomeration, um die ursprünglichen kolloidalen Eigenschaften zu erhalten. Daher liegt der Hauptfokus dieser Arbeit auf der Kontrolle der Interaktion zwischen Nanopartikeln. Der Transfer von Nanopartikeln wird hierbei entweder durch Assemblierung zu Überstrukturen oder durch Einbetten in ein Matrixmaterial erreicht.

In dieser Arbeit werden für den Transfer von Nanopartikeln in den festen Zustand bekannte Methoden vertieft und ausgeweitet sowie neue Strategien für den Transfer entwickelt. Zunächst werden die Interaktionen zwischen zwei Kolloiden in Dispersion untersucht. Durch die Interaktionen zwischen Kohlenstoffquantenpunkten und Polystyrol-Nanopartikeln wird die Photolumineszenz stark erhöht. Als nächstes werden die Interaktionen zwischen CdSe-Nanoplättchen kontrolliert, um deren kollektive Anordnung zu untersuchen. Die kontrollierte, kollektive Anordnung wird benötigt, um die anisotropen Eigenschaften der Nanoplättchen in definierter Weise zu modifizieren. Die Orientierung in selbstassemblierten Filmen wird durch Ausnutzung kinetischer Effekte bei unterschiedlichen Verdampfungsraten an der Flüssig-Flüssig-Grenzfläche kontrolliert. Die Kontrolle der Partikelinteraktionen ist nicht nur nötig, um die Partikelorientierung oder Eigenschaften verändern zu können, sondern spielt auch eine große Rolle beim Transfer von Nanopartikeln in ein Matrixmedium. Um Agglomeration bei der Dispergierung in stereolithographisch bearbeitbaren Photoharzen zu verhindern, werden die Nanopartikel mit dem Photoharz ähnlichen Polymeren funktionalisiert. 3D-Druck, eine Anwendung der Photoharze, ist eine vielversprechende Technologie um hochkomplexe Strukturen zu erzeugen, die mit herkömmlichen Herstellungsverfahren nicht oder nur sehr aufwendig zugänglich sind. Beim stereolithograpischen 3D-Druck wird ein Laser verwendet, um das Photoharz zu polymerisieren und auszuhärten. Jedoch können Interaktionen zwischen Nanopartikeln und dem Laser oder photogenerierten Radikalen auftreten. Das Verständnis dieser Interaktionen ist von höchster Wichtigkeit, um die Eigenschaften von Nanopartikeln, zum Beispiel Photolumineszenz, Magnetismus oder Leitfähigkeit mit der 3D-Druck Technologie verbinden zu können und somit komplexe Strukturen mit zum Beispiel

magnetischen, optischen oder elektronischen Eigenschaften zu drucken. Darüber hinaus sind Nanoplättchen vielversprechende Kandidaten für die Verwendung als neuartige Fluorophore in der Mikroskopie oder in LEDs. Jedoch müssen auch für solche Anwendungen die Interaktionen sorgfältig eingestellt werden.

Zusammenfassend werden neue Strategien und Methoden entwickelt, um die Interaktionen zwischen Nanopartikeln zu kontrollieren und den Einfluss auf deren Eigenschaften, wie zum Beispiel Photolumineszenz, zu untersuchen. Durch Kontrolle der Interaktionen können Nanopartikel ohne oder ausschließlich mit gezielter Agglomeration von der kolloidalen Dispersion in den feste Zustand transferiert werden. Durch die kontrollierte, kollektive Zusammenlagerung von Nanoplättchen in einem Film (alle aufrechtstehend oder liegend), werden so kollektive, steuerbare Eigenschaften, wie polarisierte Photolumineszenz oder Photoleitfähigkeit, erzeugt. Durch das Verständnis der Nanopartikelinteraktionen ist es des Weiteren möglich, Nanopartikel in den 3D-Druck Prozess ohne Agglomeration zu integrieren, um komplexe Strukturen mit gezielten Eigenschaften, wie zum Beispiel mit Photolumineszenz, zu drucken.

Abstract

Nanoparticles can be synthesized with size-tunable properties. To further explore, the correlation between inter-particle interaction and the generation of new properties for novel applications, like enhanced or polarized photoluminescence or photoconductivity, the nanoparticles have to be transferred from the colloidal dispersion to the solid-state. One of the challenges is to inhibit uncontrolled agglomeration in the solid-state in order to preserve their original colloidal properties. Therefore, the main focus of the thesis is to control the interaction potential between nanoparticles. To approach the transfer of nanoparticles, assembling into superstructures or dispersing into a solid host material are applied.

In this work, existing methods are expanded and new strategies are developed to transfer nanoparticles from the dispersion to the solid-state. First, the interactions between two colloids in dispersion are investigated. Through the interaction between carbon dots and polystyrene nanoparticles, the photoluminescence can be strongly enhanced. Next, the interactions between CdSe nanoplatelets are controlled in order to investigate their collective orientation in thin films. The controlled collective orientation is required, to access, to study and to modify the anisotropic properties of the nanoplatelets. The orientation is controlled by the exploitation of kinetic effects through adjusting the evaporation rate in self-assembly experiments at liquid-liquid interfaces. Controlled particle interactions are not only important to alter particle orientation and properties, they also play a crucial role when transferring the nanoparticles into a different medium. To avoid agglomeration, nanoparticles are functionalized with photoresin-like polymers for the dispersion in stereolithographic photoresins. 3D printing is a promising technology for the manufacturing of highly complex structures, which are not or hardly accessible with traditional manufacturing methods. Stereolithographic 3D printing applies a laser to polymerize and cure the photoresin. However, interactions of nanoparticles with the laser or photogenerated radicals can occur. Understanding the interactions of nanoparticles in the 3D printing process is of utmost importance in order to combine the properties of nanoparticles, like photoluminescence, magnetism or conductivity, with the 3D printing technology, in order to realize highly complex structures with adjustable properties, like fluorescence. Furthermore, nanoplatelets are promising candidates for novel fluorophores in microscopy or in light-emitting diodes. However, interactions have to be carefully adjusted for such applications.

In conclusion, new strategies and methods are developed to control the interaction between nanoparticles and to study the effect on their properties, like photoluminescence. By the control of the interaction, nanoparticles can be transferred from the colloidal dispersion to the solid state without or with selective agglomeration. By the controlled collective assembly of nanoplates in a film (all face-down or edge-up), new tunable properties, such as polarized photoluminescence or photoconductivity, are generated. Upon the understanding of nanoparticle interactions, it is further possible to integrate nanoparticles without agglomeration in the 3D printing process and realize complex structures with desired properties, like fluorescence.

1. Introduction

Already in the Roman time and in the middle age, the outstanding properties of nanoparticles were used, without knowing the existence of nanoparticles. For example, the famous Lycurgus cup owes its color to finely dispersed gold nanoparticles and the color of church windows is based on gold or silver nanoparticles. Upon this time no one knew about the existence of nanoparticles and the processes involved when mixing tiny amounts of gold or silver into the liquid glass were unclear. Nowadays the special properties and benefits of colloidal materials are well known, like the high surface area beneficial for example for catalysts or the small particle size required for drug delivery applications. In our daily life, we get in contact with a wide variety of nanoparticles. They can be found for example as pigments in coatings[1], as UV absorber in sun screens[2], as food additives to prevent "caking" and aggregation[3], or as additives in wound dressings due to the antibacterial activity of silver nanoparticles for instance[4] and even more[5].

Nanoparticles are defined according IUPAC as particles of any shape with dimensions between 1 nm and 100 nm, nanofibers and tubes with only two dimensions below 100 nm are includes as well[6]. Due to the size of nanoparticles in the nanometer regime, the surface-to-volume ratio is large compared to bigger particles with the same volume of material. Due to the large surface-to-volume ratio, the physical and chemical properties (e.g. absorption, photoluminescence, chemical reactivity or melting temperature) are no longer only determined by the material but also by the size and the morphology. For example, for gold clusters, the electron affinity changes by around 2 eV as a function of size (1 atom to 70 atoms in the cluster)[7]. Furthermore, optical properties like the emission is strongly size dependent. For example, the emission of highly fluorescent semiconducting quantum dots can be changed by simply varying the size of the particles[8]. Furthermore, by changing the shape of metal nanoparticles, one absorption band (sphere) or two absorption bands (rod) are obtained[9]. In addition, anisotropic nanoparticles (e.g. rods or platelets) features anisotropic properties like polarized light emission. However, the anisotropic properties, like polarized light emission, of the individual particles superimpose in dispersion, because the orientation of the particles is random, and isotropic ensemble properties are obtained, e.g isotropic light emission. By the choice of material (polymer-based materials, inorganic materials, carbon-based materials), control of the morphology (spheres, rods, platelets, etc.), adjustment of the size and the choice

of material composition (core-shell materials) of the nanoparticles, the chemical and physical properties, like the light emission or melting point, can be tailored.

Due to the unique properties of nanoparticles, they can be used for many different applications, like coatings and adhesives, drug delivery or sensors. However, applications like e.g. solar cells or displays are based on the solid-state and nanoparticles have to be transferred into films, assembled into larger structures or embedded into host materials. To use nanoparticles also in such applications, the colloidal nanoparticles have to be transferred in the solid-state. Especially, for anisotropic nanoparticles, the transfer from the dispersion to the solid-state with control over their orientation is of importance in order to get access to the anisotropic properties, like polarized light emission or anisotropic two-photon absorption[10, 11]. Interestingly, not only for anisotropic nanoparticles collective, anisotropic properties are accessible, also the assembly of isotropic nanoparticles to larger structures or integration of nanoparticles in a matrix can induce novel optical[12], plasmonic[13] or electronic[14] properties. For instance, assemblies of nanoplatelets in stacks show an improved energy transfer rate, due to the closed packing and dipole orientation[15]. The integration of individual nanoparticles in host materials, leads not only to properties of the single components but also to new physical properties, e.g. mechanical stiffness or strength, due to interactions between the components For example, nanoparticles embedded in a polymeric matrix could feature extreme high mechanical stability[16] due to high filler-matrix interfacial interactions[16]. Thus, new functional materials with properties, like photoconductivity or polarized light emission and solid state applications, like polarized light emitting diodes, can be developed.

To transfer nanoparticles from dispersion to the solid-state, different methods have been developed to integrate nanoparticles in a host material and assemble nanoparticles into larger structures composed of different sub-structures so-called superstructures. Usually, the driving force of self-assembly of nanoparticles is the reduction of the free energy. By controlling the interaction potential between the nanoparticles, it is possible to induce self-assembly and to direct the structure formation. For example, self-assembly methods can be applied to build larger structures of nanoparticles or films bottom-up. By selecting the self-assembly method and carefully adjusting the process parameters (like evaporation rate, amount of anti-solvent, or concentration), the interaction potential between the nanoparticles are tuned and the superstructure formation can be precisely controlled. In order to expand the library of accessible

structures and pave the way to novel applications, new technologies have to be taken into focus and strategies have to be developed to integrate nanoparticles in the new processes.

2. State of the art

In this thesis carbon dots, CdSe nanoplatelets and plasmonic Au and Ag nanoparticles were used. In the following, the applied nanoparticles (NPs) used in this work are introduced (see chapter 2.1) and the theoretical background of the forces acting between NPs is described (see chapter 2.2). Furthermore, the applied techniques, self–assembly (see chapter 2.3.1) and 3D printing (see chapter 2.3.2) are discussed.

2.1 Nanoparticles

NPs can be synthesized with numerous approaches from various materials. In this work, especially carbon-based NPs (carbon dots) and inorganic NPs (plasmonic and semiconductor NPs) were used. Not only the material was varied, but also the shape of the NPs was modified in order to get nanoplatelets (NPLs) with outstanding optical properties due to their anisotropy, such as narrow ensemble emission and absorption bands, high absorption cross sections and strong anisotropic light emission (see chapter 2.1.2). In the following carbon dots (see chapter 2.1.1), CdSe NPLs, and Au and Ag NPs (see chapter 2.1.2) are introduced.

2.1.1 Carbon dots

Carbon dots (CDs) are a relativity new class of carbon materials. They were discovered in 2004 during the synthesis of single-walled carbon nanotubes[17]. Since then, they are of great interest due to their photoluminescence (PL) properties, biocompatibility, and low specific toxicity[18, 19]. CDs are often quasi-spherical NPs with a size of less than 10 nm. The amorphous and nanocrystalline nuclei are composed of sp^2 hybridized carbon inserts of graphene, graphene oxide sheets and diamond-like carbon or sp^3 carbon[20]. Polar groups from starting materials are incorporated at the surface, making the CDs water-soluble[21]. The surface of CDs is easy to functionalize[18, 22] and the synthesis is performed using inexpensive materials, like biomass materials (e.g. orange juice or lignin) or waste materials (e.g. agro-industrial waste) and environmentally friendly methods which can be performed at room temperature without external energy supply (like base catalysis, self-exothermic synthesis and reduction methods)[23]. To obtain fluorescent CDs, the size and the functional groups on the surface has to be precisely adjusted by selecting the precursor materials and reaction conditions, in order to fine-tune the electronic structure[24]. Often, a post-synthesis surface functionalization or passivation of the surface is required to obtain fluorescent CDs[25, 26].

Synthesis

To synthesize CDs mainly two strategies are used. The "top-down" and "bottom-up" approach. The top-down describes the break-down of larger carbon-based materials like graphite, multi-walled nanotubes, graphene, and fullerene[19, 27]. To prepare small CDs out of the carbon materials laser ablation, arc discharge or other methods are applied[17, 27]. The bottom-up approach is based on processes such as carbonization of small molecules (like citric acid, ethylene diamine or urea) into CDs through chemical reactions[23, 28, 29]. Among others, thermal oxidation or microwave pyrolysis is widely used[30, 31]. As a precursor material, a wide range of carbon-based materials can be used. They usually contain a high content of carbon and oxygen in the form of hydroxyl groups, carbonyl groups or carboxyl groups. Often, natural materials like carbohydrates[31-34], amino acids[21, 35] and proteins[36, 37] are used. To increase the quantum yield, nitrogen-containing co-precursors can be added during the synthesis (e.g. ethylenediamine or ammonium[31, 38]).

Often, surface modifications are applied, because the PL properties of CDs are strongly determined by the surface[20]. In the "top-down" approach the surface is later modified by using, for example, a PEG polymer to create surface defects[26], whereas, in the "bottom-up" approach, the surface of the CDs can be already controlled during the synthesis using precursors with specific functional groups.

Optical proprieties

CDs feature a strong absorption in the UV region which is attributed to the π-π* transition[39]. Furthermore, a tail of absorbance in the visible range is often observed caused by n-π* transitions of functional groups with electron lone pairs[40].

The PL emission of the CDs can vary from blue to red, depending on the precursor material and the synthesis approach[41]. Even for many CDs a strong excitation-dependent PL is observed[26]. Since the synthesized CDs consists of different core structures and functional groups, no general accepted PL mechanism/contribution exists[23] Most probably, the PL is composed of different contributions of varying intensities, depending in the precursors and synthesis approach. Up to date, the most accepted PL contribution are the surface states[29, 42, 43], the quantum confinement[44-46], and the molecular fluorescence[47-50].

The most widely accepted contribution is the surface state-related fluorescence mechanism. Surface states are electronic states on the surface of the CDs which are formed due to functional

groups on the surface or surface oxidation. The fluorescence wavelength is directly related to the degree of surface oxidation and the nature of the functional groups[26]. Surface oxidation introduce surface-related defective sites which can act as capture center for exitons[51]. Ding *et al.* prepared a series of CDs with the same size, but different surface oxidation degree in a one pot synthesis and separated the CDs according to their polarities by column chromatography[29]. Only the degree of surface oxidation gradually increases which leads to a red-shift of the PL (see Figure 2.1 a), whereas the size of the CDs and the graphite structure in the core are similar[29]. It was stated, that the bandgap depends on the oxygen content on the CD surface structure and therefore the degree of oxidation is directly responsible for the observed red-shift.

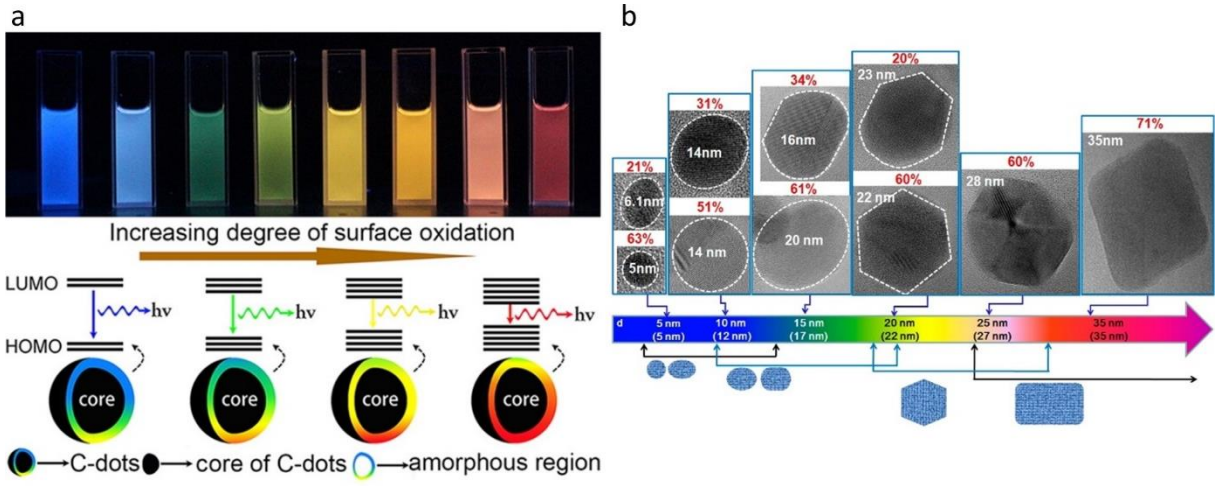

Figure 2.1: (a) The fluorescence mechanism of CDs based on the degree of surface oxidation. (Reproduced with permission from ref. 29 Copyright 2016, American Chemical Society.) (b) HRTEM images of with different shapes and sizes and their corresponding emission color (Reproduced with permission from ref. 46. Copyright 2012, American Chemical Society.)

Furthermore, also functional groups, like C=O or C=N, on the surface of CDs can contribute to the PL properties[26, 52]. By changing the functional groups on the surface, the emission wavelength can be tuned as shown by Sun *et al.*[53]. Usually, diverse functional groups are located on the surface of CDs and multicolor emission is obtained[27, 52].

A second proposed contribution is based on the quantum confinement. Quantum confinement occurs when the size of the crystal is smaller than the Bohr radius of excitons. Therefore, the energy gap is directly dependent on the size (see chapter 2.1.2 for details). This effect is mainly known for semiconducting NPs. However, this effect can be also observed for CDs. Kim *et al.* synthesized CDs with different sizes (5 nm – 35 nm) and morphologies[46]. The absorption and fluorescence spectra were recorded and a size-dependent trend was observed

(see Figure 2.1 b). By increasing the size, the absorption peak energy is decreased, which was attributed to the quantum confinement effect.

The third possible contribution was described recently. It was shown, that fluorescent impurities, formed during the bottom-up synthesis of CDs, contributed as part of the fluorescence[47]. For example, Schneider *et al.* synthesized three different CDs based on citric acid[49]. They proved, that small molecular fluorophores, formed during synthesis, are attached to the CDs and contribute to the emission. Furthermore, Essner *et al.* proved the contribution of molecular fluorophores by removing them and the resulting decrease of PL of the remaining CDs[47].

Most probably, the PL is composed of a complex mixture of all three proposed contributions and even others. Since the CD ensembles are not uniform and the structures obtained are diverse and highly complex, a universal PL contribution is hard to prove for CDs. For some CDs, the quantum confinement could play a role, whereas, for other CDs, the surface state could be crucial.

The sensitivity of the PL properties of CDs to the surrounding environment

Since the PL mechanism strongly depends on the surface of the CDs, CDs features a great sensitivity to their surroundings. The interaction with the surrounding leads to an enhancement or quenching of the PL. It is known, that the PL properties depend on the pH value[29, 54, 55], temperature[56] or the solvent[57]. Furthermore, the PL can be quenched by a lot of different ions (e.g. Cu^{2+}, Fe^{3+} or Hg^{2+})[58-63]. Agglomeration-caused quenching[22] and fluorescence quenching through electron-donating or accepting agents is known as well[64] and can be used for different sensing applications[65, 66].

Already shortly after the discovery of CDs, is was found, that polymers can be used as passivation agents to protect the CD surface from the environment and to enhance the PL[27]. Surface defect sites, produced by surface oxidation, can be passivated and reactive surface groups are shielded from the surrounding through the polymer shell which leads to improved properties of CDs (e.g. QY, enhancement of fluorescence, stability). Frequently used polymers are poly(ethylene glycol)[67], polyethyleneimine[68] and polyvinylalcohol[69]. Polymers cannot only be used as a passivating shell but also as a matrix to embed CDs in a film. Also, in this case, the polymer can have positive effects on the PL. Liu *et al.* showed that the embedment of 2,2'-

(ethylenedioxy)bis(ethylamine) functionalized CDs results in an enhancement of fluorescence emission and the quantum yield[70].

2.1.2 Inorganic nanoparticles

Besides carbon-based NPs like the above-discussed CDs, a second big class of NPs is based on inorganic materials, for example, semiconducting or plasmonic materials. Such materials exhibit special properties due to their nanoscale size through the quantum size effect or the localized surface plasmon resonances.

Anisotropic cadmium selenide nanocrystals

Direct bandgap semiconductor materials exhibit an energy gap between the conduction band and the valence band. In bulk such semiconductor materials this energy gap is a fixed value. By decreasing the size of the material into the nanometer regime (e.g. < 10 nm, depending on the material), the energy gap is increased and more discrete energy levels appear (see Scheme 2.1)[71]. This behavior is known as the quantum confinement effect. The quantum confinement effect can be explained by looking at the excited electrons. The excited electron in the conduction band is still bound to the hole located in the valence band and both together form an exciton.

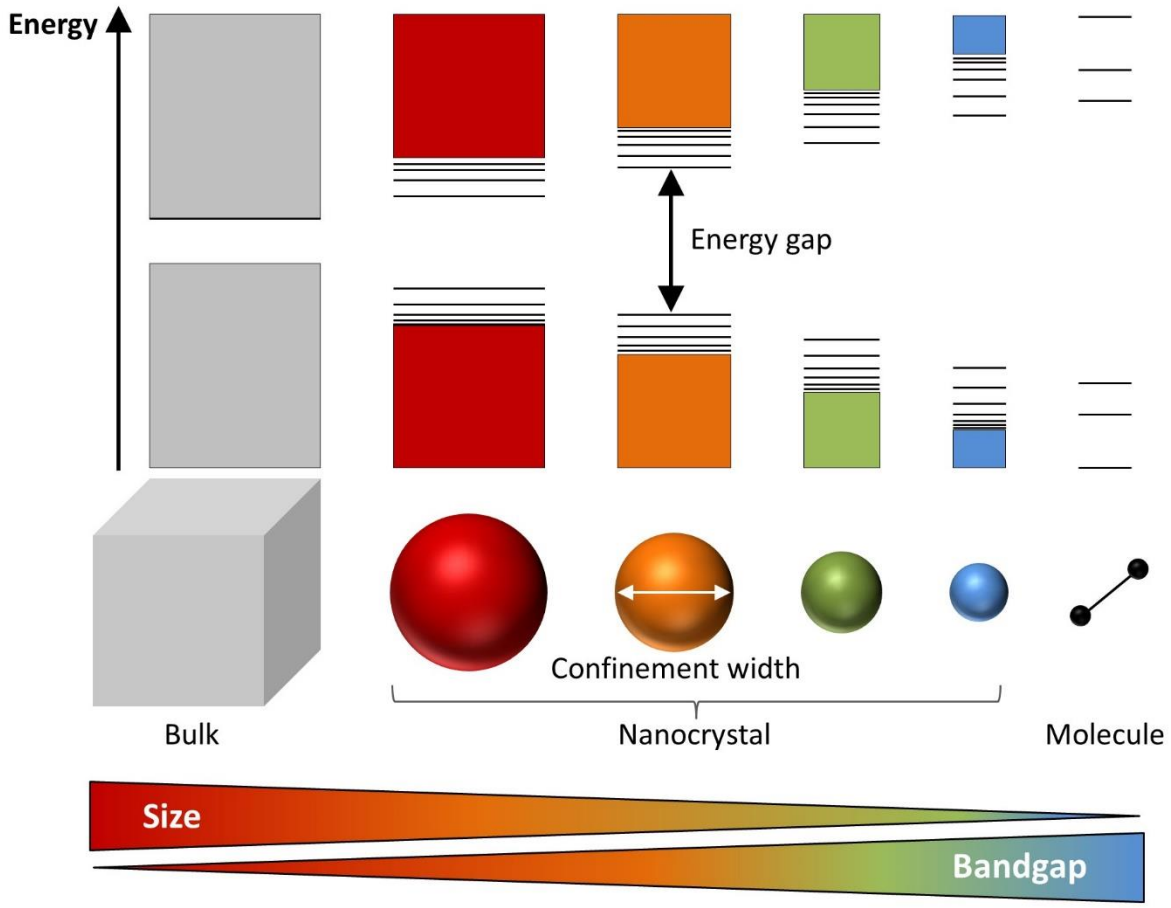

Scheme 2.1: Scheme of quantum confinement effect.

This exciton requires a specific space that is described by the exciton Bohr radius. The Bohr radius strongly depends on the material (e.g. 4 nm (CdSe); 29 nm (InAs); 104 nm (PbTe)[72]). If the boundaries of the material are significantly larger than the Bohr radius, the exciton can move freely. If the boundaries of the material approach the size of the Bohr radius, the exciton cannot move freely anymore due to confinement. By decreasing the boundaries further, the space for the exciton is decreasing and as expected from quantum mechanical considerations (particle-in-the-box) the energy gap increases. Hence, the resulting absorption and emission properties can be adjusted by the size of the nanoparticle.

Besides the change of the energy gap, also the density of states (DOS) is affected by the quantum confinement. Here especially the shape of the nanocrystal play a crucial role[71, 73]. For the bulk semiconductor (3D), the DOS is square root dependent ($\sim E^{\frac{1}{2}}$) (see Scheme 2.2). In case all dimensions are confined (QDs, 0D), only discrete energy states are allowed. In two-dimensional nanocrystals (nanosheets, NPLs or quantum wells, 2D), only one dimension exhibits quantum confinement and the DOS increases stepwise with a constant energy dependency ($\sim E^{0}$). This means, every energy is available but increases in quantified steps. In case that two dimensions are smaller than the Bohr radius and the third dimension is larger than the Bohr radius, the quantum confinement effect occurs in two dimensions (nanorods or quantum wires, 1D) and the DOS is inverse squared dependent on the energy ($\sim E^{-\frac{1}{2}}$). The DOS increases in quantified amounts but decreases rapidly between each step.

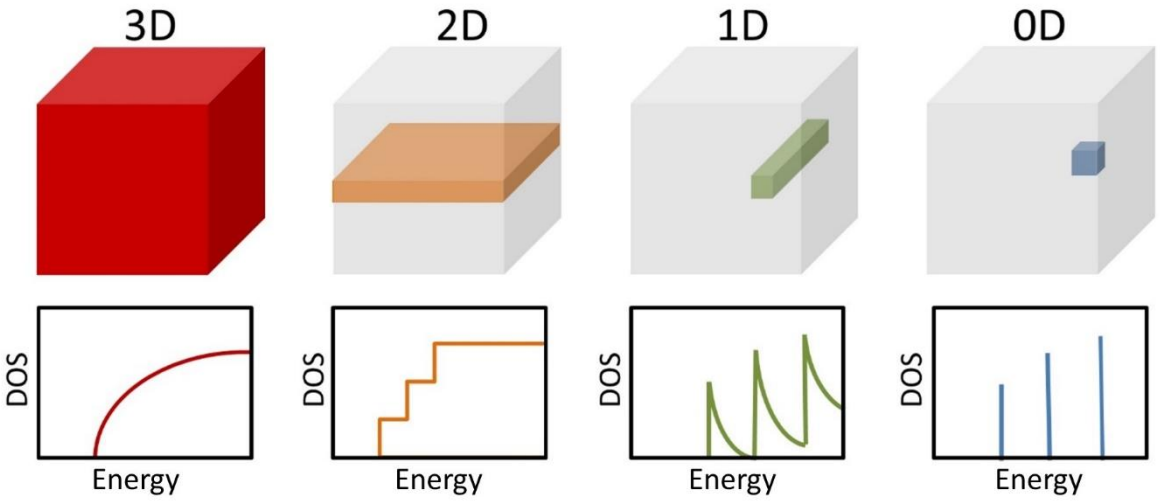

Scheme 2.2: Scheme of the density of states for different dimensional confinements.

Divers synthetic protocols exist to obtain different shaped nanocrystals with tuned quantum confinement[74-76]. In a quasi-two-dimensional NPLs, the quantum confinement exists only in one dimension since the NPLs thickness is controlled below the Bohr radius with atomic precision, whereas the lateral dimensions are expanded beyond the Bohr radius[75]. Each NPL consists of a distinct number *m* of monolayers (ML) (*m* selenium layers, and *m*+1 cadmium layers). These CdSe NPLs can be synthesized in a way that every particle in the ensemble has exactly the same thickness[77]. Since only the thickness determines the bandgap, every NPL has the same bandgap and the ensemble and single-particle spectra are nearly identical[78]. Therefore, the ensemble spectral features are extremely narrow and the problem of inhomogeneous line broadening due to size distribution is solved[75, 78, 79]. Due to this fact and other outstanding properties (high absorption cross sections[80, 81], enhanced energy transfer rates[82], boosted optical gain[83], and strong anisotropic light emission[10, 84-86]), NPLs are ideal candidates for diverse applications like light-emitting devices[10, 84-87], field-effect transistors[88], solar cells[82], and lasers[89].

Synthesis

To obtain two-dimension NPLs, the standard quantum dot (QD) growing procedure has been modified. Long-chain cadmium carboxylates are heated with elemental selenium in a non-coordinative solvent (1-octadecene). At a certain temperature (between 180 and 200 °C), a second cadmium precursor (cadmium acetate) is added, which induces the anisotropic growth of cubic zinc blend crystalites[75, 90]. Typical growth mechanisms of quasi-spherical nanocrystals are often described by the La Mer scheme which is based on a diffusion-limited growth[91]. Here, after a short nucleation period, the diffusion-controlled growth starts and nanocrystals resembling shapes predictable by the Wulff construction result. In contrast, the growth of NPLs is no longer diffusion-controlled but surface-reaction limited. The concentration of precursors in the NPL synthesis is extremely high resulting in a larger diffusion rate compared to surface

reaction rate. Therefore, the growth is dominated by island nucleation on primary particles. Small islands grow much faster than large ones caused by size-dependent nucleation barriers, and after stochastic symmetry breaking 2D growth occurs (see Figure 2.2)[53]. The thickness, and therefore the optical properties, of the CdSe NPLs, can be controlled by temperature, injection time, reaction time and the ratio between the precursors[75]. The aspect ratio of the lateral area can be controlled by the reaction time and the ratio of dry to hydrated cadmium acetate as shown by Bertrand *et al.*[92].

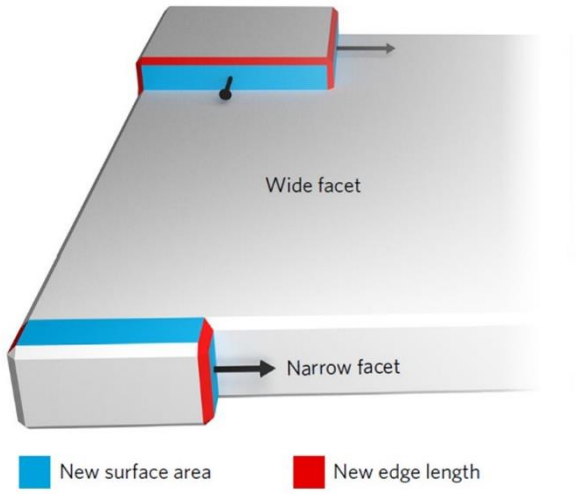

Figure 2.2: Growth of NPLs. Different growth modes on wide and narrow facets of a nanocrystal. The island on the narrow facet grows much faster than the island on the wide facet, due to the reduction of the nucleation barrier on facets smaller than the critical island size. (Reproduced with permission from ref. 53. Copyright 2017, Springer Nature.)

Optical properties

The absorption spectra of CdSe NPLs feature two transitions that correspond to the electron/heavy hole transition (lowest energy) and the electron/light-hole transition (highest energy)[75, 79]. The emission spectra show a full width at half maximum (FWHM) of less than 35 meV and almost no stokes shift[75, 79]. Besides the narrow emission spectra, other properties are also improved due to the anisotropic shape compared to quasi-spherical QDs. For example, the one-photon and two-photon absorption cross-sections are extremely high compared to QDs and directly depends on the lateral size of the NPLs[80, 93]. Furthermore, the energy transfer is enhanced as shown by Rowland *et al.*[82]. In addition, the nonradioactive Auger recombination is one order of magnitude smaller in comparison to QDs which is beneficial for light-emitting applications[94]. Furthermore, the threshold for stimulated emission is quite low for CdSe NPLs[83].

Besides these outstanding properties caused by the anisotropic shape, also anisotropic properties are expected. To study these properties and to benefit from them, the NPLs have to be collectively oriented in order to get access to these properties on macroscopic scales. Self-assembly methods and relevant inter-particle forces are further described in more detail in chapter 2.2 and 2.3.1. For instance, to orient the NPLs and to study the optical properties, NPLs and QDs in chloroform were drop cast on a water surface to obtain films as shown by Scott *et*

al.[10]. Two-dimensional k-space spectroscopy was used to study the angular emission profiles of QDs and NPLs. It could be shown that the off-resonant absorption into the continuum state is isotropic, whereas the emission of NPLs is strongly anisotropic (see Figure 2.3). The emission occurs from the heavy-hole exciton which has a highly anisotropic transition dipole orientation in-plane leading to the observed oriented light emission of CdSe NPLs. With the same method, Heckmann *et al.* could prove that in contrast to the one-photon absorption, the two-photon absorption process is highly anisotropic due to the involvement of directional intraband and interband transitions[11].

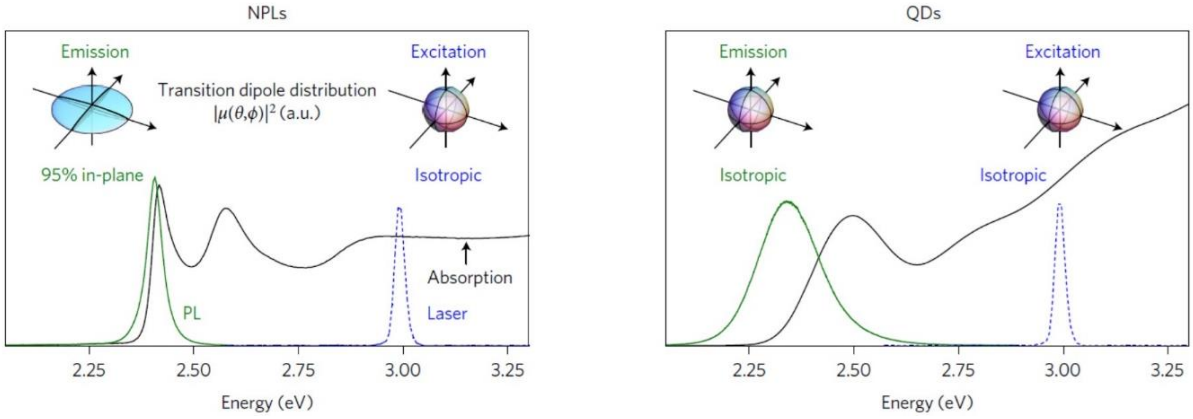

Figure 2.3: Absorption and PL spectra of the studied NPLs and QDs, together with the exciting laser. Insets: Distributions of dipole moments showing strong anisotropic emission from the oriented NPL monolayer, and random orientation in the other cases. (Reproduced with permission from ref. 11 Copyright 2017, Springer Nature.).

By arranging the NPLs into longer stacks, the directed light emission can be studied[15, 84, 95]. NPLs can be stacked with their larger planar facets facing each other by the addition of an anti-solvent or a depletion agent. The formed stacks show strongly polarized light emission in the direction perpendicular to the long axis of the stacks. Not only the individual particle feature orientation-depended properties but also the collective orientation can induce collective orientation-controlled properties. For example, due to the close packing of the NPLs in the stacks, the energy transfer between the NPLs is high with an ultra-long Förster radius of ~ 13.5 nm and an exciton migration length of 133 nm[15]. In addition, Erdem *et al.* could prove that the Förster resonance energy transfer (FRET) is highly orientation-controlled in oriented films[96]. The NPLs were deposited in the face-down or edge-up configuration and were used as an acceptor in an energy transfer model system to pair with CdZnS/ZnS core/shell QDs. They found that the FRET from QDs to an edge-up monolayer is about 50% stronger than the face-

down monolayer. This is explained by the stronger dipole-dipole coupling and the higher density caused by the stacking of the NPLs.

Plasmonic Nanoparticles

Next, the class of noble metal NPs that feature plasmonic properties, especially the Au and Ag NPs as used in chapter 5 are discussed. Due to the small size of the NPs, localized surface plasmon resonance occurs, which can be used for e.g. for sensing[97-99].

Synthesis

A wide range of solution-based synthesis approaches for Au and Ag NPs exist. Usually, metal NPs a synthesized by reducing the corresponding metal salt. The nucleation and growth of Au and Ag NPs can be described by the La Mer model[91]. In 1951, Turkevich *et al.* developed a method to synthesize Au NPs by using tetrachloroaurate as a gold precursor and reduce the Au(III) ions with citric acid[100]. The citric acid acts as a reducing agent as well as a stabilizing agent. This synthesis approach was further optimized to control the size between 10 to 100 nm. However, the functionalization with thiolate ligands of the citrate stabilized NPs is difficult, since during the functionalization process irreversible aggregation can occur[101]. In 1994, Brust and Schiffrin developed a new two-phase method to synthesize alkanethiol-stabilized Au NPs[102] soluble in non-polar solvents. Gold ions are transferred in an organic solvent using tetraoctylammoniumbromide (TOAB) as a phase transfer agent where they are reduced with sodium borohydride ($NaBH_4$). The alkanethiol-stabilized Au NPs are more stable against agglomeration compared to other Au NPs due to the strong thiol-gold interaction and high degree of van der Walls attraction between ligands allowing for a dense packing of the ligand shell[103]. For Ag NPs, similar methods (the Turkevich or Brust-Schiffrin method) are often applied as well[104].

Localized surface plasmon resonance

As already described in the introduction, colloidal noble metal NPs like Au or Ag show bright colors. The underlying effect of those colors is based on localized surface plasmon resonances. NPs are smaller than the penetration depth of the light, therefore the light can penetrate the NPs. The field inside the particle shifts the electrons in the conduction band to one side of the particle whereas the positive charges are fixed on the lattice (see Figure 2.4 a)[105]. This charge separation leads to a restoring force and a strong oscillation even at a small excitation fields occurs, which is called a plasmon. As a result of the oscillations, the electric field around the particle is strongly enhanced and the absorption of the particle has a maximum

at the plasmon resonant frequency. The position of the plasmon resonant frequency depends on the size, shape, the medium they are dispersed in, and on nanoparticle interaction. The oscillation of the electrons is damped by either a radiative decay (e.g. emission of a photon) or non-radiative decay (heat generation).

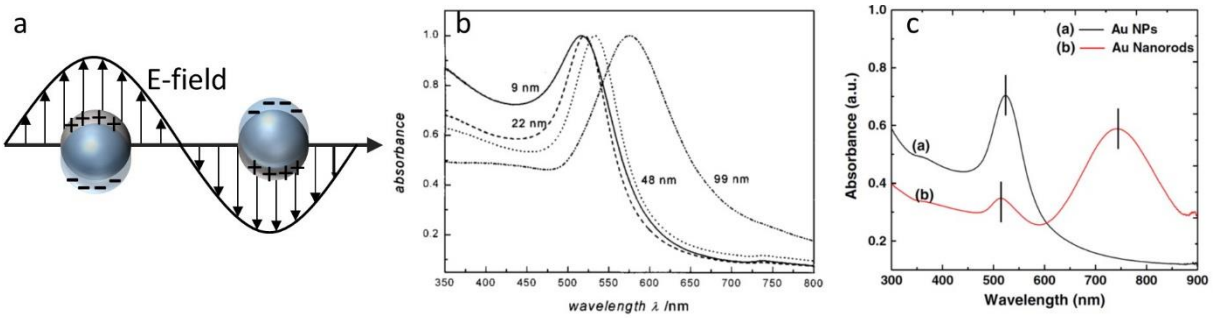

Figure 2.4: Plasmon resonance of metal NPs. (a) Scheme of plasmon oscillation; (B) dependency of the plasmon resonance on the size of the nanoparticle (here Au NPs). (Reproduced with permission from ref. 106, Copyright 1999 American Chemical Society); (c) localized surface plasmon resonance for Au NPs and Au nanorods (Reproduced with permission from ref. 9, Copyright 2013 Elsevier).

By changing the size of metal NPs in the range of 1 – 100 nm, the plasmon resonance is shifted. With increasing size, a red-shift and a simultaneously broadening of the resonance is observed (see Figure 2.4 b)[106]. When the shape is changed from a sphere to a rod, the plasmon absorption band is split into two plasmon bands (see Figure 2.4 c)[9]. The peak at longer wavelength is assigned to the longitudinal plasmon resonance along the longer axis, whereas the peak at shorter wavelength is assigned to the transverse plasmon resonance along the shorter axis. Besides the size and the shape of the NPs, also the surrounding medium can influence the plasmon resonance[97, 107, 108]. By increasing the refractive index of the surrounding medium, the resonance is red-shifted and the linewidth is decreased. Also, the agglomeration and closer distances between the NPs leads to a shift and broadening of the plasmon resonance[109]. The agglomeration of Au NPs can be followed by a color change from red to blue. This agglomeration/distance-dependent color change is applied for example in a pregnancy test[99]. The human chorionic gonadotropin, a hormone present during pregnancy, binds to antibody-modified Au NPs. The formed conjugate moves along the strip to the test region. In the test region, a second antibody is immobilized which can bind to the conjugate. Due to the interaction between the NPs, a red line occurs on the pregnancy test, indicating a positive pregnancy test.

Due to the sensitivity of the plasmon resonance to the surrounding (change in the local dielectric environment), also other sensor systems besides the pregnancy test can be build based

on the wavelength shift upon analyte absorption. Such nanosensors can sense a wide range of metal, biological molecules, as well as antigen-antibody reactions[97, 98]. Besides the direct sensing of molecules by adsorption or binding, another sensing method based on localized surface plasmon is the so-called surface-enhanced Raman scattering (SERS). The Raman scattering of the analyte is enhanced by the plasmon resonance of the NPs[110].

Besides the optical properties of noble metal NPs, Au NPs are widely used to label organic or biological materials in electron microscopy. Au NPs have a high contrast due to the high electron density and it is possible to specifically bind Au NPs to a disregard target without affecting the strucutre[111].

Due to the easy monitoring of the agglomeration state (shift in absorption) and high contrast in the TEM, Au and Ag NPs are used as model colloids in the project concerning the integration of NPs in the 3D printing process (see chapter 5).

2.2 Forces between nanoparticles and their stabilization in dispersion

One major aspect of colloidal dispersions is their colloidal stability. Different interaction forces like van der Waals (vdW) attraction, steric repulsion or double-layer repulsion have to be balanced to obtain a stable dispersion, otherwise, agglomeration occurs. If agglomeration occurs, the total surface is reduced and therefore the free energy is minimized. However, the decrease of the surface can be unfavorable for example in catalytic application where a large surface area is indispensable. Also, the increase in size of the agglomerates is not favorable for e.g. biological applications. Furthermore, the properties of the NPs are affected upon agglomeration. Coupling effects can occur altering the properties in a beneficial or non-beneficial way (see chapter 2.3.1). To prevent agglomeration and to balance the interaction forces, stabilizers are used. Such a stabilization can be of electrostatic or steric nature. The fundamental principles of electrostatic stabilization described by the DLVO theory and the steric stabilization are discussed in chapter 2.2.1 and 2.2.2. A more detailed discussion of the interaction forces can be found for example in the textbooks of Tadros and Butt[112].

2.2.1 DLVO Theory

The interaction forces for electrostatic stabilized particles have been described by Deryaguin and Landau[113] and Verwey and Overbook[114] (DLVO Theory). The attraction forces (vdW) and repulsion forces (double layer) are combined and an energy-distance curve is predicted.

Van der Waals interaction

At short distances, atoms or molecules attract each other due to intermolecular dipole interactions. The dipole interaction can be described with the vdW interaction and consists of three contributions: dipole-dipole (Keesom), dipole – induced dipole (Debey) and induced dipole – induced dipole (London) interactions. The vdW interaction between individual molecules or atoms can be described using equation (2.I), with β_{11}, a constant which includes all distance independent terms of the contributions of the two molecules:

$$G_{vdW} = -\frac{\beta_{11}}{r^6} \qquad (2.I)$$

Since colloids consists of many atoms or molecules, the vdW interaction energy is summed up for all individual molecules (Lifshitz theory, microscopic approach[115]). For two plates, the van der Walls interaction can be described in the following way (2.II):

$$G_{VdW} = -\frac{A_h}{12\pi D^2} \tag{2.II}$$

with A_h being the Hamaker constant which describes the interaction between two different materials and D being the distance between two plates. For spheres with a radius of R and distance D between the spheres smaller than the radii of the spheres, the vdW forces can be described by equation (2.III) using the Derjaguin's approximation:

$$G_A = -\frac{A_h R}{12\pi D} \tag{2.III}$$

Electrostatic interaction

A surface charge can occur due to adsorption of ionic species (for example surfactants) or by the dissociation of surface groups (e.g. OH, COOH, SO_4Na). The electric field, occurring due to the surface charges is compensated by counter ions present in solution which builds a double layer around the particle. This double layer is described by Gouy[116] and Chapman[117] as a diffuse double layer and later modified by Stern[118] who introduced the concept of specifically bound counterions in the fixed first layer (Stern layer). The surface potential ψ decreases linearly in the first layer to the potential ψ_{Stern} and then decays exponentially in the diffuse layer with increasing distance until reaching zero in the bulk solution (see Figure 2.5).

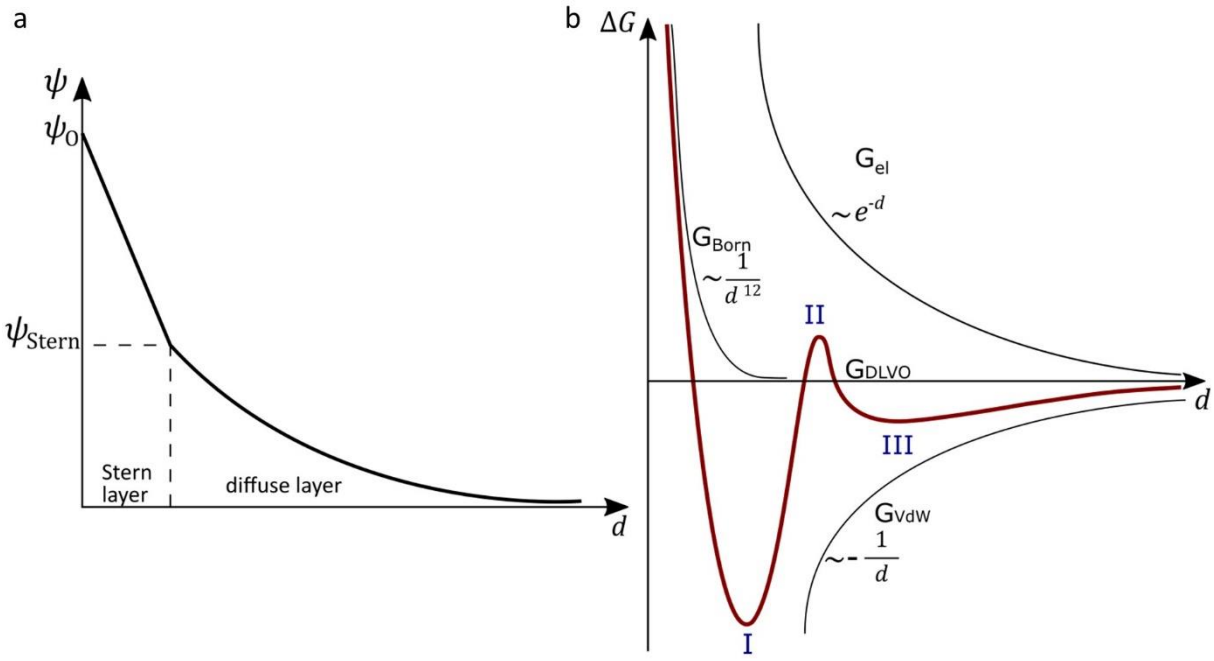

Figure 2.5: Stern model of the electric double layer: electrostatic potential versus distance diagram (a) and DLVO theory: total interaction potential of two spheres (b).

The electrostatic interaction potential G_{el} between two particles in dependence of the distance d can be described with equation (2.IV)[112], with κ, the Debey-Hückel parameter, defined in equation (2.V):

$$\boldsymbol{G_{el}(d)=\frac{64k_BTc_{Ion}\gamma^2}{\kappa}\cdot e^{-\kappa d}} \tag{2.IV}$$

$$\kappa=\sqrt{\frac{2c_0e^2}{\varepsilon_r\varepsilon_0k_BT}} \tag{2.V}$$

Here, c_{ion} is the ion concentration, γ is reduces surface potential, ε_r, ε_0 are the dielectric permittivity of the medium and of vacuum and k_B is the Boltzmann constant. The thickness of the double layer is referred to as the reciprocal of κ. Therefore, the thickness of the double layer depends on the electrolyte concentration and the valency of the ions. If two charged particles approach each other such the double layer starts to overlap, repulsion G_{el} occurs.

Total energy of interaction

The DLVO theory combines the attractive vdW forces and the repulsive double-layer forces and described the total energy of the interaction between two particles. Furthermore, the hard-sphere repulsion force (Born repulsion) which occurs at distances shorter than the particle radius can be included as well. The total energy of the interaction between two particles G_T is given as the sum of attractive and repulsive forces (equation (2.VI))[112]:

$$G_T(d) = G_{VdW} + G_{el} + G_{born} \quad \text{(2.VI)}$$

In approximation it is possible to express the total energy of the interaction as given in equation 2.VII:

$$G_T(d) = -\frac{A_h}{12\pi d} + \frac{64 k_B T c_{Ion} \gamma^2}{\kappa} e^{-\kappa d} + \frac{1}{d^{12}} \quad \text{(2.VII)}$$

Figure 2.5 b, represents the DLVO potential of two particles of the distance *d*. At short distances, the Born repulsion prevents the particles from overlapping. At slightly larger distances, a deep minimum caused by the strong vdW attractions is visible (primary minimum I). At larger distances, a shallow second minimum occurs (secondary minimum III). Between the two minima, a maximum (II) is present, which represents an energy barrier. The height of the energy barrier depends on the electrostatic repulsion. Once, the particles reach the primary minimum (referred to as aggregation), they are irreversible aggregated. To prevent the aggregation of particles, the energy barrier has to be raised by raising the electrostatic repulsion. Thus, the stability of the dispersion is determined by the height of the energy barrier. To obtain a stable dispersion (kinetically stable), the energy barrier has to be much larger than the thermal energy of the particles (>25 kT). The second minimum is referred to as the agglomeration and is reversible.

2.2.2 Steric stabilization

To prevent agglomeration of nanoparticles, stabilizers, like surfactants or polymers, have to be used. The role of a stabilizer is to increase the repulsive forces and keep the nanoparticles apart from each other. As shown above, surface charges can be introduced to create high electrostatic repulsion and agglomeration is prevented. For this electrostatic stabilization, ionic surfactants (e.g. sodium dodecyl sulfate (SDS)) can be used. Surfactants are compounds with a hydrophobic and a hydrophilic part. The surfactant adsorbs at the interface between the NPs and the medium. In case the medium is water, the hydrophilic part faces into the water phase, whereas the hydrophobic part adsorbs at the hydrophobic particle surface. Ionic surfactants feature a charged, hydrophilic headgroup that increases the electrostatic repulsion. Besides the electrostatic stabilization, also steric stabilization is possible. Here, polymers with parts that have a strong affinity to the particle surface or non-ionic surfactants are adsorbed or grafted to the particle surface (see Figure 2.6). Often block-copolymers with an A-B, A-B-A or A_nB structure are used as stabilizers (e.g. PPO-PEO-PPO; PS-PVA; PMMA-PEO-PMMA). The B block works as an anchor group to the particle surface. The block has a strong affinity to the surface and is usually insoluble in the medium. Whereas the A block is the stabilizing chain

which is highly solvated by solvent molecules. The adsorbed polymer forms a layer around the particles as shown in Figure 2.6. If two particles with an adsorbed polymer layer approach each other, at a certain distance the polymer chains may either overlap or the polymer layer is compressed. In both cases, the local segment density is increased which leads to two main effects: First, the osmotic pressure is increased, due to the reduced number of solvent molecules in the overlapping zone. As a result, solvent molecules will diffuse inside the overlapping zone in order to reduce the osmotic pressure and push the particles apart (in case of a good solvent). This unfavorable mixing of polymer is referred as the Gibbs free energy of mixing $G_{mix.}$ The mixing interaction is repulsive, as long as the solvent-chain interaction is favorable (in the case of a good solvent, Flory-Huggins parameter $\chi < 0.5$), otherwise the interaction is attractive for a poor solvent ($\chi > 0.5$) and the particles are pushed together. The second main effect is described by the elastic (volume restriction) interaction G_{el}. The interaction results from the loss in configurational entropy, due to the decreased available volume and less possible configurations of the polymer chains (referred to as G_{el}). The total free energy G_T of the system is the sum of the mixing interaction, the elastic interaction, and the vdW attraction as shown in equation (2.VIII):

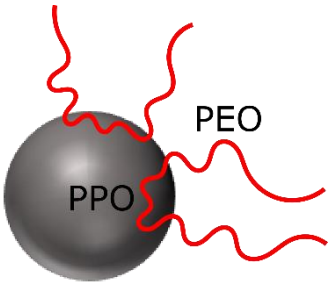

Figure 2.6: Schematic representation of adsorbed polymer layer

$$G_T = G_{mix} + G_{el} + G_{VdW} \tag{2.VIII}$$

Figure 2.7 shows the schematic representation of the different forces in dependency of the separation distance d. G_T shows only one minimum at 2δ called G_{min}. The depth of the minimum depends on the particle radius, the Hamaker constant A and the layer thickness δ (Figure 2.7 left).

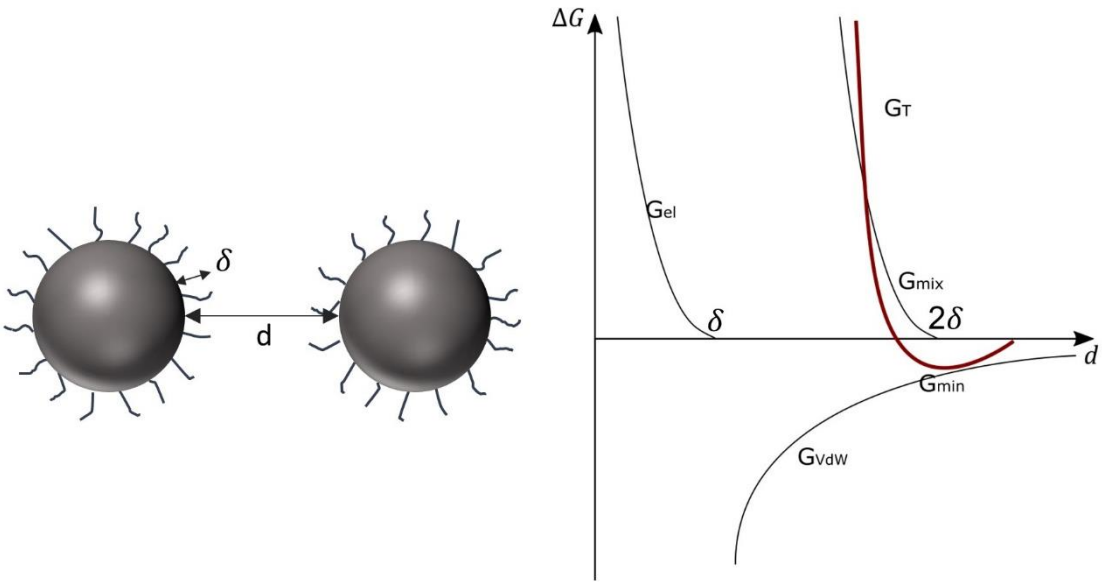

Figure 2.7: Scheme of two steric stabilized particles approaching each other and the corresponding energy diagram with attractive and repulsive forces.

By changing the molecular weight of the absorbed polymer, the layer thickness and therefore the depth at the minimum can be adjusted. Increasing the molecular weight can decrease G_{min} until no minimum occurs. At this point, the dispersion approaches thermodynamically stablility[119]. To obtain an effective steric stabilization the following criteria should be fulfilled. (I) the particles should be completely covered with polymer, bare patches could induce flocculation by vdW attraction or by bridging; (II) the polymer should be strongly adsorbed at the particle surface, (III) the stabilizing chain A should be highly soluble in the medium, and (IV) the layer thickness δ should be thick enough to have a shallow minimum, $\delta > 5$ nm.

2.2.3 Depletion attraction

Beside weak agglomeration, due to a thin layer of surface ligands, or strong aggregation, due to bad solubility of the chains in the medium, also depletion flocculation/agglomeration can occur[120]. Depletion flocculation/agglomeration occurs in the presence of free, non-adsorbing polymer. The polymer cannot approach the particle surface by a distance Δ, because the loss of entropy cannot be compensated by adsorption energy. Therefore, the particles are surrounded by a depletion zone (zone without polymer) with the thickness of Δ. If two particles approach each other closer than $<2\Delta$, so that the depletion zones overlap at a critical volume fraction, the free polymer chains are squeezed out of the overlapping zone and the osmotic pressure outside the zone increases which results in flocculation/agglomeration.

2.3 Transfer of colloidal dispersions to the solid-state

In dispersion, the properties and interactions between NPs are fairly well understood. Next, the interactions between NPs in the solid-state have to be studied towards new collective properties and applications. To explore the properties of NPs in solid materials, the NPs have to be transferred into the solid-state. Such a transfer can cause uncontrolled agglomeration. Depending on the transfer strategy agglomeration has to be prevented or can be used to advantage. To transfer NPs, the NPs can be either assembled to large superstructures (see chapter 4) or NPs can be dispersed in a medium which is later solidified (e.g. photoresin for 3D printing, see chapter 5). In the first case, the interaction forces have to be tuned to purposefully induce agglomeration. Through the control of the agglomeration, self-assembled superstructures can be produced. In chapter 2.3.1 self-assembly approaches and the underlying forces are discussed. In the second case, the dispersion of the NPs in different media can induce agglomeration, due to changing interaction forces caused by the poor solubility of ligands, depletion attraction or screened electrostatic charges. To prevent aggregation and to preserve the properties of the individual NPs, the interaction forces have to be understood and precisely adjusted, as shown in chapter 5. In chapter 2.3.2 the 3D printing technology is introduced, as a new technique to embed NPs in a solid polymer matrix.

2.3.1 Self-assembly

Self-assembly is a powerful tool that exploits interaction forces, like vdW forces, electrostatic forces or magnetic forces between the NPs, to produce functional superstructures (e.g. stacks or cubes) on the nano- to micrometer scale. Assemblies of NPs can improve the mechanical properties or display new optical, electronic or magnetic features due to coupling between the close-packed NPs[121]. The self-assembly is always driven by the reduction of free energy through finding a new energetically favored configuration ((local) minima in the free energy landscape). To control the self-assembly of NPs, the inter-NP interaction forces have to be tailored purposefully.

Self-assembly in solution

The easiest form of self-assembly is spontaneous self-assembly. The system finds a new energetically favored configuration in solution without using templates, interfaces or external fields[121]. The assembly is guided by the balance between the attractive and repulsive forces[122]. For example Kalsin *et al.* demonstrated the electrostatic assembly of NPs into binary nanoparticle crystals[123]. The spontaneous self-assembly can be further triggered by the

evaporation of the solvent[124, 125]. Liao *et al.* used different shaped Au nanocrystals, to tailor the shape of the formed superstructures upon solvent evaporation[125].

Another way to self-assemble NPs in solution is to bring the system out of equilibrium[84, 126]. Out-of-equilibrium states can be obtained for instance by the addition of antisolvents or depletion agents[112, 126]. By the addition of an anti-solvent or dispersing NPs capped with non-polar ligands in a polar solvent, attractive solvophobic interactions are induced[112]. The anti-solvent is a poor solvent for the ligands and the ligand shell collapsed resulting in an attractive force (see chapter 2.2.2). If two particles come close to each other and the surface starts overlapping, the total surface area, as well as the total surface energy is decreasing due to the attractive forces, and agglomeration occurs[127]. By the addition of depletion agents (e.g. polymers), attractive depletion forces are introduced (chapter 2.2.3). For example, Kumar *et al.* used block-co-polymers to induces depletion attraction between charged silica NPs[126]. The induced depletion attraction was stronger than the electrostatic repulsion as evidenced by small-angle neutron scattering. Furthermore, it could be shown that the depletion attraction strongly depends on the size of the particles. Besides the size of the particles, also the shape of the NPs plays a crucial role in the strength of the depletion force. The depletion attraction for nanorods is higher than for spherical particles because the overlap volume is higher[128]. For NPLs the depletion attraction is even higher, because of the extended flat planes. Therefore, the stacking of the NPLs is facilitated in comparison to rods or spherical NPs. This shape-dependent forces can be used to separate NPs of different shapes or sizes in the dispersion.

Self-assembly using templates or interfaces

Instead of performing the self-assembly in a solvent, also interfaces or templates can be applied[85, 96, 129]. This enables particularly the formation of two-dimensional structures such as films. Especially for anisotropic NPs, the formation of two-dimensional structures is of importance. Since anisotropic NPs feature anisotropic properties (as shown in 2.1.2), the collective orientation is required to get access to these properties. Also, solution-based methods (like described above) are existing to self-assemble anisotropic NPs. For example, Abécassis *et al.* used an antisolvent to stack NPLs into large anisotropic needle-like supraparticles[84]. Due to the large lateral dimension, the vdW attraction is much larger compared to spherical particles, resulting in a high stacking tendency. However, as long as the formed superstructures are dispersed in solution, the anisotropic properties cannot be used. Therefore, self-assembly

methods based on templates or interfaces are ideal to collectively assemble and orient anisotropic NPs over large scales.

For the formation of larger monolayered films of NPs, different tools can be used, like simple drop casting[130], spin coating[131], vertical deposition[132] or horizontal deposition based on convective and capillary forces[133]. These processes allow the deposition of close-packed NP films on large substrates. However, often the substrates cannot be freely chosen and many parameters, particularly for the vertical and horizontal deposition have to be adjusted to obtain close-packed films. Furthermore, the orientation of anisotropic NPs is hardly to control.

For better spatial placement of the NPs on the substrate, templates can be used. Templates can carry the information of the final placement of the particles, which is usually hard predictable in pure self-assembly approaches. Most often, predefined substrates are used to control the placement of the particles[129, 134-137]. Zhang *et al.* used a block-copolymer thin film with parallel nanoscale channels to aligned CdSe nanorods along the channels[136]. To perform the self-assembly, a film flotation method was used and the channels were exposed to the nanorod dispersion for 10 to 12 h. After rinsing the channels, the CdSe nanorods were found to accumulate at the channels. To get a controlled orientation, the channels have to be slightly larger than the width of the rods but smaller than the length of the rod. Besides the use of large expanded substrates, also other smaller interfaces, like the interface of other colloids can be applied as a template. In chapter 0, a polymer crystal in the micrometer range is applied as a template to collectively orient NPLs in the face-down configuration. Also, in the template approach, the choice of the template material is limited and is based most often on the required interaction between NPs and templates. However, in some applications, e.g. electronic applications, (e.g. solar cells or LEDs), a template or substrate could be obstructive, due to unwanted properties (e.g. electrical insulation) of the template/substrate material.

Liquid-liquid self-assembly for the collective orientation of nanoplatelets

One template-free, and substrate independent method to control the collective orientation of NPLs is the self-assembly at liquid-liquid interfaces. Murray and co-workers developed the method to produce transferable superlattice structures on the centimeter scale[138]. The particles are dispersed in a low-boiling point solvent (usually hexane) to allow evaporation, which is added on a liquid subphase. The subphase does not mix with the upper phase, is usually chemically inert, and typically exhibits low vapor pressures (e.g. diethylene glycol, see Figure 2.8 a). In this scenario, the upper phase is left to evaporate and NPs deposit at the liquid interface

of the lower phase. After full evaporation of the upper phase, the formed NP film can be transferred on solid substrates. To control the orientation of the NPLs, the interaction potential between the NPLs and the interface has to be controlled. Gao *et al.* used this approach so assemble CdSe NPLs (discussed in chapter 2.1.2) in monolayered films (Figure 2.8 b)[85]. They controlled the orientation by the addition of oleic acid to the subphase. Oleic acid can act as a surfactant and can be located at the interface altering the interfacial tension. If oleic acid is present, the NPL ligand shell can interact with the oleic acid layer and the NPLs deposit face-down. If no oleic acid is present, the interfacial tension is higher and the interaction between the NPLs to the interface is unfavored. Instead of using oleic acid as an agent to altering the interfacial tension, it is also possible to control the interfacial tension by changing the subphase as shown by Erdem *et al.*[96]. In chapter 4 the liquid-liquid self-assembly method was used and a new way was developed to control the collective orientation of NPLs. Instead of controlling the interfacial tension, it is demonstrated that the evaporation rate of the solvent can be the determining factor for the orientation.

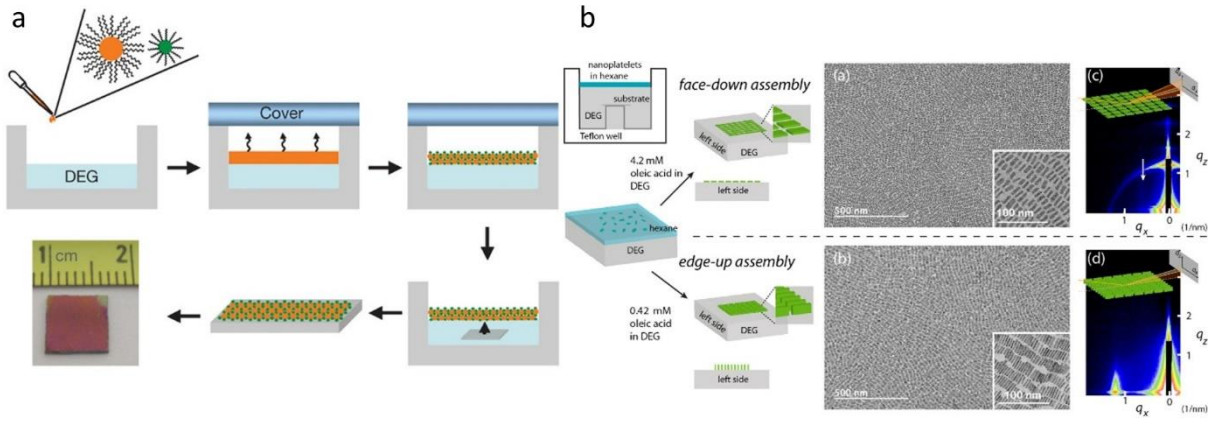

Figure 2.8: Schematic illustration of self-assembly on a liquid/air interface (a), (Reproduced with permission from ref. 138, Copyright 2010 Springer Nature); CdSe NPLs assembled into monolayered films in controlled configuration (edge-up or face-down) (b), (Reproduced with permission from ref. 85, Copyright 2017 American Chemical Society)

Coupling effect of nanoparticle assemblies

As already mention in chapter 2.1.2, the assembly and organization of NPs can lead to strong coupling effects between NPs and could therefore affect, among others, the optical[12], plasmonic[13] or electronic[14] properties. For example, besides the enhanced energy transfer mentioned in chapter 2.1.2[15], a radiative energy transfer, due to the small Stokes shift and reabsorption of the photon by neighboring platelets in a stack at low temperatures is observed[12]. Due to this collective effect, an additional emission line occurs, which is attributed to the

longitudinal optical phonon replica of the band-edge exciton. In the case of plasmonic NPs, a plasmonic hybridization between the NPs occurs due to the strong coupling[13]. A bonding and anti-bonding hybridization mode are formed and the localized plasmon resonance frequency shifts. Based on these coupling effects, new applications with novel properties are developed[121, 139].

2.3.2 Additive manufacturing

Besides the self-assembly approach to transfer NPs to the solid-state, NPs can also be integrated into solid matrix materials. One way to integrate NPs in solidified 3D structures is based on additive manufacturing. Additive manufacturing methods such as 3D printing are considered as an advanced technology to process materials into a 3D complex structure. In the 1980s the first 3D printer based on stereolithography (SLA) was developed by Charles Hull. Further techniques were developed like, fused deposition molding, selective laser sintering, binder jetting, digital light processing, sheet lamination and paste extrusion among others in the following years[140]. Compared to other manufacturing methods, 3D printing allows quick prototyping of highly complex geometries and mulitcompositions, and allows the application of 3D printing in many fields from microelectronics and microsystems to aerospace structures[141]. Besides other 3D printing techniques, stereolithography is still one of the most used 3D printing techniques. SLA is based on a liquid polymer resin which can be cured using UV light. The photoresin is placed in a reservoir and a UV laser cures the photoresin at programmed positions and a layer-by-layer structure is formed[142]. In conventional SLA the curing process is based on one-photon absorption (1PA) and the resolution is limited. The resolution in the lateral dimension depends mainly on the size of the laser spot[143, 144]. The laser spot diameter on a standard SLA-250 stereolithography machine is 250 µm[143-145]. This leads to a final minimum feature size of around half of the laser beam. To reduce the resolution, for example a single mode instead of a multimode HeCd laser can be used (80 – 100 µm)[143]. In addition, the resolution can be further reduced by focusing the laser spot more accurately on the surface of the photoresin. For this, the optics of the system have to be adapted and the position of the surface has to be continuously measured (vector-by-vector scanning)[144]. However, these techniques are still limited by the diffraction limit of the applied laser wavelength. Hence, to improve the resolution further to the nanometer regime, more advanced techniques, that a not based on the diffraction limit, like two-photon polymerization, are necessary.

Two-photon polymerization 3 D printing

To further reduce the resolution beyond the diffraction limit and improve the printing accuracy, a two-photon polymerization (TPP) process can be used[146, 147]. With this technique, resolutions up to the nanoscale can be realized. Here, the polymerization of the photoresin is induced by a third-order nonlinear absorption within the focal plane and the resolution can be

beyond the optical resolution limit[147]. In general, the resolution limit depends strongly on the laser power (LP) and the exposure time[148].

The two-photon absorption (2PA) is a third-order nonlinear optical phenomenon described theoretically in the 1930s by Goeppert-Mayer and was proven experimentally in 1961 by Kaiser[149, 150]. A molecule is excited from the ground state to an excited state by quasi simultaneously absorbing two photons. 2PA is mediated by a virtual state with an extremely short lifetime. Only when the second photon is absorbed before the decay of the first photon 2PA is possible. The photons can have the same energy or different energies (degenerate case and non-degenerates case, see Figure 2.9). After excitation, the system quickly relaxes into the lowest vibrational level of the lowest-energy excited state by internal conversion or vibrational relaxation. Finally, the system returns into the ground state by radiative or non-radiative paths.

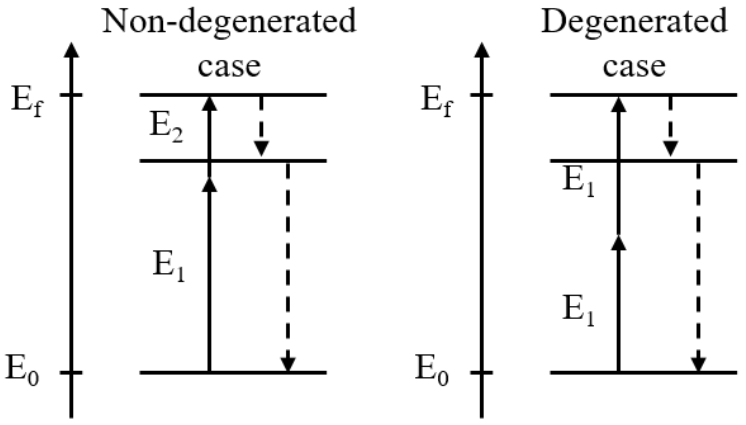

Figure 2.9: Principle of two-photon absorption.

The probability for two-photon absorption depends on the square of incident light intensity of the laser used for excitation when two photons have the same energy. These requirements are best met in the focal spot of the laser beam and therefore the 2PA excitations are strongly confined. Thus, high printing resolutions can be achieved.

To realize 3D printing based on 2PA, usually a femtosecond laser with a wavelength in the NIR (e.g. 780 nm-800 nm Ti:sapphire) is used[151]. The laser is focused using an objective inside the photoresin (see Figure 2.10 a). Only in the focal volume, the resin can be cured. The spot size of the laser is determined by the diffraction limit. For example, a laser with a wavelength of 800 nm focused by an oil immersion objective (NA 1.4) has a resulting spot size of 350 nm[152]. Due to the energy threshold for the 2PA, it is possible to further improve the resolution by adjusting the LP and exposure time[147, 148]. Only the central part of the Gaussian profile of the laser spot exhibits enough energy to overcome the 2PA threshold and induced the polymerization (see Figure 2.10 b) and resolutions down to 100 nm are feasible[148].

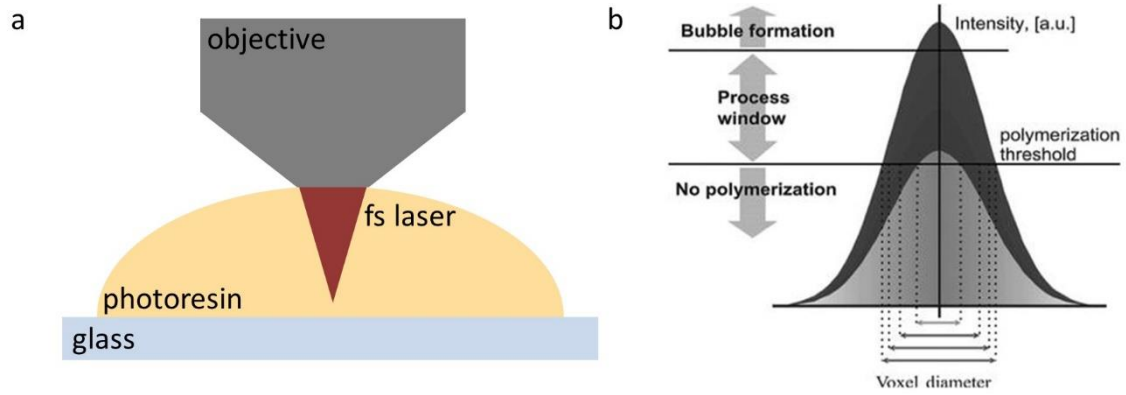

Figure 2.10: (a) Principle of TPP 3D printing in the dip-in configuration; (b) Gaussian intensity profile of the laser spot. Above the polymerization threshold, the photoresin can be cured, (Reproduced with permission from ref.148, Copyright 2008 Springer Science Business Media, LLC).

Incorporation of nanoparticles

The combination of 3D printing and colloidal nanotechnology offers huge potential creating 3D engineered materials with tunable properties and multifunctionality and opens even more application fields. By integration of NPs with specific properties, such as e.g. conductivity[153], magnetism[154] or fluorescence[155], the final 3D printed materials own these properties. For example, Ceylan *et al.* constructed a microrobot loaded with iron oxide NPs which allows the magnetically driven motion of the swimmers[154]. Leigh *et al.* used carbon black as a filler to prepare electronic sensors[153]. The properties of the final material depend not only on the individual properties of the host material and the nanomaterial but also on the morphology of the nanomaterial and the interfacial interaction between host material and nanomaterial[151]. For instance, the combination of host material and a nanofiller can improve the mechanical properties of the final material. Often a chemical modification of the surface of the nanofiller is applied to ensure a high interfacial interaction between host material and nanofiller[156, 157]. For example Yugang *et al.* studied the effect of TiO_2 NPs on the mechanical properties of a 3D printed structure[16]. The NPs were functionalized in order to create hydroxyl groups on the surface to allow better interaction with the polymer. It is described that already an addition of 0.25 wt% NPs, the tensile strength increased by 89%, the modulus increased by 18% and the flexural strength increased by 6% compared to the pure cured photoresin[16].

By combining NPs with a polymer as host material not only the properties of the printed structures are affected. Also, the printing process itself can be influenced by the presence of NPs. For instance, the viscosity of the liquid photoresin can be influenced[158], or what is

especially important for TPP 3D printing, the interference of the nanofiller with the laser light can play a role since the absorption of the laser light by the NPs could affect the resolution of printed structures, respectively. For example, Jonušauskas *et al.* studied the influence of Au NPs on the printing performance[159]. They used SZ2080 as photoresin, a so-called negative photopolymer, which can be cured with a laser at 515 nm. They found that the line width for a photoresin containing Au NPs ($3.9 \cdot 10^{-3}$ wt%, 7 nm diameter) induces an increased linewidth by up to 14.8%. Therefore, it is possible to replace 0.1% of the commercial initiator Igarcure 369 in terms of photosensitivity. The observed effect can be explained by the plasmonic effect of the added Au NPs[160, 161]. The same group expanded the study to a PEG-DA-700 hydrogel based photoresin[162]. In this case, the linewidth is reduced upon the addition of Au NPs. Besides Au NPs, the effect of QDs on the printing was studied by Peng *et al.*[155]. A pentaerythritol triacrylate monomer as photoresin was mixed with CdSe/ZnSe QDs (different sizes; λ_{em} = 460 nm; 510 nm; 620 nm) and printed using a TPP 3D printer. It was shown that the presence of QDs improves the spatial resolution of the printed structures. In the presence of QDs, the polymerization rate is reduced and the improved resolution might be due to the absorption of the laser light by the QDs. However, the improved resolution is only observed for the red-emitting QDs, although the other two QDs species are also able to absorb the laser light. Besides the absorption of the laser light, also other effects like radical quenching can occur. These effects are further analyzed in chapter 5.

2.4 Motivation and Outline

As shown in chapter 2.1, NPs have size-tunable chemical and physical properties. Especially the synthesis of NPs in the colloidal dispersion allows a precise control of the size, shape, composition and surface (e.g. core-shell nanoparticles, 2D nanoplatelets, QDs in different sizes). The usage of NPs in various applications (e.g. LEDs) is a logical step to improve existing applications (e.g. improved color purity of displays) and develop new technologies (e.g. polarized LED). For many applications, the NPs have to be transferred into the solid state, e.g. by forming superstructures, films or by embedding the NPs in a host material. However, the transfer of the nanoparticles can cause unwanted agglomeration which can result in the loss of properties (e.g. agglomerates of plasmonic nanoparticles loss their plasmonic features). But also new collective properties in the solid-state like photoconductivity can be achieved by controlled agglomeration. To investigate the resulting collective properties of nanoparticles in the solid state, unwanted and uncontrolled agglomeration have to be inhibited. Therefore, the focus must be on the control of the interaction potential between NPs during the transfer. Next, the interactions between nanoparticles can be selectively modified to tailor the properties and to introduce new functions, like photoconductivity, into the solid-state through coupling effects between nanoparticles when in close proximity. Directional interactions between anisotropic nanoparticles can be introduced for orientation control in films, to access and adjust anisotropic, ensemble properties, like polarized light emission or photoconductivity.

The aim of this work is to study and adjust the interaction between nanoparticles in order to control the properties (like photoluminescence), the arrangement and orientation (face-down or edge-up of NPLs in films) and the dispersibility of nanoparticles in different media (photoresin, PDMS oil, photoconductivity polymer) for 3D printing, microcopy and LED applications.

So far, the optical properties of CDs are improved by the usage of passivation agents, like a polymer coating. In **chapter 3**, it is shown that not only a polymer coating but also the interaction of CDs with a polymeric nanoparticle have a beneficial effect on the optical properties. A CD-polystyrene nanoparticle system is developed that shows a strong photoluminescence enhancement (~5 fold) due to the interaction between carbon dot systems and the interface of polystyrene NPs. These results show the potential of the combination of different nanomaterials due to interactions.

In **chapter 4**, a self-assembly method based on evaporation kinetics is developed to control the collective orientation of NPLs in order to study and access anisotropic properties (e.g. photoconductivity, polarized light emission). The produced monolayer film with controlled orientation (edge-up or face-down), exhibiting long range ordering of transition dipole moments and macroscopically polarized light emission. In comparison to existing methods, this method avoids insulating additives, making it ideal suited for optoelectronics. Furthermore, a strongly orientation dependent charge transport in a single nanoplatelet layer can be observed. This new approach paves the way towards novel optoelectronic devices such as polarized light-emitting diodes.

In **chapter 5**, the interaction between the NPs are adjusted by modifying the surface of NPs with a thiolated PMMA polymer. By the surface modification the dispersion of NPs without agglomeration in high concentrations in an acrylate based photoresin is realized. Therefore, it is now possible to study the interference of NPs on the TPP 3D printing process independent on the presence of agglomerates. The effect of NPs on the TPP 3D printing process is analyzed in a concentration-dependent manner using three different NP materials (Au, Ag and CdSe) with complementary optical properties (plasmonic and fluorescence, 1PA and 2PA). Due to interaction with the laser light and photogenerated radicals, the printing resolution is improved. However, at the same time, the printing process can be more challenging due to thermal decomposition, respectively. The understanding of successful colloidal stabilization and interference of NPs with the TPP 3D printing process has to be considered when printing new functional NP-loaded polymeric structures, like gratings for enhanced light outcoupling.

Finally, in **chapter 6**, ongoing collaborative projects, mainly focused on two possible applications of anisotropic NPs are highlighted, namely the usage of NPLs as fluorescent stain in microscopy and the integration of NPLs in organic light-emitting diodes. Additionally, a simple template-assisted self-assembly method for NPLs is developed. Due to the outstanding optical properties and high stability against degradation, CdSe/CdZnS NPLs could be excellent candidates for fluorescent staining in PDMS oils. The aim is to disperse CdSe/CdZnS NPLs in a PDMS oil without agglomeration and high loadings, in order to obtain a PDMS oil with a high photoluminescence. Here, the stability of the NPLs dispersed in PDMS oil plays a crucial role, because the oil must be stained homogenously to obtain the best possible imaging quality. To improve the dispersibility of NPLs in the PDMS oil, the NPL surface is modified with PDMS chains. Therefore, two different methods (ligand exchange and polymer coating) were

applied. It is found that the size of the formed agglomerates decreases, using the polymer coating technique. In the second application related project, NPLs are used in organic light-emitting diodes. An approach previously applied for spherical QDs, which is based on energy transfer between excited photopolymers and QDs[163], should be transferred to the anisotropic NPLs to further increase the efficiency and color purity of the light-emitting device. In this approach, the electron trapping can be avoided by using a polymeric shell around the particles. To achieve this insultation layer, the surface of the NPLs is modified with a polymer shell. Two different approaches (ligand exchange and polymer coating) are applied and the dispersibility of the NPLs in the conduction polymer were analyzed. Furthermore, first experiments show a successful electron trapping for NPLs modified with the polymer coating approach. In the last project, a template assisted self-assembly approach is developed to collectively control the orientation of NPLs in the face-down configuration and simultaneously control the distance between two NPLs layers. By the precise distance control, it possible to study optical effects caused by the NPLs spacing. As template for the self-assembly, flat, crystalline polymer flakes, with precisely adjustable thickness, are used. The formed polymer flake NPL composites are analyzed using transmission electron microscopy and optical spectroscopy.

3. Enhanced photoluminescence properties of a carbon dot system through surface interaction with polymeric nanoparticles

The work described in chapter 3 is based on the paper published in the journal *Journal of Colloid and Interface Science*, volume 517, 2018, p.11-20. Reproduced with permission from copyright 2018 Elsevier Inc.

This chapter focus on the surface interaction between carbon dot systems (CDSs) and polymer colloids and the influence on the fluorescent properties were investigated. In the presence of specific molecules or ions, the fluorescence properties of CDSs can be strongly influenced. While several passivating polymers have been directly attached to the carbon dot systems, the interaction of carbon dot systems with the polymer surface of colloids has not been investigated as a way to activate or enhance the photoluminescent properties. We show that depending on the synthesis route (*in situ* or mixing), the carbon dot systems are either covalently attached (*in situ*) or electrostatically bound (mixing) to the surface of the nanoparticles. Regardless of the preparation methods of the investigated carbon dot – polymer nanoparticle system and the interaction (chemical or physical) with the surface, the fluorescence intensity is strongly enhanced and the fluorescence lifetime prolonged.

My contributions to the project were the synthesis of the carbon dots and the development and characterization of the CDS-nanoparticle systems. Lifetime measurements were performed by Dr. Irina Rörich (MPI-P) and Dr. Simon Bretschneider (MPI-P), fluorescence microscopy were performed by Dr. Sandra Ritz (IMB) and FACS experiments were performed by Dr. Manuel Tonigold (MPI-P).

3.1 Introduction

Recently, a new class of fluorescent carbon nanomaterials, so-called CDSs, has attracted great attention due to their excellent PL properties[26, 64] and low-toxicity[39]. Additional advantages are a high water-dispersibility and photostability, a strong chemical inertness as well as easy surface functionalization[18].

One interesting feature of CDSs is the strong surface-dependent sensitivity of their PL properties. Small changes in the surrounding environment can lead to a strong change in the

PL. As such, CDSs can be sensitive towards changes of the pH value of the surrounding medium[29, 54] which changes the protonation state of the surface functionalities of the CDS and affect the optical properties. Furthermore, the polarity of the surrounding medium affects their PL properties[164].

Also, molecules, such as ascorbic acid[165], or sugars[166], or specific ions, such as Fe^{3+} or Cu^{2+} can influence the PL properties[167]. Therefore, CDSs are highly versatile fluorescent sensors for diverse applications, like a sensor for ferric ions in biological systems or monitoring of glucose[168]. The surface sensitivity of the fluorescent properties of CDSs is also displayed in the activation of the fluorescence properties through passivation agents such as a polymer coating[169-171]. In this process of surface coating (e.g. with poly(ethylene imine)[170] or poly(ethylene glycol)[27]), CDS which hardly possess fluorescent properties are being activated and display a much stronger fluorescence after coating. Such a thin layer of passivation agent around the CDS protects them from the environment and the effect of contaminants in the surrounding on the fluorescence properties is reduced[26]. Furthermore, the fluorescence lifetime is prolonged if the CDS is passivated[172]. It is supposed that CDSs become emissive due to the reduction of non-radiative recombination by stabilizing the trap states via passivation with surface passivation agent[27, 173]. Besides the activation of the PL properties through direct attachment of passivating polymers, enhanced PL properties of CDS has been observed when embedding them in a polymer film[70, 174]. While it is an established procedure to activate the PL properties of CDSs through direct attachment of passivating polymers, a different approach, attaching CDS through their physical interaction with the surface of polymer colloids has never been used to induce a stronger PL.

In this study, the interaction of CDS with polymer colloids is investigated. To introduce CDS – polymer NP interactions, CDS in the range of few nanometers are either generated in one-step in the presence of polystyrene (PS) NPs in a microwave (MW) assisted synthesis (*in situ*) (Scheme 3.1, upper part) or in two steps, first CDS were synthesized in the MW and afterward mixed with PS NPs (mixing) (Scheme 3.1, lower part). Interestingly, the interactions between the surfaces of both species (CDS and PS NP) strongly increased the fluorescence intensity and lifetime of the CDSs in the same order of magnitude for both approaches. The enhancement mechanism is however difficult to reveal and has to be further studied in the future in more detail. While the *in situ* reaction yielded a covalently attached CDS on the surface of the PS NPs, the mixing method resulted in physically adsorbed CDS which could be removed by

changing the electrostatic interaction between the CDS and PS NPs via pH-change. Since both attachment mechanisms yield a similar increase in fluorescence properties, the enhancement mechanism can be assumed independent of the attachment type (covalently bound or electrostatically adsorbed). Furthermore, both systems were characterized by electron microscopy to investigate the surface morphology of the PS NPs before and after CDS coverage and flow cytometry to show the homogeneous attachment of CDS on the surface of the PS NPs. Additionally, cell uptake of CDS-labeled PS NPs was performed and visualized by fluorescence microscopy to demonstrate the efficient labeling of PS NPs with surface-activated CDS.

3.2 Experimental Part

Chemicals. Acetic acid, acrylic acid, chitosan (low molecular weight), polyvinylpyrrolidone (PVP, MW 55000) and styrene were purchased from Sigma-Aldrich. 2,2'-Azobis(2-methylbutyronitril (V59) was procured from Wako, 1,2-ethylenediamine (EDA) from Fluka and hexadecane from Merck. Poly(ethylene glycol)-p-(1,1,3,3-tetramethylbutyl)-phenylether (Triton X-100) was purchased from Thermo Fischer and sodium dodecyl sulfate (SDS) was procured from Alfa Aesar. Sodium chloride (0.1 N) was purchased from Roth and sodium hydroxide (1 N) was purchased from VWR. Lutensol AT50 was procured from BASF. All chemicals, except for styrene, were used without further purification. Styrene was passed through a silica column to remove the stabilizer. For all experiments, only MilliQ water (18.2 MΩ·cm) was used.

PS nanoparticle dispersion. Carboxyl-functionalized PS NP (PS-COOH NP) dispersions were prepared by a miniemulsion polymerization technique[175]. Styrene (3.3 mL, 0.03 mol), hexadecane (0.162 mL, 0.55 mmol), serving as ultrahydrophobe, acrylic acid (0.57 mL, 9.96 mmol) and the hydrophobic initiator V59 (0.05 g, 0.26 mmol) (and 1.5 mg Bodipy 520/535 (sample PS_COOH_7, Figure 3.1 for chemical structure) were added to the aqueous phase containing 0.3 wt% SDS solution (24 mL).

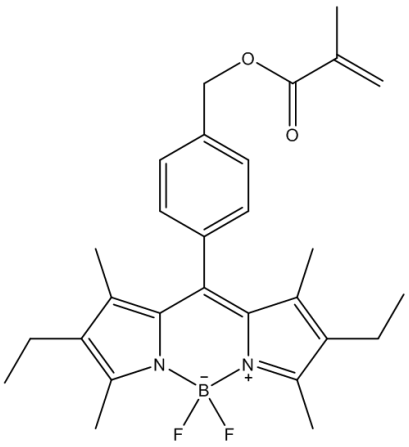

Figure 3.1: chemical structure Bodipy 520/535.

After 1 h preemulsification (stirring at 500 rpm at room temperature), the mixture was sonicated for 120 s at 70% amplitude (Branson sonifier W450 digital, ½ inch tip, 120 s, ice cooling). The copolymerization was performed for 20 h

at 71 °C with the stirring rate fixed at 500 rpm. Afterward, the miniemulsion was filtrated through a KimWipe and dialyzed against water for 2 days (MWCO 50,000). To synthesize PS NPs without a comonomer, the same procedure was used without the addition of acrylic acid. The characteristics of the synthesized PS NPs are summed up in Table 3.1.

PS microsphere dispersion. For Flow cytometry measurements larger particles were required**.** PS-COOH MSs were therefore synthesized according to a slightly modified procedure described by Song *et al.*[176]. Briefly, styrene (3.44 mL, 0.03 mol) was dissolved in ethanol (11.88 mL). The stabilizer polyvinylpyrrolidone (0.5 g, MW 55000), co-stabilizer (Triton X 100) (0.175 g) and initiator V59 (0.125 g, 0.65 mmol) were added under vigorous stirring. After the first polymerization step (70 °C, 500 rpm), a mixture of ethanol (11.88 mL), acrylic acid (0.24 mL, 4.19 mmol) and styrene (3.44 mL, 0.03 mol) was heated up to 70 °C and added to the reaction mixture. The copolymerization was performed for 24 h at 70 °C with a fixed stirring rate of 500 rpm. For purification, the dispersion was centrifuged at 6654 rcf for 5 min (Sigma 3-30 K) and redispersed in MilliQ water. The procedure was repeated twice. The characteristics of the synthesized PS MSs are summed up in Table 3.1.

Table 3.1: Characterization of PS particle dispersions with different particle sizes and surfactants. a) determined by particle charge detection; b) determined by dynamic light scattering; c) determined by scanning electron microscopy.

PS_ID	Functionalization	co-monomer	groups/ nm^{2} a)	surfactant	ζ/ mV	R_h/ nm	solid content
PS_COOH_1	carboxyl group	acrylic acid	1.1	SDS	-57 ±11	70 ± 10 b)	10 wt%
PS_COOH_2	carboxyl group	acrylic acid	Not estimated	SDS	-53 ± 10	65 ± 10 b)	10 wt%
PS_COOH_3	carboxyl group	acrylic acid	/	PVP (55000 g/mol) & Triton X 100	– 22 ± 4	1630 ± 510 c)	2 wt%
PS_COOH_4	carboxyl group	acrylic acid	1.1	SDS	Not estimated	50 ± 5 b)	14 wt%
PS_COOH_5	carboxyl group	acrylic acid	1.6	SDS	- 67 ± 8	70 ± 30 b)	13 wt%
PS_COOH_6	carboxyl group	acrylic acid	1.1	SDS	- 58 ± 14	65 ± 30 b)	12 wt%
PS_COOH_7	carboxyl group	carboxyl group	1.0	SDS	-44 ± 12	85 ± 20 b)	13 wt%
PS_1	/	/	/	Lutensol AT 50	/	130 ± 30 b)	9 wt%

Preparation of CDS-nanoparticle system. The CDS-NP systems were synthesized according to a modified procedure described by Gong *et al*[31].

In situ. The particle dispersions and the volume ratios of the ingredients used in the reaction are given in Table 3.2. The samples prepared with the *in situ* method are referred to as IS. PS_ID indicates the name of the used particle dispersion (listed in Table 3.2). $c_{PS\ disp}$ displays the weight concentration of the particle dispersion. A NP dispersion and a chitosan solution (0.01 wt% in relation to mass of chitosan stock solution, 1% v/v acetic acid for chitosan solution; served as a carbon source) were mixed in a 1:10 volume ratio. EDA (different volumes, served as nitrogen source) were added. The reaction in the MW (Discover SP, CEM) was performed at 100 °C with a power of 100 W for 15 min. After the MW treatment, the dispersions were purified by centrifugation (30 min, 16351 rcf) (Sigma 3-30 K, Sigma) and redispersed in MilliQ. The purification procedure was repeated twice.

Table 3.2: Used parameters for the generation of CD-polymeric NP systems (*in situ* IS and mixing MI).

In situ (IS)	**Sample Name**	**PS_ID**	**$c_{PS\ disp.}$/ wt%**	**Volume ratio PS disp. : chitosan solution : EDA**
	IS_1	PS_COOH_5	8.8	1 : 10 : 0.25
	IS_2	PS_COOH_1	10	1 : 10 : 2
	IS_3	PS_COOH_3	2	1 : 10 : 1
	IS_4	PS_COOH_2	10	1 : 10 : 1
	IS_5	PS-COOH_7	13	1 : 10 : 0.25
Mixing (MI)	**Sample Name**	**PS_ID**	**$c_{PS\ disp.}$/ wt%**	**Volume ratio PS disp. : CDS disp.**
	MI_1	PS_COOH_4	14	1 : 10
	MI_2	PS_COOH_6	10	1 : 1.25
	MI_3	PS_COOH_4	10	1 : 10
	MI_4	PS_COOH_5	10	varied (0:1 – 2:1)
	MI_5	PS_COOH_6	10	1 : 1.25
	MI_6	PS_1	10	1:2

Mixing. The used particle dispersions and volume ratios of the ingredients are given in Table 3.2. The samples prepared with the mixing method are referred to as MI. PS_ID indicates the name of the used particle dispersion (listed in Table 3.2). $c_{PS\ disp}$ displays the weight concentration of the particle dispersion. 1 g of chitosan was mixed with 10 mL 8 v/v% acetic acid in a MW vial and 5 mL EDA have added afterward. The reaction was performed in the MW (Discover SP, CEM) for 15 min at 100 °C and a power of 100 W. To the reaction mixture, 30 mL water was added. The mixture was centrifuged at 10397 rcf for 30 min. After freeze-drying the supernatant, the solid CDS were redispersed in MilliQ water (c = 1 mg/mL). To prepare the CDS-NP system, the prepared CDS dispersion was mixed with a PS-COOH NP dispersion in different volume ratios.

Cell uptake. HeLa cells were incubated for 4 h at 37 °C and 5% CO2 with a dispersion of CDS-coated PS-COOH particles and a dispersion of non-coated PS-COOH particles as a non-fluorescent reference (c = 75 μg/mL). After the incubation, the medium was removed and the cells were washed with PBS. Afterward, the cells were fixed with paraformaldehyde (4 wt%) on the substrate for confocal laser scanning microscopy.

Characterization. For the determination of the hydrodynamic diameters of the particles, dynamic light scattering (Nicomp 380 submicron particle sizer) was performed. The detection angle was fixed at 90 ° at 25 °C and the laser wavelength was 635 nm. The zeta potential was determined by electrophoretic light scattering (Malvern Instruments Zeta Nanosizer) at a detection angle of 173 ° in an excess of 10^3 M KCl aqueous solution. The laser wavelength was 633nm. The surface charge was determined via particle charge titration using a particle charge detector (PCD 02 Mütek GmbH, Germany). The sample (1 wt%, aqueous dispersion) was titrated with a cationic polydiallydimethyl ammonium chloride (Poly-DADMAC) polyelectrolyte at a neutral pH value. The solid content of the applied dispersions was investigated gravimetrically using freeze-drying.

Molecular weight and weight distribution were determined by gel permeation chromatography (GPC) using a PSS SECcurity device (Agilent Technologies 1260 Infinity). The freeze-dried samples were dissolved in tetrahydrofuran and eluted at a flow rate of 1.0 mL min−1 at 30 °C. PS standards were used for calibration. The glass transition temperature was determined with DSC (Mettler Toledo DSC 823e) at a heating rate of 10 K·min-1 from - 140 °C to 180 °C under nitrogen atmosphere.

SEM was performed on a Hitachi SU8000 with an acceleration voltage of 0.200 kV or 0.375 kV. The samples were diluted in water and dropped on silica wafers and left to dry. TEM was performed on a Jeol JEM-1400 with an acceleration voltage of 120 kV on a carbon-coated 300 mesh copper grid. For the high-resolution TEM, a FEI Tecnai FE 20 was used with an acceleration voltage of 200 kV. For FTIR measurements, a Perkin Elmer Spectrum Bx spectrometer was used a.

The fluorescence of the samples was measured using a Tecan infinite M1000 reader with the gain adjusted to 100 at different excitation wavelengths. For time-resolved measurements, the samples were excited with a wavelength of 400 nm utilizing the frequency-doubled output from a Ti:Sapphire laser (Coherent, Libra HE 3.5 mJ) supplying 100 fs pulses with a repetition rate

of 1kHz. The luminescence was detected by a streak camera (Hamamatsu C5680). The PL decay was collected at the spectral maximum of the luminescence peak. The instrument response function (IRF) was 0.12 ns.

Flow cytometry measurements were performed on a Partec CyFlow ML cell sorter. Furthermore, for fluorescence imaging, a Leica TCS SP5 confocal fluorescence microscope was used.

3.3 Results and Discussion

To realize an interaction of CDSs with the surface of polymer NPs, two different procedures were developed (Scheme 3.1). In the one-step procedure, the CDS were synthesized directly in the presence of PS NPs (upper part Scheme 3.1). In the two-step procedure, the CDSs were synthesized separately and afterward mixed with the PS NPs (lower part Scheme 3.1). In both cases, chitosan, acetic acid, and 1,2-ethylenediamine (EDA) were used as precursors for the CDS. Chitosan is here the main carbon source. Acetic acid, which dissolves chitosan, acts as a secondary carbon source and provides carboxyl groups for the condensation of EDA[31]. The nitrogen of EDA acts as N-dopant for the CDSs[177, 178].

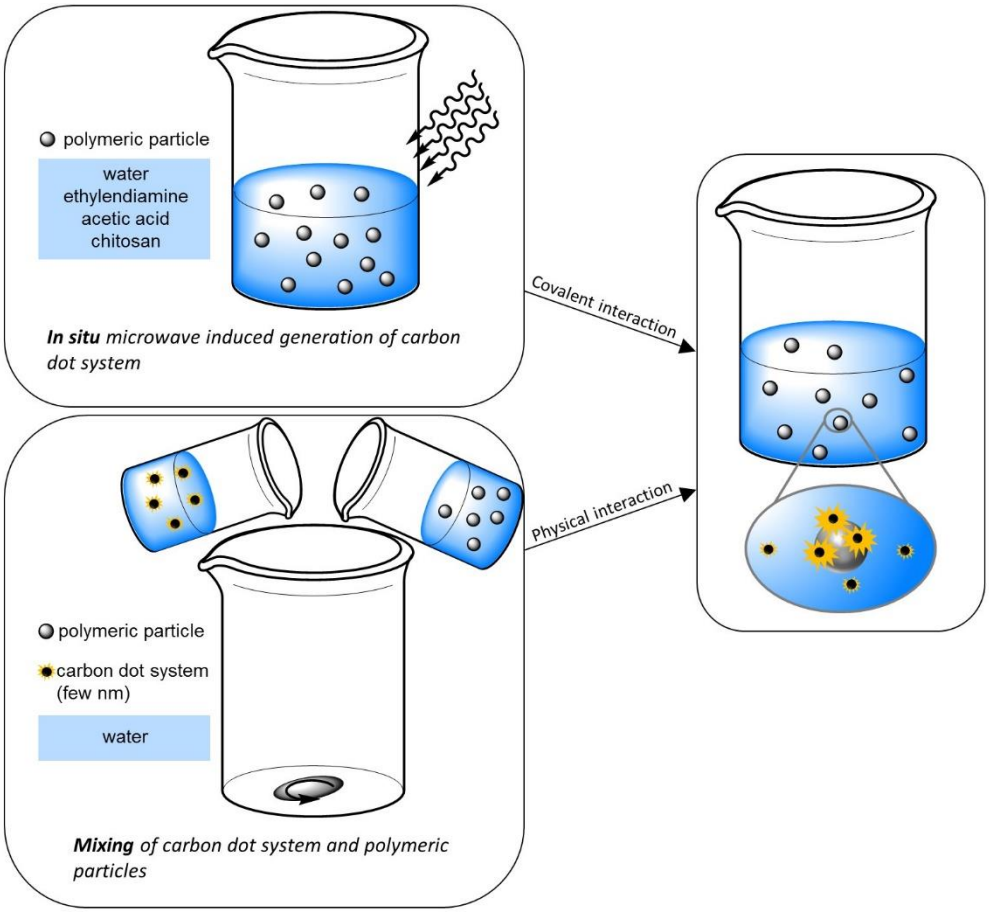

Scheme 3.1: Schematic description of the fluorescence enhancement of CDS through interaction with polymer NPs. Upper part: Polymer particles are dispersed in aqueous solution containing 1,2-ethylenediamine, acetic acid and chitosan (CDS precursors). During hydrothermal MW treatment, fluorescent CDSs are generated from the precursors and covalently attached to the surface of the polymer particles (right). Lower part: Polymeric particles dispersed in water and an aqueous CDS dispersion are mixed. Through mixing the CDSs are physically attached to the surface of the polymeric particles (right).

Here, we used carboxyl-functionalized polystyrene NPs as a center particle, since they are common and well-studied model particles. It has to be noted, however, that we also used other types of polymer particles and found some differences among the particles. Hence, the results shown in this thesis for PS NPs cannot directly be transferred to other polymer NP systems. Using a miniemulsion polymerization process, PS-COOH or PS NP were prepared (see Experimental Part 3.2) and the characteristics of the PS-COOH or PS NP dispersions are summed up in the Experimental part (see Table 3.1).

To enable the *in situ* generation of a CDS-NP system, the precursors were mixed with an aqueous PS-COOH NP dispersion. Condensation of the amine groups of EDA with the carboxyl groups on the PS-COOH NP surface could function as an anchor for the emerging CDS and couple them to the PS-COOH NP. Through a thermal treatment of the mixture in the MW, N-doped CDS were formed and bound to PS-COOH NPs in a single reaction step (see Experimental Part 3.2). To enable the generation of CDS-NP systems through mixing, the CDS precursors were first mixed and then treated in the MW in absence of NPs to synthesize N-doped CDSs. In a second step, the CDSs were mixed with PS-COOH or PS NPs, thus both species can interact with each other and form a CDS-NP system (see Experimental Part 3.2). An electrostatic interaction between amine groups of the CDSs and the carboxyl groups on the PS-COOH NP surface can lead to attachment of the CDSs to the surface of the PS-COOH NPs without a further coupling step. Independent of the reaction scheme, we observed that due to an interaction between CDS and the PS surface, the fluorescence intensity is drastically enhanced as schematically illustrated in Scheme 3.1 on the right side. In the following section, the characterization of the mentioned CDS-NP systems is described in more detail.

3.3.1 Investigation of optical properties of the carbon dots system coated polymeric nanoparticles

To investigate the effect of PS-COOH NPs on the optical properties of CDSs, the fluorescence of CDSs in the presence and absence of PS-COOH NP was studied using fluorescence spectroscopy and confocal laser scanning microscopy. The bare formed CDS already display a fluorescence even without polymer NPs, however, this fluorescence is weak (Figure 3.2 a and b, black line). The origin of this fluorescence can be explained through passivation of CDSs with chitosan and hence fluorescence even without an additional surface passivation step arises[179]. When combined with PS-COOH NPs (non-fluorescent, Figure 3.2 a and b, blue line), the CDSs (now CDS-NP system) features a strong, 4.5-5.5 fold enhancement in fluorescence intensity for both fabrication methods (Figure 3.2 a and b, red line). The emission maximum is not shifted and remains at 475 nm. The enhancement is observable at all excitation wavelengths.

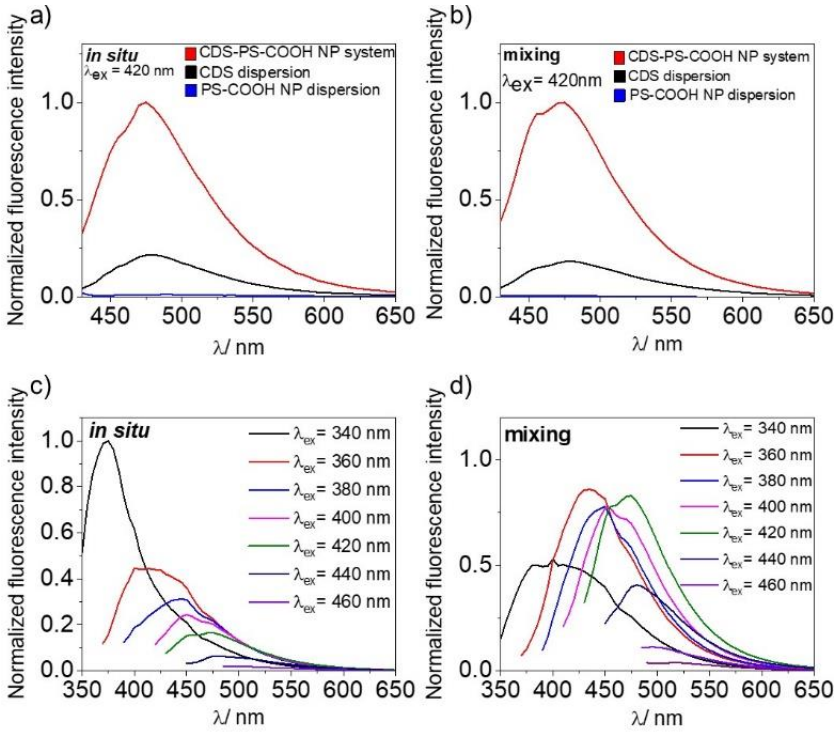

Figure 3.2: Optical properties of CD-polymeric nanoparticle system generated by *in situ* formation or by mixing. (a) Fluorescence spectra of CD-polymeric nanoparticle system generated through thermal treatment in the MW in the presence (red line, CDS- PS-COOH NP) or absence (black line, CDS) of nanoparticles (IS_1); (b) fluorescence spectra of CD system mixed with NPs (red line, CDS- PS-COOH NP) or pure CDS (black line, CDS) (MI_1); (c) fluorescence spectra of CD-polymeric nanoparticle generated *in situ* at different excitation wavelengths (IS_2); (d) fluorescence spectra of CD-polymeric nanoparticle generated by mixing at different excitation wavelengths (MI_1).

It seems that the PS-COOH NP surface interacts with the CDS and stabilizes the surface trap states of the CDSs, which are responsible for the fluorescence properties of the CDS[26]. The observed increase in fluorescent intensity could be attributed to a stabilization of the CDS surface trap states leading to a more efficient radiative recombination of excitons by the reduction of non-radiative recombination and therefore to a higher fluorescence intensity[70, 174]. CDS are known for a broad emission band which is excitation wavelength-dependent[26]. This behavior is observable for the CDS-NP system as well. The wavelength dependency of the *in situ* CDS-NP system is shown in Figure 3.2 c. The emission maximum is shifted to a higher wavelength from 445 nm to 510 nm and the intensity becomes lower, increasing the excitation wavelength from 380 nm to 460 nm. For the mixing CDS-NP system, the emission maximum is shifted to higher wavelengths, as well, but the intensity does not follow the trend (Figure 3.2 d). The spectra of the *in situ* and the mixing CDS-NP system show different shoulders for all wavelengths. For example, at an excitation wavelength of λ_{ex}= 380 nm, a shoulder at 400 nm and 475 nm, which is the emission maximum at λ_{ex}= 420 nm, is visible. Those shoulders arise from the fact that different surface states, which are responsible for the emission, are excited with one wavelength, leading to broad emission spectra with several shoulders.

The combination of CDS and PS-COOH NPs leads to enhanced fluorescence intensity. To understand this enhancement effect in more detail, the fluorescence lifetime was investigated. CDS and CDS-NP systems (*in situ* and mixing) were excited at an excitation wavelength of λ_{ex}= 400 nm, the decay of the PL measured and the lifetime calculated. To calculate the lifetime from the data, a biexponential fit was used. In Figure 3.3 the decay curves of pure CDS dispersed in water (black square), CDS-NP system (mixing) (red dots) (MI_2) and CDS-NP system (*in situ*) (blue rectangle) (IS_2) are shown. It is clearly visible that the decay of the CDS is much faster than for the combination of CDS and PS-

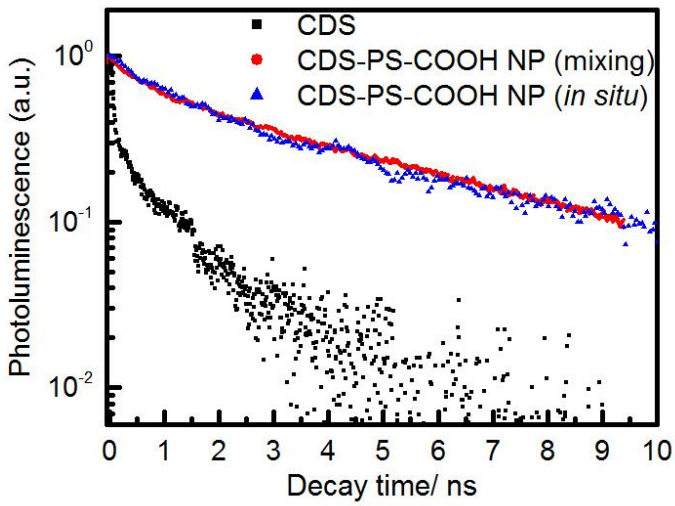

Figure 3.3: Normalized PL of CD system and CD-polymeric nanoparticle system generated by *in situ* formation (IS_2) or mixing (MI_2) over time.

COOH NPs. The fast decay directly after excitation visible in all three curves can be attributed to the Raman scattering of water.

The lifetime of bare CDS is 0.95 ns. The prolonged lifetime of the CDS-NP system generated *in situ* or by mixing is 4.97 ns and 4.73 ns, respectively. This prolongation can be attributed to a reduced contribution of short-living emissive trap states and/or a reduced contribution from competitive non-radiative processes. A prolongation of the lifetime and enhancement of fluorescence intensity is known for the passivation of CDS with polymer chains[25, 172]. A widely accepted mechanism is the presence of surface energy traps which become emissive upon a surface passivation[27]. In the case of the new CDS-NP system, a similar stabilization due to the interaction of the CDSs with the surface of the applied PS particles is possible.

3.3.2 Study of the type of attachment

To study the interaction of the CDS to the surface of the PS-COOH NP and the origin of the fluorescence enhancement, the type of bonding between CDS and PS-COOH NP was investigated. To distinguish between a permanent covalent bonding and a reversible electrostatic attachment, the pH value of the CDS-NP dispersions was changed to protonate/deprotonate surface charges (form amine and carboxylic acid groups) and change the electrostatic interaction between the two species. Afterward, the CDS-NP system was washed twice by centrifugation to remove detached CDS. The fluorescence intensity of the initial CDS-NP system, the supernatant, and the final CDS-NP system were measured at an excitation wavelength of λ_{ex}= 420 nm. The initial CDS-NP systems were washed twice to remove non-attached CDS before the measurement. The initial pH value of the CDS-NP system generated *in situ* was around 10 (Figure 3.4 a, black line) (IS_4). After lowering the pH value to around 2 and washing the dispersion twice, the fluorescence intensity did not change significantly (Figure 3.4 a, magenta line). For the mixed system, the initial pH value was around 7 (Figure 3.4 b, black line) (MI_3). After lowering the pH value to around 2 and washing the dispersion, the fluorescence intensity decreased by 3 folds (Figure 3.4 b, magenta line). Most probably, the CDS in the *in situ* system are covalently bound to the PS-COOH NP and a change in the pH value cannot interrupt the bonding. The CDS remain at the surface of the PS-COOH NP and cannot be washed away. In contrast, the CDS in the mixed system can be removed and the fluorescence intensity decreases. The decrease in fluorescence intensity indicates an electrostatic interaction between the CDS and PS-COOH NPs.

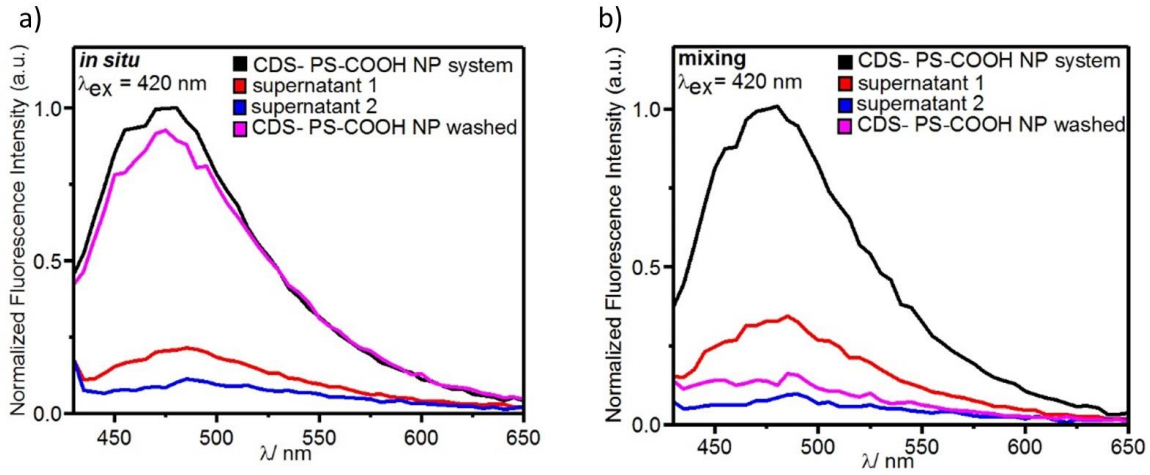

Figure 3.4: Nature of interaction between CDs and NPs. (a) Fluorescence spectra of CD-polymeric particle system (CDS- PS-COOH NP) generated by *in situ* formation at different pH values; starting at weakly basic conditions (black line) (IS_4), the pH is lowered to strongly acidic environment (~2.0) and the system centrifuged twice to give supernatant 1 (red line) and 2 (blue line) and the remaining CDS-NP system after the centrifugation steps (CDS- PS-COOH NP washed). (b) Fluorescence spectra of CDS-NP system generated by mixing at different pH values; starting at neutral pH (MI_3), the pH is lowered to strongly acidic environment (~2.0) and the system was centrifuged twice, supernatant 1 (red line) and 2 (blue line) and the remaining CDS-NP system after the centrifugation steps (CDS-PS-COOH NP washed).

By changing the pH value, the protonation state of the amine groups and the carboxyl groups are affected, the electrostatic interaction can be interrupted and the CDS washed away.

Thereby, it is shown that the enhancement mechanism is independent of the attachment type.

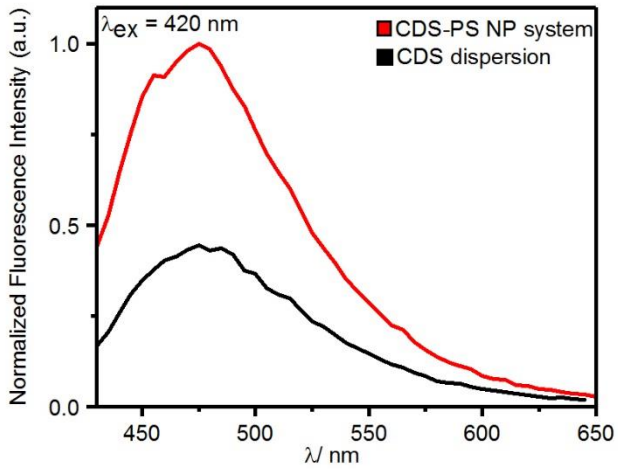

Figure 3.5: Fluorescence spectra of CD-polymeric nanoparticle system generated through mixing in the presence (red line, CDS-PS NP) or absence (black line, CDS) of unfunctionalized PS NPs stabilized with Lutensol AT 50 (MI_6).

The fact that the enhancement of the fluorescence intensity is observed for particles without functionalization mixed with CDS as well (Figure 3.5 (MI_6)), confirms that the enhancement is independent of the binding type (covalent chemical or physically adsorbed interaction). Only a weak adsorption, like in the case of the non-functionalized particles, is necessary for the enhancement and can most probably

be attributed to the interaction of the CDS with the surface of the PS NPs.

To confirm a covalent binding of the CDS with the amine moiety to the carboxyl functionality of the PS-COOH NPs for the *in situ* case, the functional moieties on the surface of the PS-COOH NPs were investigated using Fourier-transform infrared spectroscopy (FTIR). Two additional bands at 1555 cm^{-1} and 1302 cm^{-1} are visible for the treated PS-COOH NPs (Figure 3.6 (IS_2)). The two bands can be assigned to the formation of an amide bond (e.g. between the carboxylic groups on the surface of the PS-COOH NPs and the amine groups of the CDS).

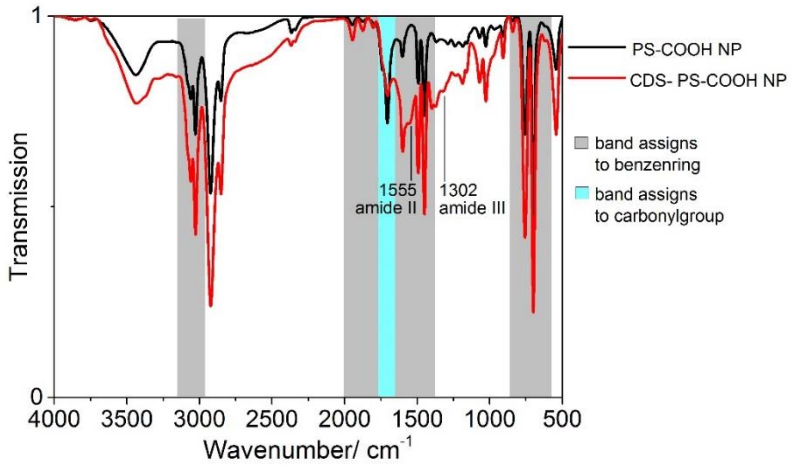

Figure 3.6: IR spectra of carboxyl functionalized PS (IS_2) NPs (black line, PS-COOH NP) and CD-polymeric nanoparticle system generated *in situ* (red line, CDS- PS-COOH NP).

In the previous section, the electrostatically interaction between CDS and PS-COOH NP after mixing is shown. In the next step, the pH dependence of the CDS-NP system generated by mixing (MI_5) was studied in more detail using fluorescence spectroscopy. The pH value was adjusted in the range of 3 to 8 and the fluorescence intensity was measured at an excitation wavelength of λ_{ex} = 420 nm. In Figure 3.7 it is visible that the used pure CDS are only weakly pH-dependent in the investigated regime (black rectangle). In contrast, the CDS-NP system shows a large pH dependency (Figure 3.7 red squares) in the observed pH range. For lower pH-values, the intensity is weak and is enhanced by increasing the pH to higher values.

By changing the protonation state of the functional groups of both species, the strength of interaction can be adjusted. A low interaction (pH 3) leads to a weak fluorescence intensity

whereas a strong interaction at higher pH-value (pH 8) results in a high fluorescence intensity (Figure 3.7). Most probably, as a result of the pH changes, the distance between the CDS and the NPs changes. Since a change in fluorescence intensity is observed, it could be possible that such a distance change plays an important role in the intensity of the enhancement. Nevertheless, further studies are required to prove this hypothesis.

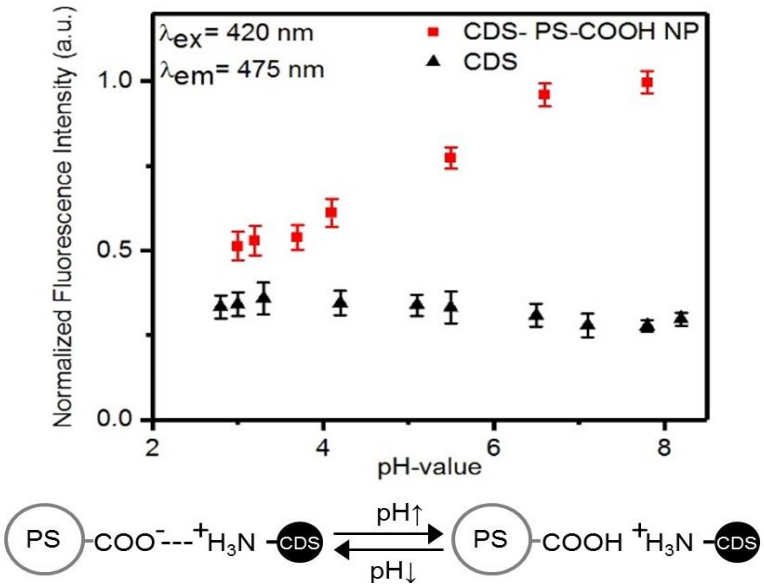

Figure 3.7: Investigation of the pH dependence of the CD-polymeric nanoparticle system generated by mixing (MI_5). Fluorescence intensity against pH value; pH dependence of CD system (black rectangles, CDS) and CDs-nanoparticle system generated by mixing (red squares, CDS- PS-COOH NP

3.3.3 Study of the attachment process

The process of the attachment was characterized further by using fluorescence spectroscopy. To an aqueous CDS dispersion (c = 1 mg/mL), an aqueous PS-COOH NPs dispersion (c = 10 mg/mL) was added stepwise and the fluorescence intensity was measured at an excitation wavelength of λ_{ex} = 420 nm (MI_4). For comparison, the pure CDS was diluted with the same amount of water. In Figure 3.8 the black rectangle indicates the fluorescence intensity of the used CDS diluted with water. The intensity decreases slightly due to the dilution of the CDS. The fluorescence intensity increases strongly when PS-COOH NPs are added to the CDS dispersion (Figure 3.8, red squares). After around 600 µL of the PS dispersion, a plateau is reached and the fluorescence intensity does not increase further. This observation can be explained by assuming that the CDS in solution attach to the surface of the particles and this attachment leads to a strong enhancement. By adding more particles, more CDS can attach to the surface and the fluorescence intensity increases more. Finally, at a certain number of particles, all CDS should attach to the particles. Further addition of particles does not lead to a further increase in fluorescence intensity and a plateau is reached.

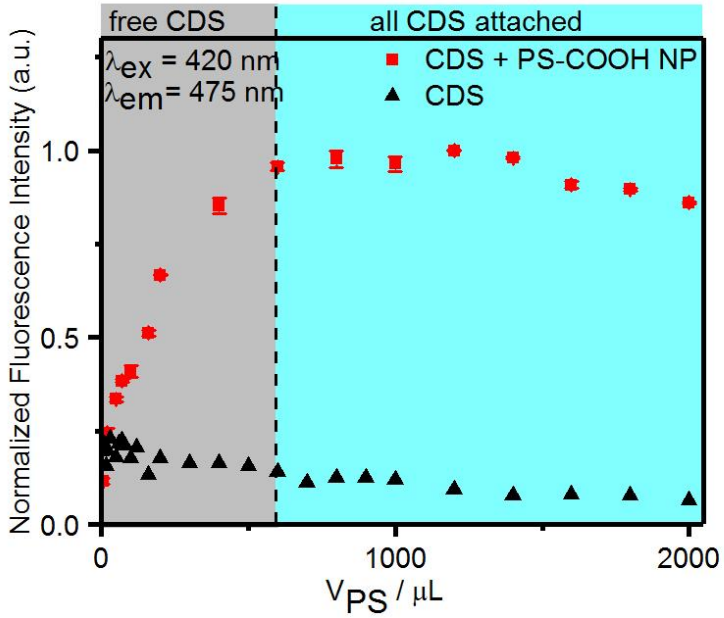

Figure 3.8: Study of the process of CDS attachment to carboxyl functionalized PS nanoparticle (MI_4). Fluorescence intensity against the added volume of PS suspension (c = 10 mg/ mL) to a CDS dispersion (1 mg/mL). CDS diluted with water (black rectangle, CDS), CDS mixed with PS NPs (red squares, CDS+PS-COOH NP).

3.3.4 Formation of carbon dot systems at the surface of the PS-COOH nanoparticles for the *in situ* system

To investigate the formation of CDS on the surface of the particles in the *in situ* system in more detail, the surface morphology of the PS-COOH NPs before and after treatment was

studied using electron microscopy (scanning electron microscopy (SEM) and transmission electron microscopy (TEM), Figure 3.9). Regardless of the absence or presence of chitosan, EDA and acetic acid in the PS-COOH dispersion, PS-COOH NPs feature a smooth surface before MW treatment as displayed in Figure 3.9 a and c. Furthermore, the aqueous PS-COOH NP dispersion exhibits no change of the surface after the MW treatment (Figure 3.9 b). Hence, PS-COOH NPs are stable in the MW and do not alter. The presence of the CDS precursors during the procedure led to a transformation of the surface from smooth to rough (Figure 3.9 d). The change in morphology is most probably due to the formation of CDS and their attachment to the PS-COOH NP surface. The TEM images (inset Figure 3.9 a and d) display the morphology change as well. Before CDS-surface labeling (inset Figure 3.9 a) the surface is smooth. After the CDS-labeling, additional rough layers around the particle are visible (inset Figure 3.9 d). The rough PS-COOH particles were studied in more detail using HRTEM (Figure 3.9 e and f). The additional layers around the particles are clearly resolved in Figure 3.9 e. Inside the additional layer, small black areas can be found (encircled in white). On closer inspection, these small black areas feature a crystalline structure (Figure 3.9 f). Each of the crystalline structures are of a round shape and have different sizes.

With Fourier transformation, the lattice distances *d* in the crystalline structures were determined (Figure 3.9 g). The measured *d* values are 0.21 nm and 0.25 nm. The two values fit the values of the in-plane graphene lattice constants which are known for CDS as well[39]. This result indicates the formation of CDS on the surface of the NPs.

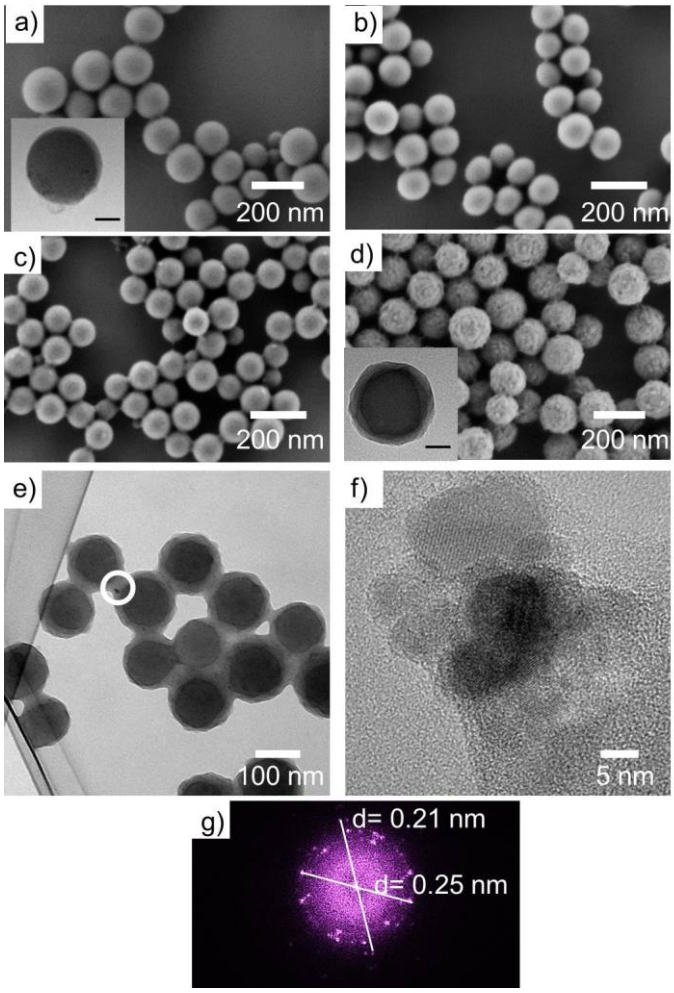

Figure 3.9: SEM and TEM images of carboxyl functionalized (PS-COOH) NPs before and after MW treatment. (a,b): SEM images of NPs dispersed in water; (c,d): SEM images of NPs from an aqueous phase containing chitosan, acetic acid (AA) and EDA; (a) and (c) shows the NPs before MW treatment, (b) and (d) after MW treatment with TEM images inlayed in (a) and (d) (scale: 40 nm); (e) HRTEM image of PS-COOH NPs shown in (d), crystalline structures encircled in white; (f) HRTEM of crystalline structures discovered in the shell of treated PS-COOH NPs; (g) FFT analysis of image (f).

To confirm the homogenous distribution of CDS on the surface of the PS NPs, the *in situ* generated CDS-PS-COOH microsphere (MS) system was analyzed using flow cytometry. For this study, larger particles (PS MS) were used to allow the analysis with flow cytometry. Analyzing forward and side scattered light as well as the fluorescence signal of individual particles in flow allows a comparison of the fluorescence intensity of the single-particle to draw a conclusion about the homogeneity of CDS attachment to the PS-COOH MSs. The analyzed particles were excited at λ_{ex} = 375 nm and the fluorescence emission was detected in the UV detection channel (< 560 nm, 455DF50 mirror in front of the detector). Before MW treatment, the PS microspheres feature only a low fluorescence intensity under 10^2 counts as shown in Figure 3.10 a. After MW treatment, the CDS-NP system features two peaks in the flow cytometry measurement (Figure 3.10 b). The left peak is at the same position as the peak of the unlabeled particles in a. The height of this peak compared to the right

peak is low. The right peak is shifted to higher fluorescence intensity over 10^2 and is much sharper than the peak of the unlabeled particles in a. The left peak indicates the pure particles and the right one the CDS-MS system. Indicated by the height difference between the two peaks, most of the particles are labeled and only a few particles are non-labeled. The right peak is relatively sharp and it can be concluded that CDS are distributed homogeneously among the PS MSs with a small number of PS spheres that remain unlabeled.

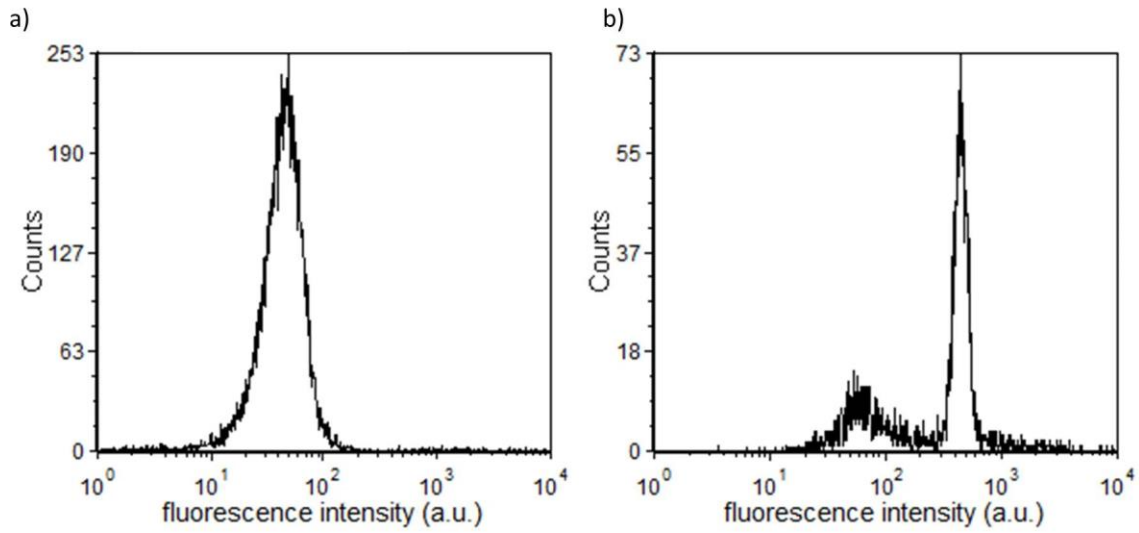

Figure 3.10: Evaluation of the homogeneous attachment of fluorescent CDS during in situ formation via flow cytometry. Flow cytometry measurement of a carboxyl functionalized PS (PS-COOH) microspheres dispersion. (a) PS-COOH microspheres before MW treatment (without CDS); (b) PS-COOH microspheres after MW treatment (with CDS); λex= 375 nm, UV detection channel (< 560 nm, 455DF50 mirror before detector).

3.3.5 Cell uptake of carbon dot-nanoparticle system generated *in situ*

To prove the applicability of CDS –NP systems as fluorescent markers, *in situ* generated CDS-NP systems were traced during their cell uptake. For the cell uptake experiments HeLa cells were used and incubated with non-labeled and labeled PS-COOH NPs (see Experimental Part 3.2). The cell uptake was observed using a confocal laser scanning microscope (cLSM). The particles were excited at λ_{ex} = 405 nm by a diode laser with a power of 5mW. The fluorescence was detected in a wavelength range between λ_{em} = 415 nm – 524 nm. The pure PS-COOH NPs are non-fluorescent and nearly not visible using the cLSM as shown in Figure 3.11 a and d for two different magnifications. The labeled PS-COOH NPs show a bright fluorescence (Figure 3.11 b and e). The differential contrast image in Figure 3.11 c and f display the normal morphology of the cells, verifying the biocompatibility of the used CDS-NP system. Comparing

the fluorescence contrast images (Figure 3.11 b and e) with the differential contrast images (Figure 3.11 c and f), it is obvious that the PS-COOH NPs are located inside the cells and are taken up without further modifications.

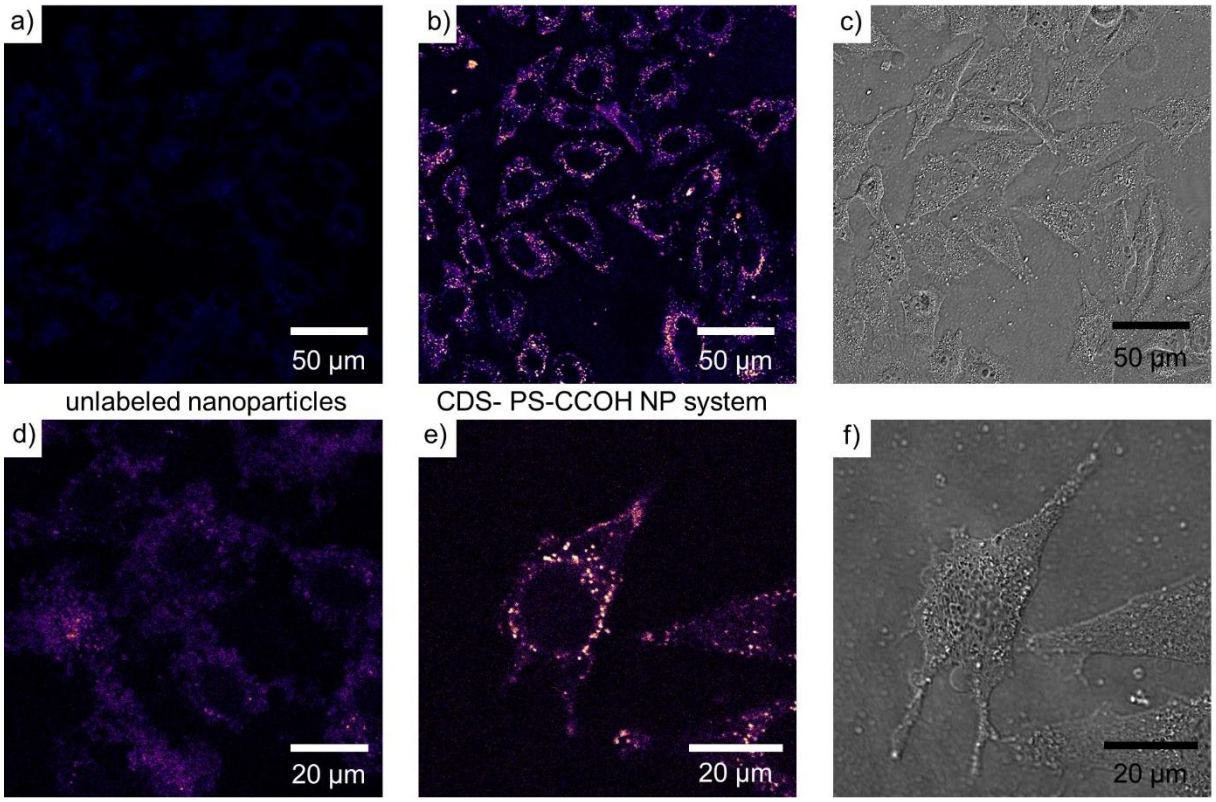

Figure 3.11: Tracing of CDS-fluorescently labeled NPs during their cellular uptake. Microscope images of HeLa cells incubated with carboxyl functionalized PS (PS-COOH) NPs. (a, d) PS-COOH NPs; (b, c, e, f) PS-COOH NPs labeled with CDs (by *in situ* formation, CDS- PS COOH NP); left side: (a, b, d, e) fluorescence contrast images taken by cLSM (λex= 415 nm – 524 nm); right side: (c, f) DIC images.

To study whether the CDS are bound permanently to the particle surface or detached during cell uptake, colocalization experiments were done. PS-COOH NPs were covalently labeled with Bodipy 520/535 as fluorescence marker and afterward, the *in situ* procedure was applied to generate CDS on the particle surface (IS_5). Using cLSM, the Bodipy 520/535 and the CDS were visualized after cell uptake (Figure 3.12).

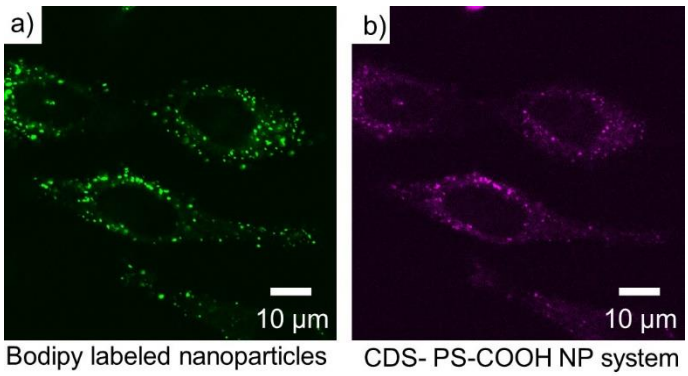

Figure 3.12: cLSM fluorescence images of HeLa cells incubated with CDS coated PS-COOH particles that contain a covalent Bodipy 520/535 label (IS_5). (a) The green spots indicated the fluorescence of Bodipy; (b) the pink spots indicate the fluorescence of CDs; λex = 405 nm (diode laser, 10%), λem= 415 nm – 524 nm.

The location of Bodipy 520/535 labeled PS-COOH NPs (Figure 3.12 a), green spots) overlaps with the location of the CDS (Figure 3.12 b), pink spots). Consequently, the CDSs are permanently bound to the surface of the particles and do not detach before/during cell uptake. These cell uptake experiments demonstrate that the surface-activation of CDS through interaction with NPs enables labeling and visualization of the CDS-NP system.

3.3.6 Conclusion

In summary, we showed that the photoluminescent properties of a CDS can be strongly influenced and enhanced through interaction with polymer NPs, a previously not investigated observation. Therefore, two different methods for the generation of a CD-polymeric NP system were developed. Firstly, the *in situ* formation generated CDSs on the surface of PS beads. Secondly, the two species were synthesized separately and mixed after synthesis. Depending on the treatment (*in situ* or mixing), the CDs are covalently bound (*in situ*) or electrostatically attached (mixing) to the surface of the polymer NPs as shown by pH variation experiments. In both investigated cases, the fluorescence intensity was strongly enhanced (~ 5-fold) and the fluorescence lifetime prolonged. The interaction between the polymer particles and CDSs could be confirmed by electron microscopy and flow cytometry analysis. These findings indicate that stabilization of the radiative states of CDS through interaction with the surface of colloidal particles is possible, a property that has not been observed previously. Thus, our findings demonstrate that the PL properties of CDS can be strongly affected/enhanced by physical or chemical interaction with colloidal surfaces such as polymer NPs. Such an activation of the PL

properties has been only observed so far through direct attachment of passivating polymers or embedding CDSs in a polymer film[27, 70, 171, 174]. These findings could pave the way to the development of colloidal CDS-hybrid systems with tuned PL properties to improve the performances of dye-sensitized solar cells, or photocatalysts.

4. Kinetic control over self-assembly of semiconductor nanoplatelets

Chapter 4 is based on an article which we have accepted for publication in the journal *Nano Letters* (doi:10.1021/acs.nanolett.9b05270). Reproduced with permission from copyright 2020 American Chemical Society. After investigation, the interaction of two colloidal systems in dispersion and tuning the properties, the interaction of a different colloidal system (CdSe NPLs) with a liquid interface were studied and controlled, in order to transfer the colloidal dispersion to solid-state films. A mechanism is described by which the collective NPL orientation in monolayers can be controlled kinetically by exploiting the solvent evaporation rate in self-assembly at liquid interfaces. Our method avoids insulating additives such as surfactants, making it ideally suited for optoelectronic applications. The well-defined monolayer films with controlled NPL orientation (either all “edge-up” or “face-down”), exhibiting record long-range ordering of transition dipole moments and macroscopically polarized light emission. Furthermore, we unveil that the substantial in-plane inter-NPL electronic coupling between NPLs enables charge transport through a single NPL layer, with an efficiency that strongly depends on the orientation of the self-assembled NPLs.

My contributions to this project were the synthesis and characterization of the CdSe NPLs, the development and improvement of the self-assembly method, as well as the characterization of the formed films using TEM and the determination of the evaporation rates. The synthesis of the cadmium precursor was performed by Henry Halim (MPIP-P), the AFM study was done by Ewald Johannes (MPI-P) and the PL measurement of the assemblies was performed by Dr. Stoyan Yordanov (MPI-P) and Dr. Kaloian Koynov (MPI-P). SAXS experiments and data analysis were done by Dr. David Doblas (INM) and Prof. Dr. Tobias Kraus (INM). Angle-dependent PL measurements and fitting of the data were performed by Dr. Daniele Braga (Fluxim) and Dr. Balthasar Blülle (Fluxim). THz spectroscopy and data analysis were done by Heng Zhang (MPI-P), Shuai Chen (MPI-P), Dr. Hai I. Wang (MPI-P) and Prof. Dr. Mischa Bonn (MPI-P).

4.1 Introduction

Quasi-two-dimensional semiconductor NPLs are atomically flat sheets of semiconductor material[75, 77, 180-183]. Across their thickness, NPLs are much smaller than the Bohr radius, while in their lateral dimensions they are much larger. Their limited thickness induces strong one-dimensional quantum confinement, leading to a highly anisotropic electronic structure[10, 75, 79]. Since the thickness of NPLs can be controlled with atomic precision, they exhibit outstandingly narrow ensemble absorption and emission bands[78, 79]. Due to their anisotropic shape, they exhibit high absorption cross sections[80, 81], enhanced energy transfer rates[82], boosted optical gain[83], and show strong anisotropic light emission[10, 84-88]. These properties make NPLs ideal candidates for light-emitting devices[87], field-effect transistors[88], solar cells[82], and lasers[89]. Here, the overall device efficiency critically depends on the electronic coupling between nanocrystals and thus on the orientation of the transition dipole moments between adjacent nanocrystals in a solid-state film. For isotropic nanocrystals (e.g. quantum dots) aligning the transition dipole moments is a challenging task, because their isotropic shape leads to a stochastic distribution of transition dipole moment orientations[10]. However, in highly anisotropic NPLs the transition dipole moments are aligned in the NPL plane[10, 184]. As a consequence, ordered NPL assemblies directly result in ordered transition dipole moment orientations, paving the way for improved optoelectronic and photonic device performances[185]. Thus, controlling the orientation of NPLs in solid-state is of utmost importance.

Colloidal self-assembly is a powerful tool to control the orientation of building blocks in highly ordered, functional materials[186-190]. In solution, CdSe NPLs can be assembled into ordered superstructures such as long stacks by the addition of polar solvents[15, 84], ligand exchange[191], or induced depletion attraction forces[95, 192]. These approaches make use of additives to tune the thermodynamics, i.e. the interaction potentials between NPLs, inducing, e.g., preferential interactions between the large, planar faces of NPLs. The formation of films has been investigated as well[10, 85]. The collective orientation of anisotropic nanorods in films can be controlled[193] by controlling the thermodynamics during the self-assembly at liquid-air interfaces[194].The Tisdale group has used this method to prepare highly ordered NPL monolayers by self-assembly at a diethylene glycol-hexane interface[85], where the orientation was controlled thermodynamically by varying the amount of oleic acid in the system to tune the interaction potentials between NPLs and the NPL-diethylene glycol interface. The use of such additives

prevents efficient charge transport through the NPL layer. Thus, methods that avoid such insulating additives are highly desirable.

We discovered a mechanism by which the collective NPLs orientation at liquid-liquid interfaces can be controlled kinetically through the evaporation rate of solvents. This allows us to avoid non-volatile, insulating additives. Both face-down and edge-up NPL assemblies were analyzed by angle-dependent PL and terahertz (THz) spectroscopy to study the orientation-dependent collective dipole orientation and the photoconductivity, respectively, of these films. We find that both the edge-up and the face-down assemblies preserve their orientation over an area of at least ~5 mm^2, with an in-plane isotropic dipole distribution for the face-down configuration and an out-of-plane anisotropic dipole distribution for the edge-up configuration, giving rise to macroscopic linearly polarized emission. Our THz spectroscopy experiments reveal that, whereas only excitons are present in isolated NPLs in dispersion, free carriers are observed in the self-assembled films, with limited photoconductivity in the face-down orientation, but remarkably higher photoconductivity in a single layer of NPLs in the edge-up configuration. We thus demonstrate here the ability to collectively orient highly anisotropic nanocrystals at interfaces by an intriguingly simple and effective method, with record long-range order of transition dipole moments and strongly orientation-dependent optical properties and charge mobilities. This previously unknown kinetic self-assembly mechanism of anisotropic nanocrystals opens up new avenues for the orientation of nanocrystals, making their anisotropic properties accessible on the macroscopic scale and thus must be added to our current understanding of collective manipulation of nanoscale building blocks.

4.2 Experimental Part

Chemicals. ODE (technical grade 90%, O806-1L) and oleic acid (technical grade 90%, 364525-1L) were purchased from Aldrich. Selenium powder (200 mesh, 9.999%) was purchased from Alfa Aesar. Cadmium acetate dihydrate (for analysis, 98%, 317131000) was purchased from Acros chemicals. N-hexane (≥ 95%, analytical reagent grade, H/0355/21) and acetonitrile (HPLC grade, A/0626/17) were purchased from Fisher. Acetone (Reah. PhEu, 20066.321) was purchased from VWR chemicals. N-heptane (p.A., K11377279) was purchased from Merck. N-octane (≥ 99 %, 8753.1) was purchased from Roth. These chemicals were used as received.

Synthesis of Cadmium myristate [Cd(myristate)$_2$]. Cadmium myristate was synthesized following the procedure described by Rossinelli *et al.*[195]. CdO (5.75 g, 44.78 mmol) and 20 mL acetonitrile were mixed in a 100 mL round-bottom flask and stirred at RT (650 rpm). Then, trifluoroacetic acid (0.7 mL, 9.15 mmol) and trifluoroacetic anhydride (6.2 mL, 43.98 mmol) were slowly added. The mixture was stirred for additional 10 min at RT. Afterward, the reaction mixture was heated up to 50 °C under stirring for 1 h. In a 500 mL beaker, 100 mL 2-propanol, triethylamine (14 ml, 100.44 mmol) and myristic acid (10.23 g 44.80 mmol) were combined. The cadmium trifluoroacetate solution was added slowly to the 500 mL baker while stirring. The white precipitate was vacuum-filtered and washed 4 times with 50 mL cold methanol. The final product was collected; dried in a vacuum oven at 40 °C overnight and stored under ambient conditions.

Synthesis of 4 monolayer thick (4 ML) CdSe Nanoplatelets (NPLs). 4 ML thick CdSe NPLs were synthesized according to a modified procedure described by Rossinelli *et al.*[195]. In a 100 ml three-necked flask, Cd(myristate)$_2$ (170 mg, 0.3 mmol) and selenium powder (12mg, 0.15 mmol) were mixed in ODE (15 mL). The mixture was heated up to 100 °C in 10 min and degassed under vacuum and reflux at 100 °C for 13 min. Under inert atmosphere (argon), the solution was heated up to 240 °C within 16 min. At 188 °C, Cd(ac)$_2$ 2H$_2$O (80 mg, 0.3 mmol) were added quickly. After 6 min at 240 °C, the reaction mixture was quickly cooled down by a water bath. At 185 °C oleic acid (0.5 mL) was added. To the obtained CdSe NPLs dispersion 5 mL hexane was added and the mixture was centrifuged for 5 min at 3743 rcf (Centrifuge Sigma 3-30K). The supernatant was discarded and the precipitated , containing the 4ML was redispersed in 5 mL hexane and centrifuged again for 5 min at 6654 rcf. The supernatants were collected and after few days, remaining 3 ML NPLs precipitated and could be removed by

centrifugation (6654 rcf, 5 min). The 4 ML NPLs were precipitated using acetone or methylacetate in order to remove residual ODE and oleic acid followed by another centrifugation step (6654 rcf, 10 min). The NPLs were redispersed and stored in hexane. The purified NPLs were characterized using optical and NMR, optical spectroscopy and TEM.

Self-assembly:

a. Preparation NPL dispersion in different solvents. For the liquid interface self-assembly, the prepared CdSe NPLs were dispersed in either n-hexane, n-heptane or n-octane. Therefore, the solvent of a stock dispersion (NPLs in hexane) was removed using the rotary evaporator and the NPLs were redispersed in the solvent. Afterward, the dispersion was diluted to a certain concentration. The concentration was determined using the lambert beer equation. The molar extinction coefficient of CdSe NPLs could be calculated as described by Yeltik *et al.*[80]. The concentration of the NPLs in the dispersion was set between 1.9×10^{-8} M to 4.5×10^{-8} M (concentrations are summed up in Table 4.1). Only for one experiment a ten times higher concentration of 2.9×10^{-7} M were used. All self-assembly experiments were carried out at 20 °C, except three experiments that were carried out at 5°C in a fridge. The solutions and equipment for the self-assembly experiment at 5 °C were equilibrated for 20 min at 5°C before performing the experiment. For the preparation of the sample for angle-dependent PL and photoconductivity measurements, the materials were equilibrated overnight to avoid thermal gradients and suppress thermally driven flow in solvents to achieve the best long-range ordering.

b. Self-assembly with various solvents and at different temperatures. For the self-assembly experiments, a Teflon well 3.5 cm x 3.5 cm x 3 cm adopted from Gao *et al.*[85] with a cylindrical hole (diameter 1.5 cm) is used (see Figure 4.1). Inside the hole, a small cylinder is placed as a plateau for the substrate as shown in Figure 4.1 on the right side. On one side of the well, a small hole is drilled which can be plugged with a rubber plug and a syringe to allow the slow removal of the lower layer. The Teflon well was filled with 2.5 mL acetonitrile and various volumes (tens of µL) of NPL dispersion were added on top. The exact volumes are summed up in. After the addition of the NPL dispersion, the well was covered with a glass petri dish to slow down the evaporation rate of the solvent. After 40 min, the petri dish was removed to allow complete evaporation of the solvent. After additional 20 min, the acetonitrile layer was carefully removed using a syringe plugged in the side of the Teflon well allowing deposition of the

formed film on a chosen substrate. During draining, a UV lamp (366 nm) was used to observe the formed film. As substrate carbon-coated copper TEM grids (PLANO, S160-4), silicon wafers (PLANO, G3390-10), or glass were used. The TEM grids and the glass substrates were used without special treatment. The silicon wafers were cleaned with acetone and 2-propanol in the ultrasound bath (10 min) (two times) before use. The obtained films were analyzed by TEM, SEM, and THz spectroscopy.

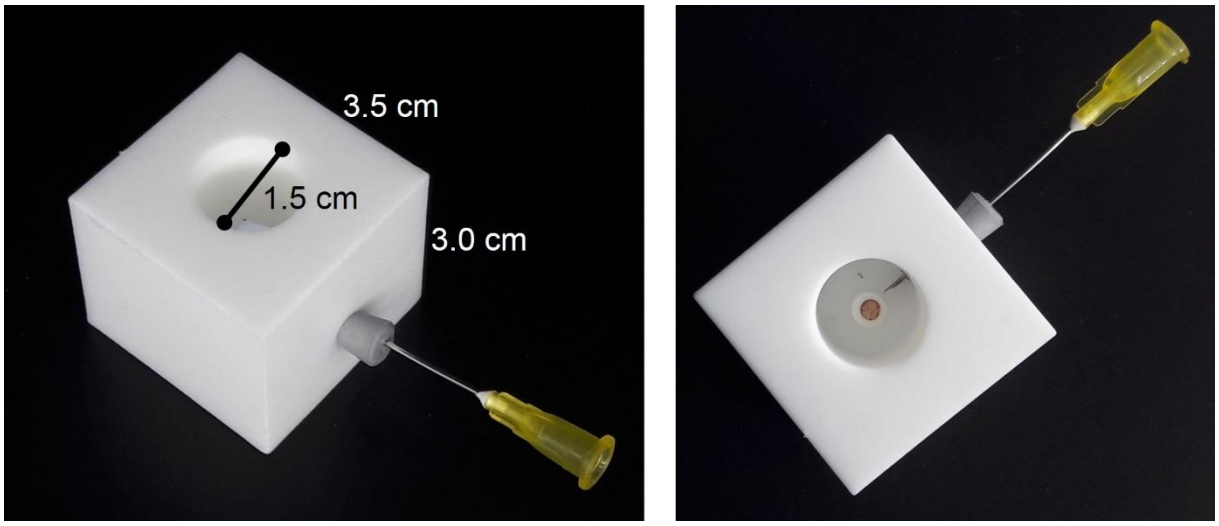

Figure 4.1: Photograph of the Teflon well with substrate used for self-assembly of NPLs at the liquid interface.

Table 4.1: Overview used parameter for self-assembly. Solvent, concentration, volume, and temperature were adjusted to control the orientation of the NPLs at the acetonitrile interface. Absorption values of the respective stock solutions were obtained using a cuvette with 1 cm optical path.

Sample no.	**solvent**	**V/ µL**	**c/** $\frac{\mathbf{mol}}{\mathbf{L}}$	**Abs @ 400 nm**	**T/ °C**
SA_1	hexane	60	$1.90 \cdot 10^{-8}$	0.1663	20
SA_2	hexane	60	$2.50 \cdot 10^{-8}$	0.1663	5
SA_3	hexane	50	$3.60 \cdot 10^{-8}$	0.3323	20
SA_4	hexane	60	$3.88 \cdot 10^{-8}$	0.2761	20
SA_5	hexane	50	$3.90 \cdot 10^{-8}$	0.3427	20
SA_6	hexane	60	$3.90 \cdot 10^{-8}$	0.3153	20
SA_7	hexane	50	$4.40 \cdot 10^{-8}$	0.2615	20
SA_8	heptane	60	$2.30 \cdot 10^{-8}$	0.1695	20
SA_9	heptane	60	$2.60 \cdot 10^{-8}$	0.1695	5
SA_10	heptane	70	$3.37 \cdot 10^{-8}$	0.3323	20
SA_11	heptane	70	$3.88 \cdot 10^{-8}$	0.2761	20
SA_12	heptane	60	$4.18 \cdot 10^{-8}$	0.3427	20
SA_13	heptane	50	$4.40 \cdot 10^{-8}$	0.3293	20
SA_14	heptane	50	$4.40 \cdot 10^{-8}$	0.3293	20
SA_15	octane	60	$1.80 \cdot 10^{-8}$	0.1247	20
SA_16	octane	60	$1.80 \cdot 10^{-8}$	0.1247	5
SA_17	octane	60	$3.37 \cdot 10^{-8}$	0.3323	20
SA_18	octane	50	$4.06 \cdot 10^{-8}$	0.2761	20
SA_19	octane	70	$4.18 \cdot 10^{-8}$	0.3427	20
SA_20	octane	50	$4.50 \cdot 10^{-8}$	0.2584	20
SA_21	octane	40	$2.90 \cdot 10^{-8}$	1.9437	20

c. Self-assembly in a controlled atmosphere. In addition to the self-assembly experiments performed in air at 20 °C or 5 °C, the self-assembly experiment was repeated in a closed system to control the alkane vapor content in the atmosphere. The setup shown in Figure 4.2 was used for the experiment. The Teflon well, where the self-assembly is performed, is placed in a glass evaporation chamber. The chamber is connected to a membrane pump (membrane pump optimal Art.-Nr. 850, Schego), and two flow controllers (Analyt-MTC, Model #: 35829, Messtechnik GmbH & Co KG, Germany). The airflow, generated by the pump, is split and directed into the two flow controllers, regulating the flow. After flow controller 1, a gas washing bottle filled with heptane is placed. The air bubbles through the heptane and enriches the gas phase with heptane. The generated heptane flow is reconnected to the airflow and directed into the evaporation chamber. By varying the flow rates of flow controller 1 and 2, the alkane content in the atmosphere is controlled. For the experiment with no heptane in the atmosphere, the setting for the controllers were 0 (Flow controller 1) and 307 (Flow controller 2) For the experiment with high heptane content in the atmosphere the setting of the controllers were 306 (Flow controller 1) and 6 (Flow controller 2). The temperature was between 21 °C and 22 °C. To perform the self-experiment, the Teflon well was filled with 2.5 mL acetonitrile and a TEM grid was placed on the small plateau. The evaporation chamber was closed and the air/heptane mixture ran for 20 min through the evaporation chamber. After 20 min, the valves before and behind the evaporation chamber were closed and additional 4 min were waited for temperature equilibration. Afterward, 60 µL of the NPLs in heptane ($c=4\cdot10^{-8}$M) was added using a syringe (Hamilton Gastight #1710, Bonaduz, Switzerland) stick through the septum. After 1 h, the evaporation chamber was opened and the acetonitrile was removed.

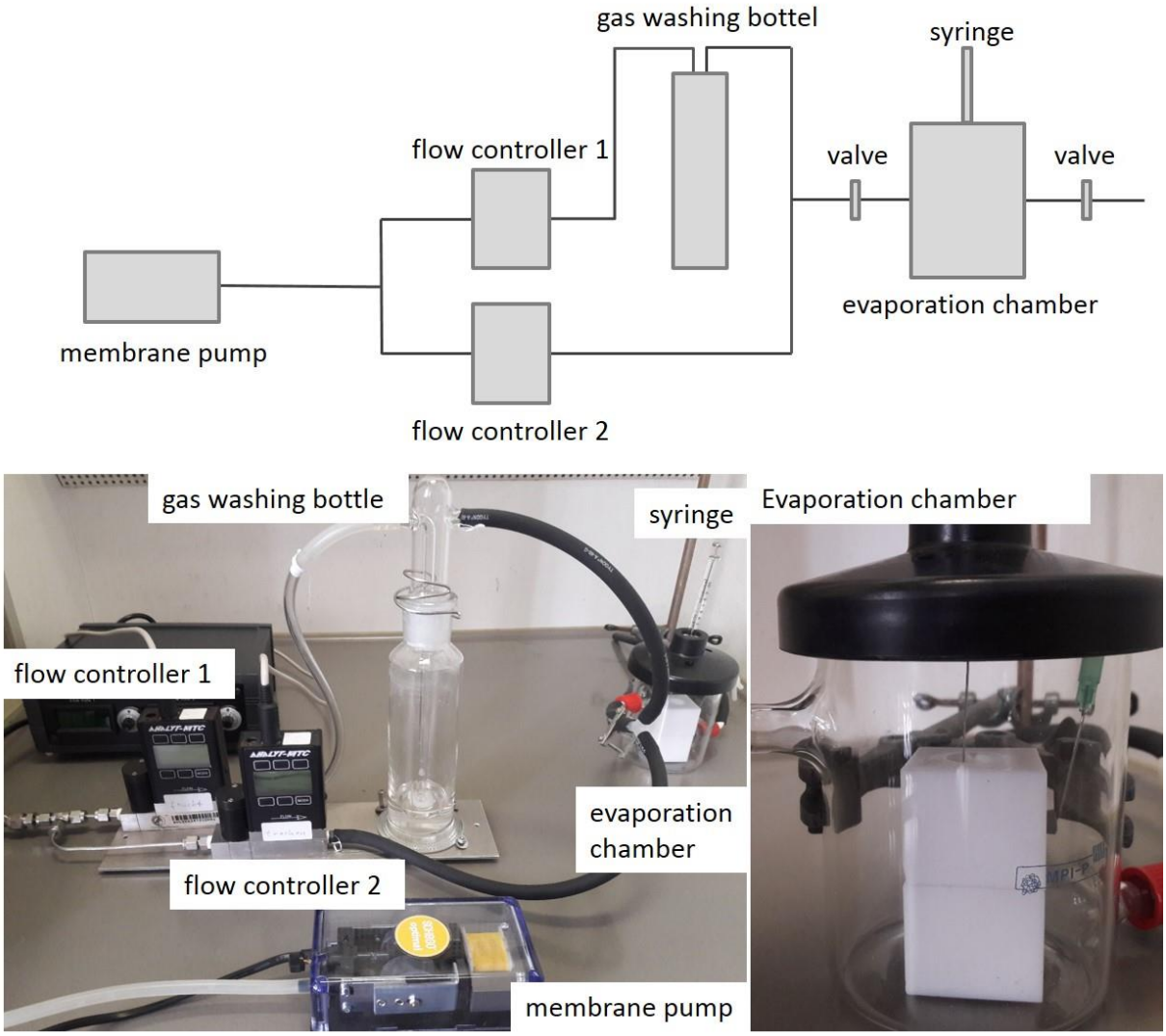

Figure 4.2: Setup for self-assembly experiment of NPLs under controlled atmosphere. Upper part scheme of the flow setup. Lower part: Photograph of the setup (left) and the evaporation chamber (right).

Determination of theoretical surface coverage. The theoretical surface coverage *c%* was calculated using equation (4.I) with *c* the molar concentration of the NPL dispersion, *V* the used volume, FP_{NPL} the footprint of one NPL in the face-down or edge up configuration, N_A the Avogadro constant and A_{well} the surface area of the well.

$$c\% = \frac{c \cdot V \cdot FP_{NPL,\ FD\ or\ EU} \cdot N_A}{A_{well}} \cdot 100\% \qquad (4.I)$$

The theoretical surface coverage varied between 77% to 15% for the face-down configuration and 23% and 243% for the edge up configuration (see Table 4.2 and Figure 4.15). For theoretical surface coverage above 100%, deposits at the wall of the well were observed.

Table 4.2: Calculated theoretical surface coverage for the face-down and edge-up assemblies.

configuration	Sample no.	c%	configuration	Sample no.	c%
Face down	SA_1	77	Edge up	SA_16	23
	SA_2	102		SA_15	23
	SA_3	122		SA_17	42
	SA_5	133		SA_18	42
	SA_7	149		SA_20	47
	SA_4	158		SA_19	61
	SA_6	159		SA_21	243

Characterization. Small Angle X-ray Scattering was performed using a Xeuss 2.0 (Xenocs SA, France) setup equipped with a copper K_α X-ray source emitting at a wavelength of $\lambda = 0.154$ nm and a PILATUS 1M (DECTRIS, Switzerland) Hybrid Photon Counting Detector at a sample-to-detector distance of 320 mm by continuously recording 2D diffraction patterns in 15 s intervals until full evaporation of the solvent. Hanging droplets were produced with a NEMESYS computer-controlled pulsation-free syringe pump (Cetoni GmbH, Germany) by pushing the NPL dispersion through a 1 mL glass syringe (Hamilton, USA) that was connected with standard HPLC tubing to a 30 μm-ID fused silica tubing (BGB Analytik Vertrieb GmbH, Germany) as described elsewhere[30]. The 2D scattering patterns were then radially integrated and analyzed using the techniques described previously[30]. As the concentration is known, and assuming that NPL dispersion is initially fully dispersed and fully agglomerated when the solvent has evaporated, we can follow the rise in the concentration by measuring the liquid volume from the solvent peak, and the agglomerate fraction from the structure factor of the platelets (see Figure 4.12).

For optical spectroscopy, NPL dispersions were transferred to a quartz glass cuvette (10mm). Absorption spectra were recorded on a Cary 60 spectrophotometer. PL spectroscopy was recorded using a Prizmatix Silver high power LED (emission peak 369 nm) for excitation and an Avantes SensLine AvaSpec-HSC-TEC for data collection.

Transmission electron microscopy was done using a JEOL1400 microscope (acceleration voltage 120 kV). The samples were deposited on carbon-coated copper grids (400 mesh) either by drop-casting or self-assembled film deposition (sample preparation see SI). SEM was performed using either a Hitachi SU8000 or a LEO Gemini 1530 microscope on various substrates (glass, Si wafer, carbon-coated copper grid).

AFM was done using a JPK NanoWizard 4 in the AC Mode with a constant amplitude. The used cantilevers (OMCL-AC160TN-R3) were purchased from Olympus with a resonance frequency of 300 kHz and a spring constant of 26 N/m.

Nuclear magnetic resonance spectra were recorded on a Bruker Avance 300 MHz spectrometer with predefined pulse programs. The samples were dispersed in deuterated chloroform, and benzene was added as an internal standard.

Angle-dependent photoluminescence spectra were recorded with the goniometric spectrometer Phelos provided by Fluxim Inc. (Phelos, Fluxim AG, www.fluxim.com; see Scheme 4.1). The samples were mounted on a rotating half-cylindrical lens (BK-7, R = 20 mm), using a refractive index matching fluid (n_D = 1.52, Cargille) to fill the gap between sample and lens surface. The NPL films were excited with a LED emitting at 365 nm over an area of 3x5 mm^2. Characterizations were performed in both forward and reverse direction, exhibiting low hysteresis and, thus, no sign of degradation upon UV exposure. To reduce stray light, the resulting PL signal was filtered through a pinhole of 1.6x3 mm^2 and collected behind a polarizer by an optical fiber connected to a CCD spectrometer. The angle-dependent PL intensity was obtained by integrating the spectral irradiance (λ_p ~ 515 nm) over the wavelength range of 495 nm to 530 nm. The measured PL patterns were analyzed using the Emission Module of the simulation software Setfos (Setfos, Fluxim AG, www.fluxim.com). , computing the light propagation in a thin film cavity by considering the polarization-dependent Fresnel coefficients of all layer interfaces involved[196-198]. Light emission is modeled by a spatial distribution of radiating electrical dipoles with a dipole moment $\vec{p}$ [197, 199, 200]. The average dipole orientation of an ensemble of radiating dipoles can be parametrized by (4.II).

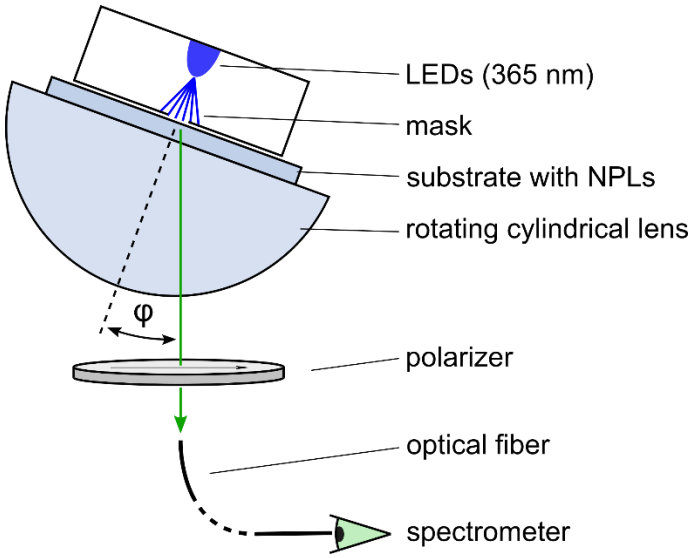

Scheme 4.1: Schematic illustration of the Phelos goniometric spectrometer. The NPL sample is mounted on a rotating half-cylindrical lens and excited by UV light (365nm). An optical fiber collects the PL signal behind a rotating polarizer.

$$\Theta = \frac{\sum p_z^2}{\sum p^2} \quad (4.II)$$

Where p_x and p_y are the in-plane components parallel to the substrate. Note that Setfos assumes an isotropic distribution within the substrate plane, i.e. $< p_x^2 >=< p_y^2 >$. The average dipole orientation Θ in a cavity of a given thickness and refractive index is reflected in a particular angle-dependence of s- and p-polarized PL signal[201]. Only two fitting parameters were used during the simulation, namely, the orientation of the emitting dipoles and the PL intensity. All other parameters, such as the thickness of the emitting layer, the dielectric constant of the CdSe NPLs and the position of the dipole within the emitting layer were kept constant. Here, the dipole orientation parameter Θ was determined by a least-square fit to the measured s- and p-polarized PL patterns, which were normalized to the respective 0° emission beforehand. Thus, the dipole orientation was used Θ as the only fitting parameter, whereas the film thickness was set to d = 4.6 nm, and d = 13 nm, for the face-down and edge-up samples, respectively. The refractive index of the NPL film was estimated as n = 1.63[85].

Micro PL measurements were performed on a commercial setup consisting of an Axiovert 200M inverted microscope and a LSM510 confocal laser scanning unit using a Zeiss Plan-Neofluar 20x NA0.5 microscope objective (all from Carl Zeiss, Jena). Samples were excited at 488 nm (Argon laser), regions of interest were selected and emission spectra were recorded by directing the emitted light to an Andor Shamrock SR-303i-B spectrometer fiber coupled to the LSM 510 module. The spectrometer was equipped with Andor iDus DU420A-OE camera detector and a diffraction grating with 1200 lines/mm (500 nm blaze wavelength), which gave 0.1 nm spectral resolution.

Table 4.3: PL of NPLs in dispersion and in the face-down and the edge-up assemblies. The peak positions and FWHM values were obtained by fitting several PL spectra with Lorenz functions.

Sample	**Peak wavelength /nm**	**FWHM /nm**
Dispersion	514.73	8.08
Face-down_1	516.45	9.83
Face-down_2	516.59	9.99
Face-down_3	516.60	10.02
Face-down_4	516.60	10.01
Face-down_avg	516.46±0.07	9.96±0.09
Edge-up_1	517.11	9.86
Edge-up_2	517.14	10.10
Edge-up_3	517.33	10.53
Edge-up_4	517.13	10.10
Edge-up_avg	517.18±0.10	10.14±0.28

In this study, OPTP spectroscopy is employed to investigate the charge states and ultrafast conductivity of photogenerated carriers in NPL dispersion and solids. In a typical OPTP study, a laser pulse (*e.g.* 400 nm in this study) with ~50 fs duration is used to optically inject electrons into the conduction band, and a THz pulse with 1-2 ps duration is employed as the probe beam. The THz conductivity of photogenerated electrons and holes is measured by recording the pump-induced modulation of the complete THz waveform by electro-optical sampling. When THz wave interacts with free charge carriers in materials, the oscillating electrical field in a single cycle of THz pulse can accelerate the free carriers back and forth within 10s of nanometer spatial range. During this interaction, the THz field is attenuated and the relative THz absorption by free carriers is proportional to their photoconductivity in the materials of interests. On the other hand, in low dimensional (*e.g.* from ML to a few layers) semiconducting materials, thanks to the strong quantum confinement and reduced screening effect, the photogenerated electron and hole experience strong Coulomb interactions, resulting in forming strongly bounded electron-hole pair, called exciton. As a charge-neutral quasi-particle, excitons do not absorb THz radiation as free carriers; instead, they induce a pure THz phase shift in the time domain measurements. As the imaginary part of the complex photoconductivity is directly correlated to such phase shift in THz pulse, strongly bounded excitons are typically characterized by an imaginary photoconductivity dominant carrier dynamics, in sharp contrast to a real photoconductivity dominant dynamics for free carriers.

Quantitative analysis of the complex THz Conductivity for excitons and free carriers

(1) Drude-Smith model for describing free carrier conductivity in the edge-up assembly

The Drude-Smith (DS) model[202] is a phenomenological model that describes the transport dynamics of free carriers, in a medium with a preferential charge carrier backscattering process. This is done by introducing the new parameter (so-called c parameter) between 0 and -1 into the classical Drude model. For c=0, the model goes back to the Drude model (4.III):

$$\sigma_{DS}=\frac{\varepsilon_0\omega_p^2\tau}{1-i\omega\tau}\times\left(1+\frac{c}{1-i\omega\tau}\right) \quad (4.III)$$

In which ε_0 is the vacuum permittivity, ω_p the plasma frequency and τ the average scattering time. The DS model describes the conductivity of free carriers. The results of DS model calculations for the edge-up sample are shown in Figure 4.21 a.

(2) The Lorentzian resonance for describing intra-exciton transitions for NPL in dispersion

The exciton resonance in the frequency domain can be described by a Lorentzian resonance originating from, e.g. 1S-2P excitonic transitions by (4.IV)[203, 204]:

$$\sigma(\omega)=\frac{i\omega\varepsilon_0\omega_p^2}{\omega_0^2-\omega^2-i\omega\gamma} \quad (4.IV)$$

Where ω_0 is the angular frequency of the oscillatory response and γ defining the width of the resonance. As two typical examples shown in Figure 4.21 b (with the 1S-2P transitions at 30 and 50 THz), the conductivity can be well fitted by the model, in line with the excitonic nature of the photogenerated species in our NPLs. Unfortunately, due to the very large exciton binding energy in NPL system (over 170 meV)[205], the 1S-2P resonance frequency ω_0 will be accordingly large (> 30 THz, when assuming 170 meV exciton binding energy and hydrogenic Rydberg series of energy levels of the excitonic states in NPLs). Due to the limited bandwidth of the THz spectrometer (up to 2 THz), a simple fit to a Lorentzian lineshape does not allow for the determination of the 1S-2P transition energy of the excitons in the NPLs. Several sets of parameters ω_0, γ yield qualitatively similar fitting results.

4.3 Results and Discussion

4.3.1 Additive-free self-assembly of nanoplatelets

Gao *et al.* could control the NPL orientation thermodynamically by adding oleic acid to the diethylene glycol subphase[85]. Oleic acid acts as a surfactant and alters the interaction potential between the large planar, myristate-passivated facets of the NPLs and the diethylene glycol interface in a concentration-dependent manner[85, 206]. A large amount of oleic acid increases the interaction potential between the NPL and the diethylene glycol interface leading to face-down assemblies[85]. Without or with just a small amount of oleic acid, the inter-NPLs interaction potential is higher, allowing for the edge-up assembly to emerge[85]. These observations indicate that the NPLs' orientation in a dense monolayer film can be controlled by simply tuning the interaction potential between the NPLs and the liquid subphase.

If this holds, we should be able to obtain NPLs in the face-down configuration by increasing the interaction potential between the NPLs and the subphase at the other liquid-liquid interfaces. Varying the interaction potential does not necessarily require surfactants. The choice of the subphase solvent alone can already change the interaction potential significantly[96].

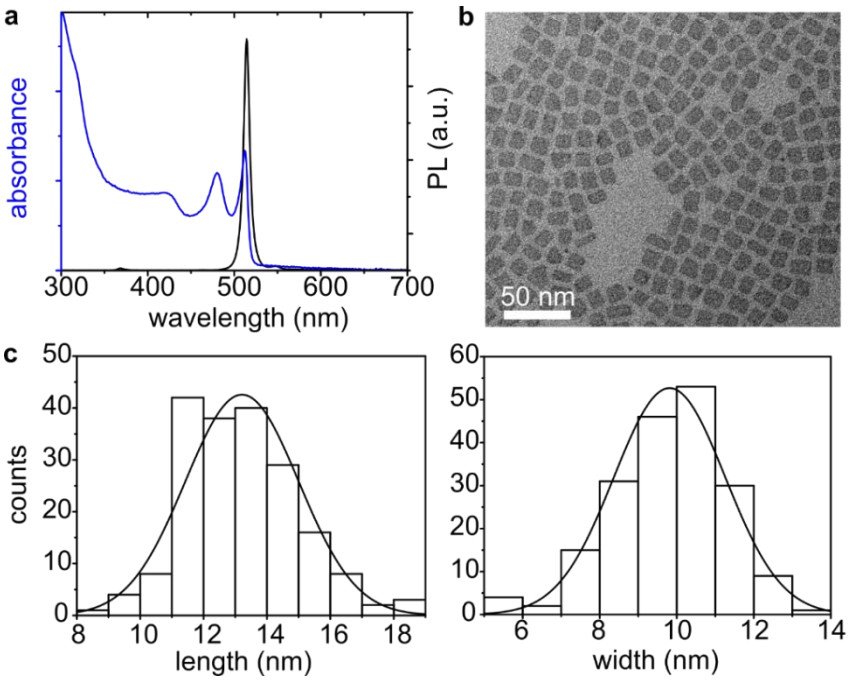

Figure 4.3: Characterization of the 4 ML CdSe nanoplatelets. (a) Emission and absorption spectra of 4 ML CdSe NPL dispersed in hexane. (b) TEM micrograph of 4 ML CdSe NPLs facing down. (c) histograms of the length and width of 4 ML NPLs, 200 NPLs were analyzed.

To test this hypothesis, we used a modified design of the Teflon well of Gao *et al.*[85] (Figure 4.1). We replace diethylene glycol by acetonitrile as subphase and add 4 ML thick CdSe NPLs (Figure 4.3) dispersed in hexane on top. We choose acetonitrile for several reasons. First, it is more volatile than diethylene glycol, making it easier to remove completely

when the monolayers are deposited on substrates. Second, it has a significantly lower polarity index compared to diethylene glycol (0.460 compared to 0.713)[207]. This matching of polarities explains the increased solubility of the myristate ligand in acetonitrile than in diethylene glycol[208, 209]. Thus, the interaction potential between the flat, non-polar, myristate-passivated NPL surfaces and the liquid interface should be significantly greater for acetonitrile than for diethylene glycol, as already demonstrate by Erdem *et al.*[96].

Thus, with acetonitrile as the subphase, we expect to observe the face-down configuration. Indeed, we observe that NPLs assembled face-down when we deposit a hexane NPL dispersion on the acetonitrile sub-phase and let the hexane evaporate at 20 °C (Figure 4.4). While this experiment supports our hypothesis that the NPL assembly configuration indeed depends on the interaction potential between the NPLs and the liquid interface, the purity of the NPL dispersion was extremely critical (Figure 4.4). 1-octadecene (ODE), the high-boiling point solvent used during the synthesis, and oleic acid used to quench the synthesis (oleic acid could contribute to the ligand shell[210]) could be identified as impurity in the as synthesized hexane dispersion (see Figure 4.5 a and Figure 4.6). The concentration of ODE in the unpurified (normal purification) hexane dispersion was determined using NMR analysis (see Figure 4.5 a and b). Benzene with a concentration of 1.5 mM was added as an internal standard. To calculate the concentration of ODE, the ratio of the normalized signal of benzene (blue) and the normalized signal of the double bond of ODE (green) were used (see box in Figure 4.5 a). The signals were normalized by dividing the integral of the signal by the number of hydrogen atoms related to the signal. Before an additional purification step, the

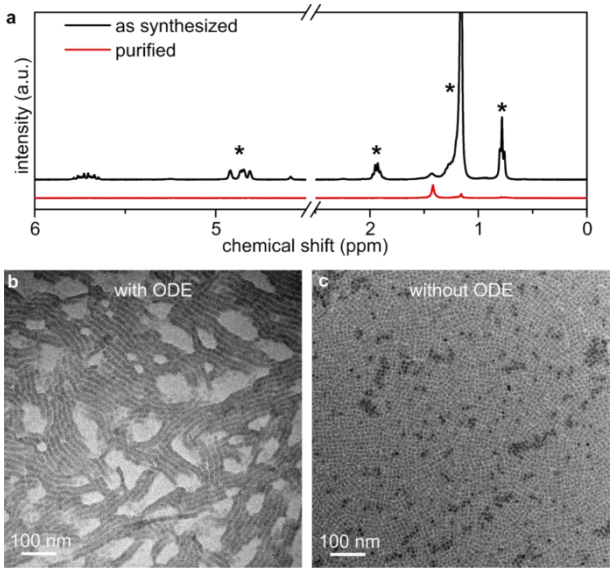

Figure 4.4: Effect of additional purification on the self-assembly of 4 ML NPLs. (a) NMR spectra of 4 ML NPL before (black line) and after (red line) additional purification. After purification, the peaks assigned to ODE (denoted with *) vanish. (b) TEM micrograph of 4 ML NPLs assembled at the liquid interface in the presence of ODE. The NPLs assembled in the edge-up configuration. (c) TEM micrograph of 4 ML NPLs assembled at the liquid interface in the absence of ODE. The NLPs assembled in the face-down configuration. Clearly, the presence of ODE contamination gives rise to heterogeneity in the assembly process; without ODE, a homogeneous face-down film is produced.

concentration of ODE is in the millimolare regime, after purification ODE is completely removed. The second identified substance is oleic acid. Since we add oleic acid when cooling down at the end of the synthesis, the surface of the NPLs could be either capped with myristic acid, oleic acid, or a mixture. To elucidate the composition of the ligands present before and after additional purification, the ^{1}H NMR spectra shown in Figure 4.4 were further analyzed (see Figure 4.6). In the unpurified sample, a small, broad signal at 5.35 ppm can be found which is attributed to the alkene protons of oleic acid[210] (see Figure S4). A resonance at 0.78 ppm is attributed to methyl protons of oleic, myristic acid, and ODE (see main text for discussion on ODE). For pure oleic acid, the ratio between the integrated intensities of the methyl and alkene resonances should be 1.5 (2 alkene protons and 3 methylene protons). Thus, before thorough purification, oleic acid is present as an impurity. However, after the additional purification step that we perform to remove the ODE the resonance at 5.35 ppm disappears completely, given our signal-to-noise. Thus, our purification protocol efficiently removes both oleic acid and ODE from the NPL dispersions (see red spectra in Figure 4.4 and Figure 4.6).

NPL samples containing ODE in the millimolar regime or oleic acid in the micromolare regime result in the edge-up configuration (Figure 4.4) and only painstakingly purified samples (see Experimental Part 4.2) that contains no measurable amount of ODE (or oleic acid) reliably deposited in the face-down configuration (Figure 4.4 and Figure 4.7). All further experiments were performed using ODE-free samples.

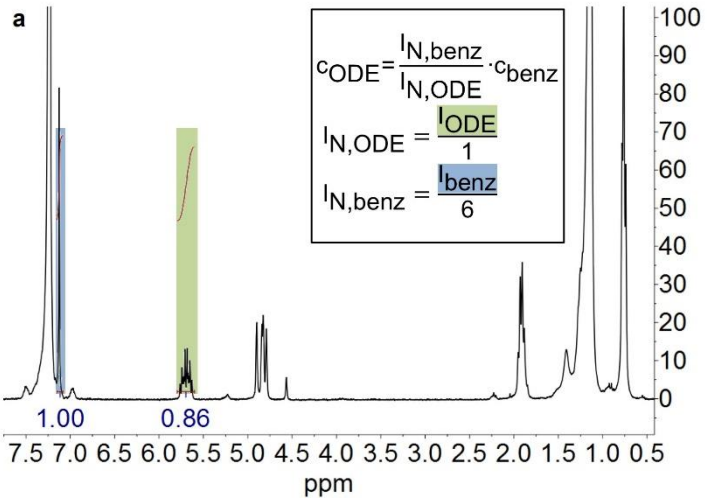

b

sample	c_{ODE} / mol/L	c_{NPL} / mol/L	c_{ODE}/c_{NPL}
1	2.90E-03	5.60E-07	5127
2	5.10E-03	3.79E-07	13541
3	2.70E-03	1.08E-06	2503
4	2.70E-03	7.20E-07	3762
5	3.40E-03	1.49E-06	2299

Figure 4.5: Determination of ODE content in 4 ML NPL dispersion after normal purification using NMR. (a) NMR of 4 ML NPL dispersion with benzene as internal standard (blue), to determine the concentration of ODE, the equation in the black box was used; (b) table summarizing the calculated ODE concentration for different 4 ML NPL samples.

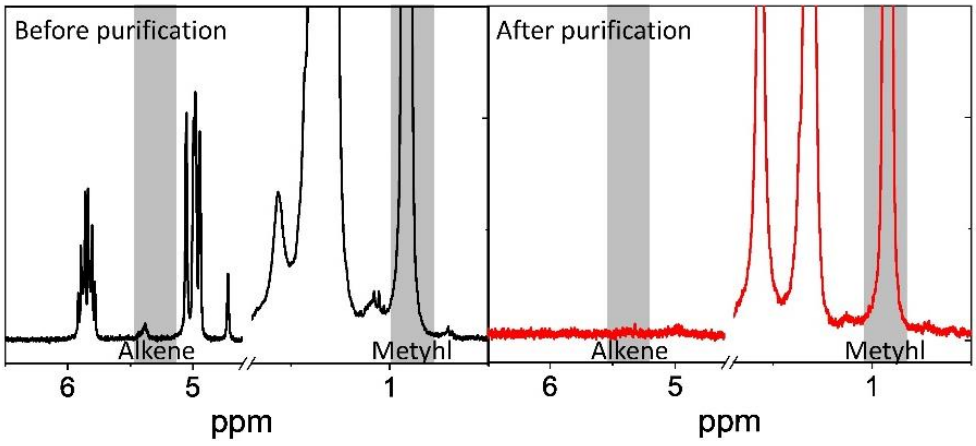

Figure 4.6: Enlarged ^{1}H NMR spectra of CdSe NPLs to analyze the resonances related to oleic acid. Left: unpurified sample; right: purified sample.

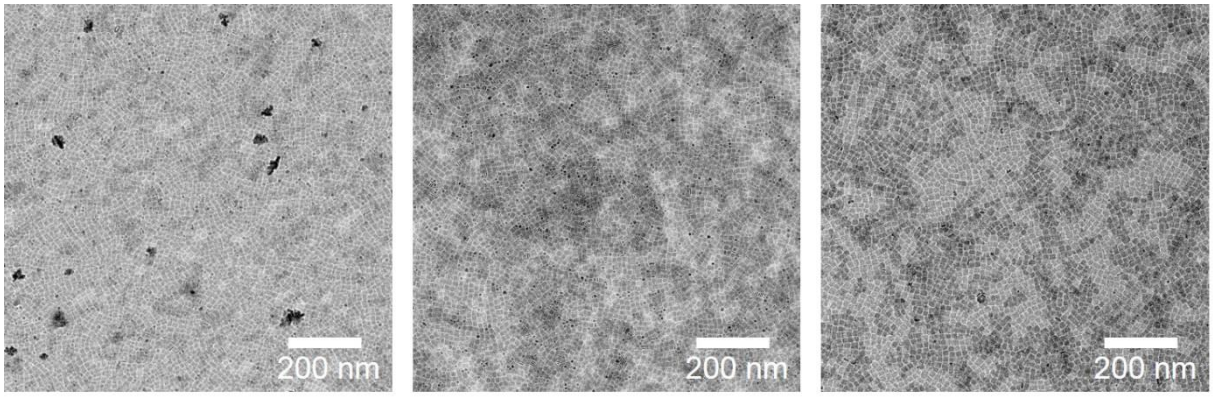

Figure 4.7: TEM micrographs of 4 ML NPLs further purified (without ODE) assembled at the acetonitrile interface. Without ODE, the face-down configuration is reproducibly obtained.

A part of the effect of ODE may be attributable to its activity as depletion agent[95, 192] in the hexane NPL dispersion, which induces stacking and ultimately leads to discontinuous NPL films in the edge-up configuration (Figure 4.4). Probably more important, however, is its effect on the kinetics. Kinetic limitations are known to strongly affect particle assembly; they can limit the process and prevail over small differences in interparticle potential[211-213]. Here, some time is required for the platelets to form stacks; if evaporation is rapid, the time is insufficient for the stacks to reach a length that stabilizes the edge-up configuration. The low vapor pressure of ODE implies that it accumulates to build up a significant concentration upon the hexane evaporation. Therefore, even a small amount will reduce the evaporation rate of the hexane NPL dispersion. Our experiments indicate that fast evaporation without ODE leads to face-down configurations, while slow evaporation with ODE yields edge-up assembly. If the orientation of NPLs in self-assembled thin films critically depends on the evaporation rate of the solvent, an entirely new and generalizable way to control the collective orientation of NPLs

in thin films opens up. However, modifying the evaporation rate by controlling the purity of NPL dispersion precisely is cumbersome. Therefore, we investigate alternative routes that do not rely on impurities such as ODE. Below we show how the collective orientation of NPLs can be kinetically driven and controlled by the solvent vapor pressure in the atmosphere over the self-assembly setup, by choice of the solvent the NPLs are dispersed in, or the temperature at which the assembly is performed.

4.3.2 Kinetically driven self-assembly of nanoplatelets

A straightforward way to modify the solvent evaporation rates is to control its partial pressure above the solution. This ensures that only the evaporation rate is modified and entropic effects, changes in viscosity or chemical effects (e.g. from impurities) can be neglected. To exploit this for our self-assembly experiments, we construct a setup allowing us to control the alkane vapor content in the atmosphere of a closed system containing our self-assembly well (Figure 4.2). With high alkane vapor content in the atmosphere, the evaporation rate of the alkane NPL dispersion is reduced. Under these conditions, the NPLs have more time to assemble and form stacks that are long enough to sustain the edge-up configuration. Indeed, self-assembly experiments with heptane NPL dispersions performed with a high content of heptane vapor in the atmosphere reliably yield edge-up assemblies (Figure 4.8). The self-assemblies performed under pure airflow (high evaporation rate) result in the face-down configuration instead (Figure 4.8). This experiment proves unambiguously that the collective orientation of NPLs in self-assemblies can be controlled using solely the solvent evaporation rate. However, to generalize this concept we investigate ways to systematically change the evaporation rate using a simpler setup.

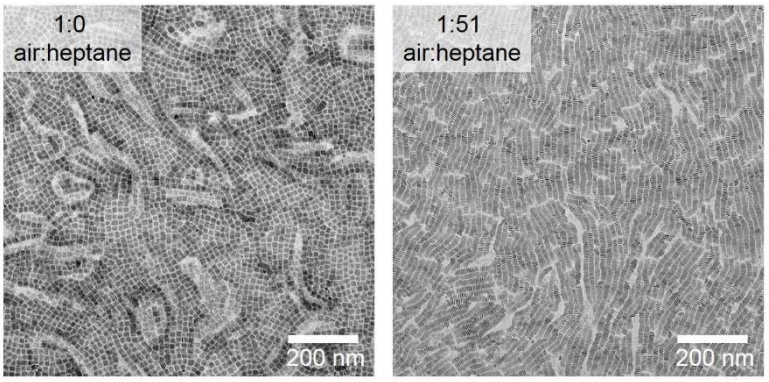

Figure 4.8: TEM micrographs of 4 ML NPLs assemblies generated in different atmospheres. Left: Self-assembly performed in the evaporation chamber in air. The NPLs are assembled in the face-down configuration. Right: Self-assembly performed in the evaporation chamber with a high content of heptane in the atmosphere. The evaporation slows down due to the high heptane content and the edge-up configuration is obtained.

To do this we performed a series of NPL self-assembly experiments on acetonitrile interfaces at 20 °C under ambient conditions, where we systematically controlled the vapor pressure (and thus the evaporation rate) by changing the NPL solvent from hexane, to heptane, to octane, keeping all other parameters constant. We determined the evaporation rate of hexane, heptane, and octane under self-assembly conditions by placing a petri dish (5 cm in diameter) on a balance, filled it with 2 mL alkane (hexane, heptane, or octane) and let it evaporate at 20 °C and 20% humidity. The weight loss was recorded as a function of time (see Figure 4.9). The slope of linear fit through the origin was divided by the surface area of the petri dish to obtain the evaporation rate normalized per unit of surface area. Since the vapor pressure (at 20 °C) decreases rapidly from hexane (162 hPa), heptane (47 hPa), and octane (14 hPa)[207], the measured evaporation rate decreases accordingly (Figure 4.9) and the time for deposition and organization at the acetonitrile interface systematically increases (Table 4.4).

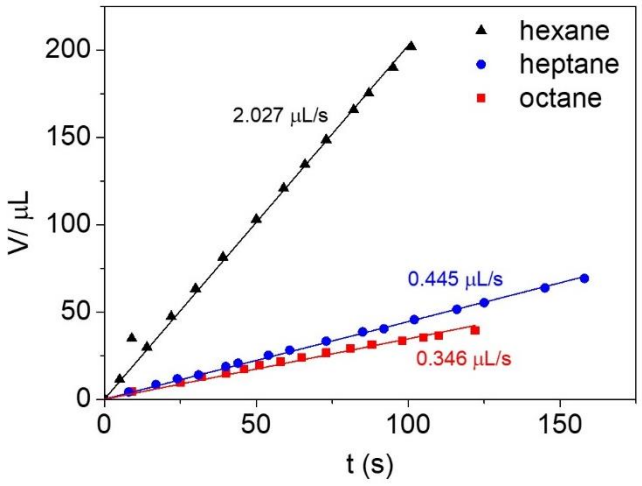

Figure 4.9: Evaporation rates of hexane, heptane and octane at 20 °C and 20% humidity determined by plotting the weight loss versus time and fitting the data points with a linear function through the origin.

Table 4.4: Evaporation rate per unit area and calculated time until complete evaporation in a typical self-assembly experiment at 20 °C (using 50 µL of NPL dispersion).

Solvent	**Evaporation rate /$\frac{\mu L}{s \cdot cm^2}$**	**Time for complete evap. (50 µL) /min**
hexane	0.103	4.6
heptane	0.023	20.5
octane	0.018	26.2

We observe distinct differences in NPL orientations depending on the type of solvent we use (Figure 4.10 a). For NPLs deposited from hexane, NPLs assemble in the face-down configuration, when deposited from octane, NPLs assemble in the edge-up configuration. Deposition from heptane results in a mix of face-down and edge-up configuration.

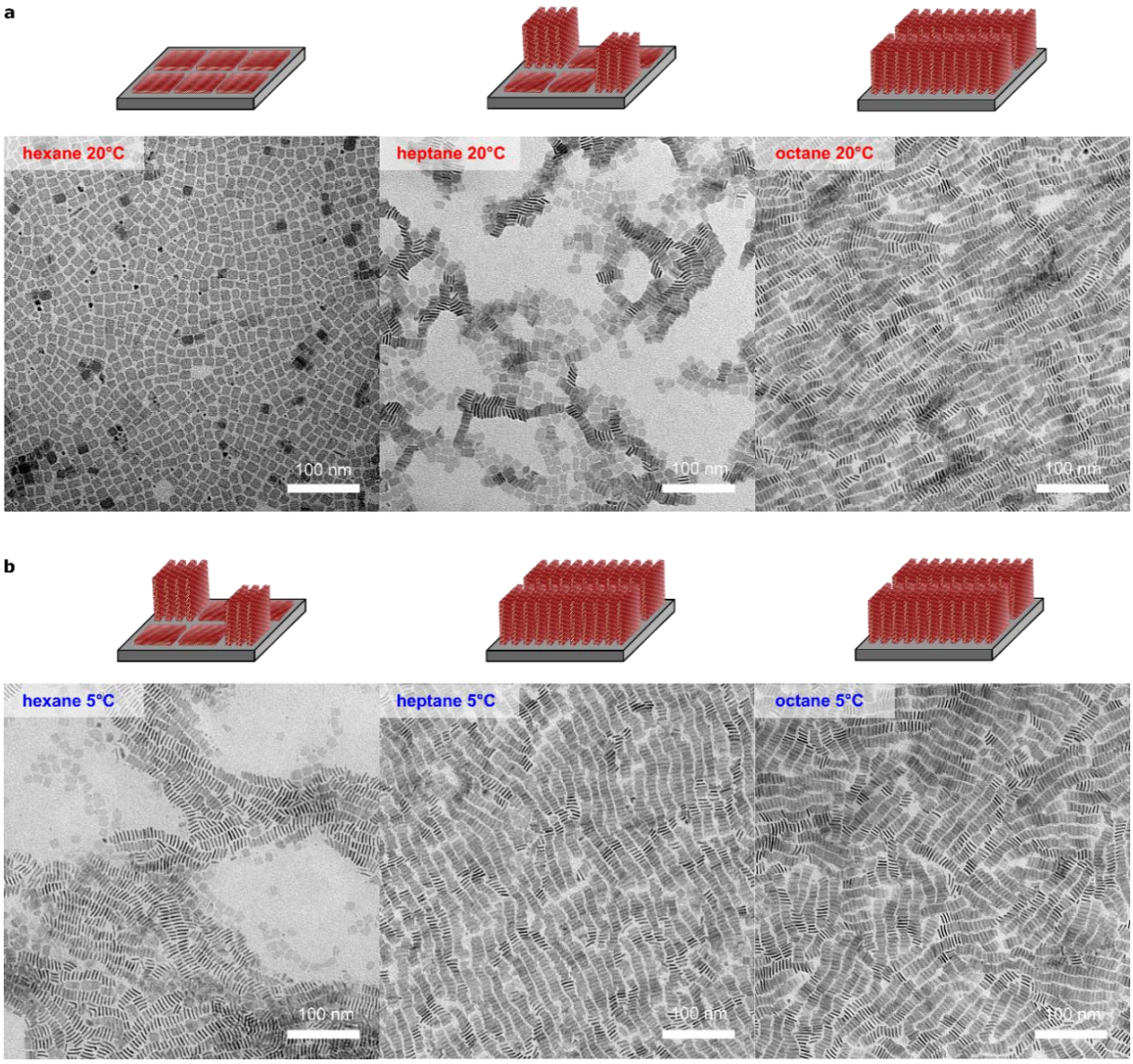

Figure 4.10: Evaporation driven self-assembly of 4 ML thick NPLs. (a) By changing the solvent from hexane to heptane to octane (systematically lowering vapor pressure) at 20 °C, the assembly can be turned from the face-down configuration (left) through a mixture (middle) to the edge-up configuration (right). (b) TEM micrographs of NPL assemblies obtained at 5 °C, the configuration is shifted to the edge-up assembly.

Therefore, the collective NPL orientation can be controlled kinetically by adjusting the evaporation rate through the choice of solvent. To generalize this further, we vary the evaporation rate by changing the temperature at which the self-assembly is performed. To estimate the evaporation rate at 5 °C, the following calculations were performed. The flux of evaporating molecules φ per time unit and area unit can be calculated from the Hertz-Knudsen equation (4.V) where p is the vapor pressure, m is the mass of one molecule, k_b is the Boltzmann constant, T is the temperature, N_a is the Avogadro constant, R is the gas constant and α is an evaporation factor[214]:

$$\varphi = \frac{\alpha p}{\sqrt{2\pi m k_b T}} = \frac{\alpha p N_A}{\sqrt{2\pi MRT}} \quad (4.V)$$

$$\rightarrow \alpha = \frac{\sqrt{2\pi MRT}\rho}{pM} \quad (4.VI)$$

The vapor pressures for the used solvents at 5 °C were calculated using the Antoine equation[215]. The evaporation factors α (4.VI) was calculated by using the experimentally determined evaporation rates at 20 °C and 20% humidity (see Table 4.4). Assuming a constant evaporation factor in the applied temperature range (5 °C to 20 °C), the mass flux at 5 °C can be estimated using the following equation (4.VII) where ρ is the density of the liquid and M the molar mass:

$$\varphi_{vol} = \frac{\alpha p M}{\sqrt{2\pi MRT}\rho} \quad (4.VII)$$

Table 4.5: Estimated evaporation factor, calculated vapor pressure at 5 °C and calculated evaporation rate per unit area at 5°C.

Solvent	**Evaporation factor**	**Vapor pressure at 5 °C /Pa**	**Evaporation rate at 5 °C /$\frac{\mu L}{cm^2 \cdot s}$**
hexane	$1.8 \cdot 10^{-5}$	7866	0.050
heptane	$1.3 \cdot 10^{-5}$	2052	0.010
octane	$3.3 \cdot 10^{-5}$	538	0.007

By decreasing the temperature to 5 °C, the evaporation rate of the NPL dispersion is reduced (see Table 4.4 and Table 4.5). Notably, the evaporation rate decreases quickly with temperature due to the exponential relationship between temperature and partial pressure, while the diffusivity only decreases linearly with temperature[216]. Thus, the time which the system has to self-assemble is prolonged and the edge-up configurations should be facilitated. To test this, we repeat the experiments shown in Figure 4.10 at 5 °C. Indeed, we observe that reducing the temperature leads exclusively to the edge-up configuration for both octane and heptane (Figure 4.10). For hexane, mixed assemblies with both edge-up and face-down configurations are formed. This data furthermore strengthens our interpretations that the evaporation rate of the solvents – and thus the time the system has to equilibrate – ultimately determines the orientation of NPLs in the self-assemblies.

4.3.3 Mechanism of kinetically driven self-assemblies

To gain deeper insights into the process, we performed small-angle X-ray scattering (SAXS) experiments on hanging droplets of an evaporating NPL dispersion while concurrently measuring particle concentration[217]. Similar to what has been observed for sterically stabilized gold nanocrystals we found a rapid onset of agglomerative stacking, visible by the evolution of an anisotropic X-ray scattering pattern (Figure 4.11) when the NPL concentration exceeds a critical concentration of 4.3 µmol/L (Figure 4.12). To determine the height of the alkane layer at which this critical concentration is reached the following equation (4.VIII) was used, with c_{ini} the initial concentration, V_{ini} the initial volume, r the radius of the well and c the current concentration during evaporation:

$$h = \frac{c_{ini} \cdot V_{ini}}{c \cdot \pi \cdot r^2} \qquad \text{(4.VIII)}$$

Our calculations show that the critical concentration is reached in the liquid film of our self-assembly process when the height of the NPL-containing alkane layer is ~3 µm thick (~0.5 µL), using a starting volume of 50 or 60 µL and an initial concentration of $4.14 \cdot 10^{-8}$ mol/L.

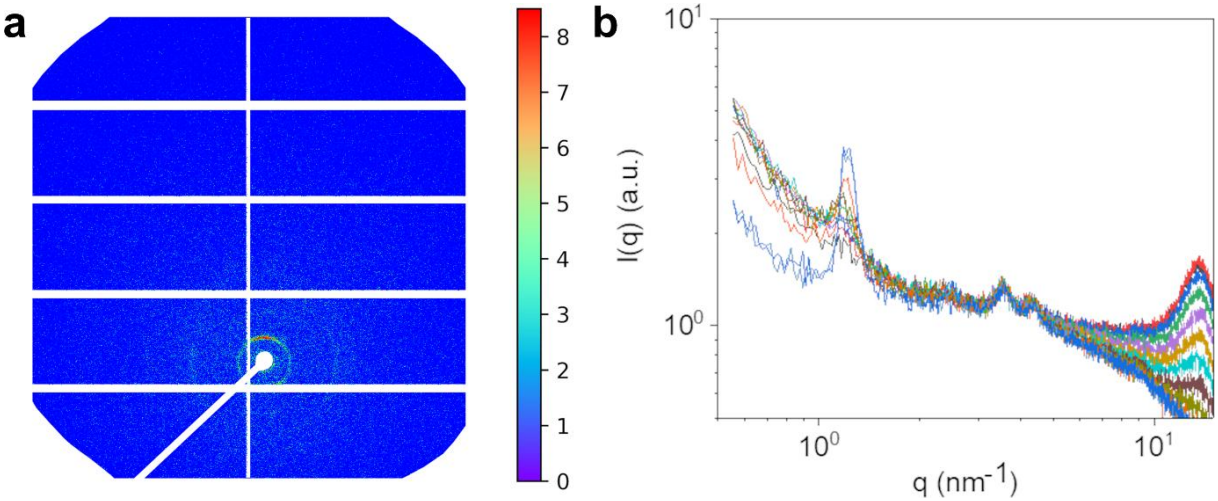

Figure 4.11: (a) Full 2D detector image of a SAXS pattern at the last stage of evaporation of a NPL dispersion in octane at RT. The exposure time was 15 s for each frame. (b) Radially integrated scattering intensity from the dried sample of NPL dispersion during the last step of the evaporation process at a time of 300 s.

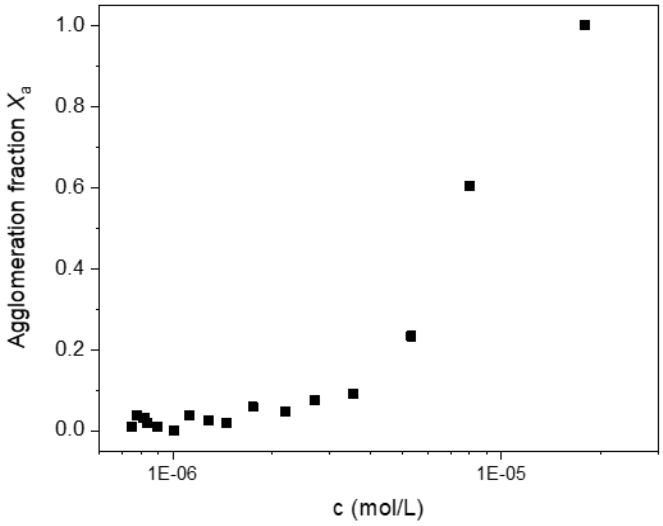

Figure 4.12: Agglomerate fraction of NPL as a function of NPL concentration in the hanging droplet during evaporation of the solvent.

Reaching this alkane layer height, the NPLs can agglomerate into stacks. Depending on the solvent, the time period until complete evaporation and therefore for agglomerative stacking is different. To correlate the final configuration with the time until complete evaporation, equation (4.IX) was used to estimate this time period. Here, t is the time, V_{ini} is the initial volume, φ_{vol} is the evaporation rate and A is the surface area of the well:

$$t=(V_{ini} - h \cdot A)\cdot\frac{A}{\varphi_{vol}} \tag{4.IX}$$

For the solvents used in this study, the time until complete evaporation ranges from ~ 3 s to ~ 39 s (see Table 4.6). For a short time period until complete evaporation and thus a quickly moving solvent front, the face-down configuration is obtained (see Figure Figure 4.13 a, yellow region). Whereas for a prolonged evaporation time periods the evaporating solvent front moves much slower and the edge-up configuration is favored (see Figure 4.13 a, green region). Between these two regions, at medium evaporation times a region of mixed NPL orientation is observed for (see Figure 4.13 a. white region). Hence, the hanging droplet experiment reveals that agglomerative stacking can occur before the alkane fully evaporates, but it depends on the evaporation rate whether there is enough time for the particles to arrange. In other words, the time the system has until complete evaporation beyond the critical filling height (volume) determines the orientation of the NPLs in the film (Figure 4.13, Table 4.6).

Table 4.6: Evaporation speed of different solvent for two temperatures (20 °C and 5 °C) and calculated time e from reaching the critical concentration and complete evaporation.

Solvent	**Temperature /°C**	**Slope Evaporation speed /$\frac{\mu m}{s}$**	**Time until complete evaporation /s**
hexane	20	-1.03	2.8
hexane	5	- 0.50	5.4
heptane	20	- 0.23	11.7
heptane	5	- 0.18	15.0
octane	20	- 0.10	27.0
octane	5	- 0.07	38.5

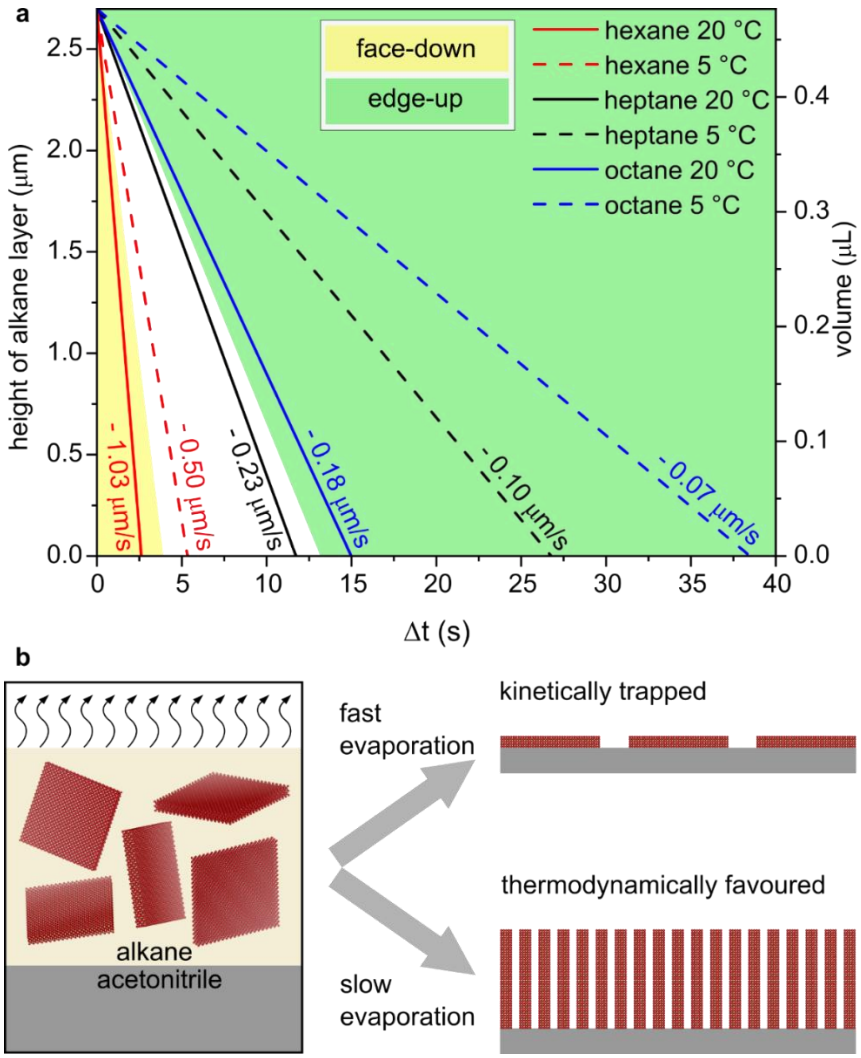

Figure 4.13: Evaporation rate determines the orientation of NPLs. (a) The height of alkane layer/ volume versus the time until complete evaporation after reaching the critical concentration [4.3 µmol/L, reached at alkane layer heights of 2.7 µm (volumes of 0.48 µL)]. Three regions (face-down, intermediate region and edge-up) can be identified. (b) Scheme of kinetically driven self-assembly. Fast evaporation leads to the kinetically trapped product, the face-down assembly. Slow evaporation leads to the thermodynamically favored product, the edge-up assembly.

Our analysis of the distances between adjacent NPLs in the self-assembled films gives us some hints about the origin of the kinetically driven self-assembly mechanism. To determine the interparticle distance of NPLs in both configurations, 200 distances for each configuration were measured. A Gaussian fit was used to calculate the mean distance and standard deviation. The distance between the NPLs in the assemblies (Figure 4.14 a and b) is significantly shorter in the edge-up configuration (2.5±0.45 nm) than in the face-down configuration (2.9±0.71 nm).

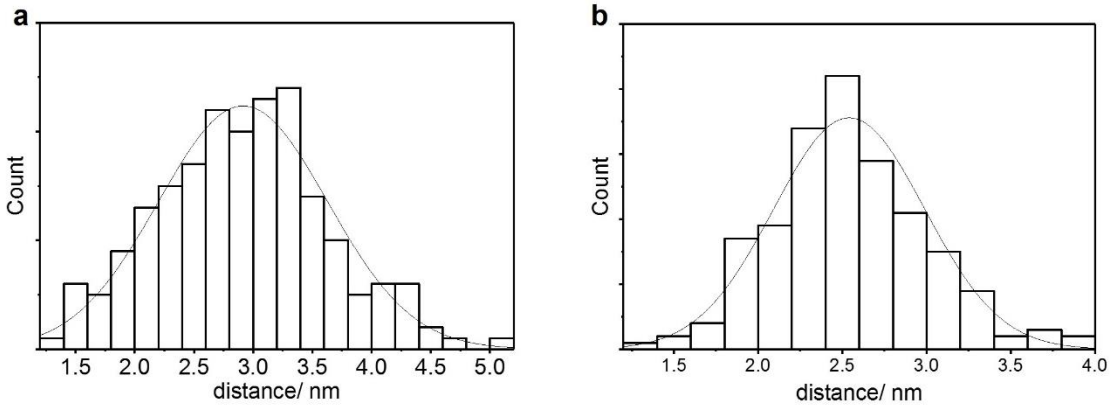

Figure 4.14: Determination of the interparticle distance of NPL. (a) 4 ML NPL assembled in the face-down configuration. The measured mean distance is 2.9 nm; (b) 4 ML NPLs assembled in the edge-up configuration. The measured mean distance is 2.5 nm.

Hence, in the edge-up configuration, the inter-NPL distance is significantly shorter than the expected distance of 3.4 nm between adjacent myristate-passivated NPLs. Thus, the NPLs ligand shells experience a significant amount of interpenetration. This requires the rearrangement and intercalation of a large number of myristate molecules on the NPL surfaces. Adopting this energetically favorable conformation requires a certain amount of time[218]. Our experiments conclusively show that slow evaporation of the NPL dispersion gives the system enough time to adopt the thermodynamically favored edge-up configuration. In contrast, upon fast evaporation, the NPLs become kinetically trapped by the quickly moving alkane solvent front[219] and deposit in the face-down configuration at the acetonitrile interface. Thus, we are able to trap the transition from the face-down to the edge-up configuration at different states (fully face-down, fully edge-up, and anything in between). This means that we are not limited to one trapped state but we can actually tune which fraction is in the face-down and edge-up configuration (Figure 4.10). Notably, NPLs adapted a well-defined collective orientation even when kinetically trapped by fast evaporation, which is in contrast to the glassy states obtained in previous works under similar conditions with nanorods[193]. Thus, our self-assembly method yields well-defined monolayer under kinetic *and* under thermodynamic control. Both the edge-up and the face-down configurations are maintained even if the NPL concentration or the NPL dispersion volume is varied (Table 4.2, Figure 4.15 and Figure 4.16), that is, even if the maximum possible surface coverage of NPLs is much lower than the total acetonitrile surface area. This further validates our proposed mechanism (Figure 4.13 b).

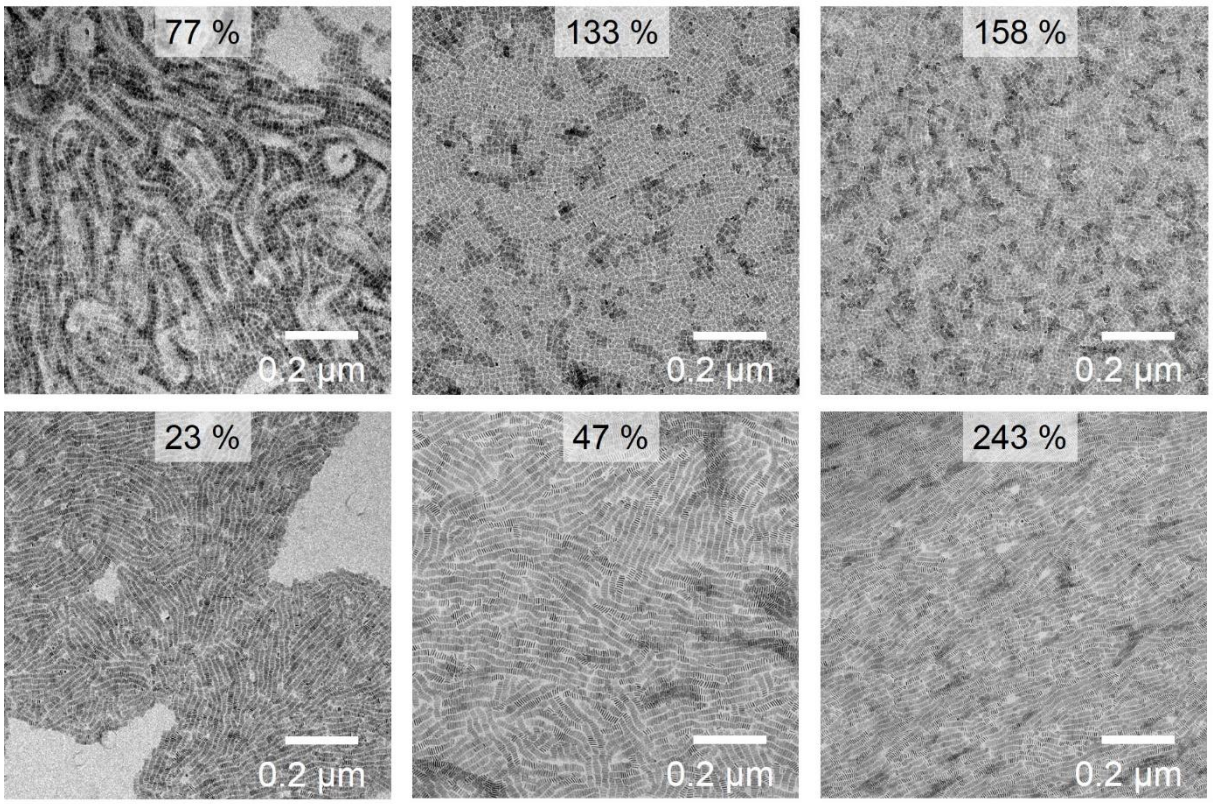

Figure 4.15: TEM micrographs of 4 ML NPLs assembled in the face-down configuration (upper row) or edge-up configuration (lower row) with varied theoretical surface coverage. Even for lower surface coverage, homogeneous films can be obtained.

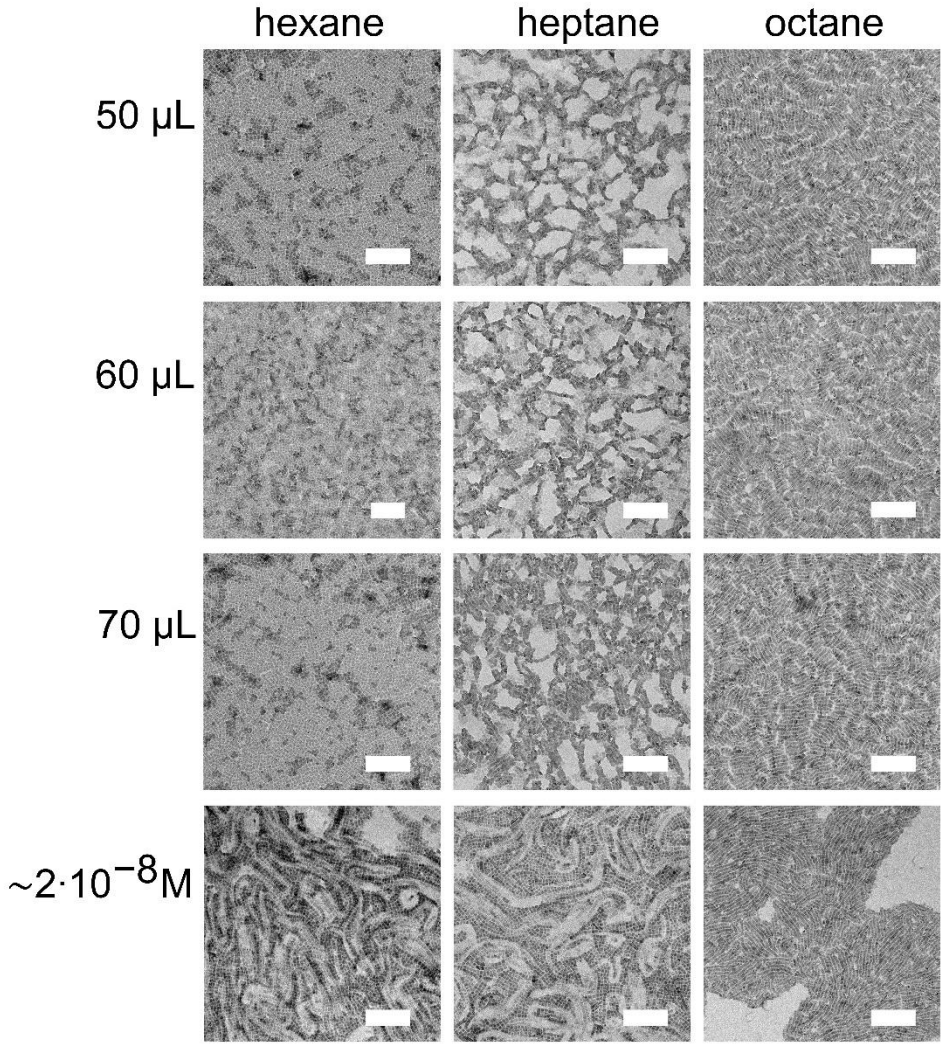

Figure 4.16: Self-assembly of 4 ML NPLs with varied volume (fixed concentration of $4 \cdot 10^{-8}$ M**)** and concentration (V= 50 µL). The same trend from face-down to edge-up by changing the solvent is observed for all volumes. The self-assembly with half concentrated NPL dispersions leads to the same trend starting from face-down to edge-up. Scalebar 0.2 µm.

Angle-dependent PL of NPL-self-assemblies

To assess the long-range order of our assemblies, we study net transition dipole moment orientations by angle-dependent PL spectroscopy (spot size ~5 mm², see Scheme 4.1). Figure 4.18 a shows the *s* and *p* radial intensity of the face-down assembly at detection angles ranging from -80° to 80° with respect to the substrate normal, and their respective fit curves obtained

by optical simulations (see Experimental Part 4.2). The fitting indicates that on the face-down sample, the dipole orientation Θ is preferentially parallel to the substrate plane (Θ = 0.16). This proves that the in-plane arrangement of the platelets observed under the TEM is maintained at least over the area of the entire spot size (~5 mm²), highlighting the uniformity of the self-assembly. Note that the fit model assumes an in-plane isotropic orientation of the dipoles. This is the case for face-down samples as evidenced by the TEM Fourier transform analysis (Figure 4.17). On the other hand, the shape of the *p*-polarized curve of the edge-up assemblies (Figure 4.18 b) differs from the face-down characteristics (Figure 4.18 a), reflecting a different arrangement of the dipoles with respect to the face-down configuration. We can derive a dipole orientation of Θ = 0.56, indicating that dipoles are preferentially oriented perpendicular to the substrate normal. The discrepancy between experimental data and simulations for the edge-up assemblies stems from the preferential orientation of NPLs along a specific in-plane direction (direction of stacking), in line with our TEM Fourier analysis (Figure 4.17). This should give rise to macroscopically observable linear light polarization. We investigate this by collecting the PL signals of face-down and edge-up assemblies at a fixed detection angle (0° with respect to the normal) and vary the in-plane polarization angle of the detector (Figure 4.18 c). For the face-down assembly no periodical variation of the signal is observed, as expected for isotopically distributed dipoles. In striking contrast, a periodical oscillation of the PL signal is found for the edge-up sample. Clearly, the preferential NPL stack-orientation is maintained over the spot size area of ~5 mm², resulting in the anisotropic in-plane PL signal.

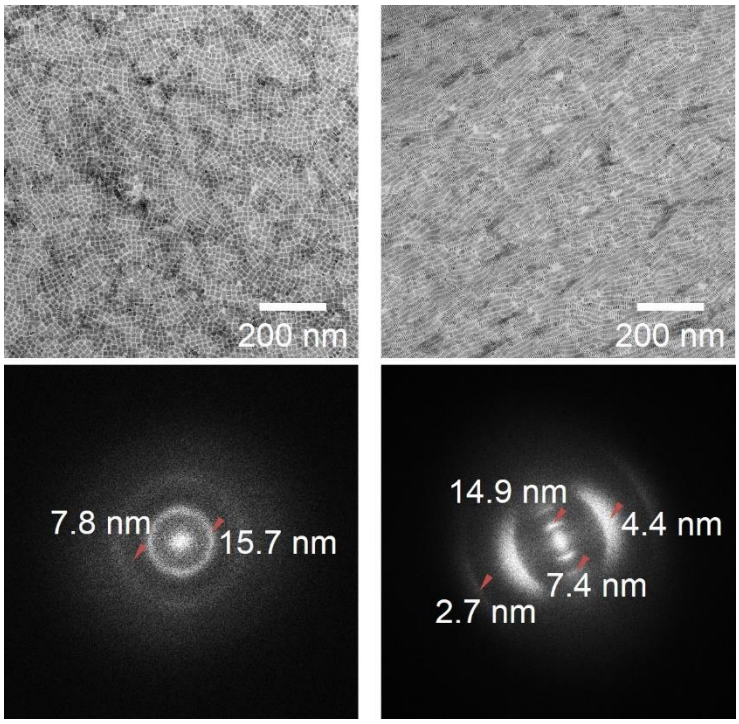

Figure 4.17: TEM micrograph of NPLs assembled in the face-down configuration (left) and edge-up configuration (right) and the relating FFTs (lower part). The measured distances can be correlated to the interparticle distances of the NPLs. While the face-down assemblies reveal their isotropic orientation by the ring-shaped FFT pattern, a preferential orientation of the stacked NPLs in the edge-up assemblies is evident from the anisotropic structure of the FFT pattern.

Thus, edge-up NPL films could have interesting applications in optoelectronics, such as the emerging field of polarized light-emitting diodes[220].

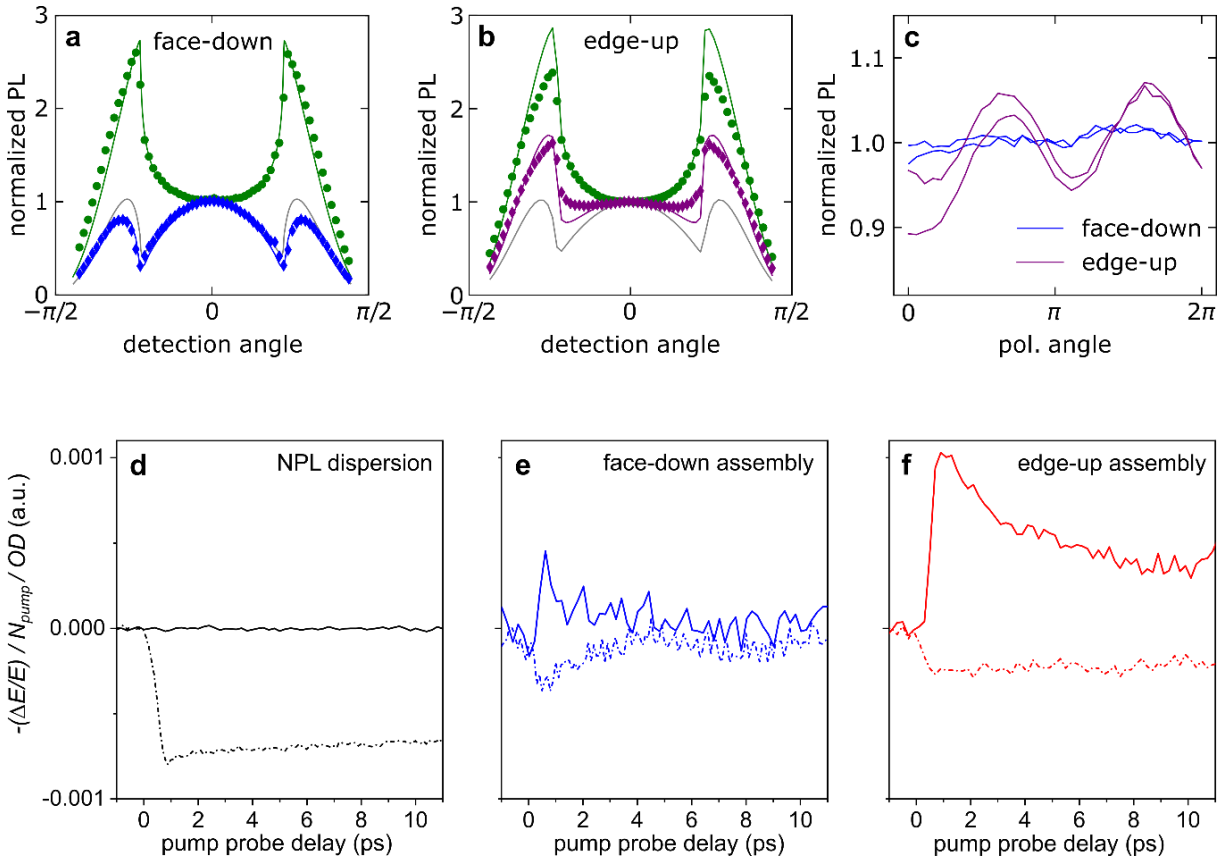

Figure 4.18: Angle-resolved PL, polarized emission and ultrafast THz conductivity dynamics for NPL self-assemblies. (a), (b), Angle-resolved PL of a face-down (a) and an edge-up (b) assembly. The s (green) and p (blue/purple) radial intensity with their fits (solid green and blue/purple line) are displayed. For comparison also the p-polarized curve corresponding to an isotropic orientation of the dipoles (Θ = 1/3, gray curve) is displayed. (c) Polarization-dependence of the PL for face-down and edge-up assemblies at a fixed detection angle of 0° with respect to the substrate normal. (d), (e), (f) Ultrafast THz conductivities for NPLs dispersed in (d) hexane, and assembled in (e) face-down and (f) edge-up configurations. The solid (dashed) lines represent the real (imaginary) part of the complex conductivity.

To integrate confined nanomaterials into optoelectronic devices requires efficient electronic coupling between the building blocks so that charge carriers can be efficiently extracted from (or injected into) the nanomaterials. Given the anisotropy of NPLs and their assemblies, we investigate the orientation-dependent photoconductivity of face-down and edge up-assemblies.

4.3.4 Photoconductivity of nanoplatelet-self-assemblies

In principle, the coupling strength in NPL solids depends strongly on the degree of wave function overlap between neighboring NPLs: the shorter the NPL-NPL distance, the higher the electronic coupling[221]. The inter-NPLs distance in the edge-up (2.5 ± 0.45 nm) is shorter than in the face-down configuration (2.9 ± 0.71 nm, Figure 4.14 and Figure 4.15). Along with the edge-to-edge distance, other parameters including the total NPL-NPL interaction area (larger for edge-up than for face-down), and the dipole-dipole interactions between NPLs play also critical roles on the inter-NPL coupling strength and thus charge transport dynamics in NPL samples. To investigate and compare the coupling strength between samples, we have measured PL of NPLs in dispersion and in assemblies (on borosilicate glass substrates, self-assembly performed with octane at 5 °C, overnight temperature equilibration of equipment). The edge-up and face-down assemblies both display broader PL spectra than NPLs in dispersion (Figure 4.19), illustrating the enhanced coupling strength in NPL assemblies. The edge-up samples show slightly broader and red-shifted emission compared to the face-down case (Figure 4.19 and Table 4.3 in the Experimental Part 4.2

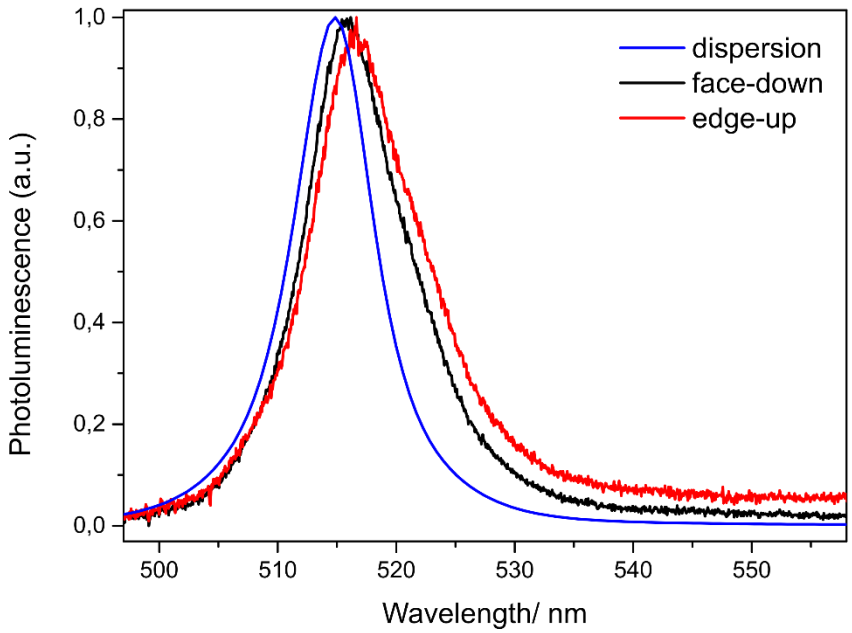

Figure 4.19: PL spectra of 4ML CdSe NPLs in dispersion, in the face-down assembly, and in the edge-up assembly (assemblies on borosilicate glass substrate).. The PL line-width broadens (dispersion < face-down < edge-up) and red-shifts (dispersion < face-down < edge-up) with decreasing distance between NPLs (see Figure 4.14 and Figure 4.15).

This redshift is larger than that expected from the different dielectric environments in dispersion and particle assemblies on borosilicate, and thus indicates stronger coupling between NPLs for the edge-up configuration.

To further investigate the role of coupling strength for charge transport properties, we measure the photoconductivity on well-defined NPL assemblies, employing time-resolved, contact-free optical pump-THz probe (OPTP) spectroscopy: a well-established tool for characterizing the nature (exciton or free carrier), and transport properties of photogenerated charge carriers in bulk or low dimensional, quantum-confined semiconductors[202] (see Experimental Part 4.2). Therefore, the assemblies were transferred on fused silica slides. To prove the orientation of the assemblies, atomic force microscopy (AFM) were used to determine the thickness of the films, since SEM is not possible on such thick glass substrates (for AFM micrographs with height profile see Figure 4.20).

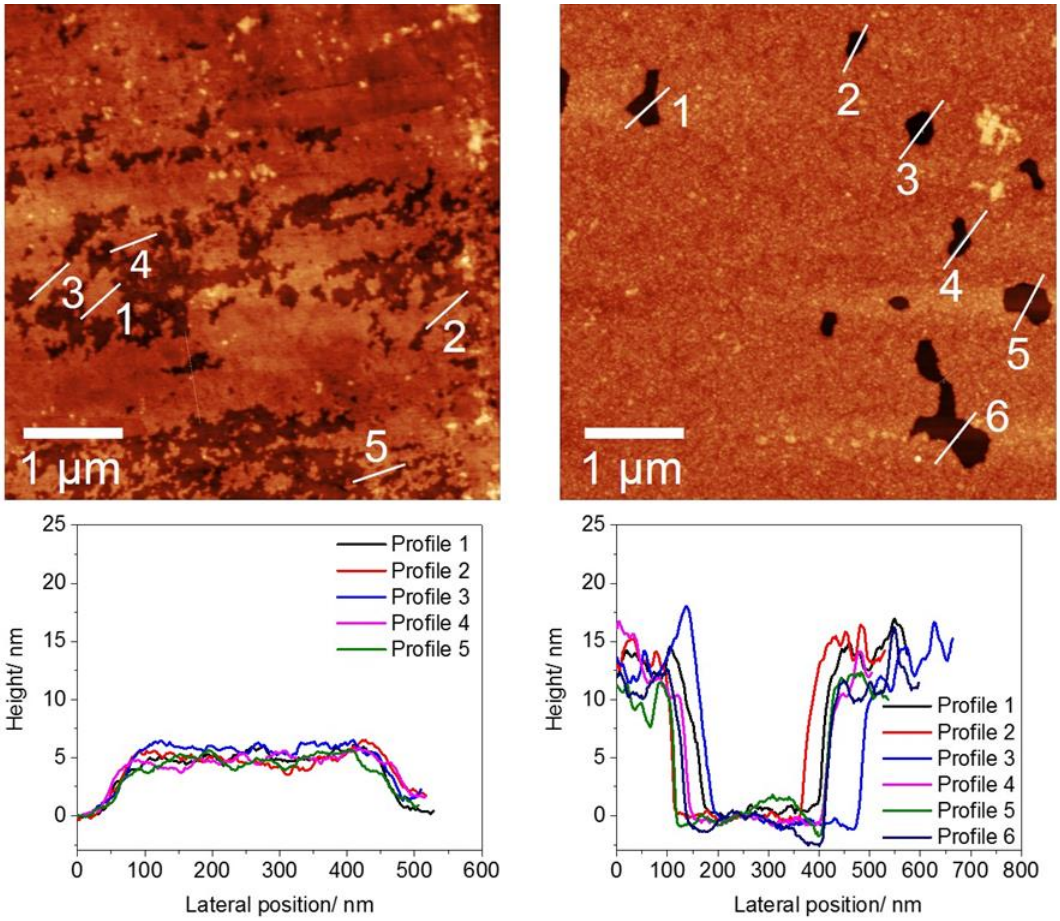

Figure 4.20: AFM images of face-down assembly (left side) and edge-up assembly (right side) transfers to a THz glass slide. Images were taken in the tapping mode at the scan rate of 1 Hz. The raw data were analyzed using the program Gwyddion. For the topographic image, the plane level tool and the align rows tool (polynomial degree 1) was used. The white lines indicate the position of the height profile shown in the lower part. The height of the face-down assembly corresponds to a monolayer of 4ML myristate passivated CdSe NPLs layer flat on the substrate. The height of the edge-up assembly corresponds to a monolayer of 4ML CdSe NPL standing vertically aligned on the substrate.

Here, we compare the THz photoconductivity in three different samples: dispersed (isolated) NPLs in hexane, and NPLs in the face-down and edge-up assemblies (Figure 4.18 d-f). The signals are normalized to the absorbed photo-density (i.e., photogenerated electron-hole pairs), and can, therefore, be compared quantitatively. For isolated NPLs dispersed in hexane, the THz response is purely excitonic (Figure 4.18 d), as evident from the purely imaginary THz photoconductivity. This observation of stable exciton states at room temperature in our NPLs indicates an intrinsically strong Coulomb interaction between photogenerated electrons and holes, leading to a large exciton binding energy E_b beyond the thermal fluctuation (~ 26 meV), in line with previous spectroscopic results (with E_b ~ 170 meV)[205]. For NPLs assemblies, the electronic coupling between NPLs allows for charge transport to occur: charge carriers in the

assemblies are sufficiently mobile to give rise to a decent THz conductivity (Figure 4.18 e-f). Here we propose two plausible scenarios accounting for the free charge carrier generation in the assemblies: (1) in a more "compact" configuration the charge carriers are screened better, resulting in a reduction of the exciton binding energy[222] and thus an increase in the fraction of free charges. Note that a decrease in exciton binding energy is not necessarily evident from the PL[223]; (2) with enhancing inter-NPL coupling strength (donor/acceptor wave function overlap), the inter-NPL charge transfer should increase. As a result, the efficiency of free charge generation by exciton dissociation is expected to increase, and free charge carriers can become delocalized. The THz photoconductivities in NPL samples (Figure 4.18 d-f) agree well with the these considerations: we observed a clear transition from pure excitonic response for isolated NPLs in dispersion to free charge carrier response in the edge-up sample as a result of enhanced NPL coupling (with the face-down as the intermediate situation). To support our experimental observations, we have further measured the frequency-resolved THz conductivity for NPLs in dispersion and in the edge-up case. For NPLs dispersed in hexane, in line with pure excitonic picture based on the dynamics shown in Figure 4.18 d, we observe that the complex conductivity is dominated by it imaginary component (see Figure 4.21 a).

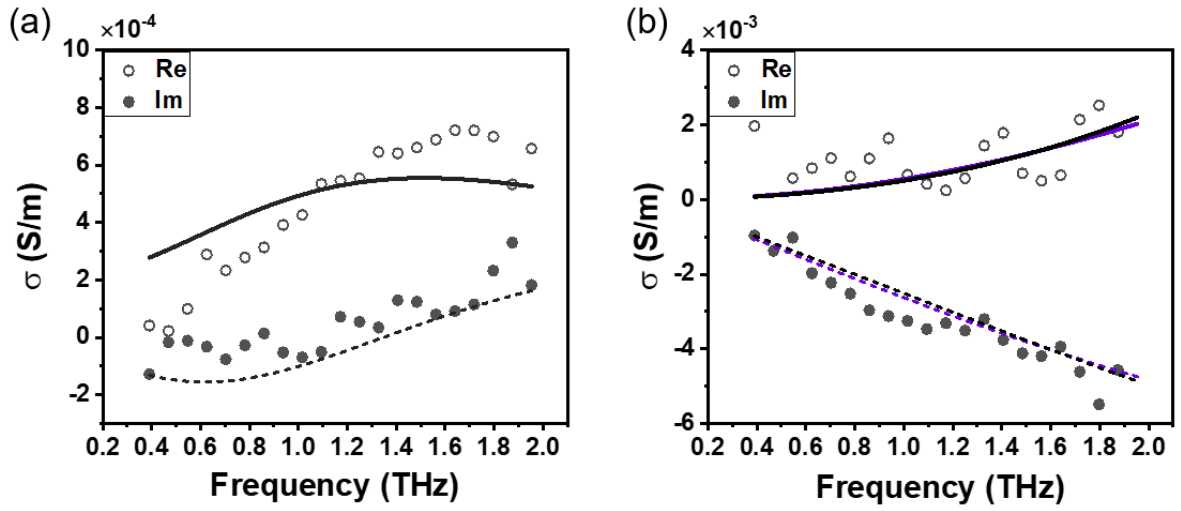

Figure 4.21: (a) Drude-Smith fitting for edge-up assembly. The fitting parameters are $\omega_p = 0.04\,THz$, $\tau = 94\,fs$, c=-0.82; (b) Lorentz model fitting for NPL in dispersion. The fitting parameters are $\omega_0 = 50\,THz$,$= 0.08\,fs^{-1}$, $\omega_p = 0.0035\,THz$ for purple color; $\omega_0 = 30\,THz$,$\gamma = 0.03\,fs^{-1}$, $\omega_p = 0.002\,THz$ for black color.

More importantly, the complex conductivity can be well fitted by a Lorentzian resonance, which has been well-established for describing intra-excitonic transitions (e.g. 1S-2P) in the excitonic material systems[224]. For NPLs in the edge-up configuration, on the other hand, we observed a free carrier dominant conductivity which can be described and fitted by a modified

Drude model (see Figure 4.21 b and associated discussion related to the Drude-Smith model) Finally, in the normalized THz conductivity dynamics, the decay time for the face-down assembly is found to be much shorter than that of the edge-up (Figure 4.22).

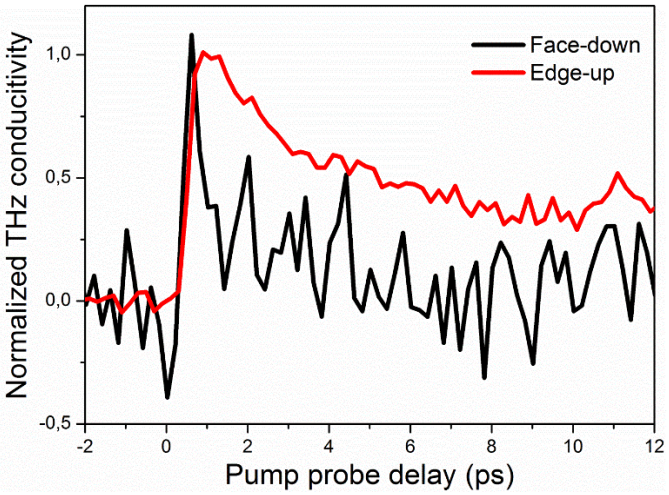

Figure 4.22: Normalized, real part of the THz conductivity for edge-up and face-down geometries.

It is worth pointing out that in our THz measurements, we probe the photoconductivity, which is proportional to the product of photogenerated carrier and carrier mobility (both of which can be time-dependent). In our study, the UV-vis absorption spectra of the two NPL solids are nearly identical and the pump fluence is set to be the same. As such, we make sure that, the initial photogenerated carrier densities are the same, and therefore the fast decay in the face-down sample can be attributed to a transition of some (if not all) of the free charges into the exciton states. During the formation of an "insulating" exciton gas, the absolute value for both the real and imaginary photoconductivity is expected to go down (which is in line with experimental result). The exciton formatation picture is further supported by observation of a long-lived imaginary and zero real conductivity (Figure 4e) following the fast decays in the dynamics, which has been reported for other excitonic systems including semiconducting polymer and graphene nanoribbons[225-227]. The long-lived (> 10 ps) lifetime of the free conductivity in the edge-up NPLs indicates the effective separation of electrons and holes in the assembly.

4.3.5 Conclusion

We discovered a method allowing for kinetic control over the collective orientation of NPLs in self-assembled monolayers. This simple and effective strategy opens up new ways to control the collective orientation of anisotropic, nanoscale building blocks in solid-state superstructures, making their anisotropic, and orientation-dependent properties accessible. By adjusting the evaporation rate of NPL dispersion, either by choice of solvent, temperature, or solvent partial pressure, NPL films in the face-down or edge-up configuration can be obtained. These assemblies show long-range order of the individual NPL transition dipole moments over

at least ~5 mm², with the edge-up assemblies possessing linearly polarized light emission due to the hierarchical stacking in the self-assembled monolayers. Therefore, these NPL assemblies could be useful to create novel optoelectronic devices, such as polarized light-emitting diodes by bottom-up approaches. Since our method does not rely on non-volatile additives that could influence charge carrier transport, it is ideally suited for optoelectronic applications. Employing THz spectroscopy, we demonstrate a clear orientation-dependent photoconductivity in self-assembled NPL solids. We unveil that such dependence originates from the different inter-NPL electronic coupling strength. We observed a transition from the excitonic response in dispersed NPLs (with the lowest inter-NPL coupling) to quasi-free carriers in the edge-up assembly (with the highest inter-NPL coupling among our samples) by enhancing the coupling strength between the NPLs.

5. On the interference of plasmonic and semiconductor nanoparticles with stereolithographic 3D printing

Chapter 5 is based on a manuscript under preparation for publication. In the previous chapter, the interaction potential of NPLs were adjusted in order to control their orientation in the solid-state. Besides adjusting the interactions between NPs to control their assembly and orientation, the interactions must also be controlled to avoid agglomeration during dispersion in another matrix. In this chapter, the NP interactions were modified in order to allow their dispersion in a photoresin applied for TPP 3D. The incorporation of nanoparticles in 3D printing offers a huge potential to create highly functional nanocomposite structures. The printing parameter space in the presence of nanoparticles can be altered, depending on the type of material and the concentration. However, to systematically assess this, it is crucial to ensure that the nanoparticles do not agglomerate during any stage of the process. Agglomeration not only leads to an uneven distribution of nanoparticles in the photoresin, but also induces scattering of the excitation beam and altered absorption profiles due to inter-particle coupling. To study the effect of a variety of non-interacting, well-dispersed nanoparticles on the 3D printing process, the stabilization of nanoparticles in the 3D printing resin is indispensable. We achieve this by functionalizing the nanoparticle with surface-bound ligands that are chemically similar to the photoresin, which allows increasing the nanoparticle loadings without inducing agglomeration. Then, we systematically studied the effect of different nanomaterials (Au nanoparticles, Ag nanoparticles, and CdSe/CdZnS nanoplatelets) in the resin on the 3D printing process. We observe that both, material specific (absorption profiles) and unspecific (radical quenching at nanoparticle surfaces) pathways co-exist by which the photopolymerization procedure is altered. This can be exploited to increase the printing resolution leading to a reduction of the minimum feature size.

My contributions to the project were the synthesis of the Au and Ag NPs and the cleavage of the CTA group pf the PMMA polymer. Furthermore, I performed the surface modification of the applied NPs with the PMMA polymer and dispersed the NPs in the photoresin. In addition, I studied the dispersibility of the NPs in the photoresin using UVVIS. I conducted the 3D printing together with Antonio Ibanez Landeta (MPI-DS). In addition, I evaluated the printing quality as well as the printed line width and studied the polymer conversion using

FTIR. Long Yang (MPIP) synthesized the PMMA-CTA polymer and Henry Halim (MPIP) synthesized the CdSe/CdZnS NPLs.

5.1 Introduction

3D printing enables the quick production of complex geometries[140]. Among existing 3D printing techniques, two-photon polymerization (TPP) stereolithography stands out for producing a large variety of micro- and nano-sized structures[152], e.g., photonics[228], micro optics[229], micromachines[230], biomedicine[231] or microfluidics[146] applications. Here a spatially controlled fs-pulsed long-wavelength (e.g., 780 nm) laser is used to crosslink a photoresin via two-photon absorption to build complex polymeric structures. Due to the non-linearity of the two-photon absorption process for curing, the resolution is improved compared to UV curing [148].

Commonly used purely organic photoresins for TPP, mainly ensure the good structural integrity of the printed object, but lack off more specific functionality, such as optical, electrical or magnetic activity. To further expand the library of printable, functional materials and access even more fields of applications, like micro- and nanomachines, and (opto)electronics, the integration of different materials is a widely used method[140, 232]. Depending on the properties of the filler material, properties like conductivity[153], magnetism[154] or piezoelectricity[233], can be integrated. Especially the combination of 3D printing and nanotechnology opens new ways towards materials with tunable properties and functionality, like optical, electronic or magnetic properties. For example, Ceylan *et al.* constructed a polymeric microrobot loaded with iron oxide nanoparticles (NPs), which allow the magnetically driven motion of the swimmers due to the superparamagnetic behavior of the NPs[154].

The integration of nanomaterials in a printable resin not only introduces functionality to the printed device but may also affect the printability and processability of the resin[151]. Especially the stereolithographic technique, which is based on optical excitations, can be strongly affected by nanomaterials since the integrated materials can interact with the light source (by absorption or scattering). Jonusauskas *et al.* showed that, in plasmon-assisted 3D micro structuring of gold-doped polymers[159, 162], the printed linewidth strongly depended on the concentration of the Au NPs. Increasing the Au NP concentration increases the printed feature size, whereas, for low concentrations, the line width decreases. This observation leads to the suggestion that Au NPs could replace the photoinitiator to some extend. The effect was explained by the plasmon effect of Au NPs[160, 161]. Also, for quantum dots, an improvement of the resolution and simultaneously a reduction of monomer conversion was observed by Peng *et al*. upon the integration of CdSe quantum dots to a photocurable resin[155]. Liu *et al.* developed a method to produce 3D printed

structures loaded with silver nanowires to achieve electrical conductivity[234]. Also here, a decrease of the linewidth was observed, but not further analyzed.

Thus, the integration of optically active nanomaterials in polymeric matrices in TPP 3D printing can be used to transfer their functionality to the final printed structure. Depending on the type of nanomaterial used, it can significantly interfere with the light used to cure the photoresin. However, not only the functionality of the later printed object is changed, but NPs – depending on the materials used – can also directly influence the printing process itself. Plasmonic and semiconductor NPs can interact with the light excitation either via 1 photon absorption (1PA) or 2 photon absorption (2PA)[93, 235, 236] hindering the efficient formation photo-generated radicals[155]. Furthermore, NPs can also quench the polymerization directly when radical species come in contact with their surface[237-239]. Both processes influence the TPP 3D printing process significantly. This can be further complicated if NPs agglomerate in the photoresin. Here, especially plasmonic NPs will exhibit altered optical responses depending on their colloidal state as agglomeration-induced plasmonic coupling can shift the plasmon resonance substantially. The dispersion of NPs in the photoresin at high loading without agglomeration is often a non-trivial and challenging task due to attractive forces between NPs that drive the agglomeration process. Notably, agglomeration can occur even before the printing process is started, e.g., when the NPs are introduced in the uncured phororesin[240, 241]. Since agglomeration can influence the properties of the NPs[240] (e.g., through plasmonic coupling), not only the final properties of the printed structures are affected, but also interference with the printing process itself can be expected. Here, especially agglomeration-induced scattering or absorption of the curing laser light by the agglomerates have to be considered. So far, the agglomeration of nanoparticles upon dispersion in the photoresin or upon printing was not studied systematically. Hence, to date is it still challenging to assess if the previously reported effects of NPs on the 3D printing process stem from interactions of the curing laser with individual, non-interacting NPs or with NPs agglomerates.

To study the influence of individual nanoparticles on the TPP 3D printing process, we first investigate the dispersibility of NPs in the uncured resin and then modify the surface with tailor-made acrylate surfactants to enhance dispersibility in the photoresin allowing for significantly increased NP loadings compared to pristine NPs. After having ensured that NPs are well dispersed in the photoresin, we systematically investigate the effect of non-interacting NPs on the 3D TPP process. For this, we integrated three different types of NPs in the photoresin due

to their complementary optical properties. Au NPs (diameter ~1.7 nm), Ag NPs (diameter ~1.8 nm) and CdSe/CdZnS core/shell NPLs (17 nm x 32 nm) were used with different volume concentrations (0.0013 v/v% to 0.06 v/v%).

5.2 Experimental Part

Chemicals. 1-Octadecene (technical grade 90%, O806-1L), oleic acid (technical grade 90%, 364525-1L), cadmium nitrate tetrahydrate ($CdNO_3(H_2O)_4$, 98%, 642045-100G), zinc nitrate hydrate ($ZnNO_3(H_2O)$, 99.999%, 230006-25G), hydrochloric acid (puriss p.a. ≥37 %), nitric acid (purris p.a., 30709-1L-GL), 1, 4-Dioxane (anhydrous, 99.8%), 2, 2'-azobis(isobutyronitrile) (AIBN, 98%), propylene glycol methyl ether acetate (PGMEA) (99.5 %) and methyl methacrylate (Contains < 30 ppm MEHQ as inhibitor, 99%) were purchased from Sigma Aldrich. Cadmium acetate dihydrate ($Cd(OAc)_2(H_2O)_2$, 98%, 317131000) and sodium borohydride (99%) were purchased from Acros Organics. Selenium powder -200 mesh (Se, 99.999%, 36208), hydrazine monohydrate (98+%) and 1-octylamine (99%, B24193) was purchased from Alfa Aesar. Hexane (95% n-hexane, analytical reagent grade, H/0355/21), toluene (≥ 99.8%), tetrahydrofurane (THF) (analytical reagent grade, T/070/17) and dichloromethane (DCM) (HPLC grade) were purchased from Fisher Chemical. Chloroform, stabilized with amylene (100%, 83627.290) and absolute ethanol (20821.330) were purchased from VWR Chemicals. Thioacetamide (TAA, >98%, T0187) was purchased from TCI. Silver nitrate (≥99%) and NaOH 0.01 M were purchased from Roth. Gold acid ($HAuCl_4$ (99.9%-Au) was purchased from STREM chemicals. Tetra-n-octyl ammonium bromide (TBOA) (for synthesis), 2-propanol (99.5 %) and 1-dodecanethiol (for synthesis) were purchased from Merck. 2-Phenyl-2-propyl benzodithioate (95%) was purchased from Acros Pharmatech Limited. The printing resin (IP-D and IP-S) were purchased from Nanoscribe. Methyl methacrylate was passed through a column of inhibitor remover prior to use. AIBN was recrystallized from ethanol. All other chemicals were used without further purification.

Thiol-terminated Poly(methyl methacrylate) (PMMA-SH)

Raft polymerization of PMMA (PMMA-CTA). The PMMA polymer was synthesized according to a described procedure by Roth *et al.*[242]. 25g (250 mmol) of methyl methacrylate, 1.36 g (5 mmol) of 2-Phenyl-2-propyl benzodithioate as the chain transfer agent (CTA), 102.5 mg (0.625 mmol) of AIBN and 25 mL of freshly distilled dioxane were combined in a dry schlenck flask, the mixture was degassed by three freeze pump thaw cycles and then heated at 70°C for 9 hours. The polymer (monomer conversion = 80%; Mn = 4727 g/mol , M_w/M_n =1.49) was precipitated 3 times in cold methanol

Hydrazinolysis (PMMA-SH). The CTA group of the synthesized polymer was cleaved according to a slightly modified procedure by Fan *et al.*[243] The PMMA-CTA polymer (4.339 g, 0,92 mmol) was dissolved in DMF (30 mL). The solution was degassed by three freeze pump thaw cycles. At RT, hydrazine monohydrate (0.4 mL, 8.23 mmol) was added. After stirring for 2 h at RT, the polymer was precipitated in an excess of cold, 1.2M HCl aqueous solution. The product was filtered, washed several times with cold methanol and dried in the vacuum at 45 °C overnight. The successful cleavage of the CTA group was proved by NMR (see SI 1).

Synthesis of hydrophobic Au NPs. Au NPs were synthesized by a liquid-liquid synthesis route according to a described procedure by Riedinger *et al.*[244]. Briefly, $HAuCl_4$ (300 mg, 0.88 mmol) was dissolved in MilliQ water (25 mL). Tetraoctylammoniumbromid (TOAB) (2.17 g, 3,97 mmol) were dissolved in toluene (80 mL). Both solutions were combined in a 500 mL separation funnel and shaken for 5 min. The gold precursor was transferred from the aqueous phase to the organic phase indicated by a color change from colorless to dark red. After complete separation, the aqueous solution was discarded. The organic phase was transferred to a 250 mL flask. Under stirring, $NaBH_4$ (334 mg, 8.83 mmol) dissolved in 20 mL MilliQ water was added dropwise to the organic phase. A color change from red to violet could be observed due to the reduction of Au^{3+} to Au^0. The solution was stirred for 60 min and then transferred to a separation funnel. The solution was washed once with 25 mL 10mM HCl, once with 25 mL 10 mM NaOH and four times with 25 mL MilliQ water. The aqueous phase was discarded and the organic phase was stirred overnight to obtain a narrow size distribution through Ostwald ripening.

To stabilize the nanoparticles further, either 1-dodecanethiol or a PMMA-SH polymer were used. To stabilize the nanoparticles with 1-dodecanethiol, 1-dodecanethiol (10 mL, 41.8 mmol) was added and the solution was heated to 65 °C under stirring for 2 h. The solution was centrifuged at 2000 rpm (416 rcf) for 5 min to remove bigger aggregates. The solution was divided into four 50 mL centrifugation tubes and filled up with methanol to precipitate the NPs. The solution was centrifuged at 2000 rpm (416 rcf) for 5 min. The precipitate was redispersed in 8 mL Chloroform. To functionalize the Au NPs with the PMMA-SH polymer, 10 mL of the Au NP containing solution was mixed with the polymer (825 mg) and stirred for 30 min at RT. The solution was heated up to 65 °C under stirring for 2 h. Then it was stirred overnight at RT again. The Au NP were precipitated with methanol. The solution was kept in the fridge for

several days and was then centrifuged at 2000 rpm (416 rcf) for 5 min. The precipitate was redispersed in DCM.

Synthesis of hydrophobic Ag NPs. Ag NPs were synthesized according to a slightly modified protocol of Niskanen *et al.*[245]. The Ag NPs are stabilized with the synthesized thiol-terminated PMMA polymer. The polymer (0.189 g, 0.04 mmol) was dissolved in 200 mL ethanol/THF (1:1 v/v). $AgNO_3$ (0.0679 g, 0.4 mmol) dissolved in 0.4 mL MilliQ water and $NaBH_4$ (0.152g, 4 mmol) dissolved in 1.6 mL MilliQ water was added under stirring. Immediately after the addition, hexane was added to precipitate the formed Ag NPs. The solution was centrifuged at 4000 rpm (1664 rcf) for 5 min and redispersed in DCM.

Synthesis of Core/Shell CdSe Nanoplatelets.

Synthesis of 4ML thick CdSe NPLs. 4ML thick CdSe NPLs were synthesized by a modified procedure published by Mahler *et al.*[246] Briefly, 60 mL of 1-octadecene, 320 mg (1.20 mmol) of $Cd(OAc)_2(H_2O)_2$, and 879 µL (787 mg, 2.79 mmol) of oleic acid were combined inside a 100 mL three-necked flask attached to a water-cooled condenser. The mixture was stirred and degassed under vacuum at 110 °C for 90 min. After stopping the vacuum line, the flask was filled with argon and 48 mg (0.607 mmol) of Se powder was swiftly added into the flask. Then the temperature of the heating mantle was set to 240 °C. When the temperature in the flask reached 205 °C, 160 mg (0.600 mmol) of $Cd(OAc)_2(H_2O)_2$ was added into the mixture and the reaction proceeded for 15 min at 240 °C. Afterwards the flask was then cooled to room temperature using a water bath and 6.7 mL of oleic acid was injected. The mixture was centrifuged for 10 min at 5000 rpm (2599 rcf), the supernatant was discarded. Finally, the precipitated NPLs were re-dispersed in 12 mL hexane.

Synthesis of $Cd_{0.33}Zn_{0.67}S$ Shell. The CdZnS shell was synthesized using a one-pot method, modified from an existing procedure[246]. Briefly, 6 mL of the as-synthesized 4ML NPLs (with optical density at 510 nm = 30) were added into a 50 mL round bottom flask containing a stir bar. In a separate flask, 300 mg (3.99 mmol) of TAA, 3 mL (18.2 mmol) of octylamine and 9 mL of chloroform were gently mixed and then sonicated in an ultrasound bath until all the TAA dissolved. The TAA solution was added to the NPL solution while stirring. After a couple of minutes, 500 µL of $CdNO_3$ solution (0.2 M in ethanol) and 1000 µL of $ZnNO_3$ solution (0.2 M in ethanol) were added into the mixture. The flask was sealed with a glass stopper and left to stir for 24 hours in ambient conditions.

To be able to precipitate the NPLs, the mixture was first concentrated by evaporating a portion of the solvent using a rotatory evaporator at approximately 280 mbar, 40°C for a couple of minutes. Then the concentrated mixture (volume approx. 15mL) was centrifuged for 10 min at 8000 rpm (6654 g), the supernatant was discarded, and the precipitated NPLs were re-suspended in 15 mL chloroform. To better stabilize the NPLs, 300 µL of $ZnNO_3$ solution (0.2 M in ethanol) and 600 µL of oleic acid were added into the NPL dispersion while stirring and the mixture was kept at ambient conditions for a couple of days for PL recovery.

To remove the excess oleic acid introduced in this step, methyl acetate was added to the chloroform dispersion of core/shell NPLs (in the ratio of chloroform:methyl acetate = 1:1 v/v). The NPLs were precipitated by centrifugation and re-dispersed in chloroform.

Surface functionalization of CdSe/CdZnS NPLs with PMMA-SH. To modify the surface of the NPLs, PMMA-SH (7 mg) was mixed with the NPL dispersion (100 uL, 4.5 mg/mL, theoretical 23000 chains/nm²) and stirred for 20 min at RT. Afterward, the mixture was heated up to 60 °C under stirring for 1 h. The mixture was allowed to cooled down to room temperature and stirred for additional 20 min. Afterward, methanol was added (methanol : reaction mixture 1:2 v/v) to precipitate the NPLs. The precipitate was centrifuged at 6500 rpm (4393 rcf) for 5 min and redispersed in 100 µL DCM.

Adjustment of the concentration of the nanoparticle dispersion. To determine the concentration of the Au NPs and Ag NPs, ICP-OES was performed in order to determine the concentration of metal. Therefore the dried NPs (Au and Ag) were dissolved in aqua regia and later diluted with MilliQ water, to reach a metal concentration range between 2-20 mg/L. The concentration of the of Au and Ag NP dispersion were set to 10 mg/mL. The concentration of the NPL dispersion was determined by measuring the absorbance and applying a calibration curve (absorbance vs determined weight concentration by ICP). Therefore the concentration of water dispersed core/shell NPLs were measured using ICP [247]. The weight concentration of the NPLs in dispersion can be found by adding the metal ion concentration measured by ICP together with the estimated Se and S concentration based on the stoichiometry (see (5.I)).

$$NPL\ concentration\ \left(\frac{mg}{mL}\right) = \\ Measured\ Cd^{2+}\ concentration + Measured\ Zn^{2+}\ concentration \\ + Estimated\ Se\ \ concentration + Estimated\ S\ \ concentration \tag{5.I}$$

Dispersion of NPs in resin. The resin was diluted in DCM (1mL resin in 1 mL DCM) to lower the viscosity. A certain volume of the NPs/NPLs dispersion was added to reach a set final concentration (see Table 5.1). To facilitate the dispersion of the flat CdSe/CdZnS NPLs, the dispersion was diluted and the resin was slightly heated. After mixing using a Vortex mixer, the solvent were removed using a rotary evaporator. The prepared resins were stored in the dark at 5 °C in the fridge.

Table 5.1: NPs/NPLs dispersed in resin for 3D printing in various concentrations.

Ag NPs in IP-Dip	**Au NPs in IP-Dip**	**CdSe/CdZnS NPLs in IP-Dip**	**CdSe/CdZnS NPLs in IP-S**
0.013 v/v%	0.02 v/v%	0.06 v/v%	0.05v/v%
0.007 v/v%	0.01 v/v%	0.026 v/v%	
0.0013 v/v%	0.002 v/v%	0.013 v/v%	

Printing with Nanoscribe 3D printer. The structures printed were pyramids and woodpile structures. All were fabricated using a NanoScribe Photonic Professional (GT) 3D-printer. In order to start printing a desired structure, it is needed to either convert a 3D-model (in .stl format) onto a printer-readable format or to write your own printer-readable file from scratch. Both can be done using the software DeScribe, which is supplied by NanoScribe GmbH. In this case, the pyramids were processed from an already existing .stl file, whereas the woodpile structures and gratings were programmed. The woodpile structure is composed of 10 stacked layers. Each layer has 15 consecutive parallel lines, each 1 µm apart from each other, and each consecutive layer is rotated 90 degrees, creating a grid. The pyramid array consists of 9 square pyramids, each having a dimension of 10 µm x 10 µm x 5 µm. The square gratings have fixed number of lines of 150 with varied the pitch distance from 500 nm to 1800 nm.

The structures were printed inside a droplet of negative photoresin (IP-Dip, or IP-S (for grating)) using Dip-in Laser Lithography (DiLL), where the objective is immersed directly onto the photoresin. The 63x N.A 1.4 immersion objective and a 700 µm thick fused silica slide as substrate was used. Afterward, the excess photoresin was rinsed off of the structure via immersion on Propylene glycol methyl ether acetate (PGMEA) for 30 minutes, followed by immersion on isopropanol for 5 minutes and gentle drying with nitrogen. Depending on the

structure shape and size, different parameters must be used for printing: The LP determines the size of the individual voxels that compose the structure, which in turn determines the minimum in-plane distance each printed line must have. If the distance between lines is too short, bubbles appear on the printed area due to local overheating [248], destroying the sample. If the distance is too large, the lines are unconnected. This is desirable in the in-plane direction for the woodpile structure, but not for the "continuous" pyramid. On the vertical axis, in both cases, connected voxels are desired. If they are not properly connected, the voxels will float on the un-polymerized resin and be washed away alongside the excess resin during the development process. On the "continuous" structures, the in-plane line distance is governed by the Hatching Distance (HD) parameter, which gives the distance in micrometers that the center of two consecutive lines will be spaced apart. The vertical distance between two voxels is controlled by the Slicing Distance parameter (SD), whereas for the woodpile and grating structures, this is controlled by the ZOffset parameter. Since the voxel size not only depends on the LP but also on the photoresin and NP loading, a parameter sweep of not only voxel distances but also LP is needed for each NP-doped photoresist.

Characterization. For optical spectroscopy, NP/NLP dispersions were transferred to a quartz glass cuvette (10mm). The NP-loaded uncured resins were deposited on a glass slide and covered with a glass coverslip Absorption spectra were recorded on a Cary 60 spectrophotometer. Photoluminescence spectroscopy (only NPL dispersion) was recorded using a Prizmatix Silver high power LED (emission peak 369 nm) for excitation and an Avantes SensLine AvaSpec-HSC-TEC for data collection.

To analyze the printed structures using TEM, the samples were coated with a Pd layer and a thin lamella was prepared by using a focused ion beam (FIB) system (FEI Nova 600 NanoLab FIB). Transmission electron microscopy was performed using a JEOL1400 or Tecnai FEI 20 microscope (acceleration voltage 120 kV and 200 kV, respectively). EDX spectra were recorded using an EDAX detector unit. The samples were deposited on carbon-coated copper grids (400 mesh) by drop-casting or by using the focused ion beam. Scanning electron microscopy was performed on a Hitachi SU8000 with an acceleration voltage between 0.100 kV and 0.187 kV.

1 H NMR spectra were recorded with a Bruker Avance spectrometer operating at 300 MHz. The molecular mass of the IP-DIP resin were determined by GPC using a PSS SECcurity device

(Agilent Technologies 1260 Infinity). The resin was dissolved in THF and a calibration curve for PMMA in THF was applied.

ICP-OES measurements were performed with an ACTIVA M spectrometer (Horiba Jobin Yvon, Bernsheim, Germany) equipped with a Meinhardt-type nebulizer, a cyclone chamber, and controlled by ACTIVAnalyst 5.4 software. The forward plasma power was set 1200 W, the Ar flow to $12\,\mathrm{L}\cdot\mathrm{min}^{-1}$ and the pump flow to 15 rpm. Measurements were performed three times per emission line, using three different elemental emission lines.

For the FT-IR study, a drop of the uncured resin with and without nanoparticles was placed on a glass substrate and cured under a commercial UV-lamp (Model E0101, UV-A lamp type 3, 9W) for 6 min. Afterward, non-polymerized resin was washed away and a thin polymerized film remained. The film was analyzed using a Perkin Elmer Spectrum Bx IR spectrometer (16 scans, absorbance spectra).

5.3 Results and discussion

5.3.1 Dispersion of nanoparticles in the uncured resin

First, we assessed the dispersibility and colloidal stability in the uncured photoresin to allow for a homogenous distribution of the NPs and to exclude effects caused by particle agglomerates. A commercial acrylate-based resin (IP-Dip, Nanoscribe) was used for the study. The resin consists of a mixture of multifunctional acrylates. Either the dispersion of NPs can be problematic, due to incompatible solubility of the nanoparticles' surfactants in the resin or agglomeration can occur through depletion forces induced by the oligomeric components in the photoresin[120].

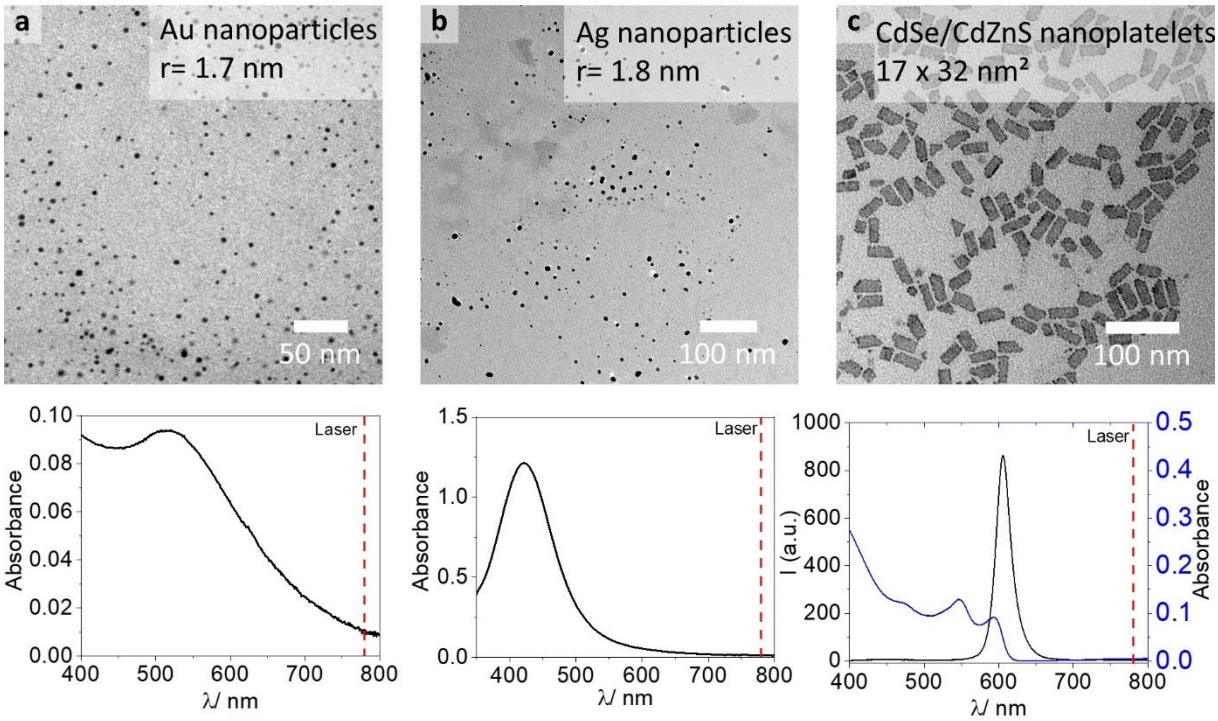

Figure 5.1**:** NPs used in this study in conjunction with a commercial acrylate-based resin for 3D printing NP/polymer composites. Upper row: TEM micrographs of NPs; lower row: Corresponding absorption spectra and in case of CdSe/CdZnS NPLs the emission spectra. The dashed vertical line represents the pulsed laser wavelength at 780 nm.

The pristine NPs are coated with dodecanethiol (Ag and Au NPs) or oleic acid (CdSe/CdZnS NPLs). To mix NPs with the photoresin different procedures are tested: (i) the NPs and the resin were both dissolved in dichloromethane (DCM) and mixed, the DCM is removed afterward, (ii) the NPs dispersed in DCM were mixed with the pure photoresin, the DMC is removed afterward, (iii) dried NPs are mixed with undiluted photoresin. When these pristine NPs are mixed with the photoresin agglomeration occurs immediately independent of the mixing

procedure. This is obvious for high loadings of NPs where agglomeration is macroscopically visible. At seemingly low loadings, particle-particle interactions could occur without being macroscopically visible.

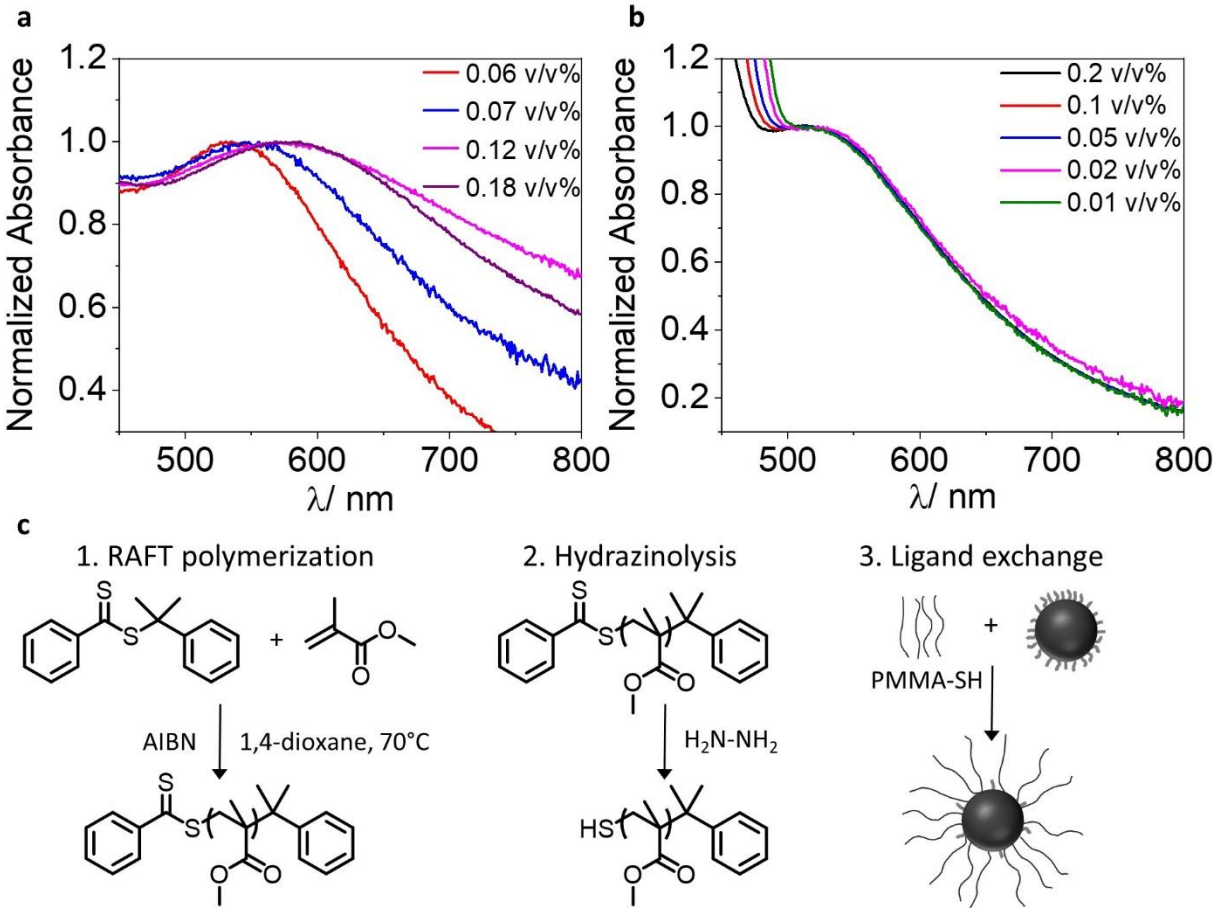

Figure 5.2: Absorption spectra of Au NPs stabilized with dodecanethiol (a) or PMMA-SH (b) dispersed in IP-Dip photoresin. (a) The spectra broadens and red-shifts with increasing concentration, indicating the NP-concentration-dependent agglomeration tendency of Au NPs in the photoresin due to depletion attraction forces; (b) The spectra are not shifted or broaden, no agglomeration; (c) reaction scheme of PMMA-SH synthesis and ligand exchange for particle modification.

To test this in detail, we used the optical signal of Au NPs. Au NPs have distinctly different absorption spectra when in close contact with neighboring NPs due to plasmonic coupling and a consequent red-shift and broadening of the plasmon band. Indeed, we observed a redshift and broadening of the absorption spectra agglomerates even for the NP loading contents around 0.1 v/v% when Au NPs stabilized with dodecanethiol were used (see Figure 5.2 a). This means that even though the sample seems optically clear to the eye, there is significant particle-particle interaction and formation of agglomerates, which leads to altered optical properties of the final composite material. We note that there should be significantly more interaction with the NIR

laser with the Au NP-loaded photoresin when agglomerates are present. Hence, the TPP printing process will depend on the agglomeration degree of the NP in the photoresin. Since the dispersibility of the NPs depends on the solubility of the surfactant covering the NPs the in the photoresin and pure dodecanethiol and oleic acid are not soluble in the photoresin, we conclude that the observed agglomeration of NPs is likely induced by the chemical incompatibility of the NP's surfactant shell with the photoresin. To obtain a better dispersibility of the NPs in the resin by minimizing the attractive forces between particles and enhance the compatibility of the NP's surfactant shell, the particles were modified with thiol-terminated polymethylmethacrylate (PMMA-SH) (M_n ~ 5000 g/mol) (see Experimental 0 and Figure 5.3 for NMR).

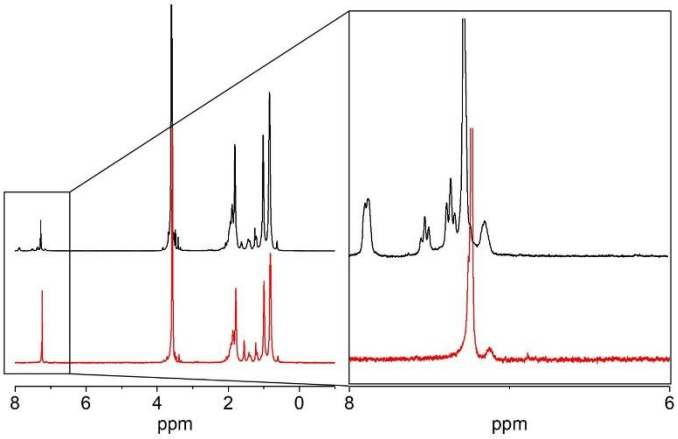

Figure 5.3: NMR of PMMA-CTA (black) and PMMA-SH (red).

The synthesis of the polymer ligand is a two-step process. First, RAFT polymerization is used to polymerize the methyl methacryltate monomer (Figure 5.2c, left), and then the CTA end-group is cleaved by hydrazinolysis to obtain the thiol end-group (Figure 5.2 c, middle). Thiols are known to have a strong affinity to metals and are widely used as surfactants for metal NPs[249-251]. With a ligand exchange step, the pristine surfactants (oleic acid and dodecanethiol) are replaced by the PMMA-SH surfactant (Figure 5.2 c, right). Having the surfactant of the same material as the photoresin should reduce the agglomeration tendency since both components, the surfactant and the photoresin are chemically nearly identical. Thus, attractive forces between the NPs could be reduced. Indeed, the grafting of polymer chains of the same composition as the matrix is known to form a "brush" around the NPs and to decrease the attractive forces between the NPs[252, 253]. The plasmon resonance peak of the modified Au NPs does not shift upon dispersion in the resin, indicating good stability and prevention of agglomeration (see Figure 5.2 b). Here, high volume fraction up to 0.8 v/v% are possible, and the loading content is only limited by the increase in viscosity hampering the photoresin's processability. Thus, our strategy allows for significantly increased loading content and should

be generally applicable to all other NP materials. Therefore, we used this method to modify Ag NPs and CdSe/CdZnS NPLs with the same polymeric surfactant and test the colloidal stability by absorption spectroscopy. Since the absorption band of Ag NPs overlaps with the absorption band of the resin (see Figure 5.4 a), shifts of plasmon resonances are masked by the resins absorption. CdSe/CdZnS NPL absorption features do not shift when agglomerated. Thus, we assess the dispersibility of Ag NPs and CdSe/CdZnS NPLs by checking for scattering contributions ($1/\lambda^4$) in the absorption spectra (see Figure 5.4 b). In both cases, we do not observe agglomeration, highlighting the general applicability of our strategy for eliminating depletion attraction forces leading to colloidally stable NPs in the photoresin even at high loading contents. After having solved this fundamental challenge, we study the influence of well-separated NPs embedded the photoresin on the TPP 3D printing process.

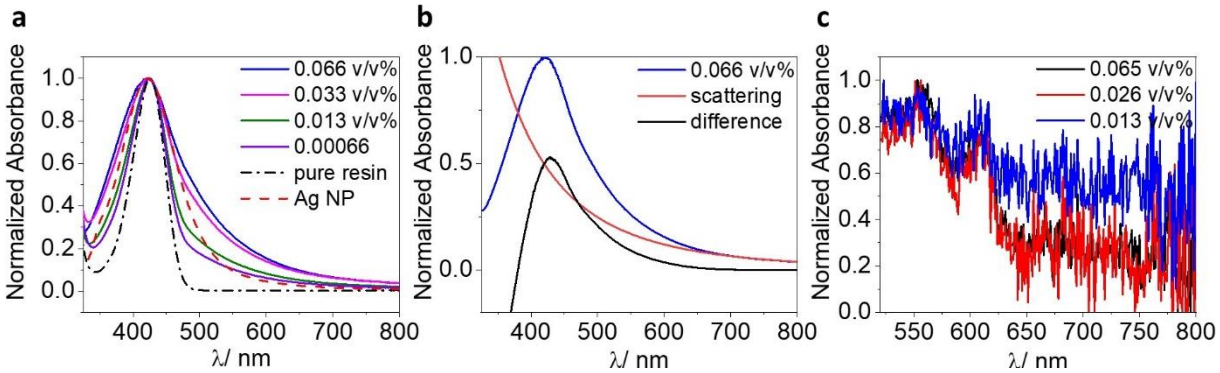

Figure 5.4: Absorption spectra of Ag NP (a) and CdSe/CdZnS NPLs (c) stabilized with PMMA-SH dispersed in IP-Dip resin. (a) Absorption of Ag NPs overlaps with the absorption of the resin; (b) Absorption spectra of Ag NPs (0.066 v/v%) and purely scattering (red). The difference of both do not represent the pure Ag NPs absorption spectra, indicating dispersed and non-aggregated nanoparticles; (c) CdSe/CdZnS NPLs are dispersed without aggregation, indicated by the absence of a tail between 650 nm and 800 nm.

5.3.2 Dispersion of nanoparticles in 3D printed objects

Even if the NPs are well dispersed in the uncured photoresin, the printing process could induce agglomeration or phase separation of the NPs, due to temperature gradients, viscosity changes, or shrinkage of the material. To assess this we first estimate the diffusion rates and the interparticle distance of the NPs in the resin (see Table 5.2 and Figure 5.6). The Stokes-Einstein equation (5.II) is used to determine the diffusion coefficient of the nanoparticles dispersed in the liquid resin:

$$D = \frac{k_B \cdot T}{6 \cdot \pi \cdot \eta \cdot R_0} \tag{5.II}$$

With k_B the Boltzmann constant, T the temperature (293 K), η the dynamic viscosity of the IP-Dip resin (2420 mPas at 20 °C) and R_0 the hydrodynamic radius of the particles. The distance, the particles move during a certain time is calculated by the following equation (5.IV):

$$\langle x^2 \rangle = 2Dt \quad \text{(5.III)}$$

$$\Delta x = \sqrt{2Dt} \quad \text{(5.IV)}$$

For the following calculations, we assume that continuous mode printing (10 mm/s) and the voxel diameter to be in the order of 0.35 µm in the x-y plane (see Figure 5.5).

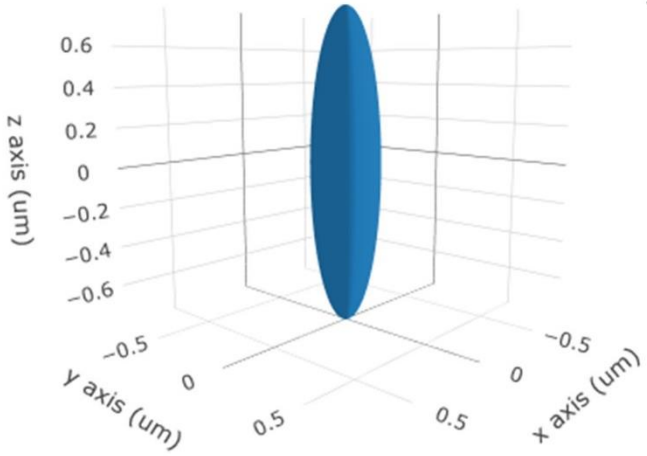

Wavelength of the laser (nm)	780
Laser Power (mW)	30
Pulsewidth (fs)	100
Laser Pulse repetition rate (MHz)	80
Laser exposure time (s)	0.5
Numerical Aperture	1.4
Refractive index of immersion liquid	1.521

Figure 5.5: Simulated voxel dimension for a LP of 30 mW. Using the two-photon lithography tool developed by Kabir *et al.* and available on the webpage nanohub.org [254].

With these assumptions, the dwell time of the laser per voxel is 0.03 ms. The diffusion of Au and Ag NPs is on average ~ 1.9 nm and CdSe/CdZnS NPLs ~ 0.62 nm within this time frame (see Table 5.2).

Table 5.2: Diffusion of nanoparticles in uncured resin.

particle type	**R_0/ nm**	**D / m²/s**	**Δx (t= 0.035 ms)**	**Δx (t= 6 min) UV curing**
Au	1.7	$5.22 \cdot 10^{-14}$	1.91 nm	791.5 nm
Ag	1.8	$4.93 \cdot 10^{-14}$	1.86 nm	769.2 nm
CdSe/CdZnS	~14	$6.33 \cdot 10^{-15}$	0.62 nm	275.6 nm

For the chosen volume fractions (between 0.02 and 0.002 v/v% for Au NPs; between 0.013 and 0.0013 v/v% for Ag NPs; between 0.06 and 0.013 v/v% for CdSe/CdZnS NPLs) the average center-to-center interparticle distance can be calculated using equation (5.V)[255]:

$$IPS = 2r\left(\left(\frac{\phi_m}{\phi}\right)^{1/3} - 1\right) \text{ (for } \Phi \leq \Phi_m\text{)} \qquad (5.V)$$

With r the radius of the nanoparticles, Φ_m the maximum particle packing fraction and Φ the particle volume fraction. The maximum volume packing fraction for random loose packing is 0.59[256]. The calculated interparticle distance is between 45 nm and 125 nm for Au and Ag NPs and 250 nm to 435 nm for CdSe/CdZnS NPLs (see Figure 5.6).

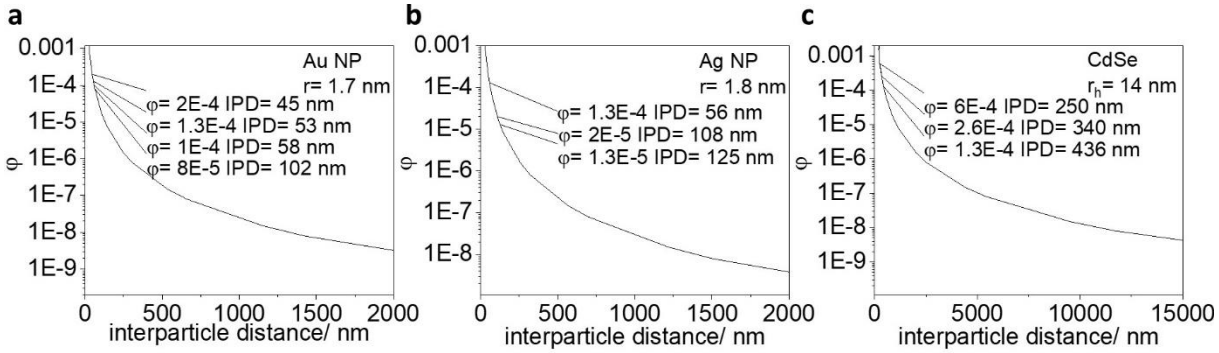

Figure 5.6: Interparticle distance of nanoparticles printed in resin.

We further analyzed the composition of the pure photoresin by NMR spectroscopy and gel permeation chromatography (see Figure 5.7 a and b) to learn more about the composition of the resin.

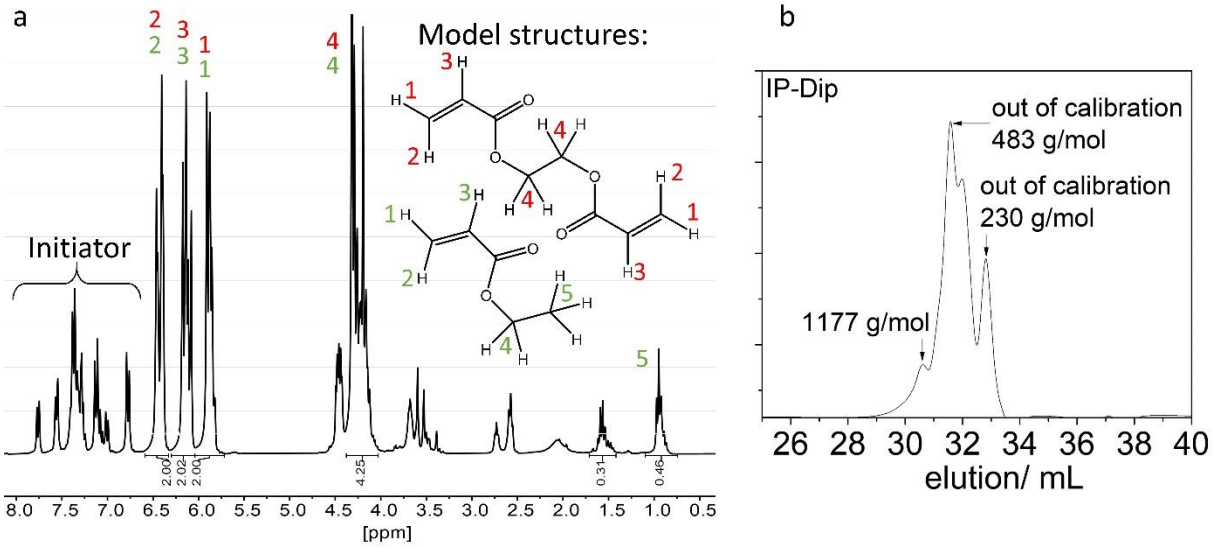

Figure 5.7 Characterization of the resin (IP-Dip); (a) NMR; (b) GPC elution curve.

^{1}H-NMR spectroscopy revealed that the resin is composed mainly of multifunctional acrylates for crosslinking (signals between 4ppm and 6.5 ppm) and that the photoinitiator (signals between 8 ppm and 6.75 ppm) is present in high concentration. This was further confirmed by our GPC analysis which shows only oligomeric macromolecules with a maximum molecular weight of ~1200 g/mol. This lets us conclude that TPP printing should lead to a high crosslinking density and little chain-growth towards higher molecular weight polymers. Due to the short dwell time, the resulting short diffusion distance and the high concentration of initiator molecules (see Figure 5.7 a), we thus expect, that the NPs should be trapped in the resin by the crosslinking before they can agglomerate to exerted attractive forces induced by the printing process.

To prove these assumptions, we assess the distribution of the NPs in 3D printed pyramids (10 µmx10 µmx5 µm) (see Figure 5.8). After printing and development, we used a focused ion beam (FIB) to prepare a thin lamella (~ 100 nm) of the 3D printed pyramids embedded in a Pd matrix. We have consecutively analyzed these lamellae using TEM. In all cases, the NPs (Au, Ag and CdSe/CdZnS) are well separated and stochastically distributed inside the cured resin (see Figure 5.9; Figure 5.10 for EDX).

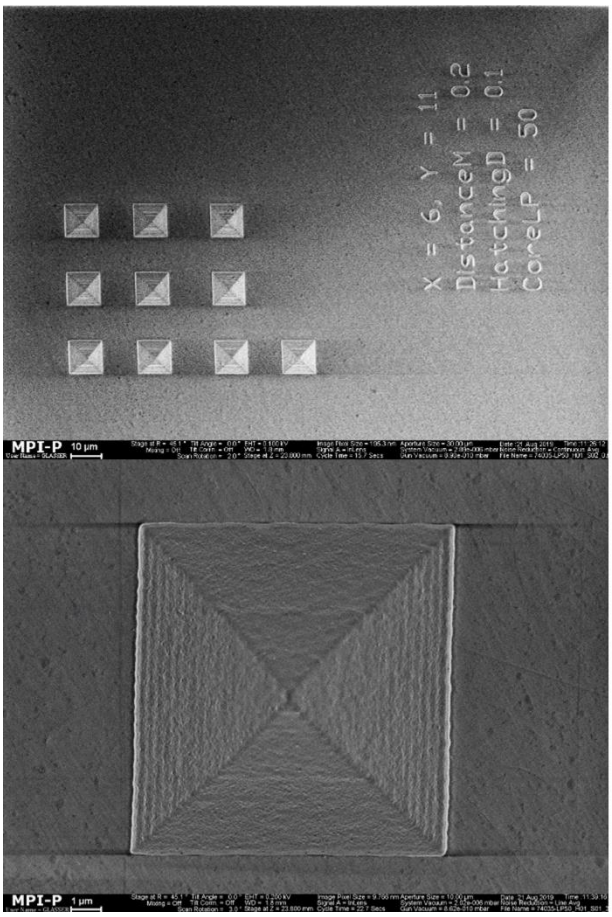

Figure 5.8: 3D printed pyramids loaded with nanoparticles. (here: CdSe NPLs 0.026 v/v%).

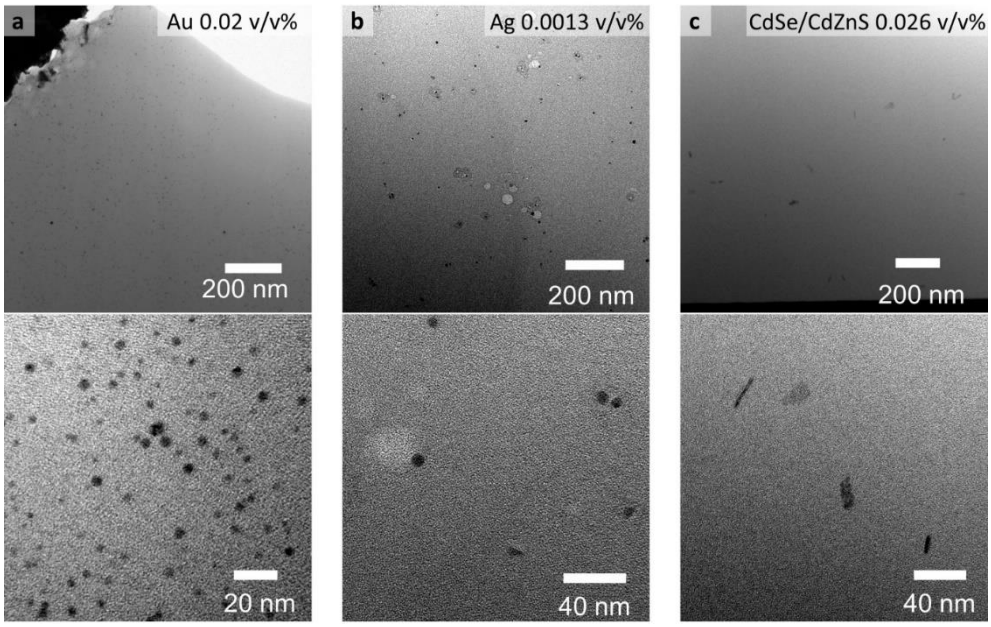

Figure 5.9: TEM micrographs of TEM lamella of 3D printed pyramids loaded with nanoparticles. (a) Pyramid loaded with Au NP; (b) Pyramid loaded with Ag NPs; (c) Pyramid loaded with CdSe NPLs; the nanoparticles are in all cases well-distributed and no aggregation is visible.

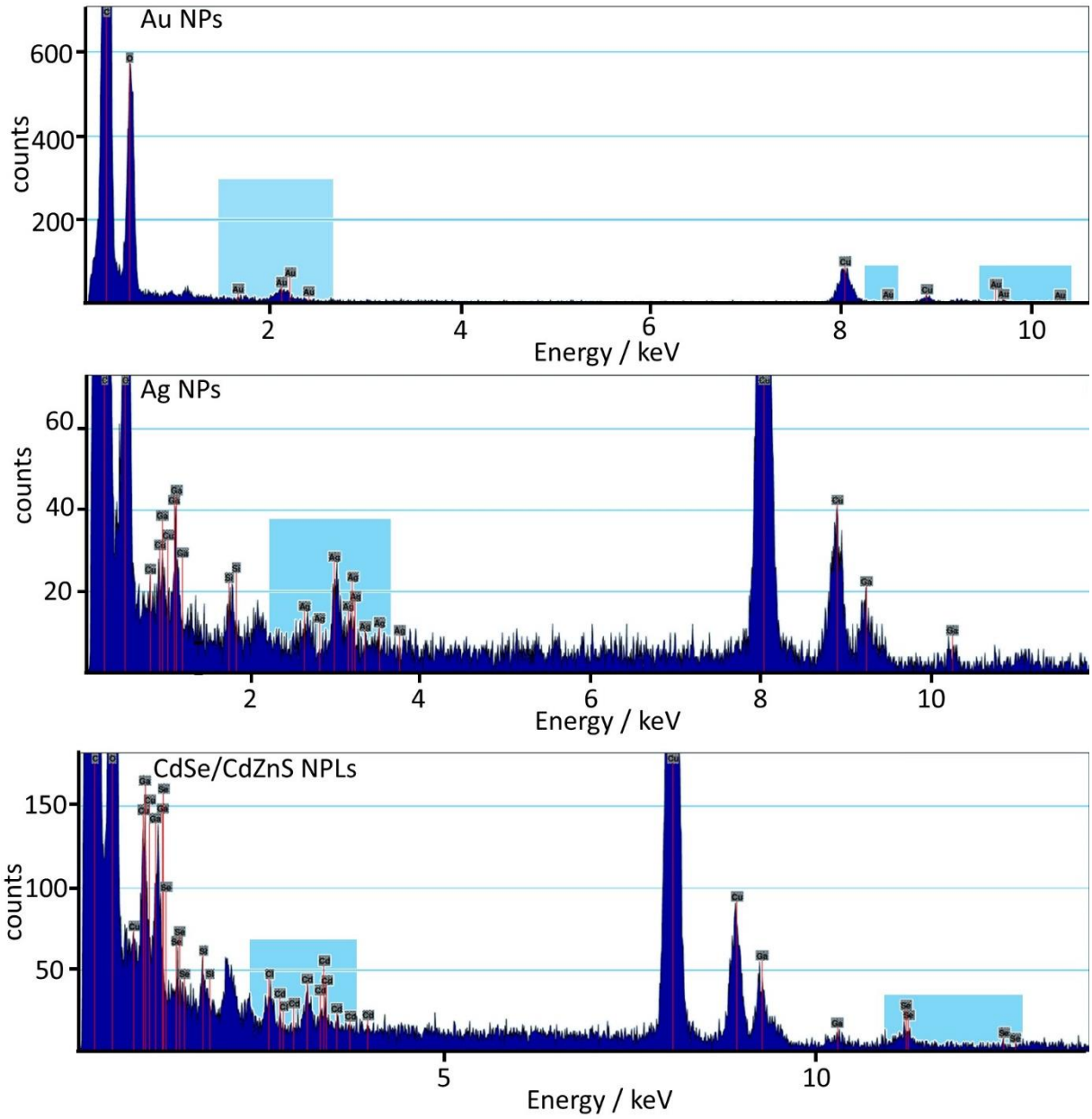

Figure 5.10: EDX spectra of TEM lamella indicating the presence of NPs. Blue boxes indicating the signals corresponding to the metal.

Since we know the thickness of our lamella and the visible area in our TEM micrographs we could estimate the observable volume. Thus, by determining the number of NPs per TEM image we can estimate the volume concentration of the NPs integrated into the TPP 3D-printed resin by using the ratio of the particle volume and the total volume of the resin (5.VI).

$$c_{vol} = \frac{V_{particle}}{V_{resin}} = \frac{N_{particle} \cdot V_{single\text{-}particle}}{100\ \text{nm} \cdot image\ size^2} \tag{5.VI}$$

$V_{particle}$ is the volume of all particles located in one TEM image, $N_{particle}$ is the number of particles in the TEM images, $V_{single\ particle}$ is the volume of one individual particle (sphere: Ag and Au; cuboid: CdSe), and V_{resin} is the total volume of the resin determined by the TEM image size and assuming a thickness of 100 nm.

Table 5.3: Nanoparticle volume concentration determined using the TEM images of the thin lamella.

nanoparticle	Au	Ag	CdSe
initial concentration /v/v%	0.020	0.013	0.026
estimated concentration /v/v%	0.023	0.014	0.024

For all NP/polymer composites, the NP concentration estimated by TEM is in good agreement with the initial concentration in the photoresin (see Table 5.3). Thus, we can conclude that the printing process with PMMA-SH modified NPs does not lead to agglomeration or phase separation, e.g. at the surface of the printed structures. After having confirmed the colloidal stability of NPs in the photoresin and their stochastic distribution in the 3D-printed structure we now discuss how the presence of the different types of NPs influence the printing process via absorption and radical quenching processes.

5.3.3 Effects of nanoparticles in stereolithographic two-photon polymerization 3D printing

In stereolithographic TPP 3D-printing, solidification of the photoresin is based on a radical polymerization and the crosslinking of e.g. acrylate-based monomers and oligomers[257]. Using a pulsed laser, the photoinitiator is activated via 2PA and radicals are formed allowing for radical polymerization and crosslinking. If the LP exceeds a specific threshold, the generated radical concentration, is high enough, and the resin is polymerized. If the energy within the volume where the polymerization occurs, the so-called voxel (volume pixel), is too high, thermal degradation occurs. If the energy input in the voxel is too low, the polymerization does not start or is terminated prematurely. By the integration of the NPs, the energy density can be affected in various ways. NPs can absorb the laser excitation either directly via 1PA (Au NPs) or via 2PA (Au and Ag NPs, and CdSe/CdZnS NPLs). Upon excitation, plasmonic NPs dissipate the absorbed energy in the form of heat, CdSe/CdZnS NPLs predominantly by the emission of photons. While both processes decrease the available photon flux in the voxel for the activation of the initiator, the influence on the TPP 3D printing process is expected to be distinctly different. Heat dissipation can cause additional thermal degradation pathways of the organic materials in the proximity of plasmonic NPs, while energy dissipation via fluorescence

from semiconductor NPs such as CdSe/CdZnS should not hamper the integrity of the polymeric matrix material. Additionally, the large surface-to-volume ratio of NPs can lead to direct radical quenching when the radical bearing (macro-) molecules are in close proximity to the NPs' surfaces. To investigate these effect on the stereolithographic TPP 3D printing process, we printed and compared woodpile structures (10 x 10 µm; 1 µm spacing, 10 layers) with and without NPs using a commercial TPP 3D printer (Photonic Professional GT2 photonic, Nanoscribe) at various laser powers and z-offsets (see Figure 5.11 and Figure 5.12).

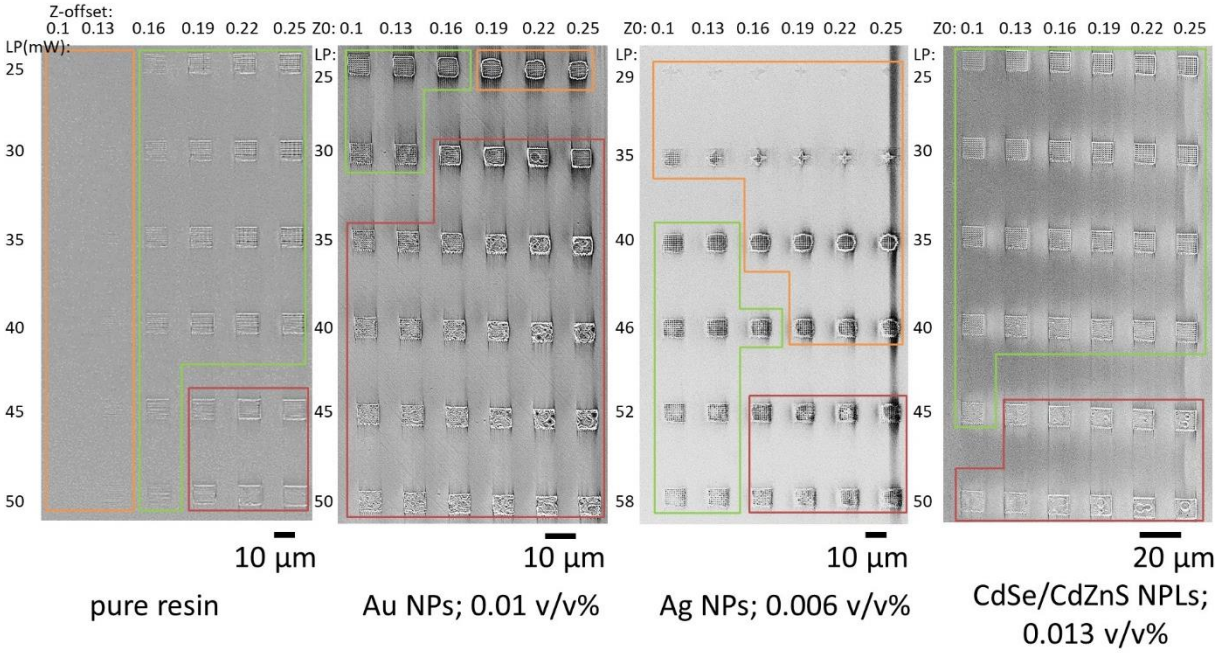

Figure 5.11: 3D printed woodpile structures in the absence and presence of different nanomaterials. Left to right: pure resin; Au NP; Ag NP, CdSe/CdZnS NPL. The integration of the NPs leads to a significant change in the printing window (green); orange box: insufficient to no polymerization, red box: burned material.

The z-offset determines the shift of the focal point along the surface normal. Within the tested parameter space, three areas can be identified: (i) the material is not or not well polymerized, (ii) the material shows a good printing quality and (iii) thermal degradation of the material (see Figure 5.11). As expected, for the pure photoresin a large variety of parameters allow for printing with decent quality. Only at the highest laser powers a tendency to thermal degradation of the material is observable. For the smallest z-offsets, almost no 3D-printed structures are visible because most of the voxel is located inside the glass substrate[258]. In the presence of Au NPs, a pronounced thermal decomposition is observed even for relatively low LP (see Figure 5.12 a and d, Figure 5.11) Only small LPs and small z-offsets lead to a good printing result. In comparison to Au NP/photoresin composites, in the presence of Ag NPs much

higher laser powers are required to obtain a good printing result. Lower laser powers lead to incomplete polymerization and crosslinking (see Figure 5.12 b and e, Figure 5.11). In clear contrast to the plasmonic NPs, the integration of semiconductor CdSe/CdZnS NPLs does not change the useful printing parameter space significantly (see Figure 5.12 c and f, Figure 5.11). Hence, in summary, plasmonic NPs require high laser powers to obtain fully polymerized structures, however high laser powers could lead to thermal degradation. Thus, only a small amount of plasmonic NPs can be loaded into the photoresin. Otherwise, a good laser power where no thermal degradation but sufficient polymerization occurs can hardly be found. Since semiconductor NPs dissipate absorbed light via fluorescence, the thermal degradation is less problematic. This shows that the type of material embedded in the photoresin is important not only in terms of direct interaction with the excitation beam, which alters the voxel volume, but the secondary effects after excitation play a similarly crucial rule and must be considered.

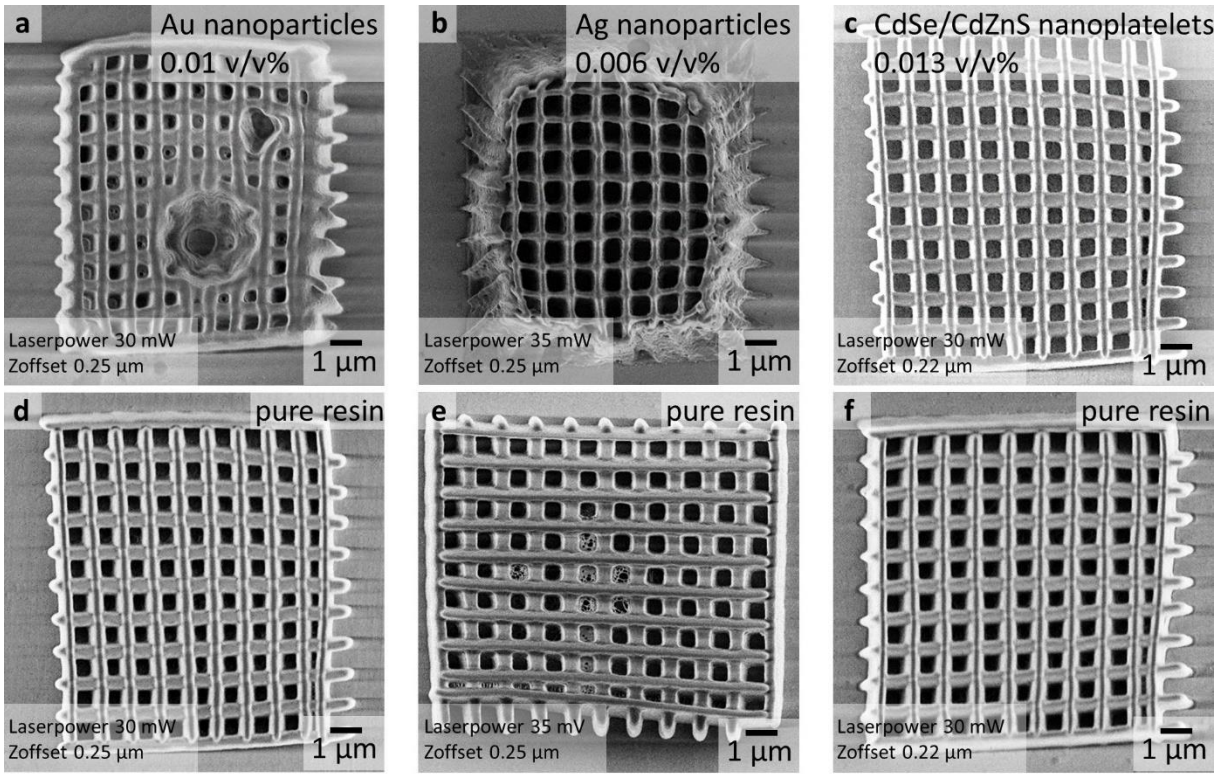

Figure 5.12 SEM micrographs of 3D printed woodpile structures with and without integrated NPs. (a) For woodpile structure loaded with Au NPs, a strong tendency for thermal degradation in comparison to the pure resin at the same printing parameters (d) is observable; (b) For woodpile structure loaded with Ag NPs, polymerization and crosslinking is insufficient in comparison to pure resin (e); (c) Woodpile structure loaded with CdSe/CdZnS NPLs print nearly indistinguishable compared to the pure resin (f).

To characterize the effect of NPs on the printing process more in detail, we analyze the linewidth of the woodpile structures (see Figure 5.13). In all cases, the presence of NP decreases

the linewidth significantly (28 % - 62%). Furthermore, for all NPs, increasing the NP concentration decreases the linewidth in a concentration-dependent manner (up to 62 % decrease). Notably, Ag NPs lead to the strongest effect. Here, even for relatively low volume fractions (0.007 v/v%), the decrease in linewidth of up to 62 % can be observed, whereas for the highest Au NPs (0.02 v/v%) and CdSe/CdZnS NPLs concentrations (0.026 v/v%), the maximum decrease is 41% and 28 %, respectively.

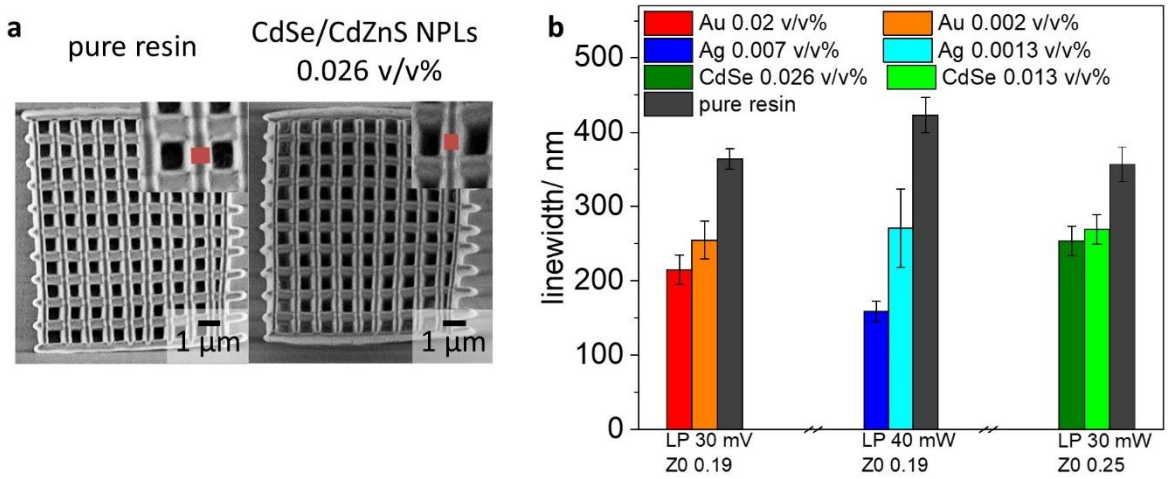

Figure 5.13: Decrease of linewidth in the presence of NPs. (a) SEM micrograph of woodpile structure in the absence and presence of CdSe/CdZnS NPLs (0.026 v/v%); (b) Measured linewidth .

5.3.4 Interference of nanoparticles with the stereolithographic two-photon polymerization 3D printing process

Depending on the NP material, we observed different onsets of effects on the printing. The main observations are (i) earlier thermal degradation of the resin in the presence of Au NPs, (ii) higher laser power required for the polymerization of the resin in the presence of Ag NPs in comparison to all other NP-loaded photoresins and (iii) a general concentration-dependent tendency of decreasing of the minimum linewidth in the presence of all studied NP. The NPs can cause mainly three different processes which are affecting the 3D printing process (see Scheme 5.1).

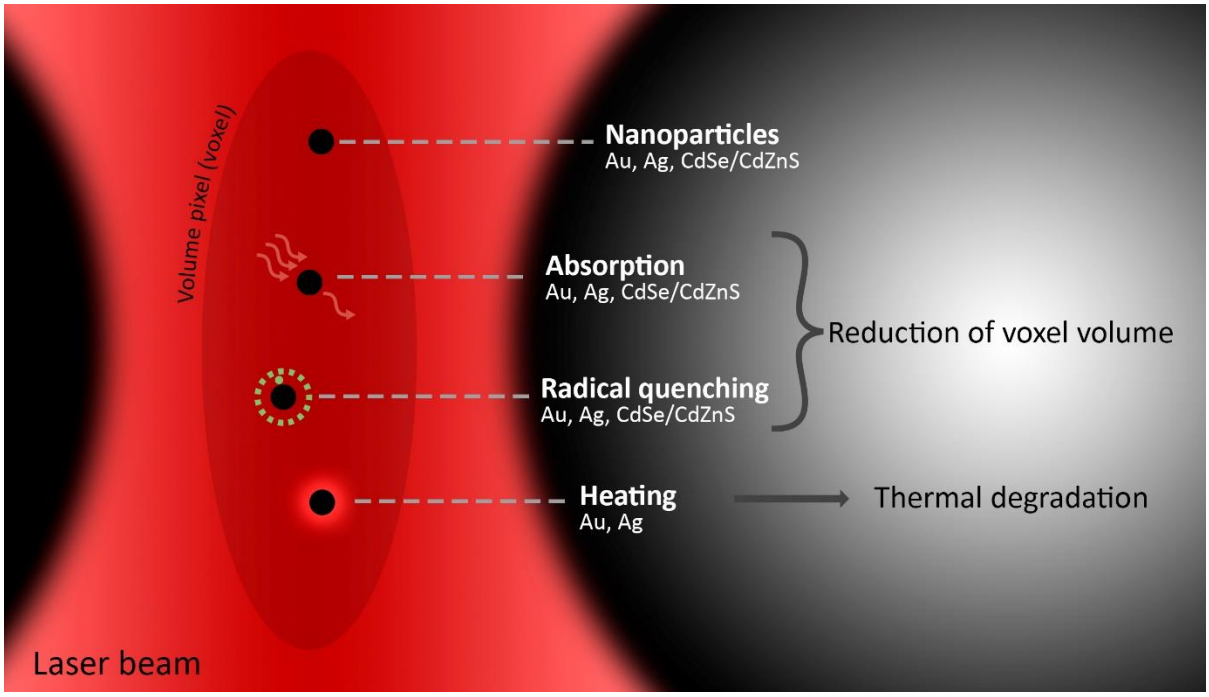

Scheme 5.1: Interference pathways of NPs with the TPP 3D printing process. NPs can absorb the laser light either via 1PA or 2PA, quench radicals created by the photoinitiator, and dissipation of absorbed energy in the form of heat. Both, absorption of laser light and quenching of radicals leads to a reduction of the voxel volume, while heating leads to thermal decomposition of the material.

The NPs can absorb light, either by 2PA (mainly in or near the focal volume where the photon flux is sufficiently high, this happens for plasmonic NPs[235, 236] and CdSe/CdZnS NPLs[93]) or 1PA if there is a direct spectral overlap of the NP absorption profile with the laser line (in the whole pathway of the laser beam). In our case, only Au NPs can undergo 1PA (see Figure 5.1 for absorption spectra, red dashed line indicates the laser wavelength). For both types of absorption pathways, the absorption of light reduces the photon flux in the focal volume and therefore few radicals are generated. Thus, the voxel volume is shrinking with increasing NP concentrations because the photon flux is not high enough to generate sufficient concentrations of radicals over a larger volume for radical polymerization. This directly leads to a reduction of the minimum printable linewidth while at the same time higher laser powers are required to generate enough radicals. Moreover, the absorption of light can induce heating of the Au and Ag NPs[259]. This explains the strong thermal decomposition of the resin in the presence of Au NPs since they absorb the laser light predominantly via direct 1PA. For Ag NP the thermal decomposition effect is less prominent because fewer photons are absorbed since 2PA is a non-linear effect that requires a high density of coherent photons (as found in the focal point, but not further away from the focus). Similarly, semiconductor CdSe/CdZnS NPL-loaded photoresin lead to a reduction in the voxel volume due to 2PA in the focal spot. However, the

energy is dissipated as fluorescence and thermal decomposition is mitigated. While these findings can explain our observation regarding the concentration-dependent reduction of minimal printable feature size and the tendency for thermal decomposition for some NPs, other material specific effects play a similarly important role.

Besides the absorption of light, also direct interaction of the NPs with the radicals in their proximity is possible[237-239]. Indeed, radicals can be quenched simply by the presence of NPs. Thus, this effect can also reduce the voxel volume. This could be material specific in our case since for the three different NPs we observe different extents of printing linewidth reduction. We observe the strongest effect for Ag NPs and the weakest effect for CdSe/CdZnS NPLs. To analyze the quenching effect decoupled from the 1PA or 2PA absorption effect described above, we assessed the degree of conversion of double bonds in the NP-loaded photoresins relative to the pure resin under direct UV-light curing by FTIR (see Figure 5.14).

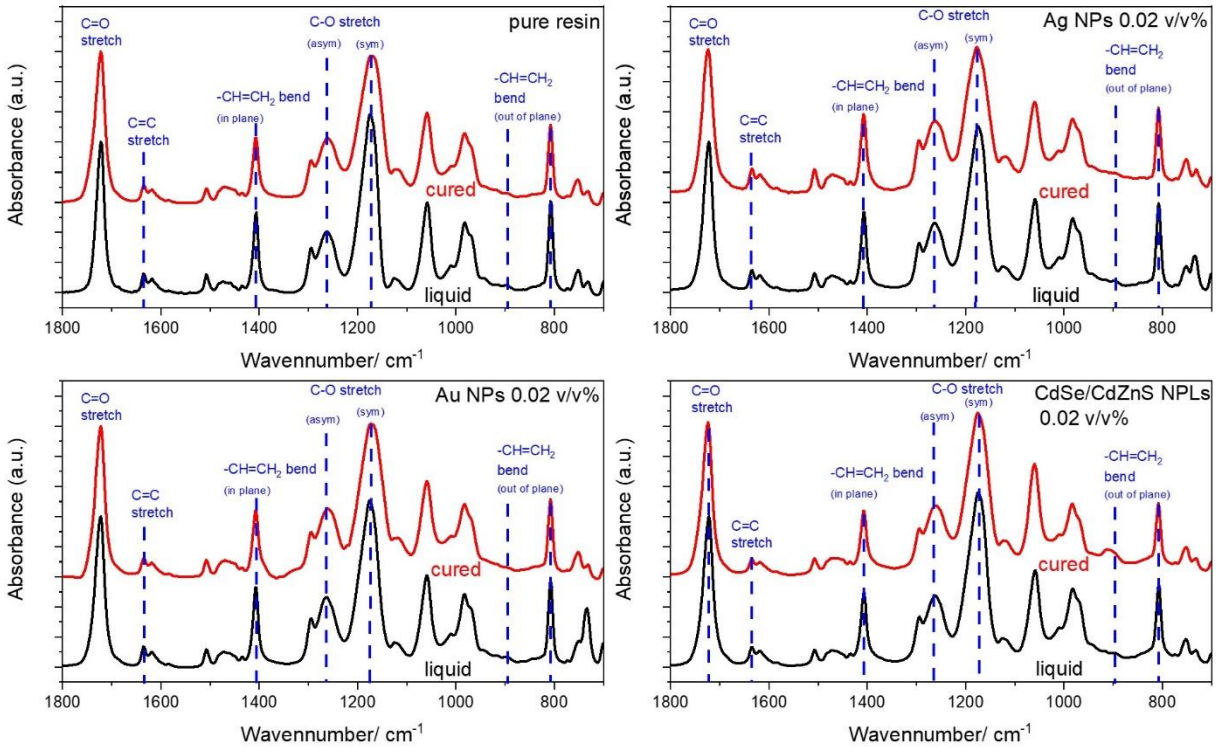

Figure 5.14: FTIR spectra of the liquid resin and cured resin in the presence and absence of NPs.

Here, the absorption of NPs does not hamper the photopolymerization because the photoinitiators (and the NPs present) are excited homogenously throughout the sample directly via 1PA at high intensities. Thus, even in the presence of NPs there is always sufficiently high UV-light to excite the photoinitiator. Vibrational bands associated with CH_2=CH, C=O, and C-

O group[260], could be assigned in all spectra. All spectra were normalized to the C=O peak (stemming from the carbonyl groups in the acrylate resin), since this signal remains constant during the polymerization reaction. The intensity of the bands assigned to the double bond decreases upon reaction (see Figure 5.15 a). The degree of relative conversion was calculated by comparing the –CH=CH_2 bending mode band to the C=O band before (A) and after UV curing (A') for the NP-loaded photoresins compared to the pure resin using equation ((5.VIII)[260] (see Figure 5.15 a and b):

$$DC = \left(1 - \frac{A'_{C=C}/A'_{C=O}}{A_{C=C}/A_{C=O}}\right) \cdot 100\% \qquad (5.VII)$$

$$relative\ DC = \frac{DC}{DC_{pure\ resin}} 100\% \qquad (5.VIII)$$

The relative degree of conversion is the highest for the resin loaded with CdSe/CdZnS NPLs (57 %), followed by Au NP (11 %) and Ag NP-loaded resins (6 %). This finding is well in line with our observed trends of linewidth reduction as a function of NP material. Our experiment shows that Ag NPs have the strongest direct radical quenching effect, followed by Au NPs and CdSe/CdZnS NPLs.

a

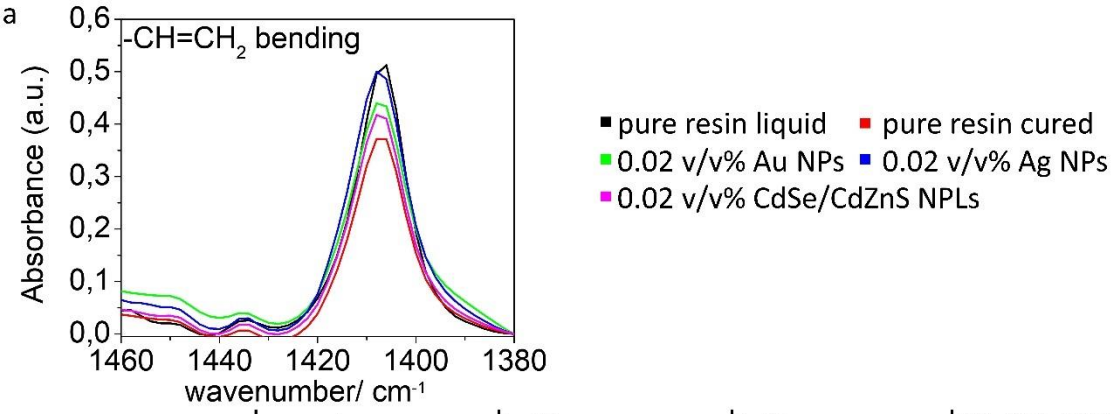

b

	pure resin: Integrated intensity		Au NPs: Integrated intensity		Ag NPs: Integrated intensity		CdSe/CdZnS NPLs: Integrated intensity	
Group and Mode	UV-cured	resin	UV-cured	resin	UV-cured	resin	UV-cured	resin
1406 cm^{-1} -CH=CH_2 bend	5.64	6.83	6.23	6.72	7.01	6.72	5.09	6.13
1722 cm^{-1} C=O stretch	26.94	22.11	26.23	25.22	26.30	24.76	26.62	26.17
relative DC	100.00		33.75		5.70		56.90	

Figure 5.15: FTIR spectra of the resin and cured resin with and without particles. The degree of conversion is determined by comparing the integrated peak intensities, of the C=O stretching and the C=C bending mode.

In addition to the different absorption behavior and the quenching properties, the difference in the interparticle distance at a given volume fraction of NPs in the resin must also be taken into account. Since the size of the used NPs are different, the interparticle distance varied for the same volume concentration (see Figure 5.6). For the same volume concentration (0.013 v/v%), the interparticle distance of CdSe/CdZnS NPLs (436 nm) is much larger compared to Au NPs or Ag NPs (53 nm and 56 nm) (see Figure 5.6). Hence, the number of NPs in the voxel volume of CdSe/CdZnS NPLs is around hundred times smaller than for Au NPs and Ag NPs (see Table 5.4) and the observed effects are expected to be less prominent.

Table 5.4: Calculated number of particles in the voxel volume.

	Min.	Max.
Laser power/ mW	25	40
Axial length/ µm	1.46	1.60
Cross-sectional diameter/ µm	0.352	0.358
Voxel volume/ µm³	0.2411	0.273
Number of Au NPs (0.02 v/v%)	2332	2653
Number of Ag NPs (0.02 v/v%)	1966	2236
Number of CdSeNPs (0.02 v/v%)	15	18

5.3.5 Towards application: Photonic gratings with fluorescent CdSe/CdZnS nanoplatelets for enhances fluorescence light out-coupling

After systematically studying the interference of NPs on the 3D printing process, the gained knowledge can be used to print new functional materials. To demonstrate the applicability of nanoparticles in the 3D printing process, fluorescent CdSe/CdZnS NPLs are embedded in polymeric photonic gratings for enhanced light outcoupling (e.g. for display applications) via TPP 3D printing. Usually, a significant proportion of the emitted light of fluorescent layers undergoes internal reflection and is trapped into wavemodes[261]. One technique to improve the light-outcoupling is the patterning of the formed films with circular or non-circular Bragg gratings[261, 262]. Instead of using multistep lithography based methods, 3D printing could be a simple and fast alternative. To show the potential of the integration of NPs in the 3D printing process, Bragg gratings were printed with a polymeric resin (IP-S) loaded with CdSe/CdZnS NPLs (0.05 v/v%) (see Figure 5.16 a). The angle θ of the out-coupling light with respect to the

surface normal for a given emission wavelength λ_{em} and a grating periodicity Λ (pitch distance) can be determined by using the Bragg condition (equation (5.IX))[262]:

$$k_o \sin\theta = \pm k_{wg} \pm m k_g = \pm \frac{\pi n_{eff}}{\lambda_{em}} \pm \mathrm{m} \frac{2\pi}{\Lambda} \tag{5.IX}$$

k_0 is the wavevector of the outcoupled light, k_{wg} is the wavevector of the waveguided light, k_g is the Bragg vector, n_{eff} is the effective refractive index of the waveguide mode, and m is the diffraction order. Waveguided light can be scattered in the out of plane direction (θ =0) for the following equation (5.X):

$$\lambda_{em} = \frac{\Lambda n_{eff}}{m} \tag{5.X}$$

The refractive index of the cured photoresin is 1.511 (at 643.8 nm)[263] and the emission wavelength of the CdSe/CdZnS NPLs is 620 nm. The pitch distance was varied between 500 nm and 1800 nm (see Figure 5.16 b, pitch distance is increasing from bottom to top). By using fluorescence microscopy with a 10x dry objective (NA 0.3), printed structures with the brightest fluorescence intensity were identified (see Figure 5.16 d). Gratings with a pitch distance of ~650 nm; ~1000 nm; ~1300 nm and ~1650 nm show the brightest fluorescence intensity. These pitch distances correspond to a diffraction order m of 2;3;4 and 5, assuming an apparent refractive index of ~1.9. The discrepancy between the apparent refractive index (~1.9) and the

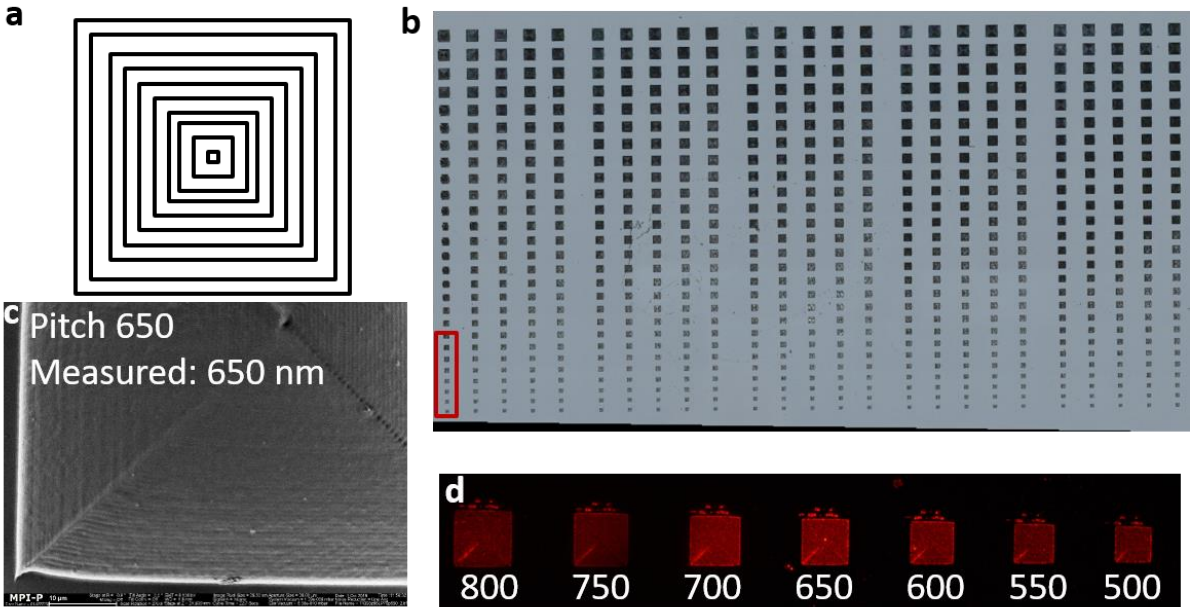

Figure 5.16: Printed grating of IP-S resin loaded with CdSe/CdZnS NPLs (0.05v/v%).

real refractive index of the material (~1.5) is not understood so far and needs to be studied. This could be related to the incorporation of NPs, however, measurements of the effective refractive index for the printed NP-polymer composites have to be recorded to test this hypothesis. Nevertheless, these preliminary results show that the combination of 3D printing and nanoparticles can offer a new platform to create functional materials.

To enhance the outcoupling efficiency further, the grating periodicity has to be printed with higher precision (see Figure 5.16 c) and effective refractive indices have to be taken into account. To print with higher accuracy a specialized resin should be used in the future which is optimized for the printing of photonic structures. For this, once more, the dispersibility of the CdSe/CdZnS NPLs has to be optimized. This should be feasible using the same approach as described in this chapter. Furthermore, the QY of NPLs and the volume fraction of the in cooperated CdSe/CdZnS NPLs should be maximized for the highest intensities of outcoupled light.

5.3.6 Conclusion

In conclusion, we studied the integration of plasmonic and semiconductor NPs in the stereolithographic 3D printing. In this work, we investigate systematically how NPs can be stabilized in the uncured photoresin and how this stability can be maintained throughout the printing process. For stabilizing the NPs in the resin, a PMMA-SH polymer was used as surfactant. Following this approach, all NPs studied could be dispersed without agglomeration in the uncured resin. Importantly, the colloidal stability was preserved throughout the printing process: the NPs do not agglomerate nor phase separate since the crosslinking is much faster than the diffusion rate of the NPs, and therefore, the NPs are trapped as isolated particles within the cured resin. Being certain that individual NPs and not agglomerates are printed in the NP/photoresin composites allowed us to study for the first time the influence of the NP materials properties on the TPP printing process in a concentration-dependent manner. For this, printed test structures were analyzed for their minimum feature size and three main conclusions could be drawn: (i) in the presence of Au NPs, strong thermal decomposition was observed due to their 1PA capability; (ii) in presence of Ag NPs, the heating effect was less pronounced since Ag NPs can only absorb laser light via 2PA, but at the same time Ag NPs exhibit the highest tendency for direct radical quenching; (iii) the decrease of the linewidth for CdSe/CdZnS NPLs is to a large extent due to 2PA, mitigating at the same time heating issues due to emissive dissipation of energy. The gained fundamental understanding of how to

integrate NPs in the resin and how NPs interfere the printing must be considered when creating NP-enriched, functional polymeric structures via TPP 3D printing.

6. Other collaborative projects

In the previous chapters, the focus was put on controlling the interaction between NPs in order to tune properties. In this chapter, the interaction between NPs plays a crucial role as well. Chapter 6 presents ongoing collaborative projects.

In chapter 6.1 CdSe/CdZnS nanoplatelets were used as fluorescent staining material for PDMS oil. Due to specific properties, PDMS oil is frequently used for micropillars or lubricant, however, the imaging quality is poor. To improve the imaging quality, CdSe/CdZnS NPLs should be dispersed in the oil due to the high photoluminescence and stability. To approach the dispersion of NPLs in the oil, the interaction forces have to be carefully adjusted to prevent agglomeration. Therefore, NPLs have to be functionalized with ligands compatible to the PDMS oil. Different NP functionalization methods were studied and characterized using microscopy techniques.

In chapter 6.2 CdSe/CdZnS NPLs are used as the emitter in an organic light-emitting diode. Organic light-emitting diodes suffer from the low long-term stability. To increase the lifetime, inorganic emitting materials can be applied. However, in this case of quantum dots electron trapping reduced the performance of the devices. Here, this approach to integrate semiconductor nanocrystals in an organic light-emitting diode is transferred to the NPLs[163] with the aim of preventing electron trapping. To do this, a polymer shell is used around the NPLs. Preliminary results of electroluminescence measurement show promising results concerning an effective avoidance of electron trapping.

Besides these two application-related chapters, chapter 6.3 is focusing on the interaction between NPLs and micrometer-sized polymer flakes in order to collectively orient NPLs at the surface of the polymer flakes and simultaneously control the distance between two NPL layers by the thickness of these flakes. As mentioned in chapter 4, it is of importance to collectively orient NPLs in order to get access to their anisotropic properties. The closer distances between two NPL layers could induce interesting coupling effects between the NPL layers, resulting in changed optical properties.

Henry Halim (MPIP) synthesized the CdSe/CdZnS NPLs used in chapter 6.1 and 6.2. My contributions were the modification of the PDMS-COOH polymer, the synthesis of the polymer for the polymer coating method (in chapter 6.1 and 6.2) as well as the modification of the NPLs in both chapters. In addition I performed the dispersion of the NPLs in the PDMS oil and studied

the agglomerate formation using fluorescence microscopy. The diblock copolymer used in chapter 6.2 was prepared by Dr. Benjamin Klöckler (University Mainz). The device preparation and electroluminescence spectroscopy are performed by Elham Khodabakhshi (MPIP). The polymers used in chapter 6.3 were synthesized by Tobias Haider (MPIP) and Dr. Hisaschi Tee (MPIP). The lifetime measurements were performed by Henry Halim (MPIP). My contributions were the preparation of the polymer flakes and the NPL-polymer composite. Furthermore, I characterized the composites using TEM und optical spectroscopy. In addition, I performed the quenching experiment with the ruthenium catalyst.

6.1 CdSe/CdZnS core-shell nanoplatelets as staining material for PDMS oil

Introduction

Polydimethylsiloxane (PDMS) is frequently used as material for micropillars or lubricant due to the biocompatibility[264], chemical stability[265], modifiable stiffness and viscosity, and ability to be reused. However, the disadvantage of PDMS is the poor microcopy imaging quality, since PDMS is translucent often a poor contrast between PDMS and other materials is obtained. To improve the imaging of PDMS, staining is required. Few organic dyes existing to stain PDMS, however, the solubility is low and aggregates are formed[266, 267]. Moreover, organic dyes tend to bleach over time when exposed to light which limits the experimental time. One way to overcome these problems is to use semiconductor nanomaterials since they are chemically stable, do not bleach and have high quantum yield[268]. CdSe NPLs are excellent candidates for imaging because of the narrow emission linewidth[79], the large one and two-photon absorption cross section[93] and the high fluorescence quantum yield[78].

The major challenge, using the NPLs for the staining of PDMS, is the dispersion of the NPLs. The PDMS polymer can act as depletion agent and can induces the aggregation of NPs[269-271]. Furthermore, due to the large flat sides of the NPLs, the tendency to agglomerate is high. To improve the dispersibility and reduce depletion attraction, the surface of the NPLs have to be covered with polymer chains which are miscible with the surrounding polymer solution.

Experimental Part

Chemicals. Hexane (95% n-hexane, analytical reagent grade, H/0355/21) and dichloromethane (DCM) (HPLC grade), tetrahydrofuran (THF) (analytical reagent grade, T/070/17) were purchased from Fisher Chemical. Chloroform stabilized with amylene (100%, 83627.290) and acetone (Reah. PhEu, 20066.321) were purchased from VWR Chemicals. Amine terminated Polystyrene (M_n=5000g/mol, PDI ≤ 1.2), poly(isobutylene-*alt*-maleic anhydride) (85%, average M_w ~ 6000, 12–200 mesh, 531278-250G), mono hydroxyl-terminated PDMS (Mn ~ 4670 g/mol), pyridine (puriss p.a.), hydrochloric acid (puriss p.a. ≥37%) were purchased from Sigma Aldrich. 1-dodecylamine (>97%, D0980) was purchased from TCI. 4-(Dimethylamino)-pyridine (DMAP) (for synthesis), methylacetate (for synthesis) and *N*,*N*′-dicyclohexylcarbodiimide (DCC) (for synthesis) were purchased from Merck

Millipore. Poly(dimethylsiloxane), monoaminopropylterminaded (PDMS-NH_2) (*Mw* = 6000 g/mol) abcr GmbH.

Synthesis of Core/Shell CdSe Nanoplatelets. See chapter 0 for the synthesis of the 4 ML CdSe NPLs and the synthesis of the $Cd_{0.33}Zn_{0.67}S$ shell.

Modification of CdSe/CdZnS NPLs *via* ligand exchange

Carboxyl terminated PDMS. Carboxyl terminated PDMS was synthesized according to a procedure describes by Scofield *et al*.[272]. Briefly, mono hydroxyl-terminated PDMS (9.34 g, 2 mmol) (Mn ~ 4670 g/mol) were mixed with DMAP (0.3 g, 3 mmol) and pyridine (0.24 mL, 3 mL) in dry DCM and heated to 40°C for 16 h. Afterward, the solution was precipitated in hexane. The precipitate was removed and the supernatant was washed three times with 100 mL HCL (0.25 M) and 100 mL MilliQ water. The organic phase was dried with sodium sulfate and the solvent was removed using a rotary evaporator.

Ligand exchange and dispersion in PDMS. CdSe/CdZnS NPLs (20 µL, stock solution dissolved 1:9 or 1:18) in hexane or chloroform were mixed with an excess of carboxyl terminated PDMS (20µL, *c*= 42.55 mM) dissolved in hexane or chloroform. The modified NPLs were used for dispersion in PDMS without further purification. The PDMS (500 cSt) was dissolved in hexane (PDMS: hexane 1:1 v/v) to lower the viscosity. The PDMS solution (400 µL) was added to the modified NPL dispersion. Afterward, the hexane was evaporated either by keeping the vial open overnight, using the rotary evaporator or freeze-drying.

Modification of CdSe/CdZnS NPLs *via* polymer coating

Synthesis of dodecyl/polystyrene/PDMS-grafted-poly(isobutylene-*alt*-maleic acid). The amphiphilic polymer was synthesized according to the method described by Parak *et al*.[244]. 105.3 mg (0.662 mmol monomer units/1.10 × 10^{-5} mmol polymer) of poly(isobutylene-*alt*-maleic anhydride), and various amounts of amino terminated PS, amino terminated PDMS and 1-dodecylamine (see Table 6.1) were mixed in THF (25 mL). The reaction mixture was stirred under reflux (80 °C) overnight. The THF was removed using a rotatory evaporator. 13.24 mL of chloroform was then added to prepare a polymer solution of 0.05 M (based on monomer concentration).

Table 6.1: Used amounts of polymer/ dodecylamine to synthesize the amphiphilic copolymer.

	Dodecylamine	**PS-NH_2**	**PDMS-NH_2**
Polymer 1	92 mg (0.497 mol, eq. to 75% of monomer units)	66 mg (0.013 mol, eg. to 2% of monomer units)	
Polymer 2	92 mg (0.497 mol, eq. to 75% of monomer units)	660 mg (0.13 mol, eq. to 20% of monomer units)	
Polymer 3	92 mg (0.497 mol, eq. to 75% of monomer units)		749 mg (0.13 mol, eq. to 20% of monomer units)
Polymer 4	60 mg (0.326 mol, eq. to 50% of monomer units)		1.746 g (0.294 mol, eq. to 45% of monomer units
Polymer 5	92 mg (0.497 mol, eq. to 75% of monomer units)		

Grafting of PDMS to dodecyl-grafted- poly(isobutylene-*alt*-maleic acid). Polymer 5 was further modified with aminopropyl terminated PDMS. Therefor 105 mg of polymer 5 ($1.765 \cdot 10^{-5}$ mol, ~ 38 monomer units) was mixed with PDMS-NH_2 (4,0242 g, eq. to 100% of monomer units), DMAP (0.0818 g) and DCC (0.166 g) in chloroform and stirred overnight at room temperature. The precipitate was filtrated, washed with MilliQ water and dried (Polymer 5-mod). 13.24 mL of chloroform was then added to prepare a polymer solution of 0.05 M (based on monomer concentration).

Polymer coating of CdSe/CdZnS NPLs. For the polymer coating, CdSe/CdZnS NPLs dispersed in chloroform (1 mL) were mixed with the copolymer dissolved in chloroform (205 µL, 0.05M (based on monomer concentration). After mixing, the solvent was removed using the rotary evaporator. The precipitate was redispersed in chloroform and the solvent was evaporated again. This cycle was repeated two times. The coated NPLs were redispersed in chloroform, precipitated with acetone and centrifuged at 6500 rpm (4393 rcf). The precipitate was redispersed in chloroform (1mL).

Dispersion of modified CdSe/CdZnS NPLs in PDMS. PDMS (~ 500 µL, 50 cSt) dissolved in chloroform was mixed with few drops of the coated NPL dispersion. After mixing, the chloroform was removed used the rotary evaporator.

Characterization. For optical spectroscopy, NPL dispersions were transferred to a quartz glass cuvette (10 mm). PL spectra were recorded using a Prizmatix Silver high power LED

(emission peak 369 nm) for excitation and Avantes SensLine AvaSpec-HSC-TEC for data collection.

TEM was done using a JEOL1400 microscope (acceleration voltage 120 kV). The samples were deposited on carbon-coated copper grids (400 mesh) by drop-casting.

For the fluorescence microscopy, a STED Leica Laser Scanning Confocal Microscope consisting of an inverse fluorescence microscope DMI 6000 CS equipped with multi-laser-combination was used. The objective was a 63x1.2 water objective and the laser (458 nm) was set to 20% (~ 1 mW).

^{1}H NMR spectra were recorded by were recorded on a Bruker Avance 300 MHz spectrometer with predefined pulse programs. The samples were dispersed in deuterated chloroform.

Results and discussion

Here, two different methods were investigated to modify the NPLs surface to allow the dispersion of NPLs in a PDMS oil (50 cSt) in order to improve the staining quality (see Scheme 1). CdSe/CdZnS core-shell NPLs were used as nanomaterial (further referred to as NPLs).

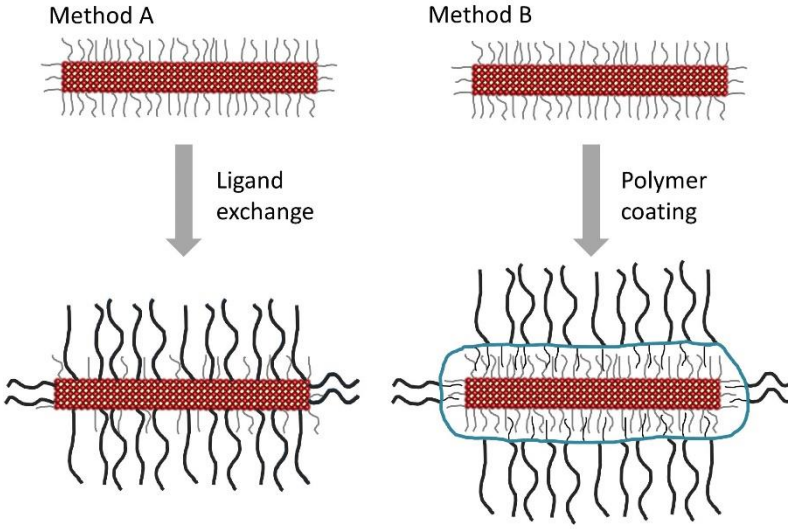

Scheme 6.1: Surface modification of nanoplatelets. Method A (left) is based on a ligand exchange; method B (right) is based on a polymer coating.

Method A is based on a ligand exchange of initial oleic acid molecules to carboxylic acid terminated PDMS as the ligand. Method B is based on a polymer coating strategy already applied for isotropic NPs[244, 273] and recently applied also for anisotropic NPLs[247].

For method A, a commercially available aminopropyl monoterminated PDMS (M_n=4670 g/mol) was functionalized with a carboxylic end group (Figure 6.1 a). The carboxylic end group can be attached to the Cd terminated NPL surface and replaces the oleic acid molecules.

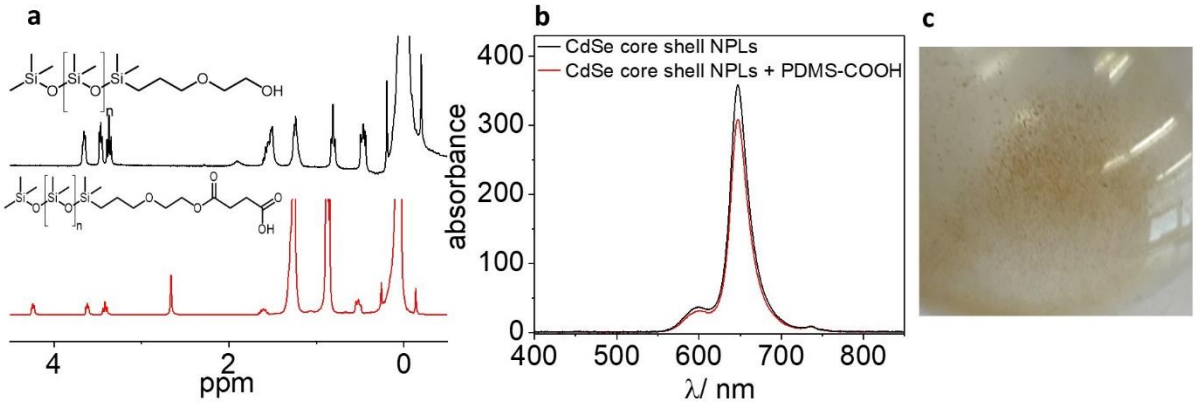

Figure 6.1: CdSe/CdZnS core-shell NPLs stabilized with PDMS-COOH to enable dispersibility in PDMS. (a) ^{1}H NMR spectra of PDMS with carboxylic end-group termination; (b) PL spectra of NPLs with and without PDMS ligand; (c) CdSe/CdZnS NPLs in PDMS, aggregates are visible.

In order to functionalize the NPLs with the modified polymer, the polymer and the NPLs were simply mixed. The addition of the polymer and replacement of the oleic acid molecules does not quench the PL of the NPLs (Figure 6.1 b). The dispersion of NPLs in various concentration in PDMS leads to direct or delayed aggregation of the NPLs after one day (see Figure 6.1 c). Most probably the density of the polymer on the NPL surface is not high enough and attractive depletion forces induce aggregation. To further increase the polymer chain density, method B was applied. Instead of grafting the polymer chains directly to the NPLs surface, a block-co-polymer was used, which covers the NPLs and protects additionally the surface. Therefore, poly(isobutylene-*alt*-maleic anhydride) was functionalized with PS-NH_2/ PDMS-NH_2 and dodecyl amine side chains with different percentages respecting to the monomer units (see Scheme 6.2). The percentage of monomer units functionalized with dodecyl amine or PS-NH_2/ PDMS-NH_2 is given in Table 6.2. Dodecyl amine interacts with the initial ligand shell of the NPLs and the PS/ PDMS chains facing to the outside and interact with the environment[244, 273]. The surface of the NPLs is better protected and the grafting density is easily adjustable, by the functionalization reaction.

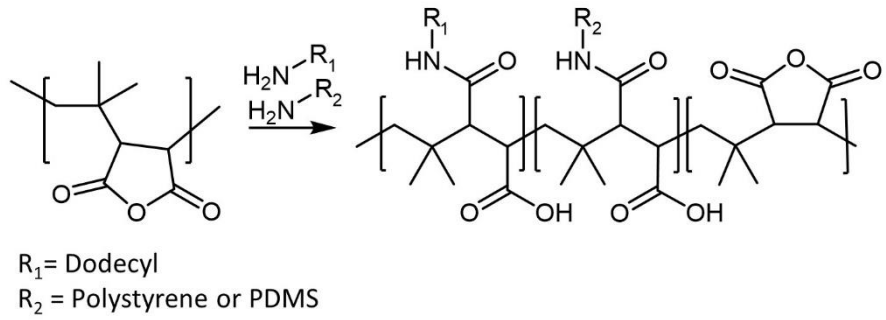

Scheme 6.2: Modification of polymer for polymer coating (method B).

Table 6.2: Functionalization of polymer for the polymer coating.

	R_2	**% R_1/R_2**	**Post-treatment with R-NH_2 (DCC/DMAP linkage)**
Sample 1	PS	75/2	/
Sample 2	PS	75/20	/
Sample 3	PDMS	70/20	/
Sample 4	PDMS	50/50	/
Sample 5	PDMS	75/0	1 PDMS per unit

After polymer coating, the NPLs are still dispersible in chloroform and no visible aggregates were observed. Also, in the TEM, the NPLs appear better distributed and non-aggregated (see Figure 6.2 a). By mixing some drops of the coated NPLs dispersion with PDMS (50 cSt) a slightly better dispersibility is observed by eye (see Figure 6.2 b). Non coated NPLs flocculate directly after mixing, whereas coated NPLs (sample 2) only slightly increases the turbidity of the dispersion.

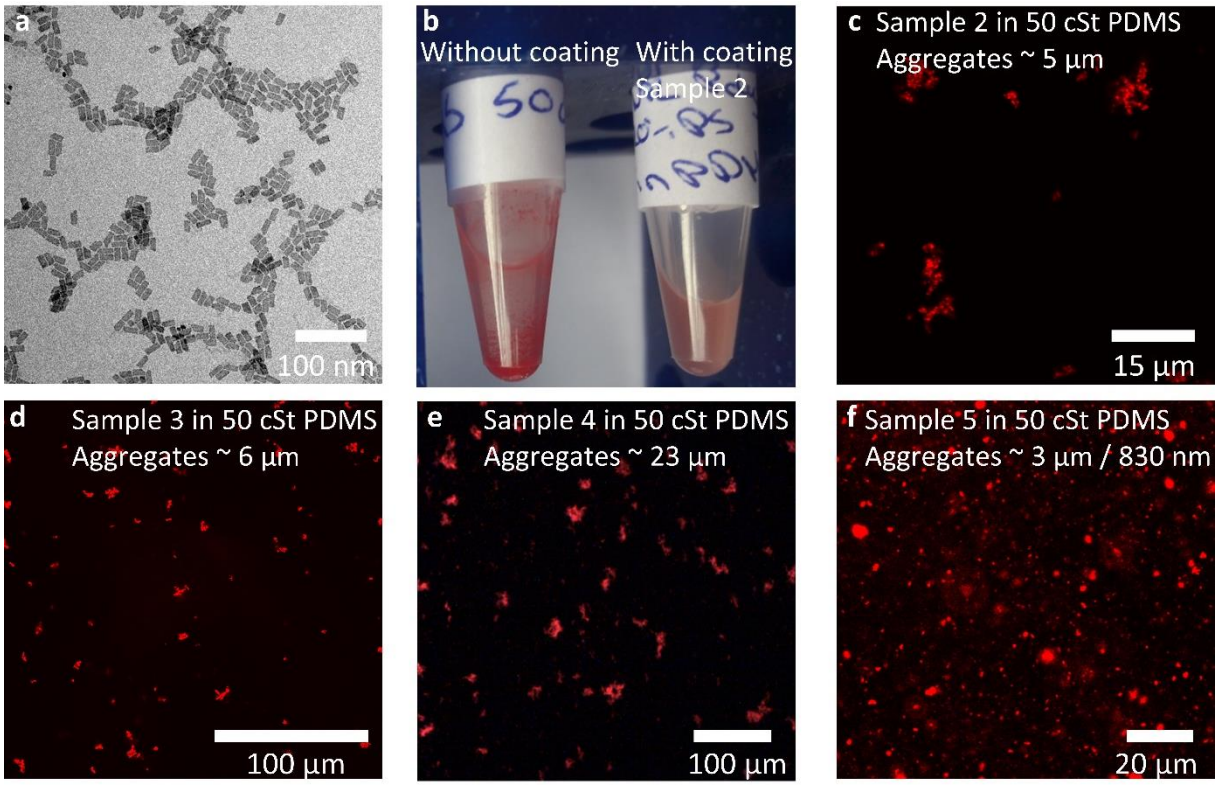

Figure 6.2: Dispersion of CdSe/CdZnS NPL coated with polymer in PDMS. (a) TEM micrograph of modified CdSe/CdZnS NPLs; no aggregates are visible; (b) photograph of unmodified (left) and modified (right) CdSe/CdZnS NPLs in PDMS. Both times the NPLs are aggregated, however, the aggregation of the modified NPLs is not as strong; (c-f) Fluorescence microscopy image of CdSe/CdZnS NPLs dispersed in PDMS.

However, while checking the dispersion using fluorescence microscopy, aggregates in the size of few micrometers were found (Figure 6.2 b-e). Also, changing the side chain from PS to PDMS, or changing the grafting density does not increase the dispersibility significantly. To increase the density of PDMS on the surface of the NPLS, the modified polymer (sample 5) was further functionalized with PDMS using a DCC/DMAP coupling reaction. Therefore, it is possible to link to each monomer unit one PDMS polymer chain. This high density of polymer chains leads to better dispersibility. The aggregate size reduces to ~ 3 µm and a second species of ~ 830 nm is found.

In conclusion, the NPL surface was modified either via ligand exchange or polymer coating. Method A leads to the complete aggregation of the NPLs in PDMS, whereas method B shows smaller aggregates. Especially, the high density of PDMS chains by the DCC/DMPA coupling leads to an improvement of the dispersibility. However, fully dispersed NPLs in PDMS are not achieved so far. Maybe the grafting density is still too low, the thickness of the ligand shell is to thin or the procedure to disperse the NPLs in PDMS is not ideal. For example, the dilution of the PDMS and/or the NPLs dispersion could lead to a better dispersibility as applied in chapter 5. Once a good dispersibility is achieved, PDMS can be stained with NPLs to improve the imaging quality in microscopy studies using PDMS as on oil for lubrication or as material for soft structures like micropillars. This opens the opportunity to study surface interaction in more detail. Furthermore, the quantum yield of the NPLs has to be improved, to allow a low content of NPLs needed for microscopy to exclude any possible change in properties of the PDMS (e.g. flow properties like viscosity) caused by the dispersion of NPLs.

6.2 Nanoplatelets in light-emitting diodes: Suppression of electron trapping of nanoplatelets using a polymer coating strategy

Introduction

Organic light-emitting diodes[274] are applied in displays and are promising candidates for large-area lighting panels[275]. The major drawback of the organic light-emitting diodes is the low long-term stability and the broad emission spectrum. By blending a blue-emitting organic semiconductor and a green or red-emitting dye, the emission spectra can be narrowed[276]. Due to the small bandgap of the blended dye, charge trapping occurs and the efficiency is strongly reduced[277]. One idea to improve the performance of LEDs is to combine organic semiconductor with inorganic quantum dots, because they are stable, have tunable emission and high quantum yield[268]. The working principle is the same as for the dye-based LED. The energy of the excited blue-emitting organic semiconductor is transferred *via* FRET to an red-emitting inorganic quantum dots. However, the bandgap of quantum dots is lower than the bandgap of the blue-emitting organic semiconductor and therefore electron trapping can occur also here. Furthermore, the blend morphology and the homogenous distribution of the quantum dots determines the device performance[278].

One recently published strategy describes the reduction of electron transfer using an insulation polymer shell around the quantum dots[163]. They used a PS-shell to protect the quantum dots from electron transfer and trapping and still allows FRET. To achieve this, the insulating shell has to be thicker than the hopping distance for charge carriers (1.5 -2 nm)[279] and thinner than the Förster radius (5-8 nm)[280]. In addition to the suppression of electron transfer, the polymer shell helps to distribute the quantum dots homogenously in the host material (poly(dioctylfluorene) (PFO)).

Experimental Part

Chemicals. Chlorobenzene (99.9 %) was purchased from Acros Chemical. Absolute ethanol (20821.330) was purchased from VWR Chemicals. Methylacetate (for synthesis) was purchased from Merck Millipore.

Synthesis of poly(styrene-*block*-cysteamine methyl disulfide) (P(S-*b*-SSMe)). The synthesis of (P(S-b-SSMe) was performed by Benjamin Klöckler according to a procedure described by Khodabakhshi *et al.*[163].

Synthesis of Core/Shell CdSe Nanoplatelets. See chapter 0 for the synthesis of the 4 ML CdSe NPLs and the synthesis of the $Cd_{0.33}Zn_{0.67}S$ shell.

NPLs/polymer hybridization. The NPLs were surface-functionalized with polymer chains by the procedure describes elsewere[163] The NPLs (400 µL, c = 9.05 mg/mL) were precipitated in methylacetate and redispersed in chlorobenzene (150 µL). 3.5 mg P(S-*b*-SSMe) were added to the dispersion and was sonicated for one hour. Ethanol (1.5 mL) was added to precipitate the NPLs. The precipitate was redispersed in chlorobenzene (1.5 µL), sonicated for one additional hour and precipitated again with ethanol. The precipitate was redispersed again in chlorobenzene, sonicated for one hour and precipitated with hexane. Finally, the precipitate was redispersed in (400 µL) chlorobenzene.

Synthesis of dodecyl/polystyrene-grafted-poly(isobutylene-*alt*-maleic acid). See chapter 6.1 for the synthesis of the copolymer. Polymer 2 (see Table 6.1) were used for the following polymer coating.

Polymer coating of CdSe/CdZnS NPLs. See chapter 6.1 for the polymer coating process. After polymer coating, the coated NPLs were dispersed in chlorobenzene.

Mixing of Modified NPLs in PFO matrix and device fabrication. The mixing and device fabrication is performed by Elham Khodabakhshi according to a procedure described by Khodabakhshi *et al.*[163].

Methods. For optical spectroscopy, NPL dispersions were transferred to a quartz glass cuvette (10mm). PL spectroscopy was recorded using a Prizmatix Silver high power LED (emission peak 369 nm) for excitation and Avantes SensLine AvaSpec-HSC-TEC for data collection.

TEM was done using a JEOL1400 microscope (acceleration voltage 120 kV). The samples were deposited on carbon-coated copper grids (400 mesh) by drop-casting.

Results and discussion

Here, the recently developed approach described by Khodabakhshi *et al.*[163] should be transferred to CdSe/CdZnS NPLs due to the outstanding properties of NPLs[78, 79, 93]. Especially the extreme sharp emission of the NPLs makes them to promising candidates for light-emitting applications[79, 87, 281]. The surface of the NPLs has to be protected with an insulating layer to prevent electron transfer. To modify the surface of the NPLs, the same methods as described in the previous section was used (see Scheme 6.1). As a ligand for the ligand exchange, the diblock copolymer poly(styrene-block-cysteaminemethyldisulfide) as described by Khodabakhshi *et al.*[163] was used (see Figure 6.3, method A). For the polymer coating (see Figure 6.3, method b), poly(isobutylene-*alt*-maleic anhydride) was modified with dodecyl amine (75% of monomer units modified) and PS (20% of monomer units modified) (M_n= 5000 g/mol). As reference also bare NPLs stabilized with oleic acid were used. The NPLs modified following method A shows a long tail in absorption for higher wavelength and in TEM the accumulation of NPLs is visible,

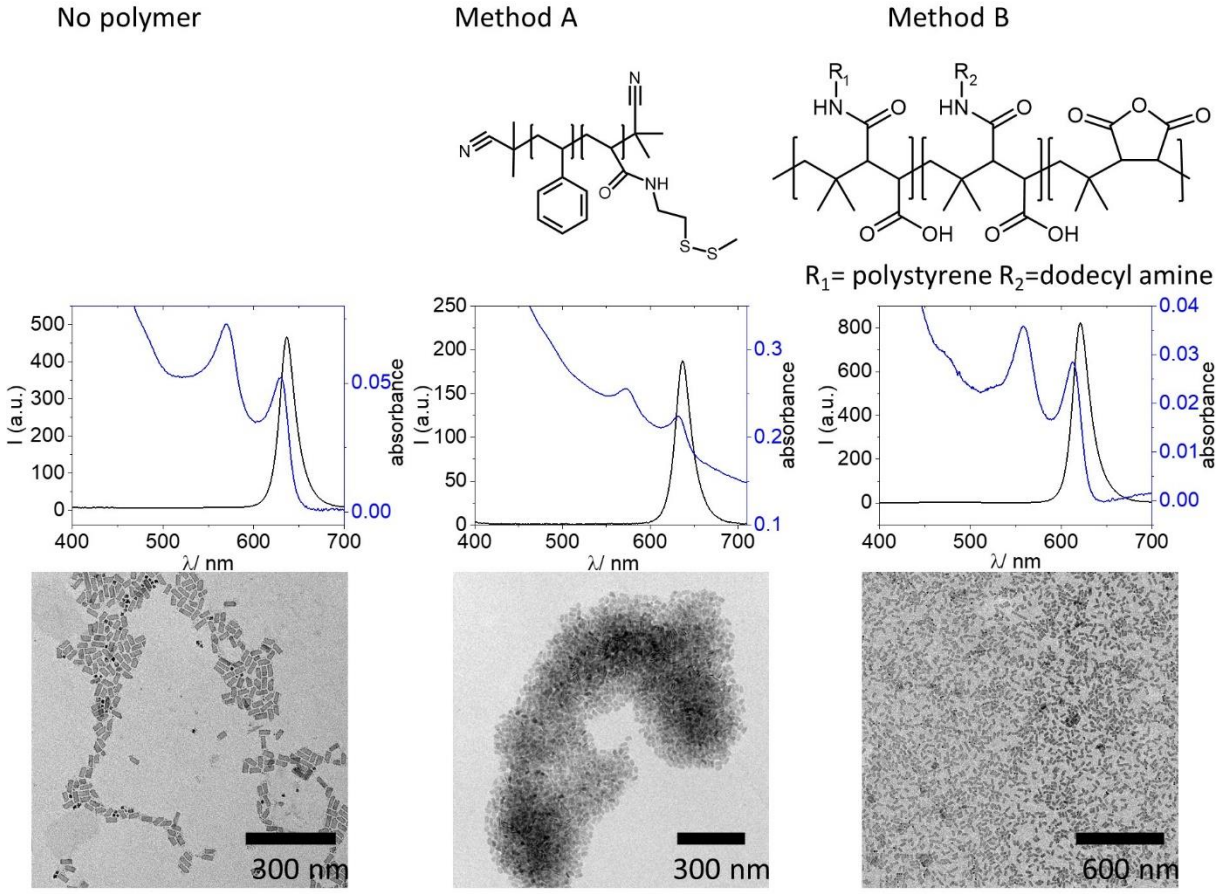

Figure 6.3: Modification of CdSe/CdZnS NPLs. Left: stabilized with oleic acid; middle: modified with PDMS following method A; right: polymer coated with PDMS following method B.

indicating the aggregation of the NPLs already in dispersion (see Figure 6.3, method A). The NPLs modified by using method B, are still well dispersed and non-aggregated after modification.

The NPLs are well separated from each other as shown in the TEM image and the inter-particle distances are larger compared to the non-modified NPLs. The unmodified NPLs and the modified NPLs (method B) were blended in PFO and the distribution of the NPLS was analyzed using SEM (see Figure 6.5). In both cases, the NPLs form islands located on the top of the PFO layer. The size of the islands is reduced from ~450 nm to ~190 nm using a protection layer around the NPLs. Also, more individual NPLs can be observed for the protected NPLs. This shows, that the layer around the NPLs helps to disperse the NPLs in the PFO host matrix. To analyze whether the observed islands are agglomerates distributed in the whole film volume or islands formed due to demixing during film preparation, the top and the bottom of the PFO layer were analyzed (see Figure 6.4). On the top of the PFO film, the island and some individual NPLs are visible (see Figure 6.4 a), however, on the bottom well distributed, randomly oriented NPLs are visible. By doubleling

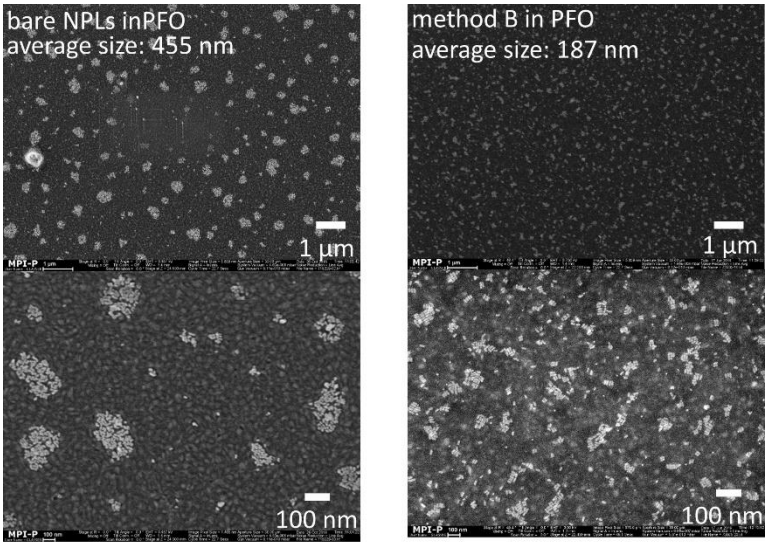

Figure 6.5: Films of PFO blended with NPLs. Left: bare NPLs stabilized with oleic acid; right: NPLs modified via polymer coating.

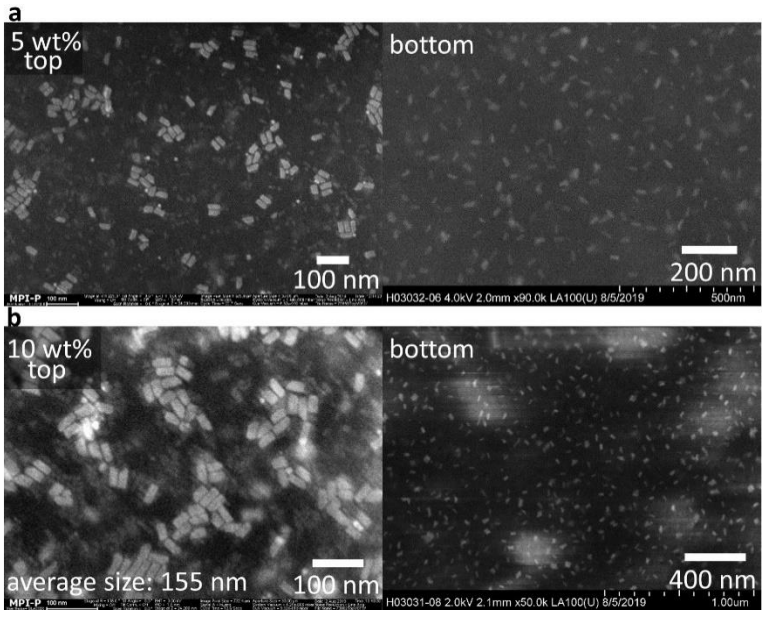

Figure 6.4 SEM images of NPLs (5 wt% and 10 wt%) dispersed in PFO, top and bottom of the film.

the weight concentration of the NPLs to 10 wt% (see Figure 6.4 b), the size of the islands do not increase, and on the bottom of the film still well distributes NPLs can be located. This finding indicates, a demixing process rather than an agglomeration process since for agglomeration, the agglomerates would be distributed in the whole film volume and the size of the agglomeration should increase with increasing NPL volume fractions.

Voltage-dependent electroluminescence (EL) spectra were recorded for bare NPLs blended in PFO and modified NPLs (method B) in PFO with a weight concentration of 5 % (see Figure 6.6). The bare NPLs in PFO show a strong voltage-dependent emission of the NPLs which is a strong indication for trap-assisted recombination. The insulating shell of oleic acid molecules is only ~ 1.5 nm thick and does not suppress the electron trapping[163]. Whereas the emission of the NPLs with the additional protection layer (method B) is voltage-independent. This speaks for better suppression of electron trapping.

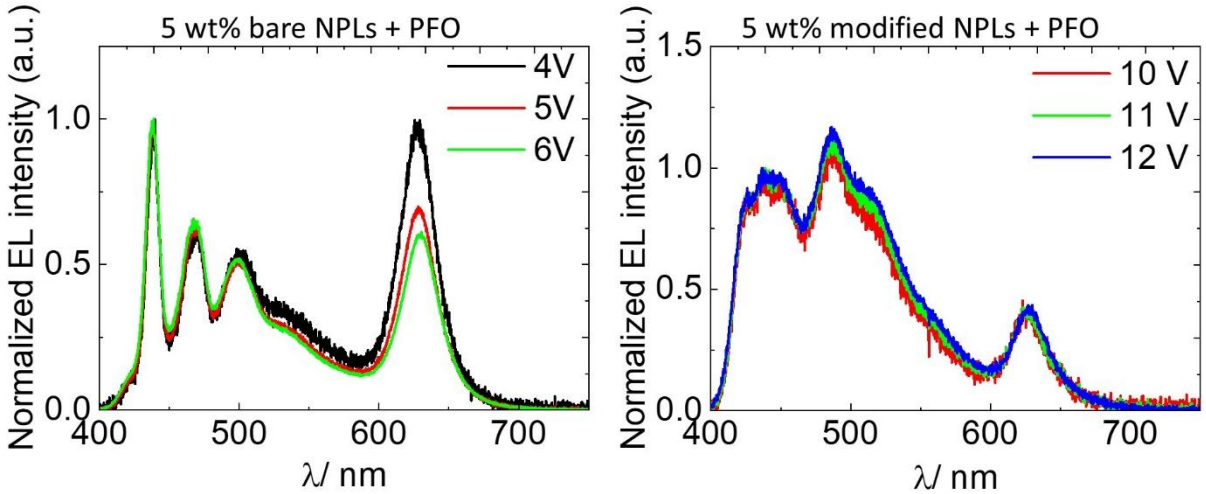

Figure 6.6: Voltage dependency of normalized EL spectra for PLED with 100 nm PFO:5 % bare NPLs blend active layer (left) and 100 nm PFO: 5 % NPL/PS-hybrid blend active layer.

In conclusion, two different methods for the modification of the NPLs surface was tested. The ligand exchange method is not sufficient to decouple electron trapping from the FRET process and the NPLs were strongly aggregated. For the polymer coating method B, better dispersibility of the NPLs could be observed and voltage-independent electroluminescence was recorded, indicating the successful suppression of electron trapping. In the future, the distribution of the NPLs in the host material has to be further improved to obtain single separated NPLs in the best case. In addition, to obtain a good performance of the device, the quantum yield of the NPLs has to be further optimized.

6.3 Template assisted self-assembly of CdSe nanoplatelets using crystalline polymer flakes

Introduction

As shown in chapter 4, the collective orientation of anisotropic NPLs is of utmost importance. The following chapter describes a different approach to collective orient the NPLs. Here, highly crystalline polymer flakes were used as a template to assemble the NPLs.

Polymers can mediate the self-assembly of NPs in order to help to build NP-polymer composites for applications ranging from electronic devices to catalysis[282]. For example, using block-co-polymers, NPs can be selective accumulated and oriented in one domain[283]. In addition, NPs can adsorb at polymeric interfaces and form aligned structures[129, 137]. By varying the surfaces, for instance using block-copolymer films, the interaction between the surface and the nanomaterial can be changed and the assembly can by directed[137, 284]. Especially the orientation of anisotropic NPs is of importance since the anisotropic properties are only accessible when the anisotropic NPs are collectively oriented[187]. For example, anisotropic CdSe NPLs exhibit strong anisotropic light emission[10, 84-86], high absorption cross sections[80, 81], enhanced energy transfer rates[82], and boosted optical gain[83]. Methods to form stacks out of the NPLs or films in the edge-up or face-down configuration are known in literature[84, 85, 192]. However, controlling the orientation of NPLs in bi-layers and simultaneously controlling the distance between the layers is difficult. Here, highly crystalline polyphosphoesters that form flat crystals in the size of several micrometers were used as a template to assemble the NPLs[285]. The crystalline polymers are synthesized using the acyclic diene metathesis (ADMET) polymerization technique[286]. The thickness of the polymer crystals can be precisely adjusted through equidistantly placed phosphoester groups acting as defects. The precisely controlled thickness of the polymer crystals can be later used to define the distance between two NPL layers assembled on each side of the flat polymer crystals. Furthermore, the side chain which is assumed to be excluded from the bulk crystallite can be varied[285] and therefore the surface with which the NPLs can interact can be modified.

Experimental Part

Chemicals. Octane (≥ 99%) were purchased from Roth.

Synthesis of 4 monolayer thick (4 ML) CdSe Nanoplatelets (NPLs). See chapter 4.2 for the synthesis of CdSe NPLs.

Synthesis of polyphosphorester polymers. The polymer with a chain length of 20 CH_2 units and the ethyl side chain was synthesized by Hisaschi Tee following the procedure described by Zheng *et al.*[285]. The polymers with a chain length of 20, 30 and 40 CH_2 repeating units and a phenyl side chain, were synthesized by Tobias Haider according to a procedure described in his Ph.D. thesis.

Preparation nanoplatelets-polymer flakes composite. The polymer (1 mg) was mixed with n-octane (1 mL). The mixture was heated up to 85 °C in an oil bath while stirring for 2 h. After dissolving the polymer, the heating was removed and the solution was cooled down overnight. The polymer crystallizes into flakes and the solution gets turbid. 400 µL polymer flake dispersion was mixed with the NPL dispersion in octane (10 µL or 20 µL).

Characterization. For optical spectroscopy, NPL-polymer flakes dispersions were transferred to a quartz glass cuvette (10 mm). PL spectra were recorded using a Prizmatix Silver high power LED (emission peak 369 nm) for excitation and Avantes SensLine AvaSpec-HSC-TEC for data collection.

Fluorescence lifetime measurements were conducted by Henry Halim with a FluoTime200 time-correlated single-photon counting setup. Samples were excited with a blue laser at 380 nm which was controlled by PicoQuant PDL 800-D. The signal was detected using a microchannel plate photomultiplier tube that was connected to PicoHarp 300 time-correlated single-photon counting system. The instrument response function was measured using a dispersion of silica NPs (LUDOX® HS-40 colloidal silica) in water. Time-resolved fluorescence intensity was measured at 512 nm. The measured data was fit to a double exponential function. The fitting was done with the following equation (6.I):

$$I(t)= \int_{\infty}^{t} IRF(t') \sum_{i=1}^{2} A_i e^{-\frac{t-t'}{\tau_i}} dt' \qquad (6.I)$$

IRF is instrument response function, A_i the amplitude of the ith component, in counts, τ_I the lifetime of the ith component, in nanoseconds and X^2 the quality of fitting.

TEM was done using a JEOL1400 microscope (acceleration voltage 120 kV). The samples were deposited on carbon-coated copper grids (400 mesh) by drop-casting.

For the fluorescence microscopy, a STED Leica Laser Scanning Confocal Microscope consisting of an inverse fluorescence microscope DMI 6000 CS equipped with multi-laser-combination was used. The objective was a 63x1.2 water objective and the laser (458 nm) was set to 20% (~1 mW).

Results and discussion

The polymer flake crystals (in the following referred to as polymer flakes) were prepared by dissolving the polymer (1mg/mL) in hot octane and cooling it down to room temperature. To study the interaction between 4ML CdSe NPLs and polymer flakes, CdSe NPLs were mixed with freshly prepared polymer flakes with different chain lengths (C20 and C30) and side chains (ethyl and phenyl). To allow complete attachment of the NPLs to the polymer flakes, the solution was kept standing for at least 4 h. The solution was drop casted on a TEM grid to study the attachment of the NPLs at the polymer flakes. The CdSe NPLs can be located on the surface of the polymer flakes (see Figure 6.7 a). Almost no free NPLs are found on the sample, indicating a strong affinity of the NPLs to the polymer flake surface. The NPLs are mainly oriented in the face-down configuration on the polymer flakes. Using the confocal fluorescence microscopy, it was proved that the NPLs are already attached to the polymer flakes in dispersion and the observed attachment is not caused by drying effects (see Figure 6.7 b).

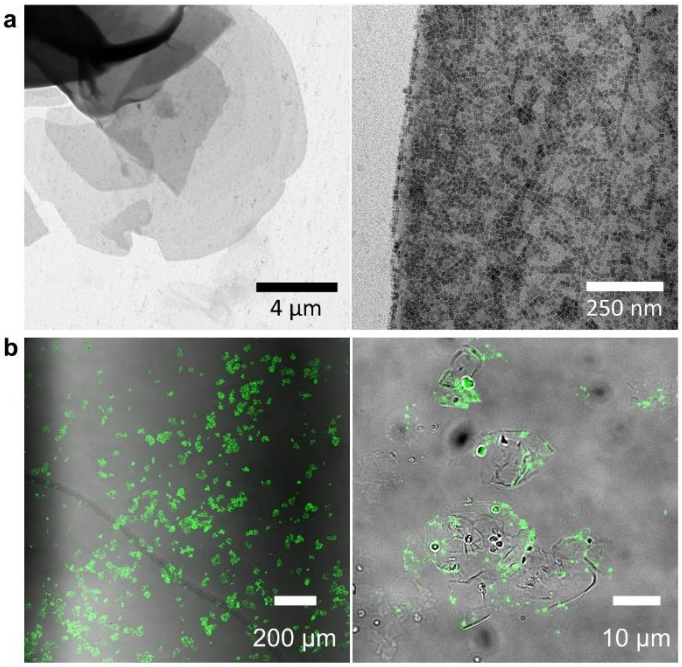

Figure 6.7: Assembly of CdSe NPLs on the polymer flake (C20, ethyl). (a) TEM micrograph of CdSe NPLs polymer flake composite. The CdSe NPLs are preferentially oriented in the face-down configuration; (b) fluorescence image of NPLs overlaid with bright field image of the polymer flakes (C20, phenyl).

The amount of NPLs was varied systematically to study the alignment of the NPLs on the polymer flake in more detail (see Figure 6.8). Using a small amount of NPLs, the polymer flakes are not completely covered, however, the NPLs are homogeneously distributed on the surface of the flakes in the face-down configuration. However, the edges of the polymer flake are preferentially covered with the NPLs compared to the flat surfaces. By increasing the NPL amount the coverage is increased and small stacks on top of the face-down assembly are observed.

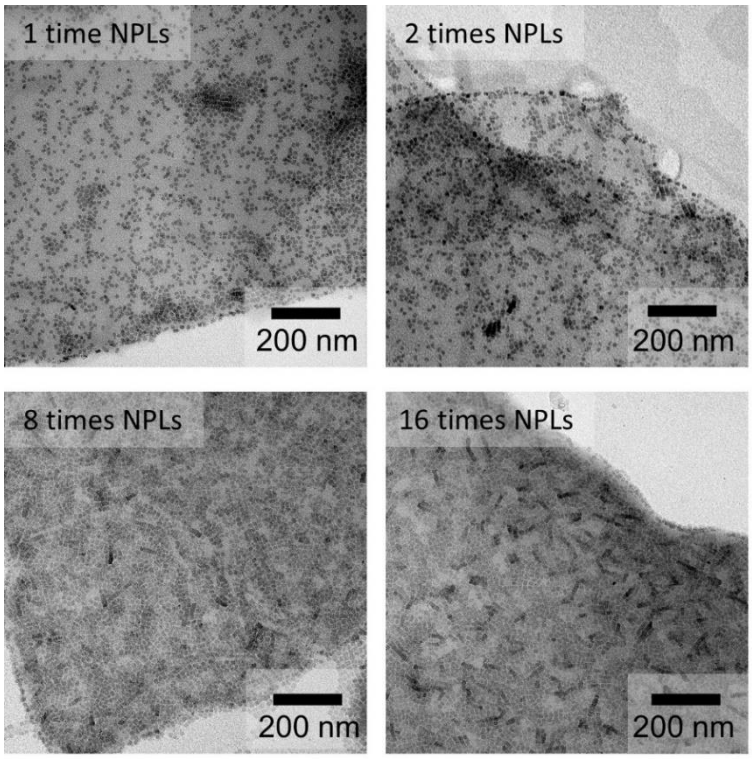

Figure 6.8: Increasing amount of NPLs covering the polymer flakes (C20, phenyl).

The adsorption of the NPLs to the polymer flakes can be described by hydrophobic/ vdW interactions between the alkyl based ligand shell of the myristate passivated NPLs and the polymer flakes. Neither the type of side chain in the polymer flakes(ethyl or phenyl) (see Figure 6.7 and Figure 6.8) nor the length of the repeating unit (C20 or C30) (see Figure 6.7 and Figure 6.9) changes the adsorption behavior. The polymer flakes themselves do not carry a charge and thus are not electrostatically or sterically stabilized. As a consequence, the large surface area exhibits high surface energies. By adsorbing NPLs in the face-down configuration at the polymer flake surface, the

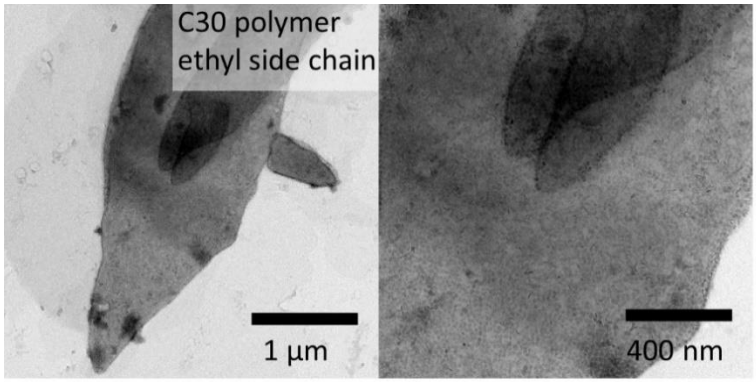

Figure 6.9: TEM micrographs of CdSe NPL- polymer flake composites. CdSe NPLs mixed with C30 polymer flakes with ethyl side chain.

surface energy of the polymer flakes and the NPLs is decreased by decreasing the high energy polymer flake surface area. Since edges are energetically every more expensive compared to flat surfaces, the edges are covered first.

The attachment of the NPLs to the polymer flake surface leads to closer distances between the NPLs. The thickness of the C20 polymer flake (lamellae thickness 3.1 nm) is smaller compared to the C30 polymer flake (lamellae thickness 4.8 nm) and the NPLs are closer together. The closer distance between NPLs affect the PL intensity and the lifetime of the NPLs due to energy transfer between the NPL layers (see Figure 6.10 a and b)[15]. The lifetime shortens from t_1=3.917 ns (pure NPL dispersion) to t_1=1.761 ns (NPL polymer flakes mixture (C30, ethyl)) and t_1=2.279 ns (NPL polymer flake mixture (C20, ethyl) (see Table 6.3).

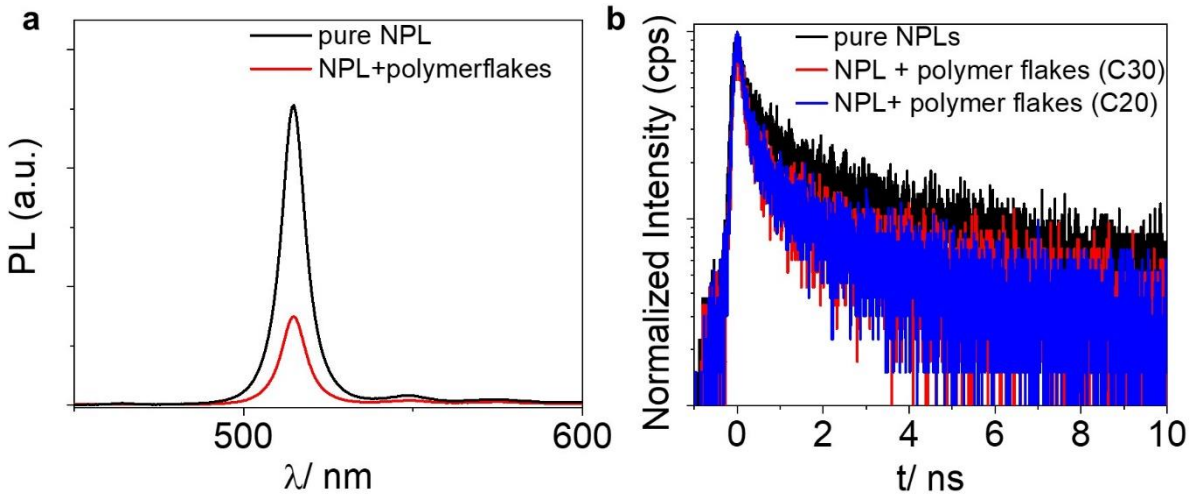

Figure 6.10: Optical properties of NPL- polymer flake composite. (a) PL spectra of pure NPLs and NPLs mixed with polymer flakes (C30, ethyl); (b) Lifetime of pure NPL and NPL mixed with polymer flakes (C30, ethyl).

Table 6.3: Fit data of lifetime measurements.

Sample	**X^2(reduced) [σ]**	**A_1/counts**	**τ_1 /ns**	**A_2/counts**	**τ_2/ns**
NPL	1.0228	28.5	3.917	63.2	0.525
NPL+ polymer flakes (C30)	1.0623	28.0	1.761	119465.4	0.002
NPL + polymer flakes (C20)	0.9696	25.3	2.279	291.0	0.152

However, a significant difference between the lifetimes of the NPLs aligned on a C20 polymer flake and C30 polymer flake is not observable. Here, it has to be noted, that due to the synthetic protocol ruthenium ions (originates from the used Grubbs I catalyst) are present as an impurity, which do strongly affect the optical properties of the CdSe NPLs. To test the effect

of the catalyst (Grubs catalyst generation I), the NPL stock solution were mixed with few milligrams of the catalyst. The PL intensity was recorded directly before and after addition of the catalyst (Figure 6.11). A strong reduction of the PL intensity in the presence of the catalyst is observed, indicating the quenching effect of ruthenium. Therefore no clear trend in the life-time data of the polymer flake-NPL assemblies could be obtained.

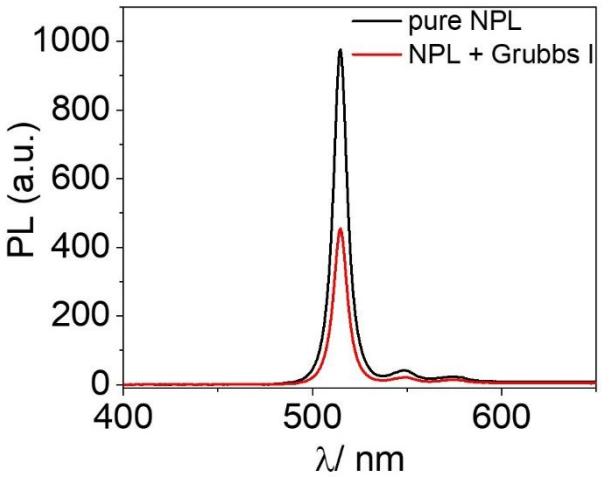

Figure 6.11: PL spectra of NPLs in the before and after the addition of the ruthenium-based catalyst for the ADMET polymerization. The PL intensity decrease upon addition of the ruthenium catalyst.

To further analyze the interaction between NPLs and polymer flakes and to use polymer flakes as a template for the directed assembly, a way to synthesize the polymers without the usage of any heavy metal catalyst is required. In addition, it would be interesting to study the distance dependency of the optical properties in more detail and to vary the distances between the bilayers over a broader range. However, so far, the polymer flakes containing C40 chains resulting in a lamellae thickness of 7.2 nm do not form nicely shaped flakes and could not be used in the study. Additionally, the content of ruthenium impurity is the highest for the C40 polymer and the PL of the NPLs is quenched completely in the presence of the polymer. Furthermore, to get access to the anisotropic properties in solid-state, the NPL-polymer flake composite has to be transferred onto substrates without folding of the polymer flakes. Since the polymer flakes are quite flexible, they tend to fold upon deposition on a substrate. Possible ways to improve the transfer to a substrate could be using smaller, less flexible flakes or film floatation techniques[136]. To do this, the formation process of the polymer flakes must be studied in more detail and optimized for our purpose.

7. Conclusion

In this thesis, promising perspectives and possibilities are shown to enhance existing properties of nanoparticles (chapter 3), induce new properties (chapter 4), control the orientation of nanoparticles in a film (chapter 4 and 6), and disperse nanoparticles without agglomeration in a host material for 3D printing, light emitting devices or microscopy (chapter 5 and 6) by successfully controlling the interaction between nanoparticles in dispersion. This work contributes to develop new assembled structures with properties like photoconductivity or polarized light emission, which are highly attractive for applications like polarized light emitting diodes.

In chapter 3, it is revealed that the interaction between carbon dots and polystyrene nanoparticles strongly enhance the photoluminescence (~5 fold). The enhancement is independent of the type of interaction (electrostatic or chemically bound) and can be reversible. So far, such an enhancement effect is only observed for directly adsorbed polymer chains but not for polymeric colloids. As perspective, this developed new colloidal carbon dot-polystyrene nanoparticle hybrid systems with tuned photoluminescence properties can be used in dye-sensitized solar cells, or photocatalysts to improve the performance.

Furthermore, a method for the controlled collective orientation of nanoplatelets is developed which avoids insulating additives (chapter 4). Our method is based on the kinetically control over the interactions between nanoplatelets. By adjusting the evaporation rate of a nanoplatelet dispersion, either by the choice of solvent, temperature, or solvent partial pressure, nanoplatelet films in the face-down or edge-up configuration can be obtained. The obtained films exhibit collective anisotropic properties like polarized light emission over on macroscopic scales making them useful for novel applications like polarized light emitting diodes. Furthermore, we reveal that the photoconductivity of these films strongly depends on the orientation. We could unveil that such dependence originates from the orientation-dependent inter-nanoplatelet electronic coupling strength. Our results can contribute to the development of novel nanoplatelet-based electroluminescent devices and photodetectors. The oriented films can be for example implemented in light emitting diodes or luminescent solar concentrators with enhanced light outcoupling.

Additionally, the interaction between nanoparticles are modified in order to avoid agglomeration during dispersion in a photoresin used for 3D printing (chapter 5). By preventing

the agglomeration, it was now possible to study the interference of individual dispersed nanoparticles on the two-photon polymerization 3D printing process. Such an understanding of the interferences and the resulting effects is indispensable to be able to print functional structures with embedded nanoparticles. To achieve high loadings of nanoparticles in the photoresin without agglomeration, the nanoparticles are modified with a tailor-made acrylate polymer. It is shown, that through material-dependent interaction of the properly dispersed nanoparticles with the laser beam or photo generated radicals, the resolution and the minimum feature size is improved. Additionally, strong thermal degradation of the resin occurs due to the absorption of light by metallic nanoparticles. The obtained fundamental understanding of the interaction of nanoparticles in the two-photon polymerization 3D printing process must be considered when creating nanoparticle-enriched, functional polymeric structures. As shown as perspective, fluorescent nanoplatelets are finally integrated in 3D printed gratings for enhanced light outcoupling. To improve the performance of the gratings a better printing accuracy and higher loadings are required.

In the last chapter of the thesis, ongoing projects are introduced (chapter 6). First, nanoplatelets are modified with a polydimethylsiloxane polymer to allow the dispersion in polydimethylsiloxane oil for fluorescence microscopy. Two different modification methods (ligand exchange and polymer coating) are studied. The polymer coating method leads to smaller agglomerates. However, the complete suppression of agglomeration is not achieved, yet and the surface modification must be optimized. In the second project, the same surface modification methods for nanoplatelets are applied using polystyrene. In this project, nanoplatelets are integrated in an organic light emitting diode. To achieve a good performance of the light emitting diode, an insulation layer around the nanoplatelets is required which suppresses electron trapping but allows energy transfer. The polymer coating of the nanoplatelets yield a remarkably reduction of the electron trapping. To further optimize the performance of the organic light emitting diode, the quantum yield of the nanoplatelets must be improved and a better distribution of the nanoplatelets in the host material to enhance the energy transfer is necessary. In the last project, flat crystalline polymer flakes are used to assemble nanoplatelets in the face-down configuration while simultaneously control the distance between two nanoplatelet layers. By such a distance control, it is possible to study optical and electronic effects (e.g. energy transfer) caused by the spacing of nanoplatelets. However, due to Ru-impurities in the polymer flakes which affect the photoluminescence of the nanoplatelets, it is

not possible to study the distance related effects. The purification protocol of the applied polymers must be optimized to remove all impurities.

Overall, the thesis demonstrated the possibility to achieve new properties by assembling nanomaterials. In the future, those assembled structures can be potentially in applications like light emitting diodes, solar cells or lasers. In addition, the expansion of the presented methods to nanoparticles with other properties (like magnetism, catalytic activity) opens a way to even more functional materials which can be applied in a wide variety of applications.

References

1. Pilotek, S.; Tabellion, F., Nanoparticles in coatings: Tailoring properties to applications. *Eur. coat. j* **2005,** (4), 170-176.
2. Monteiro-Riviere, N. A.; Wiench, K.; Landsiedel, R.; Schulte, S.; Inman, A. O.; Riviere, J. E., Safety Evaluation of Sunscreen Formulations Containing Titanium Dioxide and Zinc Oxide Nanoparticles in UVB Sunburned Skin: An In Vitro and In Vivo Study. *Toxicological Sciences* **2011,** *123* (1), 264-280.
3. Athinarayanan, J.; Periasamy, V. S.; Alsaif, M. A.; Al-Warthan, A. A.; Alshatwi, A. A., Presence of nanosilica (E551) in commercial food products: TNF-mediated oxidative stress and altered cell cycle progression in human lung fibroblast cells. *Cell Biology and Toxicology* **2014,** *30* (2), 89-100.
4. Herzog, F.; Clift, M. J. D.; Piccapietra, F.; Behra, R.; Schmid, O.; Petri-Fink, A.; Rothen-Rutishauser, B., Exposure of silver-nanoparticles and silver-ions to lung cells in vitro at the air-liquid interface. *Part Fibre Toxicol* **2013,** *10*, 11-11.
5. Naito, M.; Yokoyama, T.; Hosokawa, K.; Nogi, K., *Nanoparticle Technology Handbook*. Elsevier Science Publishers B. V.: 2018.
6. Vert, M.; Doi, Y.; Hellwich, K.-H.; Hess, M.; Hodge, P.; Kubisa, P.; Rinaudo, M.; Schué, F., Terminology for biorelated polymers and applications (IUPAC Recommendations 2012). In *Pure and Applied Chemistry*, 2012; Vol. 84, p 377.
7. Roduner, E., *Nanoscopic Materials: Size-Dependent Phenomena*. The Royal Society of Chemistry: Cambridge, 2006.
8. Neeleshwar, S.; Chen, C. L.; Tsai, C. B.; Chen, Y. Y.; Chen, C. C.; Shyu, S. G.; Seehra, M. S., Size-dependent properties of CdSe quantum dots. *Physical Review B* **2005,** *71* (20), 201307.
9. Thatai, S.; Khurana, P.; Prasad, S.; Kumar, D., A new way in nanosensors: Gold nanorods for sensing of Fe(III) ions in aqueous media. *Microchemical Journal* **2014,** *113*, 77-82.
10. Scott, R.; Heckmann, J.; Prudnikau, A. V.; Antanovich, A.; Mikhailov, A.; Owschimikow, N.; Artemyev, M.; Climente, J. I.; Woggon, U.; Grosse, N. B.; Achtstein, A. W., Directed emission of CdSe nanoplatelets originating from strongly anisotropic 2D electronic structure. *Nature Nanotechnology* **2017,** *12*, 1155.
11. Heckmann, J.; Scott, R.; Prudnikau, A. V.; Antanovich, A.; Owschimikow, N.; Artemyev, M.; Climente, J. I.; Woggon, U.; Grosse, N. B.; Achtstein, A. W., Directed Two-Photon Absorption in CdSe Nanoplatelets Revealed by k-Space Spectroscopy. *Nano Letters* **2017,** *17* (10), 6321-6329.
12. Tessier, M. D.; Biadala, L.; Bouet, C.; Ithurria, S.; Abecassis, B.; Dubertret, B., Phonon Line Emission Revealed by Self-Assembly of Colloidal Nanoplatelets. *ACS Nano* **2013,** *7* (4), 3332-3340.
13. Prodan, E.; Nordlander, P., Plasmon hybridization in spherical nanoparticles. *The Journal of Chemical Physics* **2004,** *120* (11), 5444-5454.
14. Murray, C. B.; Kagan, C. R.; Bawendi, M. G., Synthesis and Characterization of Monodisperse Nanocrystals and Close-Packed Nanocrystal Assemblies. *Annual Review of Materials Science* **2000,** *30* (1), 545-610.
15. Guzelturk, B.; Erdem, O.; Olutas, M.; Kelestemur, Y.; Demir, H. V., Stacking in Colloidal Nanoplatelets: Tuning Excitonic Properties. *ACS Nano* **2014,** *8* (12), 12524-12533.
16. Yugang, D.; Yuan, Z.; Yiping, T.; L., D., Nano-TiO2-modified photosensitive resin for RP. *Rapid Prototyping Journal* **2011,** *17* (4), 247-252.

17. Xu, X.; Ray, R.; Gu, Y.; Ploehn, H. J.; Gearheart, L.; Raker, K.; Scrivens, W. A., Electrophoretic Analysis and Purification of Fluorescent Single-Walled Carbon Nanotube Fragments. *Journal of the American Chemical Society* **2004,** *126* (40), 12736-12737.
18. Li, H.; Kang, Z.; Liu, Y.; Lee, S.-T., Carbon nanodots: synthesis, properties and applications. *Journal of Materials Chemistry* **2012,** *22* (46), 24230-24253.
19. Zhao, Q.-L.; Zhang, Z.-L.; Huang, B.-H.; Peng, J.; Zhang, M.; Pang, D.-W., Facile preparation of low cytotoxicity fluorescent carbon nanocrystals by electrooxidation of graphite. *Chemical Communications* **2008,** (41), 5116-5118.
20. Li, Z.; Wang, L.; Li, Y.; Feng, Y.; Feng, W., Frontiers in carbon dots: design, properties and applications. *Materials Chemistry Frontiers* **2019,** *3* (12), 2571-2601.
21. Dekaliuk, M. O.; Viagin, O.; Malyukin, Y. V.; Demchenko, A. P., Fluorescent carbon nanomaterials: "quantum dots" or nanoclusters? *Physical Chemistry Chemical Physics* **2014,** *16* (30), 16075-16084.
22. Liu, Y.; Tian, Y.; Tian, Y.; Wang, Y.; Yang, W., Carbon-Dot-Based Nanosensors for the Detection of Intracellular Redox State. *Advanced Materials* **2015,** *27* (44), 7156-7160.
23. Liu, M. L.; Chen, B. B.; Li, C. M.; Huang, C. Z., Carbon dots: synthesis, formation mechanism, fluorescence origin and sensing applications. *Green Chemistry* **2019,** *21* (3), 449-471.
24. Wang, X.; Feng, Y.; Dong, P.; Huang, J., A Mini Review on Carbon Quantum Dots: Preparation, Properties, and Electrocatalytic Application. *Frontiers in Chemistry* **2019,** *7* (671).
25. Wang, X.; Cao, L.; Yang, S.-T.; Lu, F.; Meziani, M. J.; Tian, L.; Sun, K. W.; Bloodgood, M. A.; Sun, Y.-P., Bandgap-Like Strong Fluorescence in Functionalized Carbon Nanoparticles. *Angewandte Chemie International Edition* **2010,** *49* (31), 5310-5314.
26. Lim, S. Y.; Shen, W.; Gao, Z., Carbon quantum dots and their applications. *Chemical Society Reviews* **2015,** *44* (1), 362-381.
27. Sun, Y.-P.; Zhou, B.; Lin, Y.; Wang, W.; Fernando, K. A. S.; Pathak, P.; Meziani, M. J.; Harruff, B. A.; Wang, X.; Wang, H.; Luo, P. G.; Yang, H.; Kose, M. E.; Chen, B.; Veca, L. M.; Xie, S.-Y., Quantum-Sized Carbon Dots for Bright and Colorful Photoluminescence. *Journal of the American Chemical Society* **2006,** *128* (24), 7756-7757.
28. He, H.; Wang, X.; Feng, Z.; Cheng, T.; Sun, X.; Sun, Y.; Xia, Y.; Wang, S.; Wang, J.; Zhang, X., Rapid microwave-assisted synthesis of ultra-bright fluorescent carbon dots for live cell staining, cell-specific targeting and in vivo imaging. *Journal of Materials Chemistry B* **2015,** *3* (24), 4786-4789.
29. Ding, H.; Yu, S.-B.; Wei, J.-S.; Xiong, H.-M., Full-Color Light-Emitting Carbon Dots with a Surface-State-Controlled Luminescence Mechanism. *ACS Nano* **2016,** *10* (1), 484-491.
30. Wang, H.; Sun, P.; Cong, S.; Wu, J.; Gao, L.; Wang, Y.; Dai, X.; Yi, Q.; Zou, G., Nitrogen-Doped Carbon Dots for "green" Quantum Dot Solar Cells. *Nanoscale Research Letters* **2016,** *11* (1), 1-6.
31. Gong, X.; Lu, W.; Paau, M. C.; Hu, Q.; Wu, X.; Shuang, S.; Dong, C.; Choi, M. M. F., Facile synthesis of nitrogen-doped carbon dots for Fe3+ sensing and cellular imaging. *Analytica Chimica Acta* **2015,** *861*, 74-84.
32. Li, H.; He, X.; Liu, Y.; Huang, H.; Lian, S.; Lee, S.-T.; Kang, Z., One-step ultrasonic synthesis of water-soluble carbon nanoparticles with excellent photoluminescent properties. *Carbon* **2011,** *49* (2), 605-609.
33. Liu, S.; Tian, J.; Wang, L.; Zhang, Y.; Qin, X.; Luo, Y.; Asiri, A. M.; Al-Youbi, A. O.; Sun, X., Hydrothermal Treatment of Grass: A Low-Cost, Green Route to Nitrogen-Doped, Carbon-Rich, Photoluminescent Polymer Nanodots as an Effective Fluorescent Sensing Platform for Label-Free Detection of Cu(II) Ions. *Advanced Materials* **2012,** *24* (15), 2037-2041.

34. Sahu, S.; Behera, B.; Maiti, T. K.; Mohapatra, S., Simple one-step synthesis of highly luminescent carbon dots from orange juice: application as excellent bio-imaging agents. *Chemical Communications* **2012,** *48* (70), 8835-8837.
35. Huang, H.; Li, C.; Zhu, S.; Wang, H.; Chen, C.; Wang, Z.; Bai, T.; Shi, Z.; Feng, S., Histidine-Derived Nontoxic Nitrogen-Doped Carbon Dots for Sensing and Bioimaging Applications. *Langmuir* **2014,** *30* (45), 13542-13548.
36. Wang, J.; Wang, C.-F.; Chen, S., Amphiphilic Egg-Derived Carbon Dots: Rapid Plasma Fabrication, Pyrolysis Process, and Multicolor Printing Patterns. *Angewandte Chemie* **2012,** *124* (37), 9431-9435.
37. Han, S.; Zhang, H.; Xie, Y.; Liu, L.; Shan, C.; Li, X.; Liu, W.; Tang, Y., Application of cow milk-derived carbon dots/Ag NPs composite as the antibacterial agent. *Applied Surface Science* **2015,** *328*, 368-373.
38. Liang, Y.; Zhang, H.; Zhang, Y.; Chen, F., Simple hydrothermal preparation of carbon nanodots and their application in colorimetric and fluorimetric detection of mercury ions. *Analytical Methods* **2015,** *7* (18), 7540-7547.
39. Zheng, X. T.; Ananthanarayanan, A.; Luo, K. Q.; Chen, P., Glowing Graphene Quantum Dots and Carbon Dots: Properties, Syntheses, and Biological Applications. *Small* **2015,** *11* (14), 1620-1636.
40. Baker, S. N.; Baker, G. A., Luminescent Carbon Nanodots: Emergent Nanolights. *Angewandte Chemie International Edition* **2010,** *49* (38), 6726-6744.
41. Yan, F.; Sun, Z.; Zhang, H.; Sun, X.; Jiang, Y.; Bai, Z., The fluorescence mechanism of carbon dots, and methods for tuning their emission color: a review. *Microchimica Acta* **2019,** *186* (8), 583.
42. Liu, M. L.; Yang, L.; Li, R. S.; Chen, B. B.; Liu, H.; Huang, C. Z., Large-scale simultaneous synthesis of highly photoluminescent green amorphous carbon nanodots and yellow crystalline graphene quantum dots at room temperature. *Green Chemistry* **2017,** *19* (15), 3611-3617.
43. Liu, H.; He, Z.; Jiang, L.-P.; Zhu, J.-J., Microwave-Assisted Synthesis of Wavelength-Tunable Photoluminescent Carbon Nanodots and Their Potential Applications. *ACS Applied Materials & Interfaces* **2015,** *7* (8), 4913-4920.
44. Jiang, K.; Sun, S.; Zhang, L.; Lu, Y.; Wu, A.; Cai, C.; Lin, H., Red, Green, and Blue Luminescence by Carbon Dots: Full-Color Emission Tuning and Multicolor Cellular Imaging. *Angewandte Chemie International Edition* **2015,** *54* (18), 5360-5363.
45. Li, H.; He, X.; Kang, Z.; Huang, H.; Liu, Y.; Liu, J.; Lian, S.; Tsang, C. H. A.; Yang, X.; Lee, S.-T., Water-Soluble Fluorescent Carbon Quantum Dots and Photocatalyst Design. *Angewandte Chemie International Edition* **2010,** *49* (26), 4430-4434.
46. Kim, S.; Hwang, S. W.; Kim, M.-K.; Shin, D. Y.; Shin, D. H.; Kim, C. O.; Yang, S. B.; Park, J. H.; Hwang, E.; Choi, S.-H.; Ko, G.; Sim, S.; Sone, C.; Choi, H. J.; Bae, S.; Hong, B. H., Anomalous Behaviors of Visible Luminescence from Graphene Quantum Dots: Interplay between Size and Shape. *ACS Nano* **2012,** *6* (9), 8203-8208.
47. Essner, J. B.; Kist, J. A.; Polo-Parada, L.; Baker, G. A., Artifacts and Errors Associated with the Ubiquitous Presence of Fluorescent Impurities in Carbon Nanodots. *Chemistry of Materials* **2018,** *30* (6), 1878-1887.
48. Zhu, S.; Zhao, X.; Song, Y.; Lu, S.; Yang, B., Beyond bottom-up carbon nanodots: Citric-acid derived organic molecules. *Nano Today* **2016,** *11* (2), 128-132.
49. Schneider, J.; Reckmeier, C. J.; Xiong, Y.; von Seckendorff, M.; Susha, A. S.; Kasák, P.; Rogach, A. L., Molecular Fluorescence in Citric Acid-Based Carbon Dots. *The Journal of Physical Chemistry C* **2017,** *121* (3), 2014-2022.

50. Righetto, M.; Privitera, A.; Fortunati, I.; Mosconi, D.; Zerbetto, M.; Curri, M. L.; Corricelli, M.; Moretto, A.; Agnoli, S.; Franco, L.; Bozio, R.; Ferrante, C., Spectroscopic Insights into Carbon Dot Systems. *The Journal of Physical Chemistry Letters* **2017**.
51. Bao, L.; Liu, C.; Zhang, Z.-L.; Pang, D.-W., Photoluminescence-Tunable Carbon Nanodots: Surface-State Energy-Gap Tuning. *Advanced Materials* **2015,** *27* (10), 1663-1667.
52. Wang, L.; Zhu, S.-J.; Wang, H.-Y.; Qu, S.-N.; Zhang, Y.-L.; Zhang, J.-H.; Chen, Q.-D.; Xu, H.-L.; Han, W.; Yang, B.; Sun, H.-B., Common Origin of Green Luminescence in Carbon Nanodots and Graphene Quantum Dots. *ACS Nano* **2014,** *8* (3), 2541-2547.
53. Sun, Z.; Li, X.; Wu, Y.; Wei, C.; Zeng, H., Origin of green luminescence in carbon quantum dots: specific emission bands originate from oxidized carbon groups. *New Journal of Chemistry* **2018,** *42* (6), 4603-4611.
54. Jia, X.; Li, J.; Wang, E., One-pot green synthesis of optically pH-sensitive carbon dots with upconversion luminescence. *Nanoscale* **2012,** *4* (18), 5572-5575.
55. Dong, Y.; Pang, H.; Yang, H. B.; Guo, C.; Shao, J.; Chi, Y.; Li, C. M.; Yu, T., Carbon-Based Dots Co-doped with Nitrogen and Sulfur for High Quantum Yield and Excitation-Independent Emission. *Angewandte Chemie International Edition* **2013,** *52* (30), 7800-7804.
56. Yu, P.; Wen, X.; Toh, Y.-R.; Tang, J., Temperature-Dependent Fluorescence in Carbon Dots. *The Journal of Physical Chemistry C* **2012,** *116* (48), 25552-25557.
57. Pan, D.; Zhang, J.; Li, Z.; Wu, C.; Yan, X.; Wu, M., Observation of pH-, solvent-, spin-, and excitation-dependent blue photoluminescence from carbon nanoparticles. *Chemical Communications* **2010,** *46* (21), 3681-3683.
58. Wang, J.; Sheng Li, R.; Zhi Zhang, H.; Wang, N.; Zhang, Z.; Huang, C. Z., Highly fluorescent carbon dots as selective and visual probes for sensing copper ions in living cells via an electron transfer process. *Biosensors and Bioelectronics* **2017,** *97*, 157-163.
59. Liu, J.-M.; Lin, L.-p.; Wang, X.-X.; Lin, S.-Q.; Cai, W.-L.; Zhang, L.-H.; Zheng, Z.-Y., Highly selective and sensitive detection of Cu2+ with lysine enhancing bovine serum albumin modified-carbon dots fluorescent probe. *Analyst* **2012,** *137* (11), 2637-2642.
60. Chen, T.-H.; Tseng, W.-L., Self-Assembly of Monodisperse Carbon Dots into High-Brightness Nanoaggregates for Cellular Uptake Imaging and Iron(III) Sensing. *Analytical Chemistry* **2017,** *89* (21), 11348-11356.
61. Atchudan, R.; Edison, T. N. J. I.; Chakradhar, D.; Perumal, S.; Shim, J.-J.; Lee, Y. R., Facile green synthesis of nitrogen-doped carbon dots using Chionanthus retusus fruit extract and investigation of their suitability for metal ion sensing and biological applications. *Sensors and Actuators B: Chemical* **2017,** *246*, 497-509.
62. Gonçalves, H.; Jorge, P. A. S.; Fernandes, J. R. A.; Esteves da Silva, J. C. G., Hg(II) sensing based on functionalized carbon dots obtained by direct laser ablation. *Sensors and Actuators B: Chemical* **2010,** *145* (2), 702-707.
63. Yan, F.; Zou, Y.; Wang, M.; Mu, X.; Yang, N.; Chen, L., Highly photoluminescent carbon dots-based fluorescent chemosensors for sensitive and selective detection of mercury ions and application of imaging in living cells. *Sensors and Actuators B: Chemical* **2014,** *192*, 488-495.
64. Strauss, V.; Margraf, J. T.; Dolle, C.; Butz, B.; Nacken, T. J.; Walter, J.; Bauer, W.; Peukert, W.; Spiecker, E.; Clark, T.; Guldi, D. M., Carbon Nanodots: Toward a Comprehensive Understanding of Their Photoluminescence. *Journal of the American Chemical Society* **2014,** *136* (49), 17308-17316.
65. Qu, K.; Wang, J.; Ren, J.; Qu, X., Carbon Dots Prepared by Hydrothermal Treatment of Dopamine as an Effective Fluorescent Sensing Platform for the Label-Free Detection of Iron(III) Ions and Dopamine. *Chemistry – A European Journal* **2013,** *19* (22), 7243-7249.

66. Ahmed, G. H. G.; Laíño, R. B.; Calzón, J. A. G.; García, M. E. D., Fluorescent carbon nanodots for sensitive and selective detection of tannic acid in wines. *Talanta* **2015,** *132*, 252-257.
67. da Silva Souza, D. R.; Caminhas, L. D.; de Mesquita, J. P.; Pereira, F. V., Luminescent carbon dots obtained from cellulose. *Materials Chemistry and Physics* **2018,** *203*, 148-155.
68. Hou, X.; Hu, Y.; Wang, P.; Yang, L.; Al Awak, M. M.; Tang, Y.; Twara, F. K.; Qian, H.; Sun, Y.-P., Modified facile synthesis for quantitatively fluorescent carbon dots. *Carbon* **2017,** *122*, 389-394.
69. Micro/nanoencapsulation of essential oils and fragrances: Focus on perfumed, antimicrobial, mosquito-repellent and medical textiles. *Journal of Microencapsulation* **2016,** *33* (6), 497-510.
70. Liu, Y.; Wang, P.; Shiral Fernando, K. A.; LeCroy, G. E.; Maimaiti, H.; Harruff-Miller, B. A.; Lewis, W. K.; Bunker, C. E.; Hou, Z.-L.; Sun, Y.-P., Enhanced fluorescence properties of carbon dots in polymer films. *Journal of Materials Chemistry C* **2016,** *4* (29), 6967-6974.
71. Alivisatos, A. P., Perspectives on the Physical Chemistry of Semiconductor Nanocrystals. *The Journal of Physical Chemistry* **1996,** *100* (31), 13226-13239.
72. Krauss, T. D.; Peterson, J. J., Electronic structure and optical transitions in colloidal semiconductor nanocrystals. In *Colloidal Quantum Dot Optoelectronics and Photovoltaics*, Sargent, E. H.; Konstantatos, G., Eds. Cambridge University Press: Cambridge, 2013; pp 59-86.
73. Buhro, W. E.; Colvin, V. L., Shape matters. *Nature Materials* **2003,** *2* (3), 138-139.
74. Chun, J.; Lee, J., Various Synthetic Methods for One-Dimensional Semiconductor Nanowires/Nanorods and Their Applications in Photovoltaic Devices. *European Journal of Inorganic Chemistry* **2010,** *2010* (27), 4251-4263.
75. Ithurria, S.; Dubertret, B., Quasi 2D Colloidal CdSe Platelets with Thicknesses Controlled at the Atomic Level. *Journal of the American Chemical Society* **2008,** *130* (49), 16504-16505.
76. Peng, Q.; Dong, Y.; Deng, Z.; Li, Y., Selective Synthesis and Characterization of CdSe Nanorods and Fractal Nanocrystals. *Inorganic Chemistry* **2002,** *41* (20), 5249-5254.
77. Riedinger, A.; Ott, F. D.; Mule, A.; Mazzotti, S.; Knüsel, P. N.; Kress, Stephan J. P.; Prins, F.; Erwin, S. C.; Norris, D. J., An intrinsic growth instability in isotropic materials leads to quasi-two-dimensional nanoplatelets. *Nature Materials* **2017**.
78. Tessier, M. D.; Mahler, B.; Nadal, B.; Heuclin, H.; Pedetti, S.; Dubertret, B., Spectroscopy of Colloidal Semiconductor Core/Shell Nanoplatelets with High Quantum Yield. *Nano Letters* **2013,** *13* (7), 3321-3328.
79. Ithurria, S.; Tessier, M. D.; Mahler, B.; Lobo, R. P. S. M.; Dubertret, B.; Efros, A. L., Colloidal nanoplatelets with two-dimensional electronic structure. *Nature Materials* **2011,** *10*, 936.
80. Yeltik, A.; Delikanli, S.; Olutas, M.; Kelestemur, Y.; Guzelturk, B.; Demir, H. V., Experimental Determination of the Absorption Cross-Section and Molar Extinction Coefficient of Colloidal CdSe Nanoplatelets. *The Journal of Physical Chemistry C* **2015,** *119* (47), 26768-26775.
81. Achtstein, A. W.; Antanovich, A.; Prudnikau, A.; Scott, R.; Woggon, U.; Artemyev, M., Linear Absorption in CdSe Nanoplates: The Thickness and Lateral Size Dependency of the Intrinsic Absorption. *The Journal of Physical Chemistry C* **2015,** *119* (34), 20156-20161.
82. Rowland, C. E.; Fedin, I.; Zhang, H.; Gray, S. K.; Govorov, A. O.; Talapin, D. V.; Schaller, R. D., Picosecond energy transfer and multiexciton transfer outpaces Auger recombination in binary CdSe nanoplatelet solids. *Nature Materials* **2015,** *14* (5), 484-489.

83. She, C.; Fedin, I.; Dolzhnikov, D. S.; Demortière, A.; Schaller, R. D.; Pelton, M.; Talapin, D. V., Low-Threshold Stimulated Emission Using Colloidal Quantum Wells. *Nano Letters* **2014,** *14* (5), 2772-2777.
84. Abécassis, B.; Tessier, M. D.; Davidson, P.; Dubertret, B., Self-Assembly of CdSe Nanoplatelets into Giant Micrometer-Scale Needles Emitting Polarized Light. *Nano Letters* **2014,** *14* (2), 710-715.
85. Gao, Y.; Weidman, M. C.; Tisdale, W. A., CdSe Nanoplatelet Films with Controlled Orientation of their Transition Dipole Moment. *Nano Letters* **2017,** *17* (6), 3837-3843.
86. Ma, X.; Diroll, B. T.; Cho, W.; Fedin, I.; Schaller, R. D.; Talapin, D. V.; Wiederrecht, G. P., Anisotropic Photoluminescence from Isotropic Optical Transition Dipoles in Semiconductor Nanoplatelets. *Nano Letters* **2018,** *18* (8), 4647-4652.
87. Chen, Z.; Nadal, B.; Mahler, B.; Aubin, H.; Dubertret, B., Quasi-2D Colloidal Semiconductor Nanoplatelets for Narrow Electroluminescence. *Advanced Functional Materials* **2014,** *24* (3), 295-302.
88. Lhuillier, E.; Pedetti, S.; Ithurria, S.; Heuclin, H.; Nadal, B.; Robin, A.; Patriarche, G.; Lequeux, N.; Dubertret, B., Electrolyte-Gated Field Effect Transistor to Probe the Surface Defects and Morphology in Films of Thick CdSe Colloidal Nanoplatelets. *ACS Nano* **2014,** *8* (4), 3813-3820.
89. Grim, J. Q.; Christodoulou, S.; Di Stasio, F.; Krahne, R.; Cingolani, R.; Manna, L.; Moreels, I., Continuous-wave biexciton lasing at room temperature using solution-processed quantum wells. *Nature Nanotechnology* **2014,** *9* (11), 891-895.
90. Ithurria, S.; Bousquet, G.; Dubertret, B., Continuous Transition from 3D to 1D Confinement Observed during the Formation of CdSe Nanoplatelets. *Journal of the American Chemical Society* **2011,** *133* (9), 3070-3077.
91. Mer, V. K. L., Nucleation in Phase Transitions. *Industrial & Engineering Chemistry* **1952,** *44* (6), 1270-1277.
92. Bertrand, G. H. V.; Polovitsyn, A.; Christodoulou, S.; Khan, A. H.; Moreels, I., Shape control of zincblende CdSe nanoplatelets. *Chemical Communications* **2016,** *52* (80), 11975-11978.
93. Scott, R.; Achtstein, A. W.; Prudnikau, A.; Antanovich, A.; Christodoulou, S.; Moreels, I.; Artemyev, M.; Woggon, U., Two Photon Absorption in II–VI Semiconductors: The Influence of Dimensionality and Size. *Nano Letters* **2015,** *15* (8), 4985-4992.
94. Kunneman, L. T.; Tessier, M. D.; Heuclin, H.; Dubertret, B.; Aulin, Y. V.; Grozema, F. C.; Schins, J. M.; Siebbeles, L. D. A., Bimolecular Auger Recombination of Electron–Hole Pairs in Two-Dimensional CdSe and CdSe/CdZnS Core/Shell Nanoplatelets. *The Journal of Physical Chemistry Letters* **2013,** *4* (21), 3574-3578.
95. Jana, S.; Phan, T. N. T.; Bouet, C.; Tessier, M. D.; Davidson, P.; Dubertret, B.; Abécassis, B., Stacking and Colloidal Stability of CdSe Nanoplatelets. *Langmuir* **2015,** *31* (38), 10532-10539.
96. Erdem, O.; Gungor, K.; Guzelturk, B.; Tanriover, I.; Sak, M.; Olutas, M.; Dede, D.; Kelestemur, Y.; Demir, H. V., Orientation-Controlled Nonradiative Energy Transfer to Colloidal Nanoplatelets: Engineering Dipole Orientation Factor. *Nano Letters* **2019,** *19* (7), 4297-4305.
97. Murray, W. A.; Auguié, B.; Barnes, W. L., Sensitivity of Localized Surface Plasmon Resonances to Bulk and Local Changes in the Optical Environment. *The Journal of Physical Chemistry C* **2009,** *113* (13), 5120-5125.
98. Endo, T.; Yamamura, S.; Nagatani, N.; Morita, Y.; Takamura, Y.; Tamiya, E., Localized surface plasmon resonance based optical biosensor using surface modified

nanoparticle layer for label-free monitoring of antigen–antibody reaction. *Science and Technology of Advanced Materials* **2005,** *6* (5), 491-500.
99. Su, J.; Zhou, Z.; Li, H.; Liu, S., Quantitative detection of human chorionic gonadotropin antigen via immunogold chromatographic test strips. *Analytical Methods* **2014,** *6* (2), 450-455.
100. Turkevich, J.; Stevenson, P. C.; Hillier, J., A study of the nucleation and growth processes in the synthesis of colloidal gold. *Discussions of the Faraday Society* **1951,** *11* (0), 55-75.
101. Aslan, K.; Pérez-Luna, V. H., Surface Modification of Colloidal Gold by Chemisorption of Alkanethiols in the Presence of a Nonionic Surfactant. *Langmuir* **2002,** *18* (16), 6059-6065.
102. Brust, M.; Walker, M.; Bethell, D.; Schiffrin, D. J.; Whyman, R., Synthesis of thiol-derivatised gold nanoparticles in a two-phase Liquid–Liquid system. *Journal of the Chemical Society, Chemical Communications* **1994,** (7), 801-802.
103. Love, J. C.; Estroff, L. A.; Kriebel, J. K.; Nuzzo, R. G.; Whitesides, G. M., Self-Assembled Monolayers of Thiolates on Metals as a Form of Nanotechnology. *Chemical Reviews* **2005,** *105* (4), 1103-1170.
104. Lee, S. H.; Jun, B.-H., Silver Nanoparticles: Synthesis and Application for Nanomedicine. *Int J Mol Sci* **2019,** *20* (4), 865.
105. Kelly, K. L.; Coronado, E.; Zhao, L. L.; Schatz, G. C., The Optical Properties of Metal Nanoparticles: The Influence of Size, Shape, and Dielectric Environment. *The Journal of Physical Chemistry B* **2003,** *107* (3), 668-677.
106. Link, S.; El-Sayed, M. A., Size and Temperature Dependence of the Plasmon Absorption of Colloidal Gold Nanoparticles. *The Journal of Physical Chemistry B* **1999,** *103* (21), 4212-4217.
107. Miller, M. M.; Lazarides, A. A., Sensitivity of Metal Nanoparticle Surface Plasmon Resonance to the Dielectric Environment. *The Journal of Physical Chemistry B* **2005,** *109* (46), 21556-21565.
108. Thaxton, C. S.; Rosi, N. L.; Mirkin, C. A., Optically and Chemically Encoded Nanoparticle Materials for DNA and Protein Detection. *MRS Bulletin* **2005,** *30* (5), 376-380.
109. Chegel, V.; Rachkov, O.; Lopatynskyi, A.; Ishihara, S.; Yanchuk, I.; Nemoto, Y.; Hill, J. P.; Ariga, K., Gold Nanoparticles Aggregation: Drastic Effect of Cooperative Functionalities in a Single Molecular Conjugate. *The Journal of Physical Chemistry C* **2012,** *116* (4), 2683-2690.
110. Moskovits, M., Surface-enhanced Raman spectroscopy: a brief retrospective. *Journal of Raman Spectroscopy* **2005,** *36* (6-7), 485-496.
111. Piludu, M.; Medda, L.; Monduzzi, M.; Salis, A., Gold Nanoparticles: A Powerful Tool to Visualize Proteins on Ordered Mesoporous Silica and for the Realization of Theranostic Nanobioconjugates. *Int J Mol Sci* **2018,** *19* (7), 1991.
112. Butt, H.-J.; Graf, K.; Kappl, M., *Physics and Chemistry of Interfaces*. Wiley-VCH: Weinheim, 2006.
113. Deryaguin, B.; Landau, L. D., *Acta Physicochim. URSS* **1941,** *14* (633).
114. Verwey, E. W.; Overbeek, J. T. G., *Theory of Stabilty of Lyophobic Colloids*. Elsevier: 1948; Vol. Amsterdam.
115. Lifshitz, E. M., *Soviet Physics Jetp-Ussr* **1956,** *2*, 73-83.
116. Gouy, G., *J. Phys.* **1910,** *4* (9).
117. Chapman, D. L., *Philos. Mag.* **1913,** *6* (25).
118. Stern, O., *Z. Electrochem.* **1924,** (30).
119. Tadros, T. F., *Colloidal Stability: The roel of Surface Forces I*. Wiley-VCH: Weinheim, 2007.

120. Asakura, S.; Oosawa, F., On Interaction between Two Bodies Immersed in a Solution of Macromolecules. *The Journal of Chemical Physics* **1954,** *22* (7), 1255-1256.
121. Nie, Z.; Petukhova, A.; Kumacheva, E., Properties and emerging applications of self-assembled structures made from inorganic nanoparticles. *Nature Nanotechnology* **2010,** *5* (1), 15-25.
122. Bishop, K. J. M.; Wilmer, C. E.; Soh, S.; Grzybowski, B. A., Nanoscale Forces and Their Uses in Self-Assembly. *Small* **2009,** *5* (14), 1600-1630.
123. Kalsin, A. M.; Fialkowski, M.; Paszewski, M.; Smoukov, S. K.; Bishop, K. J. M.; Grzybowski, B. A., Electrostatic Self-Assembly of Binary Nanoparticle Crystals with a Diamond-Like Lattice. *Science* **2006,** *312* (5772), 420.
124. Shevchenko, E. V.; Talapin, D. V.; Kotov, N. A.; O'Brien, S.; Murray, C. B., Structural diversity in binary nanoparticle superlattices. *Nature* **2006,** *439* (7072), 55-59.
125. Liao, C.-W.; Lin, Y.-S.; Chanda, K.; Song, Y.-F.; Huang, M. H., Formation of Diverse Supercrystals from Self-Assembly of a Variety of Polyhedral Gold Nanocrystals. *Journal of the American Chemical Society* **2013,** *135* (7), 2684-2693.
126. Kumar, S.; Lee, M. J.; Aswal, V. K.; Choi, S. M., Block-copolymer-induced long-range depletion interaction and clustering of silica nanoparticles in aqueous solution. *Physical Review E* **2013,** *87* (4), 042315.
127. Wang, T.; LaMontagne, D.; Lynch, J.; Zhuang, J.; Cao, Y. C., Colloidal superparticles from nanoparticle assembly. *Chemical Society Reviews* **2013,** *42* (7), 2804-2823.
128. Baranov, D.; Fiore, A.; van Huis, M.; Giannini, C.; Falqui, A.; Lafont, U.; Zandbergen, H.; Zanella, M.; Cingolani, R.; Manna, L., Assembly of Colloidal Semiconductor Nanorods in Solution by Depletion Attraction. *Nano Letters* **2010,** *10* (2), 743-749.
129. Liu, Z.; Pappacena, K.; Cerise, J.; Kim, J.; Durning, C. J.; O'Shaughness, B.; Levicky, R., Organization of Nanoparticles on Soft Polymer Surfaces. *Nano Letters* **2002,** *2* (3), 219-224.
130. Haes, A. J.; Van Duyne, R. P., A Nanoscale Optical Biosensor: Sensitivity and Selectivity of an Approach Based on the Localized Surface Plasmon Resonance Spectroscopy of Triangular Silver Nanoparticles. *Journal of the American Chemical Society* **2002,** *124* (35), 10596-10604.
131. Mihi, A.; Ocaña, M.; Míguez, H., Oriented Colloidal-Crystal Thin Films by Spin-Coating Microspheres Dispersed in Volatile Media. *Advanced Materials* **2006,** *18* (17), 2244-2249.
132. Dimitrov, A. S.; Nagayama, K., Continuous Convective Assembling of Fine Particles into Two-Dimensional Arrays on Solid Surfaces. *Langmuir* **1996,** *12* (5), 1303-1311.
133. Malaquin, L.; Kraus, T.; Schmid, H.; Delamarche, E.; Wolf, H., Controlled Particle Placement through Convective and Capillary Assembly. *Langmuir* **2007,** *23* (23), 11513-11521.
134. He, H. X.; Zhang, H.; Li, Q. G.; Zhu, T.; Li, S. F. Y.; Liu, Z. F., Fabrication of Designed Architectures of Au Nanoparticles on Solid Substrate with Printed Self-Assembled Monolayers as Templates. *Langmuir* **2000,** *16* (8), 3846-3851.
135. Artemyev, M.; Möller, B.; Woggon, U., Unidirectional Alignment of CdSe Nanorods. *Nano Letters* **2003,** *3* (4), 509-512.
136. Zhang, Q.; Gupta, S.; Emrick, T.; Russell, T. P., Surface-Functionalized CdSe Nanorods for Assembly in Diblock Copolymer Templates. *Journal of the American Chemical Society* **2006,** *128* (12), 3898-3899.
137. Son, J. G.; Bae, W. K.; Kang, H.; Nealey, P. F.; Char, K., Placement Control of Nanomaterial Arrays on the Surface-Reconstructed Block Copolymer Thin Films. *ACS Nano* **2009,** *3* (12), 3927-3934.

138. Dong, A.; Chen, J.; Vora, P. M.; Kikkawa, J. M.; Murray, C. B., Binary nanocrystal superlattice membranes self-assembled at the liquid–air interface. *Nature* **2010,** *466* (7305), 474-477.
139. Shipway, A. N.; Katz, E.; Willner, I., Nanoparticle Arrays on Surfaces for Electronic, Optical, and Sensor Applications. *ChemPhysChem* **2000,** *1* (1), 18-52.
140. Manapat, J. Z.; Chen, Q.; Ye, P.; Advincula, R. C., 3D Printing of Polymer Nanocomposites via Stereolithography. *Macromolecular Materials and Engineering* **2017,** *302* (9), 1600553-n/a.
141. Utela, B.; Storti, D.; Anderson, R.; Ganter, M., A review of process development steps for new material systems in three dimensional printing (3DP). *Journal of Manufacturing Processes* **2008,** *10* (2), 96-104.
142. Pham, D. T.; Dimov, S. S., Rapid prototyping and rapid tooling—the key enablers for rapid manufacturing. *Proceedings of the Institution of Mechanical Engineers, Part C: Journal of Mechanical Engineering Science* **2003,** *217* (1), 1-23.
143. Bertsch, A.; Jiguet, S.; Bernhard, P.; Renaud, P., Microstereolithography: a Review. *MRS Proceedings* **2002,** *758*, LL1.1.
144. Bertsch, A.; Renaud, P., Microstereolithography. In *Stereolithography: Materials, Processes and Applications*, Bártolo, P. J., Ed. Springer US: Boston, MA, 2011; pp 81-112.
145. *Three-Dimensional Mircofabrication Using Two-Photon Polymerization Fundamentals, Technology, and Applications*. Elsevier: Waltham, 2016.
146. Sakellari, I.; Kabouraki, E.; Gray, D.; Purlys, V.; Fotakis, C.; Pikulin, A.; Bityurin, N.; Vamvakaki, M.; Farsari, M., Diffusion-Assisted High-Resolution Direct Femtosecond Laser Writing. *ACS Nano* **2012,** *6* (3), 2302-2311.
147. Kawata, S.; Sun, H.-B.; Tanaka, T.; Takada, K., Finer features for functional microdevices. *Nature* **2001,** *412* (6848), 697-698.
148. Ovsianikov, A.; Chichkov, B. N., Two-Photon Polymerization – High Resolution 3D Laser Technology and Its Applications. In *Nanoelectronics and Photonics: From Atoms to Materials, Devices, and Architectures*, Korkin, A.; Rosei, F., Eds. Springer New York: New York, NY, 2008; pp 427-446.
149. Göppert-Mayer, M., Über Elementarakte mit zwei Quantensprüngen. *Annalen der Physik* **1931,** *401* (3), 273-294.
150. Kaiser, W.; Garrett, C. G. B., Two-Photon Excitation in Ca${\mathrm{F}}_{2}$: ${\mathrm{Eu}}^{2+}$. *Physical Review Letters* **1961,** *7* (6), 229-231.
151. Farahani, R. D.; Dubé, M.; Therriault, D., Three-Dimensional Printing of Multifunctional Nanocomposites: Manufacturing Techniques and Applications. *Advanced Materials* **2016,** *28* (28), 5794-5821.
152. Sugioka, K.; Cheng, Y., Femtosecond laser three-dimensional micro- and nanofabrication. *Applied Physics Reviews* **2014,** *1* (4), 041303.
153. Leigh, S. J.; Bradley, R. J.; Purssell, C. P.; Billson, D. R.; Hutchins, D. A., A Simple, Low-Cost Conductive Composite Material for 3D Printing of Electronic Sensors. *PLOS ONE* **2012,** *7* (11), e49365.
154. Ceylan, H.; Yasa, I. C.; Yasa, O.; Tabak, A. F.; Giltinan, J.; Sitti, M., 3D-Printed Biodegradable Microswimmer for Theranostic Cargo Delivery and Release. *ACS Nano* **2019,** *13* (3), 3353-3362.
155. Peng, Y.; Jradi, S.; Yang, X.; Dupont, M.; Hamie, F.; Dinh, X. Q.; Sun, X. W.; Xu, T.; Bachelot, R., 3D Photoluminescent Nanostructures Containing Quantum Dots Fabricated by Two-Photon Polymerization: Influence of Quantum Dots on the Spatial Resolution of Laser Writing. *Advanced Materials Technologies* **2019,** *4* (2), 1800522.

156. Rong, M. Z.; Zhang, M. Q.; Ruan, W. H., Surface modification of nanoscale fillers for improving properties of polymer nanocomposites: a review. *Materials Science and Technology* **2006,** *22* (7), 787-796.
157. Sun, L.; Warren, G. L.; O'Reilly, J. Y.; Everett, W. N.; Lee, S. M.; Davis, D.; Lagoudas, D.; Sue, H. J., Mechanical properties of surface-functionalized SWCNT/epoxy composites. *Carbon* **2008,** *46* (2), 320-328.
158. Postiglione, G.; Natale, G.; Griffini, G.; Levi, M.; Turri, S., UV-assisted three-dimensional printing of polymer nanocomposites based on inorganic fillers. *Polymer Composites* **2017,** *38* (8), 1662-1670.
159. Jonušauskas, L.; Lau, M.; Gruber, P.; Gökce, B.; Barcikowski, S.; Malinauskas, M.; Ovsianikov, A., Plasmon assisted 3D microstructuring of gold nanoparticle-doped polymers. *Nanotechnology* **2016,** *27* (15), 154001.
160. Ueno, K.; Juodkazis, S.; Shibuya, T.; Mizeikis, V.; Yokota, Y.; Misawa, H., Nanoparticle-Enhanced Photopolymerization. *The Journal of Physical Chemistry C* **2009,** *113* (27), 11720-11724.
161. Murazawa, N.; Ueno, K.; Mizeikis, V.; Juodkazis, S.; Misawa, H., Spatially Selective Nonlinear Photopolymerization Induced by the Near-Field of Surface Plasmons Localized on Rectangular Gold Nanorods. *The Journal of Physical Chemistry C* **2009,** *113* (4), 1147-1149.
162. Jonušauskas, L.; Varapnickas, S.; Rimšelis, G.; Malinauskas, M., *Plasmonically enhanced 3D laser lithography for high-throughput nanoprecision fabrication*. SPIE: 2017; Vol. 10092.
163. Khodabakhshi, E.; Klöckner, B.; Zentel, R.; Michels, J. J.; Blom, P. W. M., Suppression of electron trapping by quantum dot emitters using a grafted polystyrene shell. *Materials Horizons* **2019,** *6* (10), 2024-2031.
164. Pan, D.; Vargas-Morales, O.; Zern, B.; Anselmo, A. C.; Gupta, V.; Zakrewsky, M.; Mitragotri, S.; Muzykantov, V., The Effect of Polymeric Nanoparticles on Biocompatibility of Carrier Red Blood Cells. *PLOS ONE* **2016,** *11* (3), e0152074.
165. Duan, J.; Yu, J.; Feng, S.; Su, L., A rapid microwave synthesis of nitrogen–sulfur co-doped carbon nanodots as highly sensitive and selective fluorescence probes for ascorbic acid. *Talanta* **2016,** *153*, 332-339.
166. Shen, P.; Xia, Y., Synthesis-Modification Integration: One-Step Fabrication of Boronic Acid Functionalized Carbon Dots for Fluorescent Blood Sugar Sensing. *Analytical Chemistry* **2014,** *86* (11), 5323-5329.
167. Shi, L.; Li, Y.; Li, X.; Zhao, B.; Wen, X.; Zhang, G.; Dong, C.; Shuang, S., Controllable synthesis of green and blue fluorescent carbon nanodots for pH and Cu(2+) sensing in living cells. *Biosens Bioelectron* **2016,** *77*, 598-602.
168. Sun, X.; Lei, Y., Fluorescent carbon dots and their sensing applications. *TrAC Trends in Analytical Chemistry* **2017,** *89* (Supplement C), 163-180.
169. Cao, L.; Wang, X.; Meziani, M. J.; Lu, F.; Wang, H.; Luo, P. G.; Lin, Y.; Harruff, B. A.; Veca, L. M.; Murray, D.; Xie, S.-Y.; Sun, Y.-P., Carbon Dots for Multiphoton Bioimaging. *Journal of the American Chemical Society* **2007,** *129* (37), 11318-11319.
170. Zhai, X.; Zhang, P.; Liu, C.; Bai, T.; Li, W.; Dai, L.; Liu, W., Highly luminescent carbon nanodots by microwave-assisted pyrolysis. *Chemical Communications* **2012,** *48* (64), 7955-7957.
171. Liu, C.; Zhang, P.; Zhai, X.; Tian, F.; Li, W.; Yang, J.; Liu, Y.; Wang, H.; Wang, W.; Liu, W., Nano-carrier for gene delivery and bioimaging based on carbon dots with PEI-passivation enhanced fluorescence. *Biomaterials* **2012,** *33* (13), 3604-3613.

172. Mao, X.-J.; Zheng, H.-Z.; Long, Y.-J.; Du, J.; Hao, J.-Y.; Wang, L.-L.; Zhou, D.-B., Study on the fluorescence characteristics of carbon dots. *Spectrochimica Acta Part A: Molecular and Biomolecular Spectroscopy* **2010,** *75* (2), 553-557.
173. Shen, R.; Song, K.; Liu, H.; Li, Y.; Liu, H., Dramatic Fluorescence Enhancement of Bare Carbon Dots through Facile Reduction Chemistry. **2012,** *13* (15), 3549-3555.
174. Jiang, Z. C.; Lin, T. N.; Lin, H. T.; Talite, M. J.; Tzeng, T. T.; Hsu, C. L.; Chiu, K. P.; Lin, C. A. J.; Shen, J. L.; Yuan, C. T., A Facile and Low-Cost Method to Enhance the Internal Quantum Yield and External Light-Extraction Efficiency for Flexible Light-Emitting Carbon-Dot Films. *Scientific Reports* **2016,** *6* (1), 19991.
175. Holzapfel, V.; Musyanovych, A.; Landfester, K.; Lorenz, M. R.; Mailänder, V., Preparation of Fluorescent Carboxyl and Amino Functionalized Polystyrene Particles by Miniemulsion Polymerization as Markers for Cells. *Macromolecular Chemistry and Physics* **2005,** *206* (24), 2440-2449.
176. Wohnhaas, C.; Turshatov, A.; Mailänder, V.; Lorenz, S.; Baluschev, S.; Miteva, T.; Landfester, K., Annihilation Upconversion in Cells by Embedding the Dye System in Polymeric Nanocapsules. *Macromolecular Bioscience* **2011,** *11* (6), 772-778.
177. Zhai, Y.; Zhu, Z.; Zhu, C.; Ren, J.; Wang, E.; Dong, S., Multifunctional water-soluble luminescent carbon dots for imaging and Hg2+ sensing. *Journal of Materials Chemistry B* **2014,** *2* (40), 6995-6999.
178. Liu, S.; Tian, J.; Wang, L.; Luo, Y.; Zhai, J.; Sun, X., Preparation of photoluminescent carbon nitride dots from CCl4 and 1,2-ethylenediamine: a heat-treatment-based strategy. *Journal of Materials Chemistry* **2011,** *21* (32), 11726-11729.
179. Yang, Y.; Cui, J.; Zheng, M.; Hu, C.; Tan, S.; Xiao, Y.; Yang, Q.; Liu, Y., One-step synthesis of amino-functionalized fluorescent carbon nanoparticles by hydrothermal carbonization of chitosan. *Chemical Communications* **2012,** *48* (3), 380-382.
180. Liu, Y.-H.; Wang, F.; Wang, Y.; Gibbons, P. C.; Buhro, W. E., Lamellar Assembly of Cadmium Selenide Nanoclusters into Quantum Belts. *Journal of the American Chemical Society* **2011,** *133* (42), 17005-17013.
181. Schliehe, C.; Juarez, B. H.; Pelletier, M.; Jander, S.; Greshnykh, D.; Nagel, M.; Meyer, A.; Foerster, S.; Kornowski, A.; Klinke, C.; Weller, H., Ultrathin PbS Sheets by Two-Dimensional Oriented Attachment. **2010,** *329* (5991), 550-553.
182. Joo, J.; Son, J. S.; Kwon, S. G.; Yu, J. H.; Hyeon, T., Low-Temperature Solution-Phase Synthesis of Quantum Well Structured CdSe Nanoribbons. *Journal of the American Chemical Society* **2006,** *128* (17), 5632-5633.
183. Ott, F. D.; Riedinger, A.; Ochsenbein, D. R.; Knüsel, P. N.; Erwin, S. C.; Mazzotti, M.; Norris, D. J., Ripening of Semiconductor Nanoplatelets. *Nano Letters* **2017,** *17* (11), 6870-6877.
184. Yoon, D.-E.; Kim, W. D.; Kim, D.; Lee, D.; Koh, S.; Bae, W. K.; Lee, D. C., Origin of Shape-Dependent Fluorescence Polarization from CdSe Nanoplatelets. *The Journal of Physical Chemistry C* **2017,** *121* (44), 24837-24844.
185. Antanovich, A.; Prudnikau, A.; Artemyev, M., Anisotropy of Structure and Optical Properties of Self-Assembled and Oriented Colloidal CdSe Nanoplatelets. *zpch* **2018,** *232* (9-11), 1619.
186. Boles, M. A.; Engel, M.; Talapin, D. V., Self-Assembly of Colloidal Nanocrystals: From Intricate Structures to Functional Materials. *Chemical Reviews* **2016,** *116* (18), 11220-11289.
187. Thorkelsson, K.; Bai, P.; Xu, T., Self-assembly and applications of anisotropic nanomaterials: A review. *Nano Today* **2015,** *10* (1), 48-66.

188. Reichhelm, A.; Haubold, D.; Eychmüller, A., Ligand Versatility in Supercrystal Formation. **2017,** *27* (39), 1700361.
189. Boneschanscher, M. P.; Evers, W. H.; Geuchies, J. J.; Altantzis, T.; Goris, B.; Rabouw, F. T.; van Rossum, S. A. P.; van der Zant, H. S. J.; Siebbeles, L. D. A.; Van Tendeloo, G.; Swart, I.; Hilhorst, J.; Petukhov, A. V.; Bals, S.; Vanmaekelbergh, D., Long-range orientation and atomic attachment of nanocrystals in 2D honeycomb superlattices. **2014,** *344* (6190), 1377-1380.
190. Barrow, S. J.; Funston, A. M.; Wei, X.; Mulvaney, P., DNA-directed self-assembly and optical properties of discrete 1D, 2D and 3D plasmonic structures. *Nano Today* **2013,** *8* (2), 138-167.
191. Antanovich, A.; Prudnikau, A.; Matsukovich, A.; Achtstein, A.; Artemyev, M., Self-Assembly of CdSe Nanoplatelets into Stacks of Controlled Size Induced by Ligand Exchange. *The Journal of Physical Chemistry C* **2016,** *120* (10), 5764-5775.
192. Jana, S.; Davidson, P.; Abécassis, B., CdSe Nanoplatelets: Living Polymers. **2016,** *55* (32), 9371-9374.
193. Diroll, B. T.; Greybush, N. J.; Kagan, C. R.; Murray, C. B., Smectic Nanorod Superlattices Assembled on Liquid Subphases: Structure, Orientation, Defects, and Optical Polarization. *Chemistry of Materials* **2015,** *27* (8), 2998-3008.
194. Dong, A.; Chen, J.; Vora, P. M.; Kikkawa, J. M.; Murray, C. B., Binary nanocrystal superlattice membranes self-assembled at the liquid–air interface. *Nature* **2010,** *466*, 474.
195. Rossinelli, A. A.; Riedinger, A.; Marques-Gallego, P.; Knusel, P. N.; Antolinez, F. V.; Norris, D. J., High-temperature growth of thick-shell CdSe/CdS core/shell nanoplatelets. *Chemical Communications* **2017,** *53* (71), 9938-9941.
196. Sommerfeld, A., Über die Fortpflanzung des Lichtes in dispergierenden Medien. **1914,** *349* (10), 177-202.
197. Neyts, K. A., Simulation of light emission from thin-film microcavities. *J. Opt. Soc. Am. A* **1998,** *15* (4), 962-971.
198. Yeh, P., *Optical Waves in Layered Media*. Wiley-Interscience: 2005.
199. Novotny, L., Allowed and forbidden light in near-field optics. I. A single dipolar light source. *J. Opt. Soc. Am. A* **1997,** *14* (1), 91-104.
200. Chance, R. R.; Prock, A.; Silbey, R., Molecular Fluorescence and Energy Transfer Near Interfaces. In *Advances in Chemical Physics*, pp 1-65.
201. Schmidt, T. D.; Lampe, T.; Sylvinson M. R, D.; Djurovich, P. I.; Thompson, M. E.; Brütting, W., Emitter Orientation as a Key Parameter in Organic Light-Emitting Diodes. *Physical Review Applied* **2017,** *8* (3), 037001.
202. Ulbricht, R.; Hendry, E.; Shan, J.; Heinz, T. F.; Bonn, M., Carrier dynamics in semiconductors studied with time-resolved terahertz spectroscopy. *Reviews of Modern Physics* **2011,** *83* (2), 543-586.
203. Merkl, P.; Mooshammer, F.; Steinleitner, P.; Girnghuber, A.; Lin, K. Q.; Nagler, P.; Holler, J.; Schüller, C.; Lupton, J. M.; Korn, T.; Ovesen, S.; Brem, S.; Malic, E.; Huber, R., Ultrafast transition between exciton phases in van der Waals heterostructures. *Nature Materials* **2019,** *18* (7), 691-696.
204. Kaindl, R. A.; Carnahan, M. A.; Hägele, D.; Lövenich, R.; Chemla, D. S., Ultrafast terahertz probes of transient conducting and insulating phases in an electron–hole gas. *Nature* **2003,** *423* (6941), 734-738.
205. Scott, R.; Achtstein, A. W.; Prudnikau, A. V.; Antanovich, A.; Siebbeles, L. D. A.; Artemyev, M.; Woggon, U., Time-Resolved Stark Spectroscopy in CdSe Nanoplatelets: Exciton Binding Energy, Polarizability, and Field-Dependent Radiative Rates. *Nano Letters* **2016,** *16* (10), 6576-6583.

206. Paik, T.; Ko, D.-K.; Gordon, T. R.; Doan-Nguyen, V.; Murray, C. B., Studies of liquid crystalline self-assembly of GdF_3 nanoplates by in-plane, out-of-plane SAXS. *ACS nano* **2011,** *5* (10), 8322-8330.
207. Reichert, C.; Welton, T., *Solvents and solvent effects in organic chemistry*. 3rd Edition ed.; Wiley-VCH Publishers,: 2003; Vol. 15, p 2014.
208. Sedgwick, R. S.; Hoerr, C. W.; Harwood, H. J., SOLUBILITIES OF SATURATED FATTY ACID ESTERS. *The Journal of Organic Chemistry* **1952,** *17* (2), 327-337.
209. Calvo, B.; Collado, I.; Cepeda, E. A., Solubilities of Palmitic Acid in Pure Solvents and Its Mixtures. *Journal of Chemical & Engineering Data* **2009,** *54* (1), 64-68.
210. Singh, S.; Tomar, R.; ten Brinck, S.; De Roo, J.; Geiregat, P.; Martins, J. C.; Infante, I.; Hens, Z., Colloidal CdSe Nanoplatelets, A Model for Surface Chemistry/Optoelectronic Property Relations in Semiconductor Nanocrystals. *Journal of the American Chemical Society* **2018,** *140* (41), 13292-13300.
211. Mann, S., Self-assembly and transformation of hybrid nano-objects and nanostructures under equilibrium and non-equilibrium conditions. *Nature Materials* **2009,** *8* (10), 781-792.
212. Xia, Y.; Nguyen, T. D.; Yang, M.; Lee, B.; Santos, A.; Podsiadlo, P.; Tang, Z.; Glotzer, S. C.; Kotov, N. A., Self-assembly of self-limiting monodisperse supraparticles from polydisperse nanoparticles. *Nature Nanotechnology* **2011,** *6* (9), 580-587.
213. Ramsden, J. J.; Ottewill, R. H., The stability of superspheres. **1987,** *413* (1845), 407-414.
214. Kolasinski, K. W., *Surface Science: Foundations of Catalysis and Nanoscience Second Edition*. John Wiley & Sons Inc: Chichester, 2009; Vol. 2.
215. Antoine, C., Tensions des vapeurs; vouvelle relation entre les tensions et les températures. *C. R. Acad. Sci.* **1888,** *107*, 681– 684.
216. Born, P.; Munoz, A.; Cavelius, C.; Kraus, T., Crystallization Mechanisms in Convective Particle Assembly. *Langmuir* **2012,** *28* (22), 8300-8308.
217. Doblas, D.; Kister, T.; Cano-Bonilla, M.; Gonzalez-Gariia, L.; Kraus, T., Colloidal Solubility and Agglomeration of Apolar Nanoparticles in Different Solvents. *Nano Letters* **2019,** *19* (8), 5246-5252.
218. Napper, D. H., Steric stabilization. *Journal of Colloid and Interface Science* **1977,** *58* (2), 390-407.
219. Bigioni, T. P.; Lin, X.-M.; Nguyen, T. T.; Corwin, E. I.; Witten, T. A.; Jaeger, H. M., Kinetically driven self assembly of highly ordered nanoparticle monolayers. *Nature Materials* **2006,** *5*, 265.
220. Matioli, E.; Brinkley, S.; Kelchner, K. M.; Hu, Y.-L.; Nakamura, S.; DenBaars, S.; Speck, J.; Weisbuch, C., High-brightness polarized light-emitting diodes. *Light: Science & Applications* **2012,** *1* (8), e22-e22.
221. Tisdale, W. A.; Zhu, X. Y., Artificial atoms on semiconductor surfaces. *Proceedings of the National Academy of Sciences* **2011,** *108* (3), 965.
222. Lin, Y.; Ling, X.; Yu, L.; Huang, S.; Hsu, A. L.; Lee, Y.-H.; Kong, J.; Dresselhaus, M. S.; Palacios, T., Dielectric Screening of Excitons and Trions in Single-Layer MoS2. *Nano Letters* **2014,** *14* (10), 5569-5576.
223. Komsa, H.-P.; Krasheninnikov, A. V., Effects of confinement and environment on the electronic structure and exciton binding energy of MoS${}_{2}$ from first principles. *Physical Review B* **2012,** *86* (24), 241201.
224. Tries, A.; Osella, S.; Zhang, P.; Xu, F.; Kläui, M.; Mai, Y.; Beljonne, D.; Wang, H. I., Gigantic Binding Energy and Ultrafast Dynamics of Excitons in Graphene Nanoribbons. *arXiv preprint arXiv:1911.04431* **2019**.

225. Chen, Z.; Wang, H. I.; Teyssandier, J.; Mali, K. S.; Dumslaff, T.; Ivanov, I.; Zhang, W.; Ruffieux, P.; Fasel, R.; Räder, H. J.; Turchinovich, D.; De Feyter, S.; Feng, X.; Kläui, M.; Narita, A.; Bonn, M.; Müllen, K., Chemical Vapor Deposition Synthesis and Terahertz Photoconductivity of Low-Band-Gap N = 9 Armchair Graphene Nanoribbons. *Journal of the American Chemical Society* **2017,** *139* (10), 3635-3638.
226. Hendry, E.; Schins, J. M.; Candeias, L. P.; Siebbeles, L. D. A.; Bonn, M., Efficiency of Exciton and Charge Carrier Photogeneration in a Semiconducting Polymer. *Physical Review Letters* **2004,** *92* (19), 196601.
227. Ivanov, I.; Hu, Y.; Osella, S.; Beser, U.; Wang, H. I.; Beljonne, D.; Narita, A.; Müllen, K.; Turchinovich, D.; Bonn, M., Role of Edge Engineering in Photoconductivity of Graphene Nanoribbons. *Journal of the American Chemical Society* **2017,** *139* (23), 7982-7988.
228. Straub, M.; Nguyen, L. H.; Fazlic, A.; Gu, M., Complex-shaped three-dimensional microstructures and photonic crystals generated in a polysiloxane polymer by two-photon microstereolithography. *Optical Materials* **2004,** *27* (3), 359-364.
229. Malinauskas, M.; Žukauskas, A.; Purlys, V.; Gaidukevičiu¯tė, A.; Balevičius, Z.; Piskarskas, A.; Fotakis, C.; Pissadakis, S.; Gray, D.; Gadonas, R.; Vamvakaki, M.; Farsari, M., 3D microoptical elements formed in a photostructurable germanium silicate by direct laser writing. *Optics and Lasers in Engineering* **2012,** *50* (12), 1785-1788.
230. Schizas, C.; Melissinaki, V.; Gaidukeviciute, A.; Reinhardt, C.; Ohrt, C.; Dedoussis, V.; Chichkov, B. N.; Fotakis, C.; Farsari, M.; Karalekas, D., On the design and fabrication by two-photon polymerization of a readily assembled micro-valve. *The International Journal of Advanced Manufacturing Technology* **2010,** *48* (5), 435-441.
231. Danilevicius, P.; Rezende, R. A.; Pereira, F. D. A. S.; Selimis, A.; Kasyanov, V.; Noritomi, P. Y.; Silva, J. V. L. d.; Chatzinikolaidou, M.; Farsari, M.; Mironov, V., Burr-like, laser-made 3D microscaffolds for tissue spheroid encagement. *Biointerphases* **2015,** *10* (2), 021011.
232. Carlotti, M.; Mattoli, V., Functional Materials for Two-Photon Polymerization in Microfabrication. *Small 0* (0), 1902687.
233. Marino, A.; Barsotti, J.; de Vito, G.; Filippeschi, C.; Mazzolai, B.; Piazza, V.; Labardi, M.; Mattoli, V.; Ciofani, G., Two-Photon Lithography of 3D Nanocomposite Piezoelectric Scaffolds for Cell Stimulation. *ACS Applied Materials & Interfaces* **2015,** *7* (46), 25574-25579.
234. Liu, Y.; Xiong, W.; Li, D. W.; Lu, Y.; Huang, X.; Liu, H.; Fan, L. S.; Jiang, L.; Silvain, J.-F.; Lu, Y. F., Precise assembly and joining of silver nanowires in three dimensions for highly conductive composite structures. *International Journal of Extreme Manufacturing* **2019,** *1* (2), 025001.
235. Bhushan, B.; Kundu, T.; Singh, B. P., Two-photon absorption spectrum of silver nanoparticles. *Optics Communications* **2012,** *285* (24), 5420-5424.
236. Olesiak-Banska, J.; Waszkielewicz, M.; Obstarczyk, P.; Samoc, M., Two-photon absorption and photoluminescence of colloidal gold nanoparticles and nanoclusters. *Chemical Society Reviews* **2019,** *48* (15), 4087-4117.
237. Zhang, Z.; Berg, A.; Levanon, H.; Fessenden, R. W.; Meisel, D., On the Interactions of Free Radicals with Gold Nanoparticles. *Journal of the American Chemical Society* **2003,** *125* (26), 7959-7963.
238. Chappell, M. A.; Miller, L. F.; Price, C. L., Reversible exchange of stable nitroxyl radicals on nanosilver particles. *Environmental Chemistry* **2015,** *12* (2), 198-203.
239. Maurel, V.; Laferrière, M.; Billone, P.; Godin, R.; Scaiano, J. C., Free Radical Sensor Based on CdSe Quantum Dots with Added 4-Amino-2,2,6,6-Tetramethylpiperidine Oxide Functionality. *The Journal of Physical Chemistry B* **2006,** *110* (33), 16353-16358.

240. Kumar, S. K.; Krishnamoorti, R., Nanocomposites: Structure, Phase Behavior, and Properties. *Annual Review of Chemical and Biomolecular Engineering* **2010,** *1* (1), 37-58.
241. Schaefer, D. W.; Justice, R. S., How Nano Are Nanocomposites? *Macromolecules* **2007,** *40* (24), 8501-8517.
242. Roth, P. J.; Kessler, D.; Zentel, R.; Theato, P., A Method for Obtaining Defined End Groups of Polymethacrylates Prepared by the RAFT Process during Aminolysis. *Macromolecules* **2008,** *41* (22), 8316-8319.
243. Fan, Z.; Serrano, M. K.; Schaper, A.; Agarwal, S.; Greiner, A., Polymer/Nanoparticle Hybrid Materials of Precise Dimensions by Size-Exclusive Fishing of Metal Nanoparticles. *Advanced Materials* **2015,** *27* (26), 3888-3893.
244. Riedinger, A.; Zhang, F.; Dommershausen, F.; Röcker, C.; Brandholt, S.; Nienhaus, G. U.; Koert, U.; Parak, W. J., Ratiometric Optical Sensing of Chloride Ions with Organic Fluorophore–Gold Nanoparticle Hybrids: A Systematic Study of Design Parameters and Surface Charge Effects. *Small* **2010,** *6* (22), 2590-2597.
245. Niskanen, J.; Shan, J.; Tenhu, H.; Jiang, H.; Kauppinen, E.; Barranco, V.; Picó, F.; Yliniemi, K.; Kontturi, K., Synthesis of copolymer-stabilized silver nanoparticles for coating materials. *Colloid and Polymer Science* **2010,** *288* (5), 543-553.
246. Mahler, B.; Nadal, B.; Bouet, C.; Patriarche, G.; Dubertret, B., Core/Shell Colloidal Semiconductor Nanoplatelets. *Journal of the American Chemical Society* **2012,** *134* (45), 18591-18598.
247. Halim, H.; Simon, J.; Lieberwirth, I.; Mailaender, V.; Koynov, K.; Riedinger, A., Water-dispersed semiconductor nanoplatelets with high fluorescence brightness, chemical and colloidal stability. *Journal of Materials Chemistry B* **2019**.
248. Guney, M. G.; Fedder, G. K., Estimation of line dimensions in 3D direct laser writing lithography. *Journal of Micromechanics and Microengineering* **2016,** *26* (10), 105011.
249. Zhao, P. X.; Li, N.; Astruc, D., State of the art in gold nanoparticle synthesis. *Coord. Chem. Rev.* **2013,** *257* (3-4), 638-665.
250. Battocchio, C.; Meneghini, C.; Fratoddi, I.; Venditti, I.; Russo, M. V.; Aquilanti, G.; Maurizio, C.; Bondino, F.; Matassa, R.; Rossi, M.; Mobilio, S.; Polzonetti, G., Silver Nanoparticles Stabilized with Thiols: A Close Look at the Local Chemistry and Chemical Structure. *The Journal of Physical Chemistry C* **2012,** *116* (36), 19571-19578.
251. Rogach, A. L.; Kornowski, A.; Gao, M.; Eychmüller, A.; Weller, H., Synthesis and Characterization of a Size Series of Extremely Small Thiol-Stabilized CdSe Nanocrystals. *The Journal of Physical Chemistry B* **1999,** *103* (16), 3065-3069.
252. Corbierre, M. K.; Cameron, N. S.; Sutton, M.; Laaziri, K.; Lennox, R. B., Gold Nanoparticle/Polymer Nanocomposites: Dispersion of Nanoparticles as a Function of Capping Agent Molecular Weight and Grafting Density. *Langmuir* **2005,** *21* (13), 6063-6072.
253. Smith, G. D.; Bedrov, D., Dispersing Nanoparticles in a Polymer Matrix: Are Long, Dense Polymer Tethers Really Necessary? *Langmuir* **2009,** *25* (19), 11239-11243.
254. Kabir, M. M.; Kelkar, V. A.; Adams, D. K.; Toussaint, K. C., Two Photon Lithography. 2018.
255. Hao, T.; Riman, R. E., Calculation of interparticle spacing in colloidal systems. *Journal of Colloid and Interface Science* **2006,** *297* (1), 374-377.
256. Cumberland, D. J.; Crawford, R. J., *The packing of particles*. Elsevier: 1987.
257. Bagheri, A.; Jin, J., Photopolymerization in 3D Printing. *ACS Applied Polymer Materials* **2019,** *1* (4), 593-611.
258. Zheng, L.; Kurselis, K.; El-Tamer, A.; Hinze, U.; Reinhardt, C.; Overmeyer, L.; Chichkov, B., Nanofabrication of High-Resolution Periodic Structures with a Gap Size Below 100 nm by Two-Photon Polymerization. *Nanoscale Research Letters* **2019,** *14* (1), 134.

259. Govorov, A. O.; Richardson, H. H., Generating heat with metal nanoparticles. *Nano Today* **2007,** *2* (1), 30-38.
260. Liu, Y.; Campbell, J. H.; Stein, O.; Jiang, L.; Hund, J.; Lu, Y., Deformation Behavior of Foam Laser Targets Fabricated by Two-Photon Polymerization. *Nanomaterials (Basel)* **2018,** *8* (7), 498.
261. Prins, F.; Kim, D. K.; Cui, J.; De Leo, E.; Spiegel, L. L.; McPeak, K. M.; Norris, D. J., Direct Patterning of Colloidal Quantum-Dot Thin Films for Enhanced and Spectrally Selective Out-Coupling of Emission. *Nano Letters* **2017,** *17* (3), 1319-1325.
262. Matterson, B. J.; Lupton, J. M.; Safonov, A. F.; Salt, M. G.; Barnes, W. L.; Samuel, I. D. W., Increased Efficiency and Controlled Light Output from a Microstructured Light-Emitting Diode. **2001,** *13* (2), 123-127.
263. Schmid, M.; Ludescher, D.; Giessen, H., Optical properties of photoresists for femtosecond 3D printing: refractive index, extinction, luminescence-dose dependence, aging, heat treatment and comparison between 1-photon and 2-photon exposure. *Opt. Mater. Express* **2019,** *9* (12), 4564-4577.
264. Folch, A.; Toner, M., Cellular Micropatterns on Biocompatible Materials. *Biotechnology Progress* **1998,** *14* (3), 388-392.
265. Yue, Z.; Liu, X.; Molino, P. J.; Wallace, G. G., Bio-functionalisation of polydimethylsiloxane with hyaluronic acid and hyaluronic acid – Collagen conjugate for neural interfacing. *Biomaterials* **2011,** *32* (21), 4714-4724.
266. Papadopoulos, P.; Deng, X.; Mammen, L.; Drotlef, D.-M.; Battagliarin, G.; Li, C.; Müllen, K.; Landfester, K.; del Campo, A.; Butt, H.-J.; Vollmer, D., Wetting on the Microscale: Shape of a Liquid Drop on a Microstructured Surface at Different Length Scales. *Langmuir* **2012,** *28* (22), 8392-8398.
267. Baumli, P.; Teisala, H.; Bauer, H.; Garcia-Gonzalez, D.; Damle, V.; Geyer, F.; D'Acunzi, M.; Kaltbeitzel, A.; Butt, H.-J.; Vollmer, D. Flow-Induced Long-Term Stable Slippery Surfaces *Adv Sci (Weinh)* [Online], 2019, p. 1900019. PubMed. (accessed 2019/06//).
268. Talapin, D. V.; Lee, J.-S.; Kovalenko, M. V.; Shevchenko, E. V., Prospects of Colloidal Nanocrystals for Electronic and Optoelectronic Applications. *Chemical Reviews* **2010,** *110* (1), 389-458.
269. Scheutjens, J. M. H. M.; Fleer, G. J., Effect of polymer adsorption and depletion on the interaction between two parallel surfaces. *Advances in Colloid and Interface Science* **1982,** *16* (1), 361-380.
270. Bringer, A.; Eisenriegler, E.; Schlesener, F.; Hanke, A., Polymer depletion interaction between a particle and a wall. *The European Physical Journal B - Condensed Matter and Complex Systems* **1999,** *11* (1), 101-119.
271. Feigin, R. I.; Napper, D. H., Depletion stabilization and depletion flocculation. *Journal of Colloid and Interface Science* **1980,** *75* (2), 525-541.
272. P., S. J. M.; A., G. P.; Jinguk, K.; Qiang, F.; Andri, H.; E., K. S.; G., Q. G., High-performance thin film composite membranes with well-defined poly(dimethylsiloxane)-b-poly(ethylene glycol) copolymer additives for CO2 separation. *Journal of Polymer Science Part A: Polymer Chemistry* **2015,** *53* (12), 1500-1511.
273. Pellegrino, T.; Manna, L.; Kudera, S.; Liedl, T.; Koktysh, D.; Rogach, A. L.; Keller, S.; Rädler, J.; Natile, G.; Parak, W. J., Hydrophobic Nanocrystals Coated with an Amphiphilic Polymer Shell: A General Route to Water Soluble Nanocrystals. *Nano Letters* **2004,** *4* (4), 703-707.
274. Tang, C. W.; VanSlyke, S. A., Organic electroluminescent diodes. **1987,** *51* (12), 913-915.

275. Reineke, S.; Lindner, F.; Schwartz, G.; Seidler, N.; Walzer, K.; Lüssem, B.; Leo, K., White organic light-emitting diodes with fluorescent tube efficiency. *Nature* **2009,** *459* (7244), 234-238.
276. Forrest, S. R., The path to ubiquitous and low-cost organic electronic appliances on plastic. *Nature* **2004,** *428* (6986), 911-918.
277. Nicolai, H. T.; Hof, A.; Blom, P. W. M., Device Physics of White Polymer Light-Emitting Diodes. *Advanced Functional Materials* **2012,** *22* (10), 2040-2047.
278. Bae, W. K.; Lim, J.; Zorn, M.; Kwak, J.; Park, Y.-S.; Lee, D.; Lee, S.; Char, K.; Zentel, R.; Lee, C., Reduced efficiency roll-off in light-emitting diodes enabled by quantum dot–conducting polymer nanohybrids. *Journal of Materials Chemistry C* **2014,** *2* (25), 4974-4979.
279. Kuik, M.; Wetzelaer, G.-J. A. H.; Nicolai, H. T.; Craciun, N. I.; De Leeuw, D. M.; Blom, P. W. M., 25th Anniversary Article: Charge Transport and Recombination in Polymer Light-Emitting Diodes. *Advanced Materials* **2014,** *26* (4), 512-531.
280. Anni, M.; Manna, L.; Cingolani, R.; Valerini, D.; Cretí, A.; Lomascolo, M., Förster energy transfer from blue-emitting polymers to colloidal CdSe⁄ZnS core shell quantum dots. *Applied Physics Letters* **2004,** *85* (18), 4169-4171.
281. Xiao, P.; Huang, J.; Yan, D.; Luo, D.; Yuan, J.; Liu, B.; Liang, D., Emergence of Nanoplatelet Light-Emitting Diodes. *Materials (Basel)* **2018,** *11* (8), 1376.
282. Shenhar, R.; Norsten, T. B.; Rotello, V. M., Polymer-Mediated Nanoparticle Assembly: Structural Control and Applications. *Advanced Materials* **2005,** *17* (6), 657-669.
283. Krook, N. M.; Ford, J.; Maréchal, M.; Rannou, P.; Meth, J. S.; Murray, C. B.; Composto, R. J., Alignment of Nanoplates in Lamellar Diblock Copolymer Domains and the Effect of Particle Volume Fraction on Phase Behavior. *ACS Macro Letters* **2018**, 1400-1407.
284. Brenner, T.; Paulus, M.; Schroer, M. A.; Tiemeyer, S.; Sternemann, C.; Möller, J.; Tolan, M.; Degen, P.; Rehage, H., Adsorption of nanoparticles at the solid–liquid interface. *Journal of Colloid and Interface Science* **2012,** *374* (1), 287-290.
285. Zheng, Y.-R.; Tee, H. T.; Wei, Y.; Wu, X.-L.; Mezger, M.; Yan, S.; Landfester, K.; Wagener, K.; Wurm, F. R.; Lieberwirth, I., Morphology and Thermal Properties of Precision Polymers: The Crystallization of Butyl Branched Polyethylene and Polyphosphoesters. *Macromolecules* **2016,** *49* (4), 1321-1330.
286. Wagener, K. B.; Boncella, J. M.; Nel, J. G., Acyclic diene metathesis (ADMET) polymerization. *Macromolecules* **1991,** *24* (10), 2649-2657.

Curriculum vitae

PERSONAL INFORMATION Rebecca Momper

Sex female

Date of birth 22.10.1991

Nationality german

momper@mpip-mainz.mpg.de

rebeccamomper@web.de

EDUCATION AND TRAINING

11/2016 – present

Ph.D.

Max Planck Institute for Polymer Research, Mainz

Title: From the colloidal dispersion to the solid-state: Controlling properties by inter-particle distance and orientation

Supervised by Prof. Dr. Katharina Landfester, Dr. Andreas Riedinger and Dr. Markus Bannwarth

Master of Science, Chemistry

Johannes Gutenberg- University, Mainz

overall grade: 1.5

Master thesis in the group of Prof. Dr. Katharina Landfester,

Max Planck Institute for Polymer Research, Mainz (grade: 1.3)

Title: Carbon Dots as fluorescent Labels - From fluorescent Microwave Labeling of Dispersions to Filter Membranes with End-of-Use Indication

Supervised by Prof. Dr. Katharina Landfester and Dr. Markus Bannwarth

Bachelor of Science, Chemistry

Johannes Gutenberg- University, Mainz

overall grade: 1.7

Bachelor thesis in the group of Prof. Dr. Angelika Kühnle (grade: 1.0)

Title: Einfluss des pH-Werts auf die Komplexbildung von Farbstoffmolekülen auf Calcit

High School, (Abitur)

2007- 2011 Gymnasium am Kurfürstlichen Schloss, Mainz

2002- 2007 Immanuel Kant Gymnasium, Rüsselsheim

overall grade: 1.8

WORK EXPERIENCE

08/2014 – 11/2014 **Student research assistant**
Johannes Gutenberg-University, Mainz
In the group of Prof. Dr. Angelika Kühnle

08/2012 – 08/2012 **Working student**
Celanese, Frankfurt

02/2012 – 03/2012 **Working student**
Celanese, Frankfurt

STIPEND

10/2015 – 10/2016 **Deutschlandstipend**
Funded by BASF

SEMINARS

01/2018 – 06/2019 **Ada Lovelace Mentoring Program**
Mentoring program for young female natural scientists
Mentor from industry, coaching, and seminars
Softskill courses: Self-marketing
Leadership
Voice and Body Language
Successful Negotiations

LANGUAGE

Mother tongue	german
Other language	english (fluent)

COMPUTER

MS Office	good
Origin	good

PUBLICATIONS

Rebecca Momper, Antonio Ibanez Landeta, Long Yang, Henry Halim, Héloïse Thérien-Aubin, Eberhard Bodenschatz, Katharina Landfester, Andreas Riedinger: *On the interference of plasmonic and semiconductor nanoparticles with stereolithographic 3D printing.* In preparation

Rebecca Momper, Heng Zhang, Shuai Chen, Henry Halim, Ewald Johannes, Stoyan Yordanov, Daniele Braga, Balthasar Blülle, David Doblas, Tobias Kraus, Mischa Bonn, Hai I. Wang; Andreas Riedinger: *Kinetic control over self-assembly of semiconductor nanoplatelets and their ultrafast photoconductivity.* In Nano Letters https://doi.org/10.1021/acs.nanolett.9b05270 (2020).

Rebecca Momper, Julian Steinbrecher, Matthias Dorn, Irina Rörich, Simon Bretschneider, Manuel Tonigold, Charusheela Ramanan, Sandra Ritz, Volker Mailänder, Katharina Landfester, Markus B Bannwarth: *Enhanced photoluminescence properties of a carbon dot system through surface interaction with polymeric nanoparticles.* In Journal of Colloid and interface science 518 (2018) 11-20. (Cover in issue 517 (2018))

Alice Antonello, Gerhard Jakob, Paolo Dolcet, Rebecca Momper, Maria Kokkinopoulou, Katharina Landfester Rafael Muñoz-Espí, and Silvia Gross: *Synergy of Miniemulsion and Solvothermal Conditions for the Low-Temperature Crystallization of Magnetic Nanostructured Transition-Metal Ferrites.* In Chemistry of Materials 29 (2017) No. 3, pp 985 -997

Rebecca Momper, Martin Nalbach, Karin Lichtenstein, Ralf Bechstein, Angelika Kühnle: *Stabilization of Polar Step Edges on Calcite (10.4) by the Adsorption of Congo Red.* In Langmuir 31 (2015) No. 26, pp 7283 – 7287

ORAL PRESENTATIONS

Rebecca Momper, Henry Halim, Ewald Johannes, Andreas Riedinger: Kinetically driven self-assembly of semiconductor nanoplatelets. *European Material Research Spring Meeting,* 27th to 31th of May 2019, Nice, France.

Rebecca Momper, Julian Steinbrecher, Matthias Dorn, Irina Rörich, Simon Bretschneider, Manuel Tonigold, Charusheela Ramanan, Sandra Ritz, Volker Mailänder, Katharina Landfester, Markus B Bannwarth: Enhanced photoluminescence properties of a carbon dot system through surface interaction with polymeric nanoparticles. *Particle-Based Materials Symposium* 9th – 10th of November 2017, Saarbrücken, Germany